A workability study on floating installation of monopiles using the MUST

J.B. Tjaberings

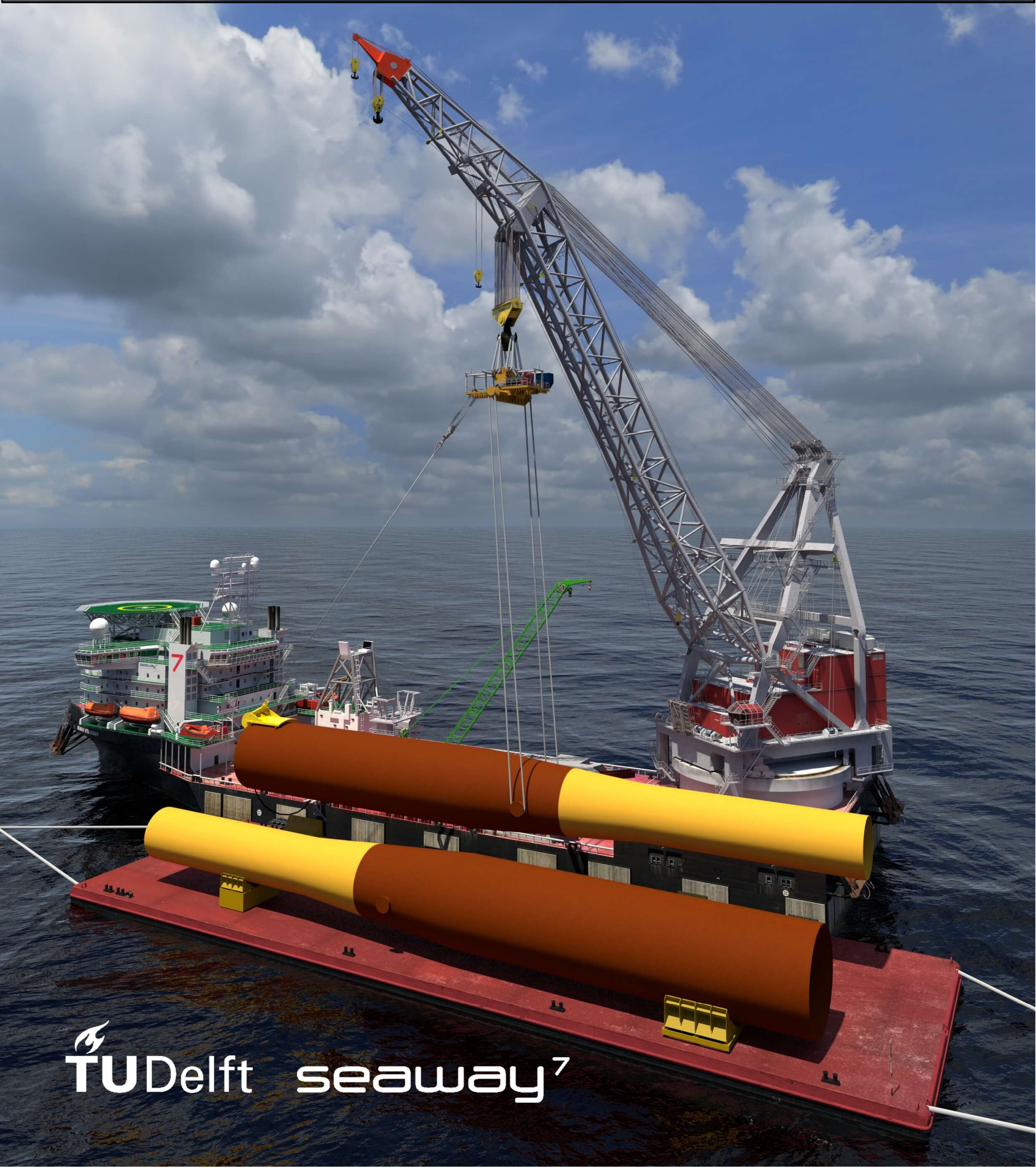

This page was intentionally left blank.

A workability study on floating installation of monopiles using the MUST

Master thesis submitted to Delft University of Technology
in partial fulfilment of the requirements for the degree of

MASTER OF SCIENCE

in **Offshore and Dredging Engineering**
Faculty of Mechanical, Maritime and Materials Engineering (3mE)

by

J.B. Tjaberings
Student number: 4362845

To be defended in public on February 14th, 2022

Graduation committee

Chairperson:	Dr. Ir. S.A. Miedema	Dredging Engineering
First Supervisor:	Dr. Ir. A. Jarquin Laguna	Offshore Renewables
Second Supervisor:	Dr. Ir. S.A. Miedema	Dredging Engineering
Third Supervisor:	Dr. S. Fazi	TPM
External Supervisor:	Ir. E. Steinebach	Seaway7
External Supervisor:	A. Mitterfellner	Seaway7

Preface

This thesis has been written as a partial fulfilment to obtain the Master's degree in Offshore and Dredging Engineering (ODE) at Delft University of Technology (TU Delft). It is one of the two theses that were written in parallel as part of a Double Master's Degree programme. This research project has shown that the combination of the curricula of ODE and Management of Technology (MoT) is very relevant for the fast-developing industry of offshore wind, which is increasingly oriented towards process optimisation and reduction of the weather dependency. I am grateful that Seaway 7 offered me the opportunity to carry out this research on a very relevant topic in a dynamic industry. Despite the fact that the COVID-19 pandemic complicated the execution of this study, I enjoyed every step of the process. It cannot be stressed enough that the latter would not have been possible without the people around me, to whom I would like to express my gratitude.

First of all, I would like to thank my committee members from TU Delft. Dr. Antonio Jarquin Laguna has been an excellent first supervisor, who showed a sincere interest in the topic and could support me with his expertise in, i.a., solving differential equations and Matlab modelling. Furthermore, I would like to thank Dr. Sape Miedema, not only for being my second supervisor and chairman, but also for helping out with all the bureaucratic difficulties that came with setting up the double degree programme.

The supervision I received from Seaway 7 was provided by Edgar Steinebach and Alexander Mitterfellner, and it has to be mentioned that I could not have been more lucky. Although it took months before I would finally meet them in person, as we were all working from home, I never felt a lack of opportunities to ask all the questions I had. They would always make time to have a meeting or to bring me into contact with the right people within the company. Edgar, Alexander and my other colleagues at Seaway 7 always made me feel welcome, for which I am thankful.

Last but not least, I would like to thank my friends, family and (ex-)roommates for providing the positive energy and distractions I needed during this graduation project. Special thanks go to my parents, brother and Demi for their unconditional love and support, but also for slowing me down every now and then.

Jorick Tjaberings
Delft, January 31st, 2022

Abstract

The exponential growth of the globally installed offshore wind capacity is not only the result of the increasing number of installed turbines, but also of their increasing capacity and size. Traditionally, the corresponding monopiles are upended offshore using upending cradles. Increasing the dimensions of these cradles according to those of monopiles is costly and requires structural modifications to the Heavy Lift Vessels (HLVs). Therefore, Seaway 7 is investigating the potential of the Monopile Upending Smart Tool (MUST), which is a platform suspended in the HLV crane, on which a winch is installed. Two grommets of constant length connect the platform with two trunnions attached to the monopile, and the winch cable suspends the bottom of the monopile. Extending the winch cable allows for in-crane upending of the monopile, which circumvents the dependency on the size of the available cradle. This study is focused on determining the workability of the application of the MUST system in the crane of the Seaway Strashnov, and identifying limitations in its design. Moreover, workability-increasing systems and solutions to reduce the limitations are proposed. For this, the nine-step workability-determining methodology by Guachamin Acero, Li, et al. (2016) is followed and adapted. A hydrodynamic simulation modelling research approach is adopted, with the software of Ansys Aqwa as a basis.

The installation of monopiles using the MUST is divided into three phases: the barge mooring / lift-off, the upending / slewing and the lowering / driving phase. From a qualitative critical event analysis is concluded that the lift-off phase is expected to be limiting. Hence, an Aqwa model is developed to quantitatively analyse this phase, which is based on five rigid bodies: the HLV, the barge, the crane hook, the MUST and the monopiles. In parallel with the model development, experimental simulations are performed, from which preliminary conclusions are drawn.

- The roll responses of the floating structures strongly depend on the incorporation of viscous roll damping, especially for incident wave frequencies close to the natural roll frequency.
- The HLV responses are marginally affected by hydrodynamic interaction effects with the barge. However, the barge responses are significantly affected by the presence of the HLV.
- The surge and sway responses of a suspended monopile are marginally affected by multiple-pendulum effects induced by the series suspension with the crane hook and the MUST.

The relative z-motion between the monopile and the saddles on the barge and the barge roll response are identified as governing parameters. To reduce the first limiting factor, a quick-release hammock seafastening system is proposed, which allows for instantaneously increasing the vertical distance between the monopile and the barge. For the lift-off of the first monopile, the average workability increase for the optimal heading at a typical location is calculated as 8.3%. For the second monopile, the increase is marginal, as the barge responses are more limiting. Furthermore, to lower the required winch capacity, it is proposed to reduce the x-distance between the trunnions and the monopile centre of gravity. Since this also lowers the stability of the monopile, the minimum x-distances that prevent the introduction of snap loads in the winch cable are iteratively calculated for a selection of limiting sea states, using a model developed in Matlab. It is found that the largest x-distances are required for sea states with peak wave periods between [redacted] and [redacted] seconds. Positioning a Passive Motion Compensator (PMC) in series with the winch cable significantly reduces the required x-distance and winch capacity. A PMC with 10% of critical damping can reduce the required winch capacity with a factor of 2.3 w.r.t. the undamped case.

It is recommended to perform follow-up studies into the phases of upending / slewing and lowering / driving, to further analyse the performance of the MUST. Also, it is advised to quantify the value of deploying a larger barge and determine the optimal x-distance (considering all phases and PMCs). Both require balancing workability and investments in the total system, for which logistical models developed in a parallel study can be used. Finally, for iterative processes, it is recommended to follow this study's method of making an estimate based on a fast simplified model, and subsequently feeding the results back into a more detailed, but slower model.

Contents

List of Figures

List of Tables

Glossary

Foundation	A foundation is defined as a structure which is in direct contact with the seabed and provides a firm supportive ground to the substructure.
Heading	The heading of a vessel is defined as the angle that the longitudinal axis of the vessel makes with the global coordinate system (i.e., the yaw-angle).
Jacket	A jacket is defined as a welded type of substructure, mostly consisting of three or four "legs" (at the corners), which are interconnected by diagonal (and horizontal) "bracings".
Monopile	A monopile is defined as a tubular type of substructure with a diameter of up to 11 meters.
Peak wave period	The peak wave period is defined as the wave period corresponding to the waves with the highest energy density in the wave spectrum.
Significant wave height	Significant wave height is a statistical parameter to describe the random waves in a sea state. It is defined as the average height of the highest one-third of the waves observed in a certain period.
Snap loads	Snap loads are defined as shock loads that can develop when a lifting cable first grows slack and then suddenly becomes taut again.
Substructure	A substructure is defined as the structure between the seabed and the structure it is designed to keep above the waterline.
Superstructure	A superstructure is defined as the part of an offshore wind turbine above the waterline, which is a combination of the tower, the nacelle, the hub and the blades.
Trunnion	A trunnion is defined as a cylindrical protrusion connected to a structure (in this case the monopile), which functions as a pivoting point.
Tugger line	A tugger line is defined as a (winch) cable connected to the crane hook or a suspended load to control the pendulum motions.
Wave encounter angle	The wave encounter angle is defined as the angle between the vessel heading and the wave heading.
Weather window	A weather window is defined as a time interval in which the weather conditions are deemed suitable to perform a certain operation or a series of continuous operations.
Workability	Workability is defined as a concept which describes the environmental conditions for which an offshore operation can be performed safely.

Acronyms

AMC	Active Motion Compensator
COG	Centre Of Gravity
DAF	Dynamic Amplification Factor
DP	Dynamic Positioning
EPCI	Engineering, Procurement, Construction and Installation
FD	Frequency Domain
FFT	Fast Fourier Transformation
HLV	Heavy Lift Vessel
JONSWAP	Joint North Sea Wave Project
LCG	Longitudinal Centre of Gravity
MH	Main Hoist
MPMSA	Most Probable Maximum Single Amplitude
MUST	Monopile Upending Smart Tool
OSV	Offshore Support Vessel
OWT	Offshore Wind Turbine
PMC	Passive Motion Compensator
PSD	Power Spectral Density
RAO	Response Amplitude Operator
RNA	Rotor Nacelle Assembly
ROV	Remotely Operated Vehicle
SDA	Significant Double Amplitude
SHL	Seaway Heavy Lifting
SOC	Siem Offshore Contractors
SSA	Significant Single Amplitude
SSCV	Semi-Submersible Crane Vessel
SWL	Safe Working Load
TCG	Transverse Centre of Gravity
TD	Time Domain
T&I	Transport and Installation
VCG	Vertical Centre of Gravity
WEA	Wave Encounter Angle

1 Introduction

This chapter provides an introduction to the topic of this thesis. Section 1.1 discusses the development of the offshore wind market over past years. Next, in Section 1.2, the problem evaluated in this study is introduced. Section 1.3 summarises Chapter 2, in which the positioning of this study w.r.t. the existing literature is evaluated and the main research question is formulated. Section 1.4 and 1.5 discuss the followed methodology and research approach respectively. Since this approach happens to be a numerical modelling approach, the applicability and validity of the used software packages is examined in Section 1.6. Lastly, in Section 1.7, the outline of this thesis is provided.

1.1 Market developments

In the last few decades, the global installed wind power capacity has been growing exponentially. In 2007, the contribution of offshore wind to the global energy market was 1 GW, whereas in 2018, this contribution had grown to 23 GW (Fernández-Guillamón, Das, Cutululis, & Molina-García, 2019). The growth of the cumulative installed offshore wind power capacity is visualised in Figure 1.1a. In 2019, an energy generating capacity of 6.1 GW was added to the global capacity, which described the largest growth in the history of global offshore wind. Furthermore, at the end of 2019, 75% of the installed offshore wind capacity was attributed to the European market. However, it is expected that the development of the markets in North America, China, Taiwan, Vietnam, Japan and South Korea will accelerate in the coming years, which is predicted to result in a new annual added global capacity of 20 GW in 2025 and 30 GW in 2030 (Lee et al., 2020). A key driver of these rapid developments is the signing of the Paris Agreement in 2015, which initiated a global movement of many countries cooperating to combat climate change. In this agreement, decarbonisation of the energy supply is considered crucial to achieving the set targets and offshore wind technology is a proposed key contributor to this process (Lacal-Arántegui & Jäger-Waldau, 2018).

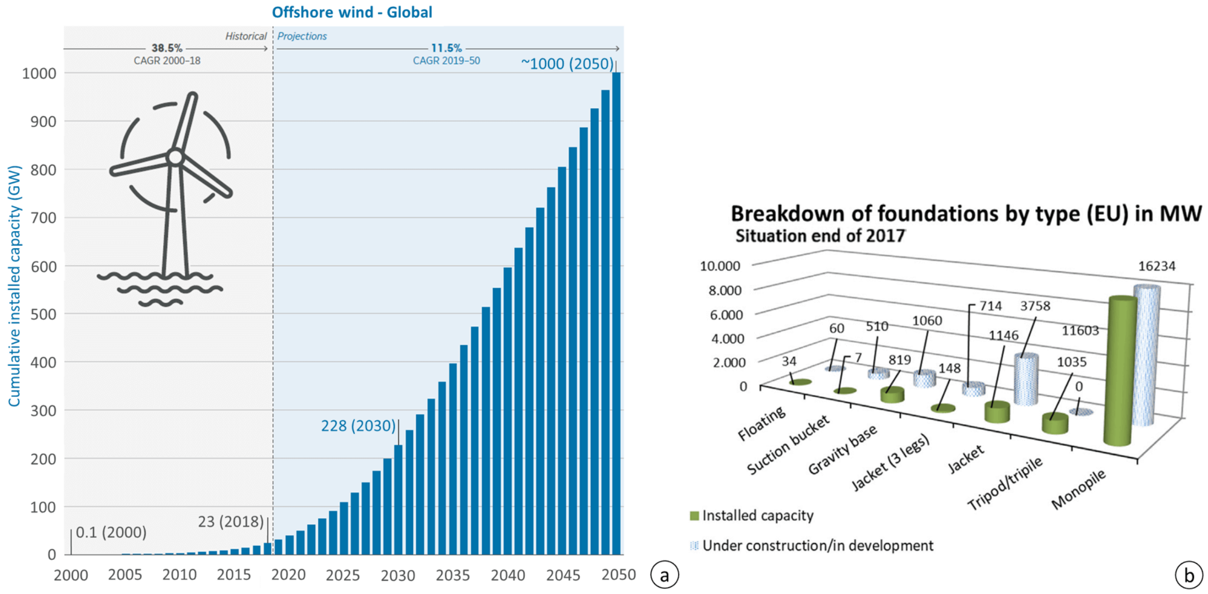

Figure 1.1: (a) Global cumulative installed wind capacity (IRENA, 2019); (b) Breakdown of offshore wind capacity per substructure type in the EU (Lacal-Arántegui et al., 2018)

The growth of the global installed capacity is not only the result of the increasing number of turbines being installed but also of the increasing size and capacity of the individual turbines. Since the first offshore wind farm, constructed in 1991 and with an average capacity of 450 kW per turbine, the global average capacity has grown to 1.5 MW in 2000 and to 7.2 MW in 2019. In May

2020, a turbine model with a capacity of 15 MW was announced to enter the commercial market in 2024 (Lee et al., 2020). However, increasing the capacity of wind turbines involves increasing the size of the "superstructures" and therefore the size of the corresponding "substructures". Moreover, as more wind farms are being developed, also further offshore sites, with greater waters depths and with extremer environmental conditions are appointed as construction area (Chartron, 2018), pushing the required substructure size even further. This development will predominantly be attributed to monopile substructures, as in recent years the industry has shown a clear preference for this type of substructures (see Figure 1.1b), which will only intensify in the coming years (Lacal-Arántegui et al., 2018). Offshore contractors specialised in the installation of monopiles will have to follow these developments and adapt their processes to keep up with the ever-changing industry.

1.2 Problem statement

Seaway 7, an offshore contractor, recognises the aforementioned trends in the offshore wind industry and aims to develop its installation methodologies accordingly. Currently, the company uses traditional upending frames to bring monopiles from a horizontal position on the vessel deck to a vertical position on the seabed. However, to install the new generation of these structures, with a diameter of up to 11 meters and a mass approaching 2500 mT (IX Wind, 2021), larger upending frames are needed, and thereby structural modifications to the installation vessels. To be independent of such frames and vessel modifications, Seaway 7 is developing a new installation methodology for monopiles that are supplied to the installation vessel by transportation barges (feeders). In this principle, a lifting frame (referred to as the Monopile Upending Smart Tool (MUST) in the remainder of this thesis), on which a winch is installed, is directly attached to the crane hook (see point A in Figure 1.2). The monopiles are prepared with two trunnions (point B), which act as the main lifting points. The connection between these trunnions and the MUST-frame is provided by two grommets of constant length, and a third lifting point, present at the bottom of the monopile (point C), is supported by the winch cable. After lifting the horizontal monopile from the barge and sailing the barge away, the monopile is upended by unwinding the winch cable. Once the monopile is in a vertical suspended position, the third lifting point is removed and the monopile is lowered to the seabed. A more elaborate discussion of the principle is provided by (Bosch & Zwart, 2021).

Figure 1.2: Demonstration of the working principle of the Monopile Upending Smart Tool (MUST)

Although this is a promising principle to eliminate the dependency on large upending frames, the method is still under development and little is known about its sensitivity to environmental conditions. Seaway 7 has identified some potential complications that could limit its workability (the environmental conditions for which an operation can be performed safely), which are mostly directed to the lift-off phase and to a less extent to the upending and lowering phase. Firstly, to minimise the required winch capacity, the installed trunnions are planned to be positioned close to the centre of gravity of the monopile, which also reduces the stability of the lifting arrangement. The barge potentially re-hitting the monopile after lift-off, in combination with this reduced stability, raises the probability of the introduction of workability limiting snap loads. This holds for the heavy new generation monopiles in particular, since these are lifted relatively slowly from the barge, which increases the probability of the barge impacting the monopile. A second potential complication is formed by excessive motions due to resonance, of which the probability is increased by the many cable and grommet connections in the proposed system. These concerns require extensive research into the weather sensitivity of the newly developed monopile installation method from a safety perspective. Since the identified potential complications predominantly concern the lift-off operation (as is substantiated in Section 3.3), the focus of this thesis is on this phase.

In addition to the safety perspective, gaining insights into the workability of the proposed method also contributes to the knowledge about the associated costs: Barlow et al. (2015) describe a strong positive effect of the weather sensitivity of monopile installation projects on the vulnerability to costly delays. Hence, increasing the workability directly targets the installation costs (Li, 2016). Moreover, it could provide flexibility to optimise the logistical processes of such operations, meaning that the installation costs can also be targeted indirectly. Therefore, researching workability-increasing measures for the installation method under analysis, in addition to establishing its weather sensitivity, could provide Seaway 7 with more value than a validated concept.

1.3 Scientific relevance and main research question

In the literature, only a limited amount of studies analysing the susceptibility of offshore lift-off operations to weather delays are encountered (as discussed extensively in Chapter 2). Moreover, while the principle of feeding monopiles to an installation vessel by transportation barges is applied in the industry with increasing frequency, the number of encountered scientific studies on barge lift-off operations is limited to four. Considering those studies, only Thurston, Swanson, and Kopp (2011) and Zhu, Li, and Ong (2017) regard snap loads as a limiting condition. However, these two studies do not consider a similar case with a reduced stability problem, which limits the relevance of their results. Furthermore, only one study researching potential lift-off workability-increasing measures was identified. Li, Karatas, Zhu, and Ong (2020) propose to apply fenders to reduce the impact between the barge and the lifted structure, and thereby reduce the weather sensitivity. However, the mass of this structure is significantly smaller than the mass of the monopiles considered in this study, which limits the applicability of this principle to the system studied here. To the writer's knowledge, no study that focuses on determining and increasing the workability of a system with similar characteristics as the MUST system has been performed. Hence, the objective of this thesis is to generate insights into the weather dependency of the lift-off operation of the newly developed monopile installation method, and to identify and quantify workability-increasing strategies. To reach this objective, a case study is performed with the Seaway Strashnov as the installation vessel, and hence the following main research question has been formulated:

How can the weather window of the application of the MUST system on monopile installation by the Seaway Strashnov be increased?

1.4 Methodology and sub-questions

According to Guachamin Acero, Li, et al. (2016), limiting sea states of offshore operations should be derived from physical responses of equipment, since determining these values based on experience inhibits the ability to trace their origin. However, Guachamin Acero, Li, et al. (2016)

and Gintautas, Sørensen, and Vatne (2016) state that relatively few studies have been published on determining operational limits based on physical responses. Therefore, Guachamin Acero, Li, et al. (2016) develop a systematic nine-step methodology to "derive response-based operational limits and assess the operability of weather-restricted marine operations". Their methodology is visualised in Figure 1.3 (delineated in black) and is explained in the following paragraphs.

Step 1 of the methodology requires a detailed description of the operational procedure to be analysed, which in this case is the newly developed process of a Heavy Lift Vessel (HLV) lifting a monopile from a transportation barge, and subsequently upending it, slewing it into the "pile gripper" and lowering it onto the seabed, using the MUST-frame. Once the monopile is vertically standing on the seabed, supported by the gripper, it is driven into the seabed. The focus is laid on the lift-off phase, but a complete depiction of the installation method is provided. Based on this description, in step 2 a preliminary collection of potentially critical events is drawn up in consultation with experts of the specific operation, using available documentation, and by performing a qualitative fault tree analysis. This leads to the following two sub-questions. Answers to these sub-questions can be found in Section 3.2 and Section 3.3 respectively.

(1) *How can the newly developed installation process for monopiles, which are supplied to the installation vessel by a transportation barge, be described in detail?*

(2) *What potentially critical events during the lift-off phase should be included in the analysis?*

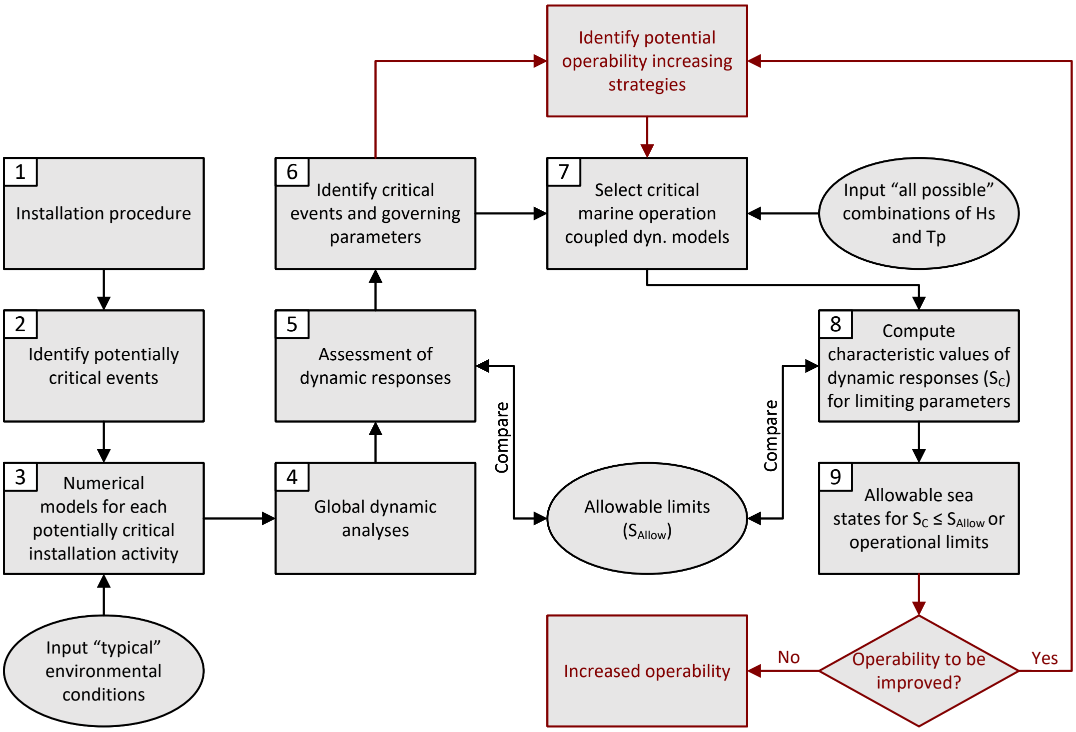

Figure 1.3: General methodology to determine limiting sea states of offshore operations. Adapted from (Guachamin Acero, Li, et al., 2016) by changing the layout of the diagram and adding an operability increase loop

Next, these potentially critical events are implemented in numerical models (step 3). These models include a coupled system of the HLV, the transportation barge, the crane hook, the lifting frame and the monopile. According to Guachamin Acero, Li, et al. (2016), Time Domain (TD) simulations are typically required in addition to Frequency Domain (FD) analyses, to constructively evaluate such offshore lifting activities. The main advantage of TD over FD simulations is that the former considers nonlinear effects. However, TD analyses are also more time consuming. It is proposed to employ the software of Ansys Aqwa for these analyses, which includes capabilities for determining hydrodynamic parameters of hydrodynamically interacting structures, and performing dynamic simulations for motion and response analyses in both FD and TD (ANSYS, n.d.). The suitability of this software is discussed more extensively in Section 1.5. Step 4 requires performing simulations of the in step 3 designed coupled system, subjected to "typical" environmental conditions. Assessment of the dynamic responses (step 5) indicates which parameters are prone to approach their maximum allowable values and are therefore governing for the operation. In step 6, the governing parameters and the corresponding critical events are identified. These steps (3 to 6) lead to the third sub-question, which is answered in Chapter 5.

(3) *What are the governing parameters for the operation of lifting a monopile from a transportation barge by an HLV, considering the newly developed installation approach?*

Before continuing to steps 7 to 9, it may be necessary to perform preliminary model optimisations, since conclusions about the governing parameters may be inaccurate without these iterative steps (e.g., at first excessive motions due to resonance could be considered governing, but after optimising the rigging arrangement, which may reduce the probability of resonance, another parameter might be limiting). In step 7, the identified limiting parameters are matched with the dynamic model of the corresponding critical operation (which is in this case the lift-off operation). Next, in step 8, the characteristic values of the limiting parameters are determined. The characteristic values relate to the targeted probabilities of exceedance, and are calculated by subjecting the critical dynamic models to a collection of environmental conditions representing all realistically possible circumstances. To determine the probable wave conditions (e.g., combinations of significant wave heights, peak wave periods, wave spreading, spectrum peak shape and directions of wave propagation) at a particular location, historical data in the form of spectra, time series or scatter diagrams can be consulted. Next, the characteristic values are compared to the allowable limits of the limiting parameters (step 9), to determine the allowable limits of the environmental conditions. This is done for any heading of the vessel and barge w.r.t. the environmental conditions the system is subjected to (the Wave Encounter Angle (WEA)). Doing this already contributes to answering the main research question, as finding an optimal WEA adds to increasing the operability.

The resulting operationally allowable sea states, depending on the wave encounter angle, represent the workability of the installation method as it is designed up to now. Without performing the preliminary optimisations (after step 6), the found limiting sea states may be suboptimal with the equipment at hand. Moreover, even if the preliminary optimisations are implemented, additional optimisations might be required after step 9, since the dependency on the WEA is added to the model after performing the preliminary optimisations. The optimised values (e.g., for the grommet length) could be different for the optimal WEA than for the initially assumed configuration, resulting in an iterative process. Once a (close to) optimal configuration is identified, the corresponding allowable sea states are considered to be the "base case". This allows for answering sub-question 4, which is done in Chapter 6.

(4) *What is the workability corresponding to the "optimised base case" of the installation system utilising the MUST?*

The next step is to increase the workability of the base case. In order to research systems potentially resulting in such an increase, a loop is added to the methodology by Guachamin Acero, Li, et al. (2016), as delineated in red in Figure 1.3. Based on the in step 6 identified critical events and governing parameters, promising strategies to increase the in step 9 identified operability are proposed. Next, steps 7, 8 and 9 are repeated such that the operability of the proposed strategies is determined and compared to the results of the base case, which leads to sub-question 5. An answer to this question is provided in Chapter 7.

(5) *What strategies that increase the workability of the newly developed monopile installation method can be identified?*

1.5 Modelling approach

As touched upon in the sections above, the software of Ansys Aqwa is used in this study to perform the hydrodynamic analyses. Aqwa consists of five core programmes (ANSYS, 2016a):

- **Aqwa-Line** is a 3-D diffraction and radiation programme, which calculates the linear responses of floating rigid bodies in regular waves. First and second order wave loadings are included in the analyses.
- **Aqwa-Librium** is a programme that performs force balance calculations to find the bodies' equilibrium positions and the corresponding mooring loads. Furthermore, it evaluates the static and dynamic stability around the found equilibrium positions and performs eigenmode analyses.
- **Aqwa-Fer** is a programme that enables to determine structure motion and mooring line tension responses to irregular waves in the FD.
- **Aqwa-Drift** is a TD programme for the analysis of structure motion and mooring tension responses to irregular waves. It is typically used for the analysis of relatively small responses.
- **Aqwa-Naut** is also a time domain programme for the analysis of structure motions and mooring line tensions. Contrary to Aqwa-Drift, Aqwa-Naut allows to determine responses to both regular and irregular waves. Additionally, where Aqwa-Drift performs its calculations with the assumption of linear hydrostatic stiffness (determined based on the mean water surface), Aqwa-Naut includes the non-linear effects in hydrostatics and incident wave forces (the calculations are performed based on the instantaneous water surface). This makes Aqwa-Naut suitable for analysing large vessel motions.

These five core programmes are run in a certain sequence to obtain desired results, which is visualised in Figure 1.4. In this study, Aqwa-Naut is used to a very limited extent, as it is expected that the motions during an installation procedure are small, and hence non-linear effects are considered to be marginally present. Aqwa-Line has to be provided with the coordinates of the nodes and panels that describe the hull of the considered floating structures. Furthermore, the static draft, heel and trim are required to determine the separation line between diffracting and non-diffracting elements and static stability properties are required to find the structure's roll and pitch stiffness. These values are determined in the software of Shipshape, which provides the ability to analyse the hydrostatic and static stability properties of floating structures. Additionally, Aqwa-Line has to be supplied with the mass properties (i.e., the mass and mass moment of inertia) of the considered structures, which are approximated by hand calculations. The output of Aqwa-Line is a hydrodynamic database, which can be used as input for the other four Aqwa programmes and it can be loaded into the software of Octopus Office. The latter allows to estimate viscous roll damping coefficients following the method described by Ikeda (see Section 4.2), which can subsequently be supplied to the Aqwa-Line model. Aqwa-Librium uses the hydrodynamic database to determine an equilibrium position, which combined with the hydrodynamic database provides the system-specific input data required for the Aqwa-Fer, Aqwa-Drift and Aqwa-Naut analyses. Finally, Matlab is used for post-processing purposes and to work around the limitations of Aqwa by modelling system components separately. The latter is explained in more detail in Section 6.3.

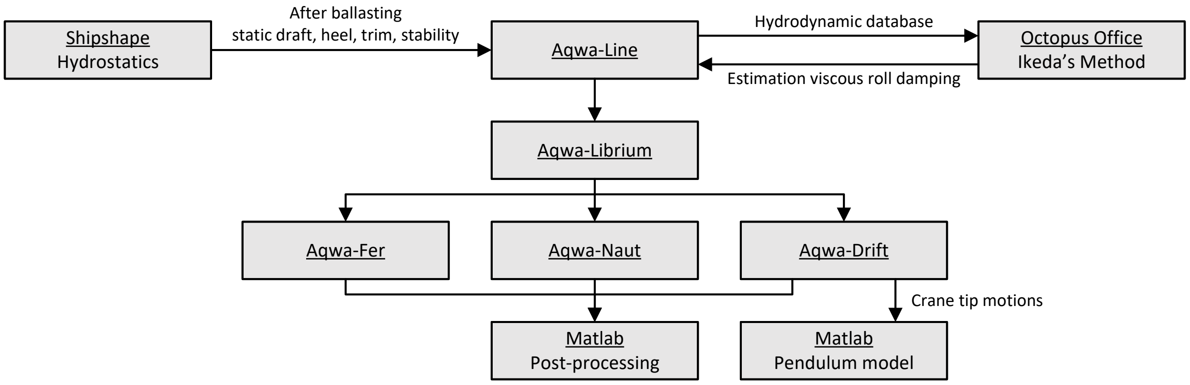

Figure 1.4: Overview of the coherence of the software packages used in this study

1.6 Validity software packages and provided models

In order to substantiate the use of the software packages, ideally (model) tests are performed of the system being analysed to validate the obtained results. However, since such experiments are outside the scope of this study, other studies considering similar set-ups are consulted. Gourlay, von Graefe, Shigunov, and Lataire (2015) compare (single body) simulation results of various commercially available software packages with model test results of three ship-shaped vessels. Aqwa (based on radiation and diffraction panel theory) and Octopus Office (based on strip theory) are among those programmes. Their general conclusion is that the numerical predictions are in good agreement with the model test results for each considered software package. Silver et al. (2008) perform a similar comparison analysis, which involves different software packages but includes Aqwa and focuses on multi-body analyses. They conclude that the motions associated with two ship-shaped vessels in close proximity (3 m distance between the vessels, which are positioned in parallel) predicted by Aqwa, are in good agreement with test results.

Following the conclusions of these studies, Aqwa is deemed to be suitable to predict ship motions in both single and multi-body analyses. However, these results do not confirm the validity of the implementation of the complex HLV hull shape considered in this study in Aqwa. Therefore, internal reports of Seaway 7 are consulted. For the Seaway Strashnov, full-scale motion response tests have been performed (Seaway 7, 2016). No other vessel or barge was in close proximity, which means that it concerns a single body analysis. A wave rider buoy was deployed, of which the results were used to construct time-varying wave spectra, and the vessel's roll and pitch motions were measured, from which the corresponding response spectra were determined. Based on the by Aqwa determined Response Amplitude Operators (RAOs) and the constructed wave spectra, also the theoretical roll and pitch response spectra were determined. By comparing the measured and calculated response spectra, it was concluded that the modelling results provide a good representation of reality, and that the hull shape has been modelled properly in Aqwa.

1.7 Thesis outline

This thesis comprises eight chapters, the first of which is an introduction to the study, as presented above. In Chapter 2, the available scientific literature on the considered topic is discussed, a scientific knowledge gap is identified and the main research question is formulated. Next, in Chapter 3, the system of analysis is defined and a critical event analysis is performed, based on which this research is further narrowed down. The decisions made in the development of a quantitative hydrodynamic model are substantiated in Chapter 4. In Chapter 5, the quantitative model is used to identify the governing parameters of the system of analysis, and in Chapter 6 to determine the workability of the base case. Next, in Chapter 7, improvements to the base design are proposed, and the advantages in terms of workability are quantified. Finally, in Chapter 8, conclusions are drawn and recommendations for future research are made.

2 Literature review

As touched upon in the introduction, only a limited number of studies have been dedicated to the lift-off process of structures from transportation barges or vessels. In Section 2.1, some of the structures that are considered in those studies are introduced. Subsequently, in Section 2.2, the findings of the available studies on the lift-off phase are discussed. These studies are supplemented with studies considering the suspended and lowering conditions, in order to provide a broader context of available approaches and findings. Moreover, studies focused on the theory behind determining weather windows are discussed. Finally, in Section 2.3, a knowledge gap in the scientific literature is identified, and the main research question is formulated.

2.1 Terminology

Although floating offshore wind turbines are mentioned in the industry with increasing frequency, the far majority of the turbines being installed is still bottom-founded (Lacal-Arántegui et al., 2018). Bottom-founded means that a "substructure" is positioned on the seabed, to keep the "superstructure" above the water line (see Figure 2.1a). There are various types of substructures applied in the offshore wind industry, but the far majority of these structures is a "monopile" or a "jacket", and it is expected that this tendency will only intensify in the near future (Lacal-Arántegui et al., 2018). A monopile is the "simplest" substructure, which can be described as a tubular structure with a large diameter of up to 11 meters (IX Wind, 2021). A jacket is a truss type of structure, mostly consisting of three or four "legs" (at the corners), which are interconnected by diagonal (and sometimes horizontal) "bracings". These structures are displayed in Figure 2.1b and 2.1c. The term "foundation" is often used interchangeably with "substructure". However, for this study, foundation refers to the structure that is in direct contact with the seabed, providing firm supportive ground to the substructure. In the case of monopiles, the substructure also provides the foundation, as it is the tubular structure of the monopile itself that is driven into the seabed. For jackets, however, separate foundation piles are installed. This is done either after ("post-piling", with piles driven through "pile sleeves") or before the jacket is installed ("pre-piling", piles driven into the seabed on top of which the jacket is installed). Figure 2.1c displays a post-piled jacket.

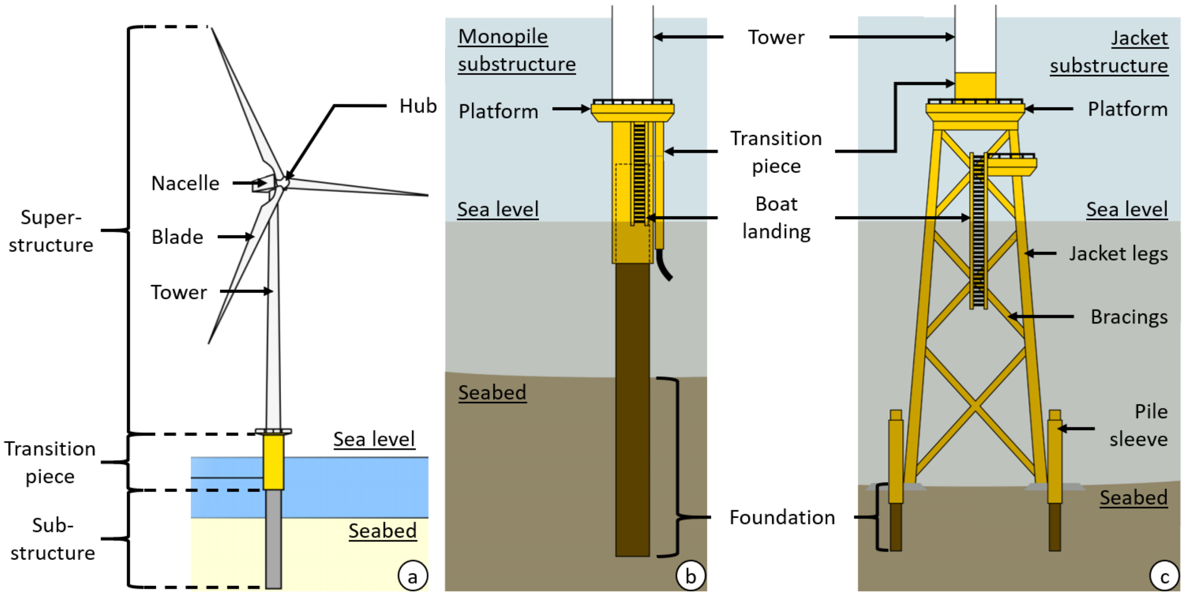

Figure 2.1: Offshore wind turbine terminology breakdown. (a) adapted from (Bhattacharya et al., 2017); (b) and (c) adapted from (IX Wind, 2021)

The part connecting the substructure with the tower is called the “transition piece”. Apart from transferring loads from the superstructure to the substructure, transition pieces also have other functionalities, such as: providing access platforms and boat landings, accommodating electrical components, and offering corrosion protection. All components above the transition piece (the tower, nacelle, hub and three blades) are considered components of the superstructure.

2.2 Research on the workability of offshore lifting operations

This section discusses the state-of-the-art scientific literature regarding the responses of floating Heavy Lift Vessels (HLVs) to environmental conditions, while performing various offshore operations. Barlow et al. (2015) identify the operations most vulnerable to weather-related delays in the offshore wind farm installation phase. By performing discrete-event simulations, they reveal that the least weather robust activities include the installation of turbine substructures (25% of the registered weather delays is due to the limitations of supply barges and 18% due to those of HLVs). Delays, in this case, are due to limitations in wind and wave conditions and the required duration of the weather window for a certain operation to take place. By varying these limits, they show that by targeting the least weather robust activities for development the potential impact on installation duration can far outweigh the potential reductions which could be achieved by simply employing vessels with increased operating capacity. Therefore, this literature review will mostly consider studies focused on simulating offshore installation operations and determining, and subsequently increasing, the corresponding weather windows.

First, in Section 2.2.1, studies that focus on offshore lifting of objects from vessels or transportation barges are discussed. Moreover, studies that discuss the interaction between an HLV and a barge in close proximity are considered. Section 2.2.2 concentrates on the subsequent phase in the installation process, in which a load is suspended in the crane and is being lowered to its final position. Thirdly, in Section 2.2.3, studies focused on the translation of system responses to weather windows are discussed.

2.2.1 Lift-off operations

Baar, Pijfers, and Van Santen (1992) present a two-body diffraction analysis of the hydrodynamic interaction effects between a Semi-Submersible Crane Vessel (SSCV) and transportation barge that is in close proximity. They demonstrate that the motions of the barge can be notably altered due to hydrodynamic interaction, whereas the motions of the SSCV are barely changed. However, they additionally conclude that the mechanical interaction effects (considering crane boom, hoisting wire and sling stiffness) when performing the lift-off of a load from the barge are an order of magnitude larger than the hydrodynamic coupling effects. Therefore, they state that the hydrodynamic interaction can be ignored from a practical point of view.

Kanotra et al. (2012) apply this knowledge in a time domain study on the dynamics of a lift-off operation of a module from a transportation barge. They ignore the hydrodynamic interaction effects, referring to the conclusion by Baar et al. (1992). The mechanical coupling effects based on slings, lashings and fenders are included in the analysis. Moreover, they compare the Dynamic Amplification Factors (DAFs) (the ratio between the magnitude of a dynamic load and the static load) of the hook load, which result from variations in cable pretension and environmental conditions. From these comparisons is concluded that the dynamic loads are higher in the lift-off than in the in-air phase and steady wind and current loads do not significantly contribute to the total hook load. Thurston et al. (2011) also analyse the lift-off of a load from a transportation barge by an HLV but focus on “snap loads”. Such shock loads can develop when a lifting cable first grows slack and suddenly becomes taut again, which could be a result of the barge impacting the load due to their relative motions. Although dynamics are involved, snap loads should not be confused with the dynamic loading used to determine the DAF. Thurston et al. present a methodology to find the probability of encountering snap loads and to estimate the magnitude.

A study by Jeong, Roh, and Ham (2016) analyses the lifting process of a structure by an Offshore Support Vessel (OSV) from its own deck. Part of their focus is on the lift-off phase, for which they take a collision between the load and the vessel as a limiting condition. By varying the values for the wave height, hoisting speed and wave period, they find the conditions for which collisions take place. Furthermore, they monitor the cable tension and calculate the corresponding DAF. A similar study is performed by Zhu et al. (2017), who analyse the limiting sea states of the lift-off and lowering phases of a tripod substructure by an HLV, in both frequency and time domain. The analysis of the lift-off phase covers the scenarios of lifting from the HLV deck and from a transportation barge. They conclude that the use of frequency domain analyses is inappropriate in these cases, the system responses in the lowering phase are smaller when using jack-ups than when using floating vessels, and a lift-off from a barge results in larger loads and more severe tripod motions than a lift-off from the own HLV deck. To the latter conclusion the additional recommendation is made to include the clearance between the tripod and the barge deck as a limiting condition, referring to possible collision-induced snap loads.

Li et al. (2020) perform a time domain simulation of the lifting of a 45 mT subsea spool piece from a barge by a crane vessel. The governing limiting factor is considered to be the re-hit action between the load and the barge deck after the lift-off is performed. To increase the allowable sea states, the properties of the fenders between the deck and the spool are varied to find a set-up resulting in a minimal impact force. They conclude that, compared to the steel-to-steel contact model, soft fender models can significantly increase the allowable sea states.

2.2.2 Lowering operations of suspended loads

Hatecke et al. (2014) develop a fast simulation method to analyse the coupled motions of an HLV with a load suspended in its crane and apply this method in a case study. The method is found to be able to accurately determine natural frequencies of the coupled motions and is suitable when very long or many simulations are required. Oh, Utsunomiya, and Saiki (2018) go a step further and build two numerical models: a "flexible" model and a "fixed" model, to describe the characteristics of a floating crane lifting a caisson structure. In the flexible model, various connections between the crane jib and the load are modelled with linear springs, whereas in the fixed model these connections are fixed. Regarding static displacement and the peak frequency of the load acceleration in transverse direction (sway), both models are in good agreement with on-site measurements. However, the models appear to underestimate the peak frequency of the load acceleration in longitudinal direction (surge).

Apart from analysing the lift-off case, Thurston et al. (2011) also consider the lowering of a structure through the splash zone. They propose a methodology to find the probability of occurrence of a slack lifting cable (which could induce snap loads) while performing such lowering operations. Gordon, Grytøyr, and Dhaigude (2013) confirm the validity of this methodology and apply it in their modelling procedure, describing the lowering of a suction pile through the splash zone. Moreover, they state that the probability of a slack cable at a certain sea state should be related to the probability of occurrence of that sea state. Solaas et al. (2017) analyse the lowering process through the splash zone for a specific type of protection cover. Their time domain simulations indicate that large protection cover motions can be expected with the structure still in the air (no tugger lines were included in the model). Once it has reached the water, the motions reduce. However, the largest force fluctuations in the slings can be expected shortly after the full submergence. This load case also results in some cases of slack slings, but the magnitude of the consequential snap loads is limited.

Li, Gao, and Moan (2013) analyse the phases of lowering, landing and steady state after landing of a monopile installation process. Their time domain simulation includes the bodies of a floating installation vessel and a monopile, between which coupling is realised by the lifting cable and a pile gripper. They find that the contact force between the monopile and the gripper, and their relative motion, is significantly affected by the gripper stiffness. In a follow-up study by Li et al. (2014), this knowledge about modelling a gripper is put into practice. They describe a model for the continuous lowering operation of a monopile by an HLV, using a gripper. Furthermore, they analyse the critical responses for a situation that accounts for vessel shielding effects and compare those to one that considers undisturbed incident wave conditions. Their conclusion states that including shielding effects can result in a significant reduction of extreme responses, depending on the vessel heading and the wavelength (large reductions are observed in short waves). In a subsequent study, they perform comparative simulations for the lifting of both monopiles and jackets (Li, Gao, & Moan, 2015a). In contrast to what is observed for monopiles, only limited reductions of responses due to the inclusion of shielding effects are observed for the lowering of jacket substructures.

Li, Gao, and Moan (2016) apply different numerical approaches to the simulation of a monopile lowering operation by an HLV, to assess the influence of four critical factors on the allowable sea states: “wave short crestedness, shielding effects from the HLV, radiation damping from the monopile and the nonstationarity of the process”. They apply the knowledge described by Li et al. (2014) to consider shielding effects and Li, Gao, and Moan (2015b) to include the effect of radiation damping of the monopile. The latter study designs an approach to include radiation damping effects during the nonstationary lowering of a monopile (which means the changing properties of the system, like damping, while lowering the monopile are included). Based on the results from an operability analysis, Li et al. (2016) recommend to include shielding effects and wave spreading in the numerical method and to apply nonstationary analysis. Moreover, they recommend to consider the radiation damping of the monopile in the case of short incident waves, and they state that it is preferable to optimise the vessel heading, depending on the environmental conditions, to increase the operability.

2.2.3 Weather window prediction

Gintautas et al. (2016) propose an approach for estimating weather windows based on actual responses of equipment, rather than on limitations to the wave height and wind velocity, which is mostly done in the literature (however, in the industry, estimating weather windows based on equipment responses is more common). They state that determining a weather window based on equipment limitations increases prediction accuracy and therefore helps to reduce the costs of offshore operations. Gintautas and Sørensen (2016) extend this study by assessing the applicability of the proposed approach with respect to the standard alpha-factor method described in (DNV-OS-H101, 2011, Section 4). By performing a synthetic case study, they conclude that the proposed approach results in a significant increase in the duration of the predicted weather windows compared to the alpha-factor method. Additionally, they emphasise that the quality of the decision support increases due to the more detailed analysis and inclusion of weather forecasting uncertainties. Drago et al. (2017) propose a similar approach to express the operational limitations more physically, i.e., in terms of allowable vessel motions. In a case study analysing a pipeline J-lay operation in Brazil, they show that using a sea state expression as the limiting condition could overestimate the time of the vessel not being operational by 50%-100%. Additionally, they state that this unnecessary stand-by time could be omitted by considering the vessel motions as the limiting condition. Furthermore, Guachamin Acero, Gao, and Moan (2016) assess the weather restrictions of a new method for installing the tower and Rotor Nacelle Assembly (RNA) of an Offshore Wind Turbine (OWT), which is based on the inverted pendulum principle. They determine the allowable sea states based on physical limiting parameters, similar to the proposed method by Gintautas et al. (2016). However, there seems to be no relationship between these studies based on the references.

Gintautas and Sørensen continue on their earlier work by estimating the probability of operation failure, based on probability distributions of equipment responses (Gintautas & Sørensen, 2017a). Next, they relate those estimations to standardised "acceptance criteria", to determine the probability of "acceptance criteria exceedance events". In the two case studies they performed, application of the proposed methodology resulted in 57% and 47% more operational hours compared to the alpha-factor method. In a following study, Gintautas and Sørensen analyse the effect of uncertainties in weather forecasts on the estimations of operational weather windows and the corresponding probabilities of acceptance criteria exceedance events (Gintautas & Sørensen, 2017b). Their analysis indicates that uncertainties in weather forecasting can "increase the variability of probability of operation failure estimates, which in turn reduce the total number of predicted weather windows."

2.3 Identification of knowledge gap and research question

Although the monopile installation process is susceptible to significant weather delays (Barlow et al., 2015), only a few studies have been performed to analyse this specific problem. Moreover, while the strategy of supplying monopiles (or other types of structures) to an installation vessel by transportation barges is applied in the industry with increasing frequency, only four studies are encountered researching the challenges of the corresponding barge lift-off operation. To the writer's knowledge, no study has been performed describing systems to reduce the probability of the barge impacting the load just after lift-off, although Li et al. (2020) apply fenders in their model to reduce the impact of the re-hit action and thereby increase the workability. However, the latter research describes the effectiveness of the fender system for a subsea spool weighing 45 mT, which makes the applicability of such a principle to the lift-off of a monopile (of up to 2500 mT) questionable. Furthermore, to the writer's knowledge, only Thurston et al. (2011) and Zhu et al. (2017) include snap loads as a limiting condition during the lift-off phase. However, they do not encounter challenges similar to those associated with the application of the MUST (e.g., the potential stability problem in combination with the limited winch capacity).

Hence, a knowledge gap in the literature can be identified regarding increasing the workability of lift-off operations in general. Since the application of the MUST for monopile installation operations has specific characteristics, and no similar systems are encountered in the literature, the lift-off phase of this method in particular is an innovative case. However, since lift-off, upending and lowering are one continuous operation, increasing the workability of the lift-off phase only pays off if this is indeed the governing stage. Therefore, before detailed research into the lift-off phase is performed, first confirmation of its relevance is sought (see Section 3.3). In general, the objective of this study is to examine the limiting parameters and the workability of the monopile installation method using the MUST, and to formulate strategies that increase the corresponding weather resistance. This objective leads to the following main research question:

How can the weather window of the application of the MUST system on monopile installation by the Seaway Strashnov be increased?

3 | Defining the system of analysis

This chapter is dedicated to steps 1 and 2 of the framework by Guachamin Acero, Li, et al. (2016), and therefore to answering sub-questions 1 and 2 (see Section 1.4). Section 3.2 provides an extensive description of the installation steps that are taken when the MUST is deployed to install monopiles. As results from this description, various other types of (auxiliary) equipment are required to perform the installation of a monopile (such as an installation vessel, which is pre-determined in the main research question). For the remainder of this thesis, it is assumed that this equipment is provided by Seaway 7. Hence, a short introduction to this company and its equipment is provided first, in Section 3.1. Finally, in Section 3.3, potentially critical events are identified for the deployment of the MUST.

3.1 Seaway 7: Company profile

In order to expand the company's services in the offshore renewables sector, Subsea 7 acquired Seaway Heavy Lifting (SHL) in 2017 (Subsea 7, 2017), and Siem Offshore Contractors (SOC) in 2018 (Subsea 7, 2018). Merging these companies resulted in Subsea 7's Renewables Business Unit being named Seaway 7 (Seaway 7, n.d.-a). The organisation of Seaway 7 can be considered to have two branches: one specialises in subsea offshore cables and is based on the former SOC, and the other specialises in offshore heavy lifting and is based on the former SHL (which got most of its experience from the oil and gas industry). Seaway 7 now represents one of the world's leading offshore contractors. Since its first offshore wind farm project in 2009, the company has installed hundreds of offshore wind turbine substructures for many of the key wind farm developers in Europe, Taiwan and the USA (Seaway 7, n.d.-c). Regarding the offshore renewables sector, the specialisms of Seaway 7 include Transport and Installation (T&I) of offshore structures and submarine cables, and Engineering, Procurement, Construction and Installation (EPCI) of various types of solutions (Seaway 7, n.d.-a).

To perform such operations, Seaway 7 owns and operates five specialist vessels: two cable lay vessels, one installation support vessel and two Heavy Lift Vessels (HLVs) (Seaway 7, n.d.-b). The latter two are most relevant to this research project, and are displayed in Figure 3.1.

Seaway Strashnov

Built:	2011
Length:	183 m
Breadth:	47 m
Draught:	8.5 - 13.5 m
Crane capacity:	5000 mT
Max. lift height above waterline:	102 m

Seaway Yudin

Built:	1985
Length:	183 m
Breadth:	36 m
Draught:	5.5 - 8.9 m
Crane capacity:	2500 mT
Max. lift height above waterline:	78 m

Figure 3.1: The two heavy lift vessels operated by Seaway 7 and their basic specifications (images from (Bakker Sliedrecht, n.d.; Offshore WIND, n.d.), vessel specifications from (Seaway 7, 2020a, 2020b))

The Seaway Strashnov and the Seaway Yudin (formerly known as the Oleg Strashnov and the Stanislav Yudin) are both equipped with revolving cranes with lift capacities of respectively 5000 mT and 2500 mT. Both vessels can be moored using an eight-point anchoring system, but the Seaway Strashnov is also fitted with a Dynamic Positioning (DP) 3 system. A DP system automatically lets a vessel keep its position by coordinating the activation of engines, thrusters and rudders. DP systems are classified in terms of redundancy, and DP3 describes the highest redundancy classification. Apart from vessels, Seaway 7 also owns and operates a wide variety of support equipment such as rigging, pile hammers and pile handling tools. This enables the company to offer its clients a complete solution with reduced dependency on third parties.

3.2 Monopile installation process with the MUST system

Before going into the details of the monopile installation process using the MUST system, the required equipment is listed. First of all, an installation vessel equipped with a heavy-lift crane is required. This crane requires sufficient capacity to perform a combined lift of the monopile to be installed and the additional equipment needed to suspend the structure in the crane hook (such as the MUST, grommets, etc.). As discussed in Section 3.1, Seaway 7 operates two HLVs, with crane capacities of 2500 mT and 5000 mT. Secondly, a transportation barge is required to supply the installation vessel with the monopiles to be installed. Such a supply barge prevents the installation vessel itself from having to shuttle between the base port and the wind farm location, and it leaves the vessel deck available to store auxiliary equipment. Thirdly, the MUST itself needs to be suspended in the crane hook. This frame supports a winch and its generator, and provides three monopile suspension points (see Figure 3.2a). The connection between the two “main suspension points” and the two trunnions installed on the monopile is provided by two grommets (see Figure 3.2b). Traditionally, steel grommets are deployed for such operations because of their relatively high strength and low costs. However, grommets made of synthetic high-performance fibres (e.g., Dyneema) are gaining in popularity because of their lower weight, reducing the risk of damaged equipment and injured personnel (Eijssen, 2011). An additional advantage of synthetic grommets is that they float, which is useful for retrieval in case they are (accidentally) dropped in the water, or for line handling during mooring. The third monopile suspension point is provided by the winch cable, making this connection variable in length. The attachment to the bottom of the monopile is fixed as long as the winch cable is taut, and is provided by a so-called “shoe”.

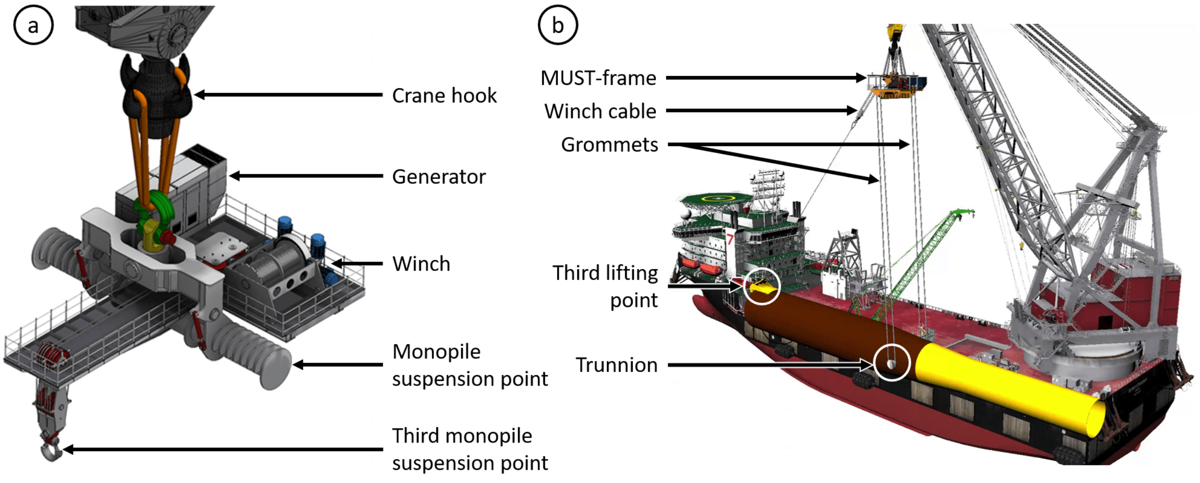

Figure 3.2: (a) Component breakdown of the MUST-platform; (b) Overview of the monopile suspension via MUST-platform. Both are conceptual images. Adapted from (D. Clunie, personal communication, 27 May, 2020)

The monopile installation procedure using the MUST was already introduced in Chapter 1. A more detailed description of the process is provided in the enumeration below (based on the sequence of actions described by Dai and Weustink (2020)).

(1) The HLV is positioned at the location where the monopile is to be installed. Position keeping can be realised by mooring cables or by DP. Seaway 7 operates one HLV that keeps its position by the first option (Seaway Yudin), and one that can do both (Seaway Strashnov, see Section 3.1)

(2) A pre-installation seabed and scour protection survey is performed by a Remotely Operated Vehicle (ROV)

(3) The transportation barge supplying the monopiles is moored along the long side of the HLV (see Figure 1.2)

(4) The MUST is suspended in the crane hook and the grommets are attached to the main suspension points of the frame. Subsequently, the lower ends of the grommets are attached to the monopile's trunnions and the winch cable is connected to the removable, pre-installed shoe (the third lifting point at the bottom of the monopile)

(5) The monopile is lifted free from the grillage structure (which provides support during transportation), and the barge is unmoored and sailed away from the HLV

(6) The winch cable is unwinded such that the lower part of the monopile is lowered into the water. This continues until the monopile is in a vertical position (this is called "upending") and the winch cable becomes slack. With a slack winch cable, the shoe at the bottom of the monopile can be removed and retrieved to the vessel (see Figure 3.3a)

(7) The monopile is slewed into an outrigger (a large "gripper"-frame, see Figure 3.3b), which helps to stabilise the monopile during positioning and to increase the installation accuracy in terms of both location and inclination. Next, the monopile is lowered through the outrigger onto the seabed. Depending on its self-weight and the soil specifications, the monopile may already partly penetrate the seabed. However, the self-weight penetration is usually not sufficient to provide free-standing stability, which means that the outrigger has to provide the required stability.

(8) The device that will drive the monopile into the seabed is installed on top. Traditionally, hydraulic impact hammers are deployed for this purpose. However, with the issue of excessive noise generation by these hammers becoming more apparent, vibratory hammers (see Figure 3.3c) are being adopted more often (Van Dorp et al., 2019). After the monopile has reached its design penetration depth, the hammer is retrieved to the vessel and follow-up operations can start (e.g., the installation of the transition piece).

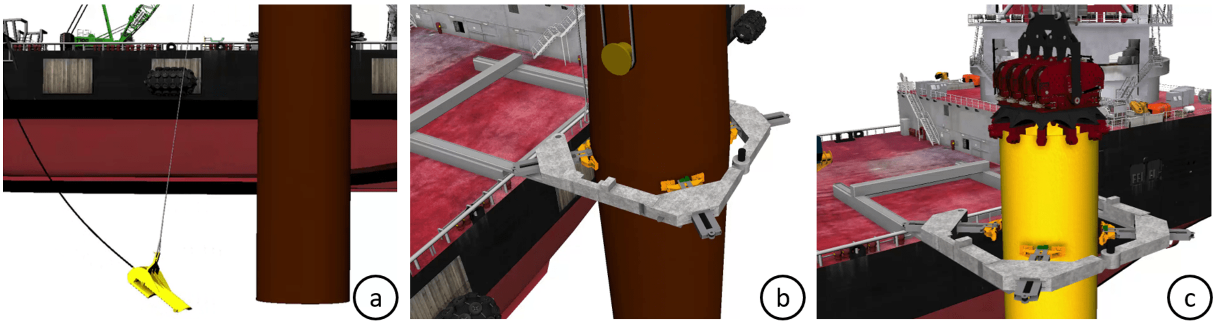

Figure 3.3: (a) Shoe removal once the monopile is vertical; (b) Monopile stabilising outrigger; (c) Vibratory hammer installed on top of the monopile (D. Clunie, personal communication, 8 July, 2020)

3.3 Critical event analysis

The selection of the critical events of analysis is of significant importance for the following phases of a workability determining procedure. Events that are left out of the further analysis should not appear to be significant after all. Therefore, Guachamin Acero, Li, et al. (2016) recommend to involve industry experts, who are experienced with the particular type of operations, in this preliminary selection. Additionally, they recommend to follow a qualitative reliability method to identify the critical events. Hence, for this thesis, a fault tree analysis is performed, as displayed in Figure 3.4, in collaboration with experienced industry experts. This diagram provides (sub-) causes that could lead to a failed monopile installation operation using the MUST. It must be mentioned that during such an installation operation, numerous events could lead to failure. However, in Figure 3.4 only the causes considered most likely to lead to failure are included (e.g., crane boom failure is left out, as it is unlikely that this would happen as long as the safe working load is considered).

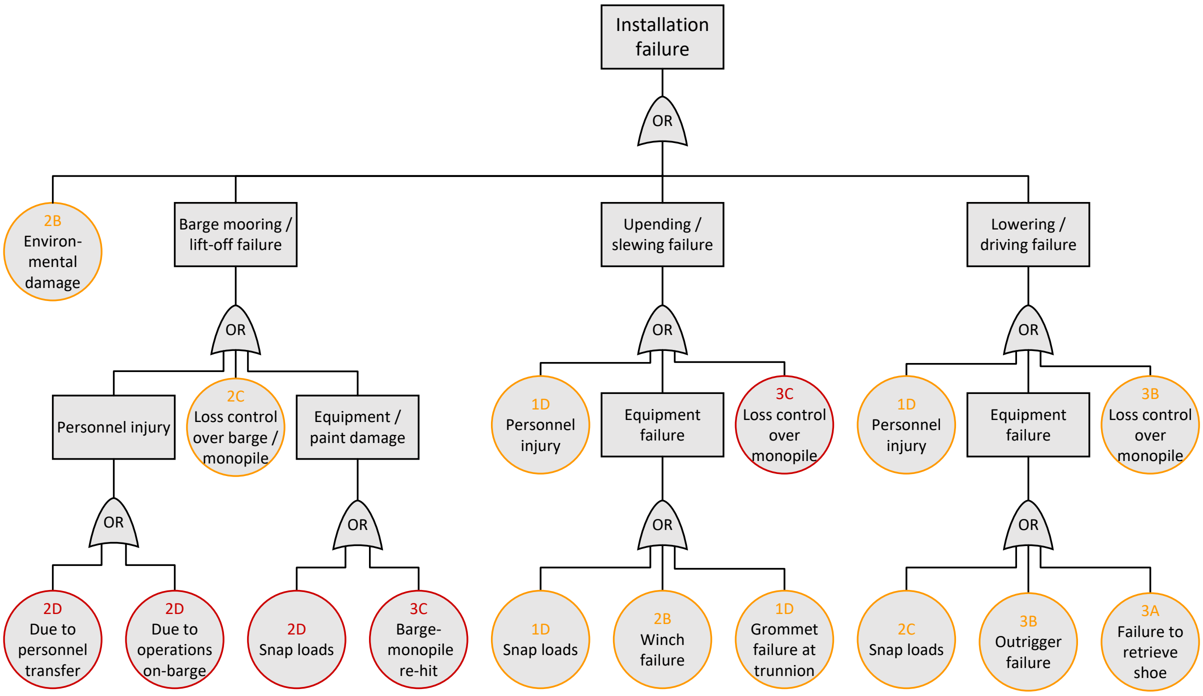

Figure 3.4: Fault tree analysis for the installation of a monopile, using the MUST

In this fault tree analysis, three main phases in which the installation operation can fail are mentioned: the barge mooring and lift-off phase, the upending and slewing phase and the lowering and pile driving phase. The most prominent hazards during the barge mooring and lift-off phase are the risks of personnel getting injured, loss of control over barge and monopile motions, and equipment getting damaged. The primary risk for personnel injuries comes from the fact that during the mooring of the barge alongside the HLV (see step 3 in Section 3.2), and the preparations of the lift-off of the monopile, personnel has to be present aboard the transportation barge. Transferring these people from the HLV to the barge is a potentially hazardous operation, mostly due to the fact that these bodies move relative to each other. Since the safety of the offshore personnel is always of primary concern, these operations should be handled with care. As indicated by Figure 3.4 in combination with the risk assessment matrix of Table 3.1, the chances of people getting injured during transfer and on-barge operations are considered “unlikely” (if the operation is performed cautiously with suitable sea states). However, since the safety of people is considered here, the risk severity is potentially “catastrophic”. Secondly, the lift-off operation could become hazardous due to uncontrolled motions of the monopile, which could lead to it impacting other structures or high crane hook loads (of which the consequences are considered of "major" severity). Such motions are mostly induced by resonance, for which a natural frequency has to be excited. With the assumption that suitable precautionary measures are taken (such as designing a suitable rigging arrangement), these resonant motions can be considered unlikely. Thirdly, just after lift-off, damage to the monopile, barge or grillage structure could be induced if the barge "re-hits" the monopile. The chances of this happening are mostly dependent on the individual responses of the HLV and the barge to wave loading, and the vertical lifting speed. Hence, such collisions are difficult to prevent and can occasionally (i.e., for relatively low sea states) cause major damage.

Table 3.1: Risk assessment matrix

		Risk severity			
		A. Acceptable	B. Minor	C. Major	D. Catastrophic
Risk probability of occurrence	1. Very unlikely	1A	1B	1C	1D
	2. Unlikely	2A	2B	2C	2D
	3. Likely	3A	3B	3C	3D
	4. Very likely	4A	4B	4C	4D

The chances of personnel getting injured during the upending and slewing phase are smaller than during the barge mooring and lift-off phase, since the barge has been sailed away at this stage and the executing personnel is aboard the HLV. Moreover, the probability of the winch cable getting slack is smaller (without the close presence of the barge, and due to the angle the winch cable makes with the monopile) and hence the probability of introducing snap loads. Since the winch is operated to upend the monopile, a component that could fail is introduced in the system. Although this could lead to the monopile being suspended stationary under an awkward angle, the chances of this happening are considered unlikely and the consequences are minor. Additionally, due to the fact that during upending the trunnions rotate in the grommet eyes, friction could be generated at these points and the grommets could fail, with the monopile crashing down as a catastrophic consequence. However, the chances of this happening are considered minimal. The largest risk for the upending phase is considered the susceptibility to large motions, which could lead to loss of control over the monopile. Since natural frequencies of pendulum systems are dependent on the cable length, and the winch cable length is changing continuously during this phase, a wide variety of natural frequencies can be activated. The possibly resulting excessive motions may be damped hydrodynamically, as the monopile may be partly submerged.

In the lowering phase, hydrodynamic forces are exerted on the monopile, making it susceptible to resonance. However, due to the presence of the outrigger, the resulting motions can be controlled more easily than during the upending. The vertical motions that cannot be controlled could induce slack grommets and therefore snap loads. However, the potential consequences are less extreme than during the lift-off phase, as the monopile will not vertically crash into another structure and it can still be controlled (to a certain extent) by the outrigger. The outrigger is another component that might fail during this phase. Although this may occasionally happen, as the outrigger is a relatively fragile component, the consequences from a safety perspective are considered minor. The retrieval of the lifting shoe after upending is deemed similar from a risk probability perspective, although the severity may be less and therefore presumed acceptable.

It must also be noted that at any moment damage can be done to the environment, as indicated in Figure 3.4. Regarding the operations performed in the three considered phases, the impact should be minor. The monopile or the MUST might drop in the water, which is not as much a concern as, e.g., oil spills in the oil and gas industry (although the generator on the MUST may release chemicals). However, the subsequent required investigations on the impact on the environment can induce significant delays in a project.

From the qualitative fault tree analysis in Figure 3.4 can be concluded that most of the operations with a “high risk” indication (indicated in red) happen during the barge mooring / lift-off phase. Hence, this stage is considered most critical in the application of the MUST. This conclusion is confirmed by the experience of industry experts with similar operations, which states that generally, the maximum allowable significant wave height is the lowest for the barge mooring and lift-off operations. A more detailed (and overlapping) fault tree analysis with a focus on this critical stage is provided in Figure 3.5. By looking into the processes of barge mooring and lift-off separately, it is found that most of the risk of injured personnel is situated in the barge mooring process. Additionally, during this phase equipment can get damaged as a yet unmoored barge may impact the HLV (and vice versa). Due to their smaller size and inertia, barges generally have higher responses to incident waves and are therefore included with a higher risk probability of excessive motions. The lift-off phase may fail due to uncontrolled motions of the monopile. Roughly stated, these motions can be induced by large HLV motions or by a resonant rigging arrangement. However, it is expected that a larger risk lies within the phase just after lifting the monopile free from the transportation barge, during which equipment may get damaged by impact forces between the transportation barge / grillage structure and the monopile. Additionally, the barge re-hitting the monopile, or large monopile motions, may introduce snap loads, which could lead to the catastrophic effect of the monopile crashing down onto the barge.

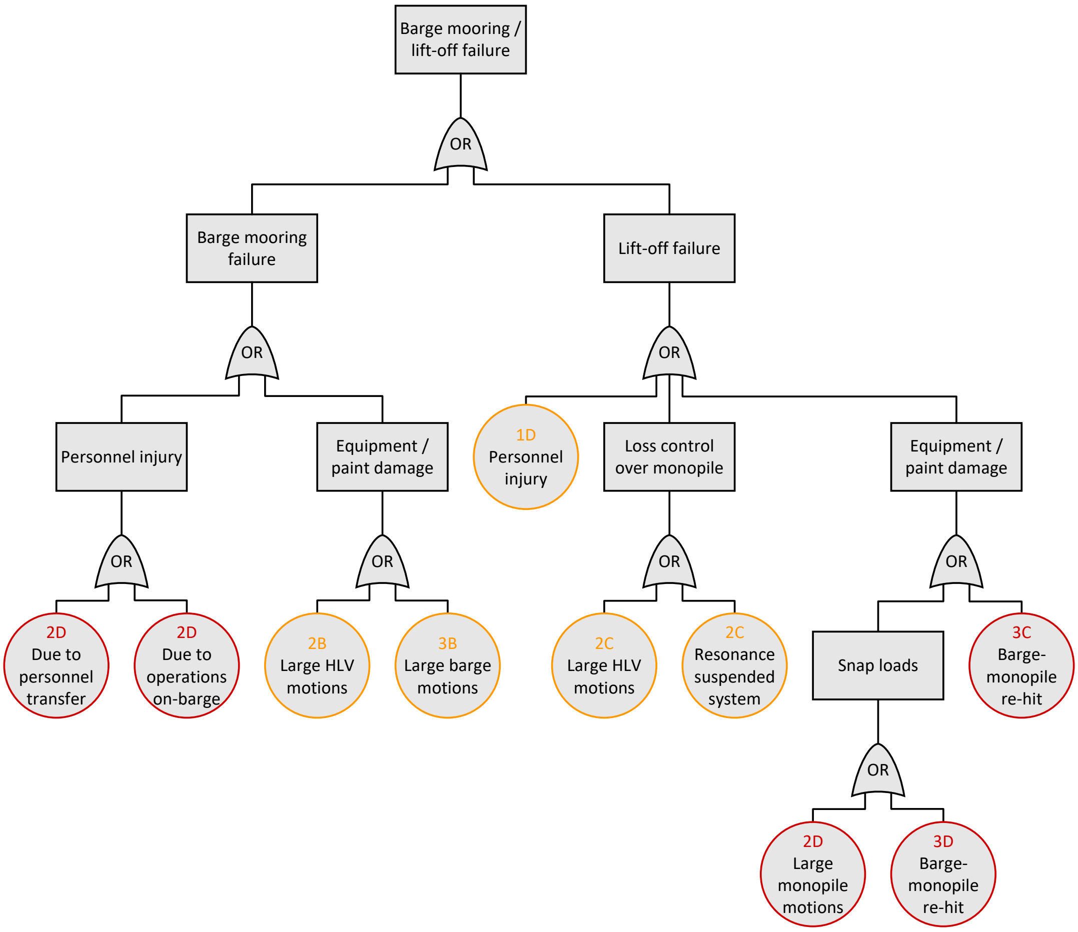

Figure 3.5: Fault tree analysis for the lift-off of a monopile from a barge, using the MUST-frame

Although the barge mooring operation is a critical stage, and operations for which the physical presence of offshore personnel is required should be performed with care, it is expected that the lift-off phase includes higher risks that limit the workability of the system of analysis. This conclusion was confirmed by the experiences and expectations of industry experts. Hence, sub-question 2 (see Section 1.4) is formulated with a focus on the lift-off phase, and an answer is provided following Figure 3.5. The expected critical events for the lift-off operation of a monopile from a barge, using the MUST are excessive monopile motions and the re-hit action between the barge and the monopile. Both may result in snap loads, which can lead to severe consequences.

3.4 Conclusions regarding the system of analysis definition

The following conclusions can be drawn from Chapter 3. Defining the system of analysis.

- The MUST is a platform that can be suspended in the crane of an HLV. On this platform, a winch is installed. From two attached suspension points, two grommets are connected to two trunnions installed on the monopile. The winch cable is attached to the bottom of the monopile by a removable shoe. Elongating the winch cable allows for in-crane upending of the monopile. Once the monopile is in a vertical position, the shoe can be removed and retrieved on deck.
- The critical events regarding the implementation of the MUST are identified by a fault tree analysis. Three phases are considered: the barge mooring / lift-off phase, the upending / slewing phase and the lowering / driving phase. From the analysis is concluded that most of the high-risk operations are performed in the first phase. This conclusion is confirmed by the experiences of industry experts.
- A second, more focused fault tree analysis is performed on the barge mooring / lift-off phase. From this analysis is concluded that the lift-off process is expected to be more critical than the barge mooring process. This conclusion is, once more, confirmed by the experiences of industry experts. Hence, in this study, the focus is laid on the lift-off phase.

4 | Model development

In order to research the workability of the MUST system, a model is constructed including the defining components. The floating system is assumed to consist of five rigid bodies that move relative to each other, but not independently: the monopile to be installed, the MUST, the crane hook, the transportation barge and the installation vessel. These rigid bodies are all introduced in Section 4.1. Next, in Section 4.2, it is explained how the effect of roll damping is implemented in the model. Section 4.3 discusses the concepts of hydrodynamic interaction and shielding effects, and how these phenomena affect the results. In Section 4.4 the effect of the rigging design on the system responses is evaluated by comparing different set-ups. Subsequently, in Section 4.5 the implementation of wind loads on the system responses is investigated and in Section 4.6 different types and set-ups of tugger line designs are compared. Lastly, in Section 4.7, conclusions regarding model development are drawn.

4.1 Rigid bodies

This section discusses the model implementation of the five rigid bodies considered in this study: the monopile (see Section 4.1.1), the barge (see Sections 4.1.2 to 4.1.4), the Heavy Lift Vessel (HLV) and its crane hook (see Section 4.1.5) and the MUST (see Section 4.1.6).

4.1.1 XXL monopiles

As touched upon in the introduction, the MUST is developed to become independent of traditional upending frames, which are growing with the increasing size of monopiles. Currently, it is expected that the mass of these "next-generation" monopiles can reach up to 2500 mT. Since monopiles with such a large mass have not been installed or constructed before, the dimensions for the monopiles considered in this study are assumed and displayed in Figure 4.1. With its total length of 80 m, it would not be the longest monopile ever produced, but in combination with a maximum outer diameter of 10 m and an average wall thickness of 130 mm it would certainly be the heaviest. Additionally, assumed initial locations for the trunnions (which will be varied in Chapter 6 and 7) and an approximated location of the Centre Of Gravity (COG) are indicated. For the assumed monopiles, the following mass properties have been determined: m = 2500 mT, $I_{xx} = 5.72 \cdot 10^7$ kg·m^2, $I_{yy} = 1.31 \cdot 10^9$ kg·m^2 and $I_{zz} = 1.31 \cdot 10^9$ kg·m^2. The fact that I_{yy} and I_{zz} (determined w.r.t. the COG) differ very marginally indicates that the trunnions only have a minimal effect on the total mass moments of inertia (as expected).

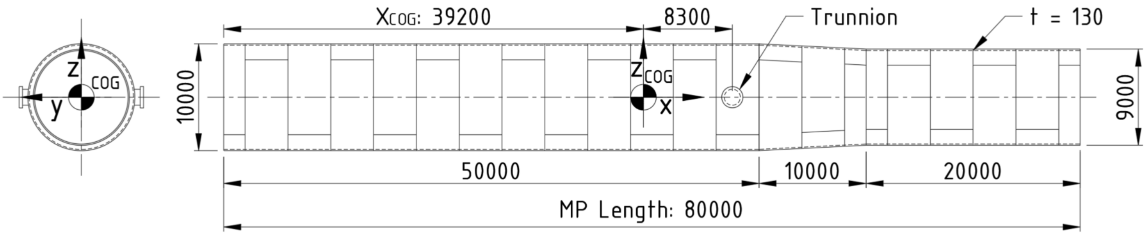

Figure 4.1: Main dimensions of assumed monopile with a mass of 2500 mT

4.1.2 Barge arrangement

The principle of the MUST is based on the supply of monopiles to the HLV by transportation barges ("feeders"). Although the monopiles considered in this study are exceptionally large, it has been decided not to analyse the implementation of extraordinarily large barges, as this would limit the generalisability of this study's results. Instead, a relatively common barge, with a length of 100 m, a breadth of 33 m and a depth of 7.6 m (300'×100'×25'), is used. Hence, only two monopiles can be transported on the barge deck, as visualised in Figure 4.2. Additionally, this figure displays the assumed "grillage". A grillage structure (in combination with seafastening) supports the monopiles during transportation, and prevents them from moving. Generally, the part of the grillage that is in direct contact with the monopile is called a “saddle”, and is shaped with the same curvature as the outer diameter of the monopile, to provide distributed support. For simplicity reasons, however, in this study a grillage structure consisting of octagonal components is assumed, as indicated by Figure 4.2. These components can be divided into three categories: longitudinal beams (60×1.5×1.5 m), transverse beams (1.5×13×1.5 m) and saddle beams (1.5×1.5×5 m). Since the outer diameter of the top of the monopile differs from the bottom part, the grillage at the front deviates in its dimensions: the front transverse beams are measuring 1.5×13×2 m and the front saddle beams 1.5×2×4.5 m. The combined weight of the grillage and seafastening is approximated as 7.5% of the corresponding monopile weight (which is used as a general rule of thumb in the offshore industry, A.Mitterfellner, personal communication, 27 May 2021).

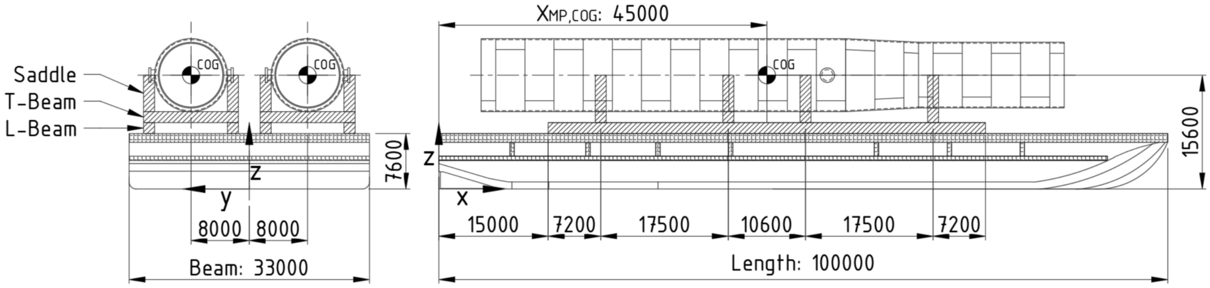

Figure 4.2: Barge arrangement of two monopiles on a barge, supported by grillage structures

4.1.3 Barge ballast arrangements

According to DNVGL-ST-N001 (2020, Table 11-15), the minimum draught at the bow (“draught fore”) of a 100 m long sea-going barge should be 2.65 m (result from linear interpolation), with a minimum trim w.r.t. the stern of 0.87 m. When three volume percent residual ballast water is assumed to be present in all of the ballast tanks, no additional ballasting is calculated (using ShipShape stability software, see Section 1.5) to result in a trim of 0.30 w.r.t. the stern. Hence, such an arrangement would not comply with the DNVGL standard. Figure 4.3, loadcase 1.1, provides the results of a ballast arrangement in which tanks 6P, 6S, 1P and 1S are ballasted to a level of 95 volume percent. This level accounts for the practical limitation of not being able to completely fill the tanks (e.g., due to air bubbles), and at the same time to minimise the free-surface effects (which reduce the stability range due to the COG-shift of ballast tank contents during roll motions). It can be concluded that this ballast arrangement provides sufficient draught at the bow, and sufficient trim (0.5 deg corresponds to 0.93 m trim w.r.t. the stern). Additionally, it complies with the by DNVGL-ST-N001 (2020, Section 11.10.9.2) recommended draught range of 35% to 60% of the barge depth. It must be noted that, to be conservative with regard to stability calculations, the unknown barge light weight COG height is taken at deck level (7.6 m).

Once the barge transporting the monopiles has arrived at the offshore location of installation, one monopile is lifted off, leaving the port side monopile on the barge. Without taking additional measures, the resulting barge heel angle is calculated as -6.1 deg (see Figure A.1 for the used coordinate system). Since such a large angle is undesirable considering the safety of on-barge personnel, the goal is set to limit the resulting angle to a minimum. Preferably this goal is pursued without the offshore deployment of ballast pumps. Therefore, flooding of ballast tanks is proposed by means of remotely controlled valves, installed in the bottom of the tanks. However, as the software of ShipShape does not support the flooding of tanks, a solution is sought by iteration. First, it is assumed that, for small angles of rotation, the waterplane in a rotating tank, rotates relatively to the tank, around the centerpoint of that plane. The orthogonal distance between this centerpoint and the bottom of the tank is $f \cdot Depth$ (see Figure 4.4), assuming that

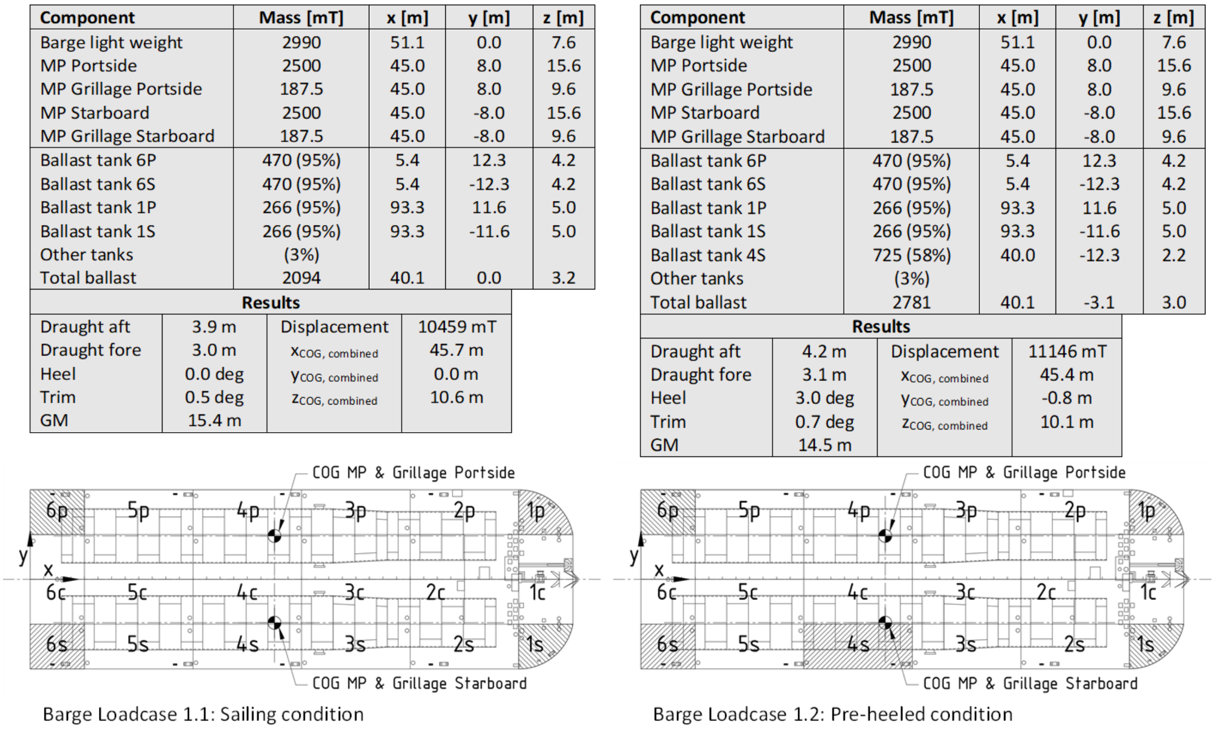

Component	Mass [mT]	x [m]	y [m]	z [m]
Barge light weight	2990	51.1	0.0	7.6
MP Portside	2500	45.0	8.0	15.6
MP Grillage Portside	187.5	45.0	8.0	9.6
MP Starboard	2500	45.0	-8.0	15.6
MP Grillage Starboard	187.5	45.0	-8.0	9.6
Ballast tank 6P	470 (95%)	5.4	12.3	4.2
Ballast tank 6S	470 (95%)	5.4	-12.3	4.2
Ballast tank 1P	266 (95%)	93.3	11.6	5.0
Ballast tank 1S	266 (95%)	93.3	-11.6	5.0
Other tanks	(3%)			
Total ballast	2094	40.1	0.0	3.2

Results

Draught aft	3.9 m	Displacement	10459 mT
Draught fore	3.0 m	$x_{COG, combined}$	45.7 m
Heel	0.0 deg	$y_{COG, combined}$	0.0 m
Trim	0.5 deg	$z_{COG, combined}$	10.6 m
GM	15.4 m		

Barge Loadcase 1.1: Sailing condition

Component	Mass [mT]	x [m]	y [m]	z [m]
Barge light weight	2990	51.1	0.0	7.6
MP Portside	2500	45.0	8.0	15.6
MP Grillage Portside	187.5	45.0	8.0	9.6
MP Starboard	2500	45.0	-8.0	15.6
MP Grillage Starboard	187.5	45.0	-8.0	9.6
Ballast tank 6P	470 (95%)	5.4	12.3	4.2
Ballast tank 6S	470 (95%)	5.4	-12.3	4.2
Ballast tank 1P	266 (95%)	93.3	11.6	5.0
Ballast tank 1S	266 (95%)	93.3	-11.6	5.0
Ballast tank 4S	725 (58%)	40.0	-12.3	2.2
Other tanks	(3%)			
Total ballast	2781	40.1	-3.1	3.0

Results

Draught aft	4.2 m	Displacement	11146 mT
Draught fore	3.1 m	$x_{COG, combined}$	45.4 m
Heel	3.0 deg	$y_{COG, combined}$	-0.8 m
Trim	0.7 deg	$z_{COG, combined}$	10.1 m
GM	14.5 m		

Barge Loadcase 1.2: Pre-heeled condition

Figure 4.3: Ballast arrangement loadcase 1: two monopiles on the barge

the tank has a cuboidal shape, and in which f is the volume fraction of the water in the tank. Subsequently, the height of the water level in the ballast tanks relative to the origin (Z'_{cwp}), in which the effects of heel (ϕ) and trim (θ) are incorporated, can be calculated using Equation 4.1. X_{cwp} and Y_{cwp} represent coordinates of the waterplane centerpoints for a horizontal barge, and $\mathbf{E}_\mathrm{x}$ and $\mathbf{E}_\mathrm{y}$ the Euler rotation matrices around the x- and y-axes. By iteration, values for the f in each tank are sought, such that Z'_{cwp} approaches the draft at the aft of the barge (D_{aft}).

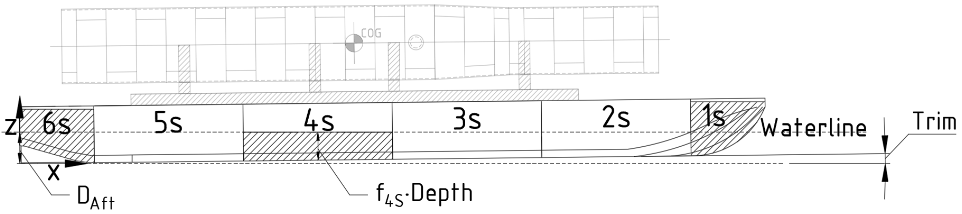

Figure 4.4: Ballast arrangement loadcase 1: two monopiles on the barge

$$\mathbf{E}_y(\theta) \cdot \mathbf{E}_x(\phi) \cdot \begin{bmatrix} X_{cwp} \\ Y_{cwp} \\ f \cdot Depth \end{bmatrix} = \begin{bmatrix} X'_{cwp} \\ Y'_{cwp} \\ Z'_{cwp} \end{bmatrix} \quad \text{Iterate towards} \quad Z'_{cwp} \rightarrow D_{aft} \tag{4.1}$$

By application of the methodology described above, the following lift-off procedure is proposed. Once the transportation barge arrives at the wind farm location, but before any monopile is lifted off, a pre-heel angle is created by flooding tank 4S (the characteristics of this ballast arrangement are described by loadcase 1.2 in Figure 4.3). Once this tank is flooded to a level of 58 volume percent, an equilibrium exists involving a heel angle of 3.0 degrees. Subsequently, the valve of tank 4S is closed and the starboard monopile is lifted off. This leads to barge loadcase 2, as presented by Figure 4.5, which involves a heel angle of -3.5 degrees. It should be noted that this loadcase provides an almost-symmetrical lift-off heel angle for the second monopile (3.0 compared to -3.5 degrees). Once the first monopile is installed and the barge is sailed to the next location of installation, the second monopile is lifted off. This leads to barge loadcase 3, which is also characterised in Figure 4.5. This loadcase involves an "empty" barge, heeled by an angle of 2.3 degrees, which is convenient as this is below the maximum value of 2.5 degrees for the offshore sailing of barges (determined based on the experience of Seaway 7 offshore personnel).

Component	Mass [mT]	x [m]	y [m]	z [m]
Barge light weight	2990	51.1	0.0	7.6
MP Portside	2500	45.0	8.0	15.6
MP Grillage Portside	187.5	45.0	8.0	9.6
MP Grillage Starboard	187.5	45.0	-8.0	9.6
Ballast tank 6P	470 (95%)	5.4	12.3	4.2
Ballast tank 6S	470 (95%)	5.4	-12.3	4.2
Ballast tank 1P	266 (95%)	93.3	11.6	5.0
Ballast tank 1S	266 (95%)	93.3	-11.6	5.0
Ballast tank 4S	725 (58%)	40.0	-12.3	2.2
Other tanks	(3%)			
Total ballast	2781	40.1	-3.1	3.0

Results			
Draught aft	3.3 m	Displacement	8646 mT
Draught fore	2.5 m	$x_{COG,\,combined}$	45.5 m
Heel	-3.5 deg	$y_{COG,\,combined}$	1.3 m
Trim	0.5 deg	$z_{COG,\,combined}$	8.5 m
GM	21.9 m		

Component	Mass [mT]	x [m]	y [m]	z [m]
Barge light weight	2990	51.1	0.0	7.6
MP Grillage Portside	187.5	45.0	8.0	9.6
MP Grillage Starboard	187.5	45.0	-8.0	9.6
Ballast tank 6P	470 (95%)	5.4	12.3	4.2
Ballast tank 6S	470 (95%)	5.4	-12.3	4.2
Ballast tank 1P	266 (95%)	93.3	11.6	5.0
Ballast tank 1S	266 (95%)	93.3	-11.6	5.0
Ballast tank 4S	725 (58%)	40.0	-12.3	2.2
Other tanks	(3%)			
Total ballast	2781	40.1	-3.1	3.0

Results			
Draught aft	2.4 m	Displacement	6146 mT
Draught fore	1.8 m	$x_{COG,\,combined}$	45.7 m
Heel	2.3 deg	$y_{COG,\,combined}$	-1.4 m
Trim	0.4 deg	$z_{COG,\,combined}$	5.6 m
GM	34.5 m		

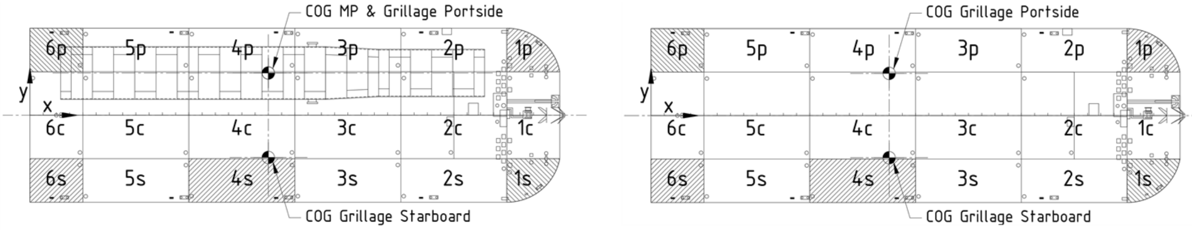

Barge Loadcase 2

Barge Loadcase 3

Figure 4.5: Ballast arrangement loadcase 2: one monopile on the barge, and loadcase 3: both monopiles lifted off the barge

4.1.4 Barge mass properties

Based on the loadcases described in Figure 4.3 and 4.5, the mass moments of inertia for the barge and its loaded components are determined. However, since those figures provide the results of static analyses, and the mass moments of inertia are required for dynamic analyses, one important change in the assumptions must be made. To provide conservative conclusions regarding the stability of the barge arrangements in Section 4.1.3, the unknown light barge COG was assumed to be located at the height of the barge deck. For dynamic analyses, this may not provide conservative results, as it results in a higher combined COG, and hence in a lower GM-value. The GM-value is linearly related to the roll stiffness (the C_{44} coefficient) (Journée et al., 2015), which means that with the current assumption a system with a relatively low stiffness is analysed, corresponding to lower accelerations than are actually present. Hence, for the further dynamic analyses, the light barge COG is assumed to be located at half the barge depth (z = 3.8 m). For the dynamic analyses this is considered to be conservative, as the COG of a barge is generally located just above half their depth. The values for $z_{\text{COG,combined}}$ and GM used in the dynamic analyses are provided by Table 4.1.

To determine the mass moments of inertia, Equation 4.2 has been derived, which is based on Steiner's Theorem. Vectors $\vec{I}$ represent the mass moments of inertia of the considered components w.r.t. their local axis system. The values for $\vec{I}_{local,MP_n}$ were already discussed in 4.1.1. Since the grillage components were assumed to consist of cuboidal elements, the values for $\vec{I}_{local,L-Beam_m}$, $\vec{I}_{local,T-Beam_m}$ and $\vec{I}_{local,Saddle_m}$ can simply be calculated by $\frac{1}{12}m(a^2+b^2)$, in which a and b constitute the dimensions of the plane perpendicular to the considered axis.

Table 4.1: Total mass moments of inertia for the three considered barge loadcases

	Loadcase 1.1	Loadcase 1.2	Loadcase 2	Loadcase 3
$z_{COG, combined, 1/2D}$ [m]	9.5	9.1	7.2	3.8
$GM_{1/2D}$ [m]	19.9	18.8	27.4	42.3
$I_{xx, global}$ [kg·m^2]	$1.48 \cdot 10^9$	$1.60 \cdot 10^9$	$1.24 \cdot 10^9$	$7.77 \cdot 10^8$
$I_{yy, global}$ [kg·m^2]	$6.29 \cdot 10^9$	$6.74 \cdot 10^9$	$5.29 \cdot 10^9$	$3.73 \cdot 10^9$
$I_{zz, global}$ [kg·m^2]	$6.54 \cdot 10^9$	$7.00 \cdot 10^9$	$5.52 \cdot 10^9$	$4.05 \cdot 10^9$

The mass component (m) in this equation is estimated by multiplying the volume fraction of the considered component relative to the total volume of the grillage components, with the total estimated mass of the grillage structure (7.5% of the monopile mass, see Section 4.1.2).

$$\begin{aligned}\vec{I}_{global} = &\sum_{n=1}^{N}\left(\vec{I}_{local,MP_n}\right) + \sum_{n=1}^{N} m_n \cdot \begin{bmatrix} r_{xx_n}^2 \\ r_{yy_n}^2 \\ r_{zz_n}^2 \end{bmatrix} + \vec{I}_{local,Barge_{m=1}} + \sum_{m=2}^{5}\left(\vec{I}_{local,L-Beam_m}\right) \\ &+ \sum_{m=6}^{13}\left(\vec{I}_{local,T-Beam_m}\right) + \sum_{m=14}^{29}\left(\vec{I}_{local,Saddle_m}\right) + \sum_{m=1}^{29} m_m \cdot \begin{bmatrix} r_{xx_m}^2 \\ r_{yy_m}^2 \\ r_{zz_m}^2 \end{bmatrix}\end{aligned} \tag{4.2}$$

The radii of gyration of the barge are approximated by Equations 4.3a to 4.3c, as proposed by Journée and Adegeest (2012). Next, the components of vector $\vec{I}_{local,Barge_{m=1}}$ are calculated using Equation 4.3d. To finally determine the components of vector $\vec{I}_{global}$, the Steiner terms are added to all local mass moments of inertia. In these terms, the distance r represents the orthogonal distance between the COG of the considered component and the corresponding global axis. For each loadcase, the calculated components of $\vec{I}_{global}$ are presented in Table 4.1.

$$k_{xx,Barge} = 0.34 \cdot \text{Beam} \tag{4.3a}$$

$$k_{yy,Barge} = 0.25 \cdot \text{Length} \tag{4.3b}$$

$$k_{zz,Barge} = 0.26 \cdot \text{Length} \tag{4.3c}$$

$$I_{ii} = k_{ii}^2 \cdot m \tag{4.3d}$$

4.1.5 Seaway Strashnov heavy lift vessel and the main crane hook

In this study, the Seaway Strashnov (introduced in Section 3.1), is taken as the HLV of analysis, which lifts and installs next-generation monopiles using the MUST. This vessel has a typical installation draught of approximately [redacted] m, and therefore this condition is taken as the starting point of this analysis. Ballasted to this installation condition, the vessel's Longitudinal Centre of Gravity (LCG) is approximately located at [redacted] m, its Transverse Centre of Gravity (TCG) at [redacted] m and its Vertical Centre of Gravity (VCG) at [redacted]. The origin to which these locations relate traditionally lies at the point where the "aft perpendicular" (an imaginary vertical line through the rudder stock of the vessel) intersects with the "baseline" (horizontal line through the lowermost point of the hull, and through the longitudinal plane of symmetry). The mass properties of the vessel in its installation condition are provided by Figure 4.6. This figure additionally provides the mass properties of the main crane hook, and the location of its origin (located in the hook's COG).

	Seaway Strashnov	Main crane hook
Mass [mT]	[redacted]	[redacted]
I_{xx} [kg·m^2]	[redacted]	[redacted]
I_{yy} [kg·m^2]	[redacted]	[redacted]
I_{zz} [kg·m^2]	[redacted]	[redacted]

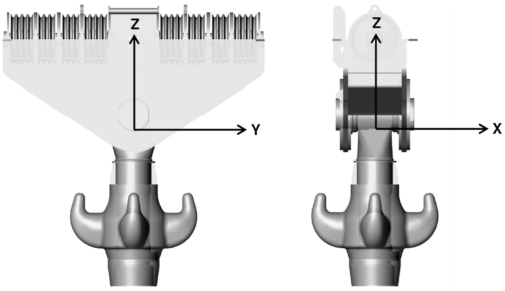

Figure 4.6: Mass properties of the Seaway Strashnov and its main crane hook (of which the COG lies in its origin)

4.1.6 MUST lift frame

The MUST-principle is based on a lifting frame that is still under development, which means that no definite design, describing its dimensions and mass properties, is available. Therefore, assumptions are made in consultation with industry experts. The main dimensions of the frame that are used to model it in Aqwa, are displayed in Figure 4.7. Other required measures are determined based on linear scaling of these dimensions. The total mass of the frame is assumed to be 10% of the maximum mass of the load it is used to upend (i.e., the monopile), which comes down to 250 mT. The distribution of this mass over the steel structure, the generator and the winch is assumed to be such that the combined COG is positioned in the longitudinal centerplane ($Y_{COG} = 0$). Furthermore, following the same assumptions and based on the steel volume distribution, the longitudinal location of the COG, X_{COG}, is estimated to be located at 3.9 m from the aft of the winch platform and at 0.6 m height from the platform's floor (Z_{COG}). Following the same assumptions, and using the same theory as was used to derive Equation 4.2, the mass moments of inertia (w.r.t. its COG) of the MUST frame are determined and provided by Figure 4.7.

	MUST-frame
Mass [mT]	[redacted]
I_{xx} [kg·m^2]	[redacted]
I_{yy} [kg·m^2]	[redacted]
I_{zz} [kg·m^2]	[redacted]

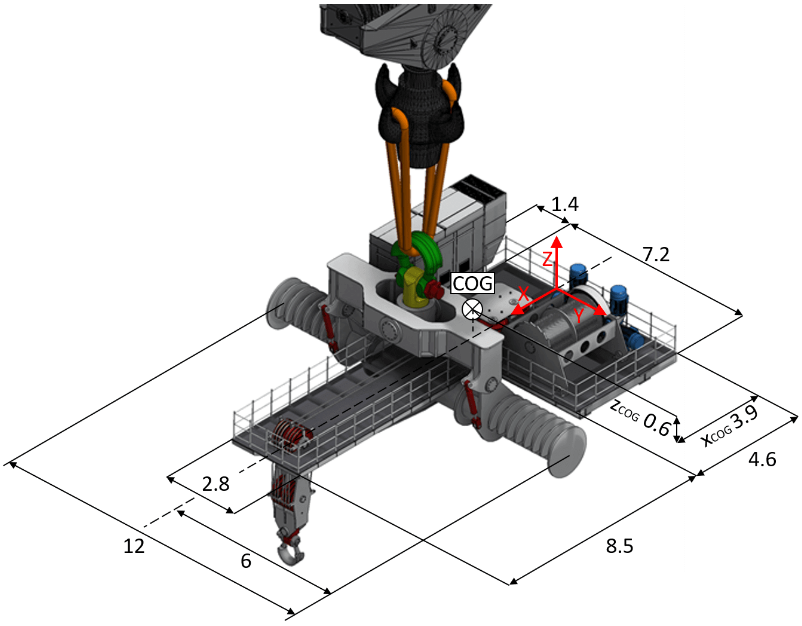

Figure 4.7: Estimated mass properties and dimensions of the MUST

4.2 Roll damping

During the considered lift-off operations of monopiles from a barge moored alongside the HLV, surge, sway and yaw motions are restrained by the anchoring system, and can be modelled as such relatively easily. Pitch and heave motions are restrained to a limited extent, but the damping corresponding to these degrees of freedom is predominantly provided by potential flow-induced forces (Korpus & Falzarano, 1997). Since Aqwa is based on potential theory, it enables to determine frequency-dependent potential damping values, and therefore, to describe the damping corresponding to heave and pitch to a large extent. However, the damping resulting from roll motions is mostly generated by turbulent and viscous flows along a vessel's hull and around its bilges. By definition, potential theory does not include such effects (see Section A.2.2), and hence Aqwa lacks the ability to accurately determine roll damping.

The roll motion of a vessel is typically a lightly damped degree of freedom (Korpus & Falzarano, 1997), which can result in significant motions when the vessel is excited by incident waves with frequencies close to the natural roll frequency of the vessel. In the system of analysis, these excessive roll motions may appear to be problematic, as they would induce significant relative vertical motions. This is the case due to the fact that the monopiles on the barge are transported significantly outside the longitudinal centerplane of the barge, and the crane tip in lift-off condition is located at a significant distance from the HLV's longitudinal centerplane. Studying the workability of the MUST system by simulation, without the inclusion of viscous roll damping, is therefore expected to provide results that significantly underestimate the system's performance. Hence, methodologies to include viscous roll damping in the analysis are studied.

4.2.1 Ikeda's method

Falzarano, Somayajula, and Seah (2015) provide an overview of methods that have been developed over the years, to determine a vessel's viscous roll damping. According to their analysis, the method proposed by Ikeda, Himeno, and Tanaka (1978) and Himeno (1981) has been the de facto industry standard for many years and is therefore considered the most applicable approach currently available. In this method, the viscous roll damping ($\mathbf{B_{44V}}$) is estimated by the summation of five linear components, as expressed by Equation 4.4, of which it is assumed that they can be determined independently and do not influence each other.

$$B_{44V} = B_{44S} + B_{44F} + B_{44L} + B_{44E} + B_{44K} \tag{4.4}$$

The first component proposed by Ikeda et al. (1978) and Himeno (1981) is the additional wave damping due to the forward speed of the considered vessel ($\mathbf{B_{44S}}$). It can be considered as a correction to the wave damping calculated by potential theory, in which the vessel is assumed to be stationary. Due to the fact that in the system of analysis both the HLV and the barge have approximately zero forward speed, this component is expected not to influence the simulation results to a large extent. $\mathbf{B_{44F}}$ represents the damping due to viscous skin friction acting on the hull. To describe this component, Ikeda et al. and Himeno use the theory developed by Kato (1957). To calculate the values corresponding to lift damping ($\mathbf{B_{44L}}$), Ikeda et al. (1978) derive an empirical expression. This expression describes the lift damping as being linearly dependent on the forward speed, providing a theoretical value of zero for a vessel without forward speed. The eddy damping component ($\mathbf{B_{44E}}$) represents the damping caused by flow separation and vortex shedding around a vessel's hull, inducing pressure variations. This component is quadratically dependent on the roll angular velocity. The fifth viscous roll damping component, $\mathbf{B_{44K}}$, describes the damping due to the presence of a bilge keel. Although this component is slightly dependent on the forward speed of a vessel, this relationship can be neglected and the damping component can be calculated without incorporating the forward speed (Ikeda et al., 1978). Hence the most relevant components for this study are $\mathbf{B_{44F}}$, $\mathbf{B_{44E}}$ and $\mathbf{B_{44K}}$.

4.2.2 Viscous roll damping in Aqwa

As stated above, Aqwa does not provide the functionality to determine viscous roll damping coefficients. However, Aqwa does allow for supplementing additional, frequency-independent damping coefficients. Such values can be determined based on field tests, model tests or using external software. For HLV the Seaway Strashnov, the viscous roll damping has been determined by field experiments (B. Dai, personal communication, 17 May 2021), and hence the applicable measured value can be implemented in the Aqwa model. Such measured values are generally considered realistic and reliable (DNVGL-RP-C205, 2019, Section 7.1.8.9), which makes estimating the damping value using methods as described above superfluous. However, to determine the applicable damping values for the different barge loadcases, the hull shape of the barge is implemented into the software of Octopus Office (a hydrodynamic analysis programme, see Section 1.5), which allows for determining roll damping coefficients according to the approach proposed by Ikeda et al.. Since the viscous roll damping is dependent on the barge's response amplitudes, and therefore on the incident wave's frequency, height and relative direction, but only a constant value can be supplemented to Aqwa, some assumptions and simplifications have to be made. Firstly, due to the fact that this study is focused on determining the workability of the system of analysis, and therefore tries to determine the limiting combinations of significant wave height, peak wave period and Wave Encounter Angle (WEA), the viscous damping at the point of the vessel reaching its limiting value for roll is considered the most relevant condition to determine the roll damping for. Secondly, the limitations of only considering potential damping particularly come into play close to the vessel's natural roll period (Falzarano et al., 2015), and therefore this period is considered most relevant. In Octopus, the significant wave height for which the barge reaches its limiting roll response is sought iteratively, considering incident waves with a peak period equal to the undamped natural roll period of the vessel (determined in Aqwa) and with a WEA of 90 degrees ("beam seas"). The latter is considered conservative, as it provides the lowest significant wave height for which the vessel reaches its limiting roll response.

In the described process, the Joint North Sea Wave Project (JONSWAP) spectrum is used as wave spectrum, which means that in addition to the significant wave height ($\mathrm{H_s}$) and peak wave period ($\mathrm{T_p}$), a third parameter is required to describe the spectrum: the peak shape parameter γ. According to DNVGL-RP-C205 (2019, Section 3.5.5.5), the value for this parameter is dependent on the values for $\mathrm{H_s}$ and $\mathrm{T_p}$, as expressed in Equation 4.5.

$$\gamma = \begin{cases} 5 & \text{for} \quad \frac{T_p}{\sqrt{H_s}} \leq 3.6 \\ e^{5.75-1.15\cdot\frac{T_p}{\sqrt{H_s}}} & \text{for} \quad 3.6 < \frac{T_p}{H_s} < 5 \\ 1 & \text{for} \quad 5 \leq \frac{T_p}{\sqrt{H_s}} \end{cases} \tag{4.5}$$

Additionally, Octopus requires an input value for the power of the wave spreading function (of which the physical meaning is explained in Appendix A, Section A.2.1). Assuming that the considered operations are performed at the North Sea (which is in line with the use of the JONSWAP spectrum), Boukhanovsky, Lopatoukhin, and Soares (2007) propose a value between two and four for weak and moderate waves, and between four and eight for storm waves. Considering the fact that delicate operations such as the one under analysis generally are not performed in high sea states, a value for the power of wave spreading of four is deemed suitable (which is within the relatively wide margins set by DNVGL-RP-C205 (2019, Section 3.5.8.8)).

By following the iterative process described above, it has been determined that for barge loadcase 1.1, with an undamped natural roll period of 7.42 s, the roll Significant Double Amplitude (SDA) limit of 1.5 deg is reached when the barge is loaded by beam sea waves, with a significant wave height of 0.39 m and a peak wave period equal to the undamped natural roll period. The results of the final iteration are displayed in Figure 4.8. Figure 4.9 provides an indication of the orientation of the WEAs w.r.t. the HLV. Graphs similar to Figure 4.8 are generated when the other barge loadcases are studied. However, those correspond to the different values for the limiting significant wave height and the undamped natural roll period of the considered loadcase. These values are presented in Table 4.2. Furthermore, Table 4.2 provides the viscous roll damping coefficients (B_{44v}) for the various barge loadcases, corresponding to the sea state-describing parameters, and it gives the value for the viscous roll damping of the HLV, which was measured during field tests, as mentioned earlier.

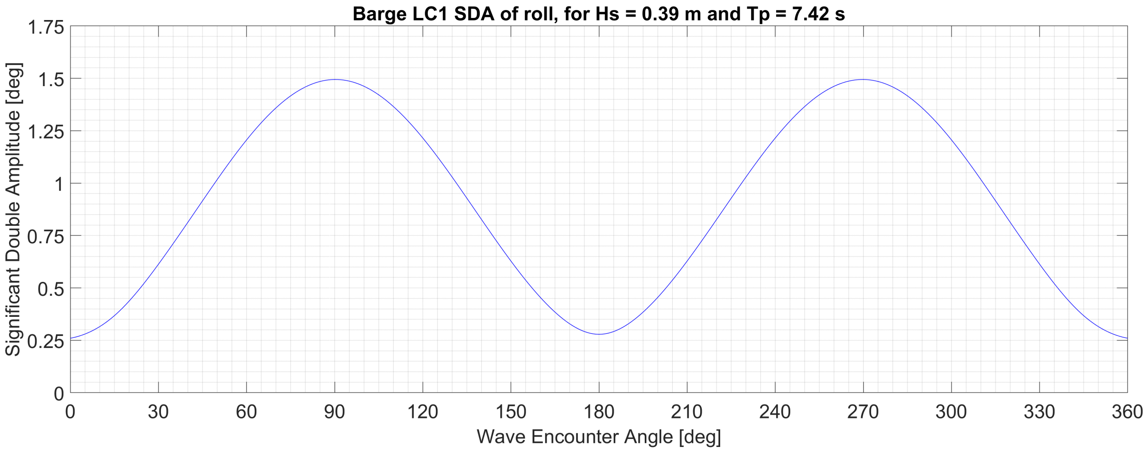

Figure 4.8: The SDA of the roll response of barge loadcase 1.1, subjected to waves characterised by an Hs of 0.39 m and a Tp of 7.42 s, plotted against the WEA. The SDA limit of 1.5 deg is reached for a WEA of 90 deg

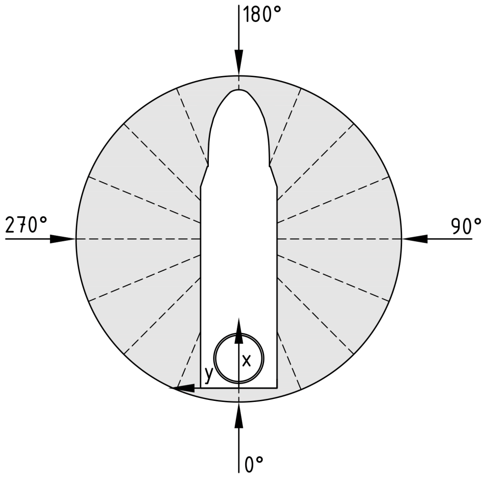

Figure 4.9: WEA-orientation w.r.t. the HLV

Table 4.2: Input and output values for the analyses performed in Octopus to determine the viscous roll damping coefficient (B_{44v}) for the barge loadcases, and the measured value of B_{44v} for the HLV

	Roll SDA-limit [deg]	Undamped natural roll period [s]	Limiting significant wave height [m]	B44v coefficient [kg·m²/s]	Fraction of critical damping [%]
Barge loadcase 1.1	1.5	7.42	0.39	$1.63 \cdot 10^8$	8.4
Barge loadcase 1.2	1.5	7.52	0.46	$1.64 \cdot 10^8$	9.6
Barge loadcase 2	1.5	6.62	0.38	$1.57 \cdot 10^8$	13.3
Barge loadcase 3	1.5	6.23	0.74	$1.49 \cdot 10^8$	17.1
Seaway Strashnov	N/A	N/A	N/A	[redacted]	[redacted]

As touched upon earlier in this section, the viscous roll damping coefficients are subsequently supplied to the Aqwa models as frequency-independent damping terms. The ratios of the resulting roll damping (which includes both potential and viscous damping) and the critical damping can next be derived for every loadcase, and are presented in Table 4.2. In order to demonstrate the importance of including the viscous roll damping in the models of this study, both simulations with and without including the determined coefficients are performed. Figure 4.10 provides this comparison for barge loadcase 1.1 (a single body analysis is performed). A significant reduction of the Response Amplitude Operator (RAO) close to the natural roll frequency is observed. Additionally, the time domain simulation results display a significant reduction of the roll angle amplitudes. Similar results are obtained for the other barge loadcases and for the HLV. Hence, including viscous roll damping in the analyses of this study is considered a requirement to prevent obtaining overly-conservative results.

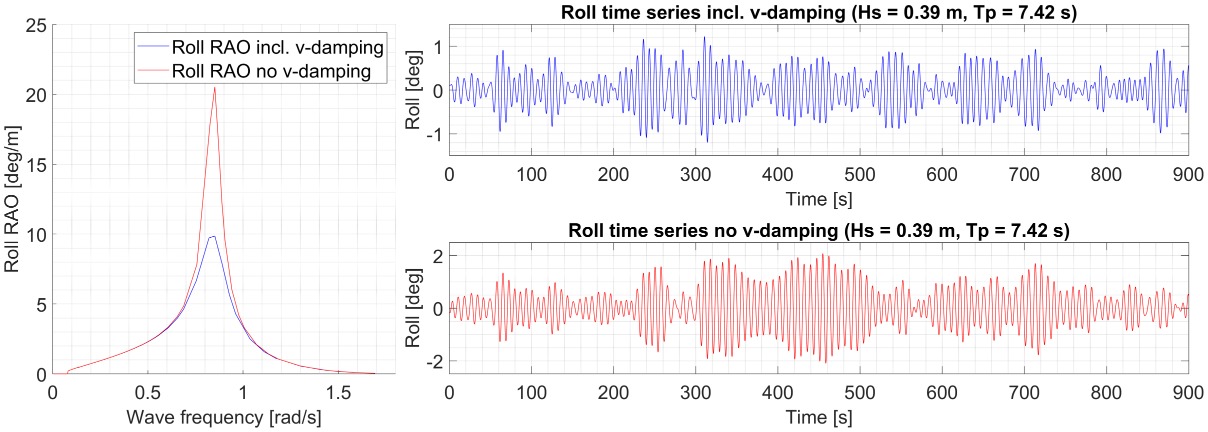

Figure 4.10: Comparison of the roll RAO curves and time series, for barge loadcase 1.1, subjected to waves with a significant wave height of 0.39 m, peak wave period of 7.42 s and a WEA of 90 deg

4.2.3 Nonlinear roll damping

The implementation of the viscous roll damping coefficient in Aqwa requires to neglect its dependency on roll amplitude and angular velocity (see Section 4.2.2), and thereby its nonlinear effects. This section evaluates the error that is introduced with this simplification.

Generally, the equation of motion including non-linear roll damping effects is written as Equation 4.6 (based on the equations presented in Section A.3), in which $\mathrm{B_L}$ and $\mathrm{B_N}$ are the linear and quadratic damping coefficients respectively. By performing a Fourier series expansion and assuming that the roll oscillations are "reasonably harmonic over each half cycle", Zhao et al. (2016) rewrite this equation to Equation 4.7. Hence, they propose to express the nonlinear roll damping coefficient as a function of the barge roll amplitude.

$$(M+A)\ddot{\phi} + B_L\dot{\phi} + B_N\dot{\phi}\left|\dot{\phi}\right| + K\phi = 0 \tag{4.6}$$

$$\ddot{\phi} + 2\zeta\omega_n\dot{\phi} + \frac{B_N}{M+A}\frac{8}{3\pi}\omega_n\phi_i\dot{\phi} + \omega_n^2\phi = 0 \tag{4.7}$$

To analyse the relationship between the nonlinear roll damping coefficient and the roll amplitude, once more Ikeda's Method is consulted using the software of Octopus Office. This software package enables to determine roll damping coefficients depending on the barge responses as discussed in Sections 4.2.1 and 4.2.2. For a WEA of 90 degrees (beam seas), the barge arrangements are subjected to sea states with peak wave periods of 5 to 15 seconds with one-second steps and at the natural barge roll period, and with significant wave heights of 0.1, 0.2, 0.3, 0.5, 0.75, 1.0, 2.0, 3.0 and 7.0 m. Hence 108 different sea states are evaluated, which result in different roll responses. Following on Zhao et al. (2016), the corresponding roll damping coefficients are plotted against the Significant Single Amplitude (SSA) in Figure 4.11a, from which a linear relationship can be identified. In this figure, the responses below the set limit (1.5 deg SDA corresponds to 0.75 deg SSA) are indicated in green and the ones above in red. By supplementing

Aqwa with a response-independent roll damping coefficient, this positive linear relationship is approximated as a horizontal line, which means that for increased responses the error of the implemented roll damping coefficient grows linearly. However, since responses considered in this study are relatively small, the errors are limited as well (the errors occur in the section of responses indicated in green in Figure 4.11a). Furthermore, while the model tests by Zhao et al. (2016) confirm the linear relationship for “large” roll amplitudes, they also find that for “small” amplitudes the roll damping coefficient is approximately constant (for the tested barge-shaped LNG-carrier, the differentiating angle lies around four degrees, see Figure 4.11b). This effect would reduce the error introduced by taking the roll damping coefficient for the limiting roll angle, when analysing smaller responses.

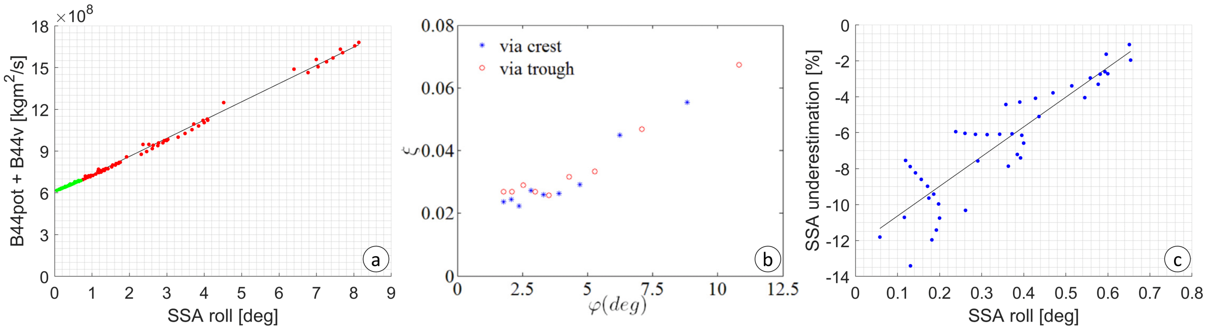

Figure 4.11: (a) Linear dependency between the SSA of the barge roll motion and the sum of the viscous and potential roll damping coefficient, (b) Measured relationship between the roll amplitude and the non-dimensional roll damping coefficient of a barge-shaped LNG-carrier (Zhao et al., 2016), (c) The roll-response underestimation due to the simplification in the Aqwa implementation, as a function of the estimated response

Due to the fact that the roll damping coefficient increases with the roll response, taking the damping value at the limiting response results in an underestimation of smaller responses. Figure 4.11c displays the relationship between the estimated roll SSA based on the constant coefficient presented in Table 4.2, and the percentage the found response is lower than the value resulting from an analysis that considers nonlinear effects. Since for a workability study the responses around the set limit are of most value, and the deviation around this limit is associated with low percentages, it is concluded that the discussed simplifications are suitable for the intended purpose. In the case that in reality the curve flattens out for lower response angles (as is the case in Figure 4.11b), it would have the positive effect of the percentages in Figure 4.11c shifting towards the zero-line.

4.3 Hydrodynamic interaction and shielding effects

In Section 4.2, analyses are performed on the individual structures that are considered in this study. However, in the system of analysis, two floating structures are positioned in close proximity. This will result in effects that, in the industry as well as in the literature, are known as “hydrodynamic interaction”. Such effects, depending on the relative position of the considered structures, “can result in a reduction or an increase of the wave-induced motions of the structures” (Pinkster, 1995). The theory discussed by Pinkster is mostly focused on describing radiation and diffraction coupling based on three-dimensional diffraction theory. Additionally, Li et al. (2014) (discussed in 2.2.2) shows that two floating structures in close proximity to each other can benefit from so-called “shielding effects”. If a floating body is positioned on the leeward side of a larger vessel, the larger vessel takes out a large part of the energy in the incident waves, such that the energy contained in the waves reaching the smaller body is reduced. According to Li et al. (2014), various studies have reached the conclusion that, while the crane tip motions of large Semi-Submersible Crane Vessels (SSCVs) may hardly be affected by incident waves, relatively small barges greatly benefit from the shielding effects provided by these vessels in terms of reduced motions. This section performs a similar analysis, in which the necessity of including hydrodynamic interaction and shielding effects for the case of a ship-shaped HLV and a barge is researched. Figure 4.12 displays those two floating bodies, modelled in Aqwa. As can be deduced from this figure, the barge is modelled for its first loadcase, in which both monopiles are still secured on the grillage. The blue elements represent the diffracting elements, which are below the still water surface.

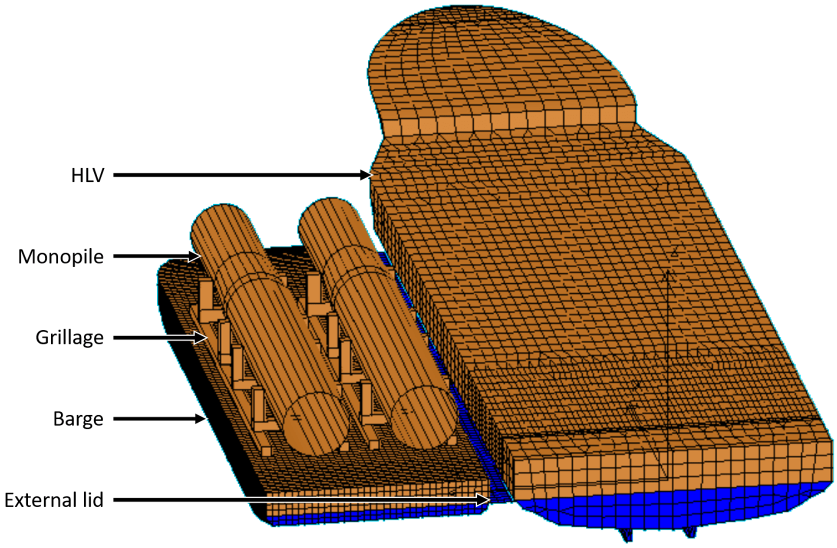

Figure 4.12: The transportation barge and the HLV modelled in Aqwa

One of the challenges of solving hydrodynamic interaction problems by potential flow theory is that standing resonant waves may develop in the gap between the structures in the model. Due to the fact that potential theory does not include viscous effects, the model accounts for significantly less damping than is actually present. To add this damping to a model based on potential theory, an "external lid" can be modelled in the gap between the structures (see Figure 4.12), as proposed by X. Chen (2011) and Peña and Mcdougall (2016). The damping effect of an external lid can be implemented in Aqwa based on Equation 4.8a, in which α_d can be recognised as a damping factor, and f_1 is a function related to the distance between the considered structures (ANSYS, 2015). This equation can be rewritten to Equation 4.8b, in which the free surface kinematic boundary condition of Equation 4.8c (Journée et al., 2015) can be recognised. Hence, the condition used in Aqwa (Equation 4.8a) is nothing more than Equation 4.8c to which damping factors are added. X. Chen (2011), Peña and Mcdougall (2016) and ANSYS (2016b) propose to use a value of 0.02 for the damping factor α_d, and hence this value is used for the models in this study.

$$\frac{\omega^2}{g} \cdot \left(\alpha_d^2 \cdot f_1 - 1\right) \Phi - 2i \cdot \frac{\omega^2}{g} \cdot \alpha_d \cdot f_1 \cdot \Phi + \frac{\partial \Phi}{\partial z} = 0 \quad \text{where} \quad z = 0 \tag{4.8a}$$

$$\frac{\partial \Phi}{\partial z} - \frac{\omega^2}{g} \cdot \Phi \left(1 + 2i \cdot \alpha_d \cdot f_1 - \alpha_d^2 \cdot f_1\right) = 0 \tag{4.8b}$$

$$\frac{\partial \Phi}{\partial z} - \frac{\omega^2}{g} \cdot \Phi = 0 \tag{4.8c}$$

In order to investigate the necessity of including hydrodynamic interaction and shielding effects in this study's simulations, some experiments are performed. Figure 4.13 compares HLV response RAOs for which hydrodynamic interaction effects are accounted for, with RAOs that are determined without including those effects. The WEA of 90 and 270 degrees are considered most relevant in this experiment, due to be parallel positioning of the floating bodies' longitudinal axes. Since the sway and yaw motions are restrained by the mooring system, only the resulting roll and heave motions are analysed. Figure 4.13d shows some reduction of the HLV's heave RAO, which is presumably the result of the vessel being shielded by the barge. However, overall it can be concluded that the HLV responses are only affected by hydrodynamic interaction effects to a very limited extent (as was also concluded regarding SSCVs by various studies reviewed by Li et al. (2014)).

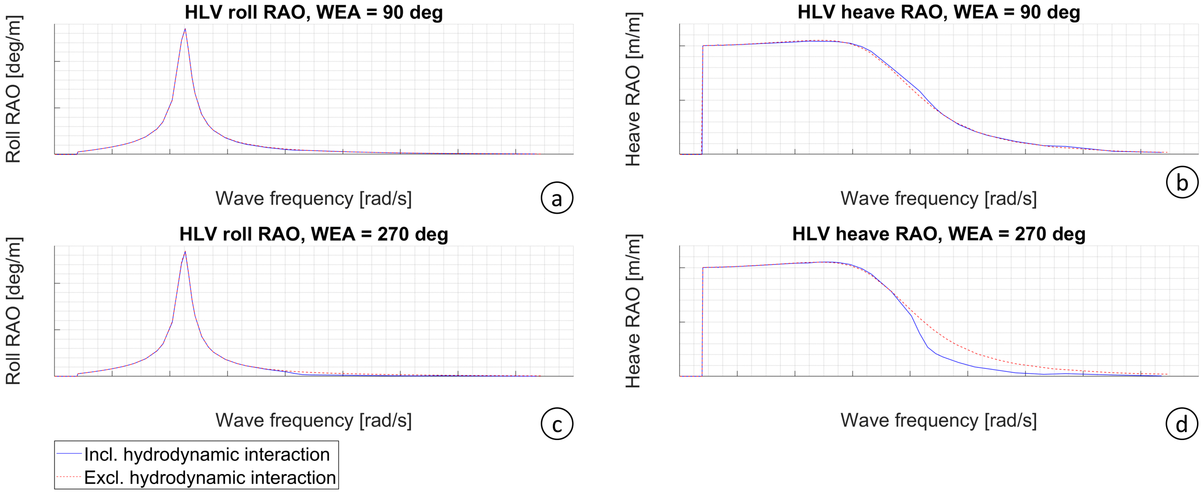

Figure 4.13: Roll and heave RAOs for the HLV

The same analysis is performed for the transportation barge, of which the results are provided by Figure 4.14. For the WEA of 90 degrees, the barge is at the leeward side of the HLV. The result of shielding effects is clearly visible in Figure 4.14a and 4.14b, as the RAOs for roll and heave are significantly reduced (especially for high-frequency, short waves). Furthermore, due to the inclusion of hydrodynamic interaction effects, relatively large "discontinuities" are introduced in the curves. For the WEA of 270 degrees, the barge is at the windward side of the HLV, which means that it does not benefit from shielding effects. Remarkable are the results displayed in Figure 4.14c and 4.14d, which show that for some frequency ranges the responses of the barge can even increase with the incorporation of hydrodynamic interaction. Similar amplification effects are reported by Li et al. (2014). Conclusively, it can be stated that including hydrodynamic interaction and shielding effects in this study's simulations is a requirement, especially regarding the responses of the barge.

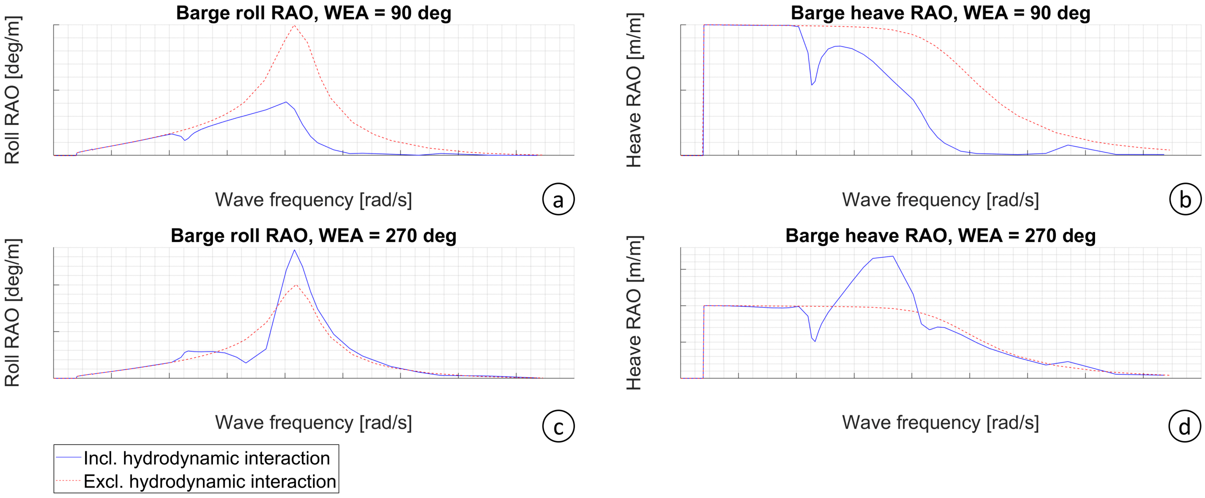

Figure 4.14: Roll and heave RAOs for barge loadcase 1.1

4.4 Rigging design

The principle of the MUST system is based on various cable connections between the HLV, the crane hook, the MUST and the monopile. Rigging multiple components in series may lead to multiple pendulum behaviour, which cannot be described by a closed-form solution and can even lead to chaotic behaviour (Braun, 2003). Therefore, it is decided to look into the behaviour of the rigging arrangement with regard to its resonant modes, and to determine the extent to which the behaviour of the MUST's rigging arrangement can be described by multiple pendulum theory.

4.4.1 Aqwa implementation

Figure 4.15 provides a visualisation of the implementation of the MUST in Aqwa for loadcase 2: the first monopile is suspended in the crane, while the other is still on the barge. The three-cable connection between the MUST and the monopile is modelled similarly to its original design (see Figure 3.2). Such a connection provides more constraints than a single cable connected to a point mass, which is the connection considered in the traditional pendulum theory. A similar conclusion can be drawn from the modelled connection between the crane hook and the MUST, which is depicted in Figure 4.15b. This connection deviates to some extent from the conceptual design provided by Figure 4.7, as in the latter the MUST-rigging connection is concentrated to a single suspension point. Based on the fact that such a connection would lead to numerical instabilities regarding the yaw-motions of the MUST and the monopile, it has been decided to model the two-point suspension of Figure 4.15. Since the one-point connection of Figure 4.7 in its turn suspends the tubular lifting beam by two hinges, it can be expected that the deviating connection modelled in Aqwa only affects the behaviour to a limited extent. Once more, this connection deviates from a theoretical multiple pendulum section as it introduces additional constraints (regarding the MUST sway, roll and yaw motions).

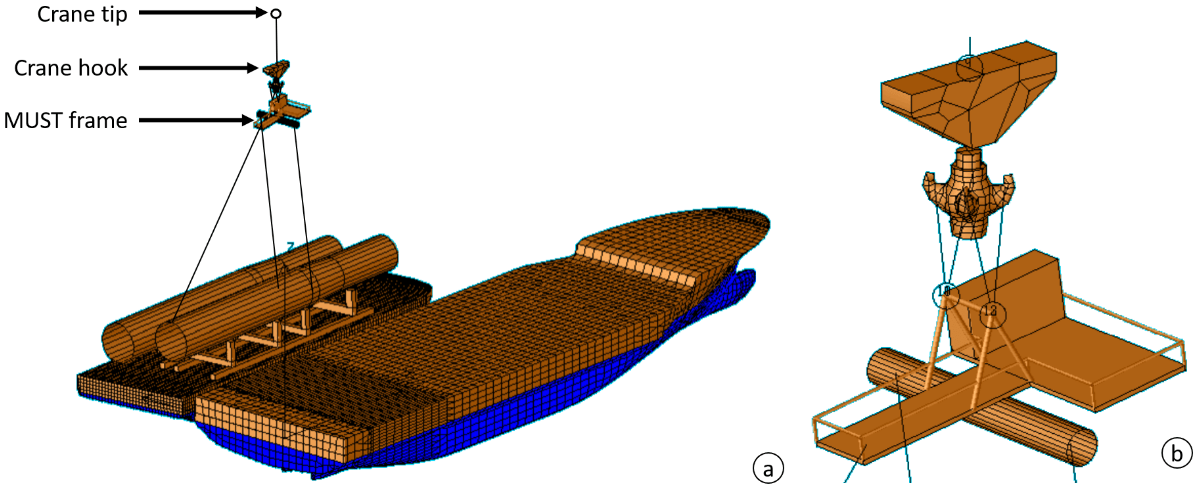

Figure 4.15: (a) General overview of the Aqwa implementation of loadcase 2: the first monopile lifted off from the barge, (b) Aqwa implementation of the crane hook - MUST connection

4.4.2 Frequency domain rigging length analysis

In the analysis of the suspended system behaviour, the focus is laid on surge and sway motions (since these represent the pendulum behaviour). It appears that the crane hook, the MUST and the monopile all three have a common (coupled) natural frequency for their surge (and pitch, which is coupled to surge) motion. In case the monopile is lifted to a height of three meters above its grillage structure (which is a standard analysis case within Seaway 7), this frequency amounts [redacted] rad/s. For the same analysis position, the sway (and roll, which is coupled to sway) motions correspond to two common natural frequencies: [redacted] and [redacted] rad/s. One non-conformality of the analysed system with a theoretical (multiple) pendulum is directly visible: the situation in x-direction differs from that in y-direction.

According to Braun (2003), the natural frequencies corresponding to multiple pendulums vary with the length of the individual cable sections. To test this statement with the system of analysis, the cable lengths in the rigging arrangement are varied while keeping the total length (i.e., the height of the suspended monopile) constant. The considered combinations of cable lengths per rigging section are presented in Table 4.3, and the resulting RAOs for the monopile surge and sway motions in Figure 4.16 and 4.17 respectively. From these figures can be concluded that only very marginal shifts in the monopile RAOs (and therefore in the natural frequencies) are the result of significant changes in the cable lengths of the rigging sections, which deviates from the expectations based on multiple pendulum theory. However, when looking into the RAOs of the crane hook and the MUST (see Figure 4.18), some significant effects are visible. In both the surge and the sway plot, additional high-frequency peaks are introduced. Furthermore, the height of the second peak in the sway plot is clearly influenced by the variation in rigging length ratios. If one of the configurations should be appointed favourable based on the Frequency Domain (FD)-analysis, the distinction would be based on the responses of the crane hook and the MUST, as the differences in the expected monopile responses are marginal. Hence, predominantly based on the peak at [redacted] rad/s in the sway RAO plot of Figure 4.18, configuration L3 is considered slightly favourable over the others.

Table 4.3: Sets of cable lengths per rigging section

	Crane tip – Crane hook [m]	Crane hook – MUST [m]	MUST – Monopile trunnions [m]	MUST – Monopile bottom [m]
L1	25.3	5.0 (x4)	46.3 (x2)	53.4
L2	10.0	5.0 (x4)	61.5 (x2)	66.0
L3	36.0	5.0 (x4)	35.8 (x2)	45.8
L4	10.0	30.9 (x4)	35.8 (x2)	45.8

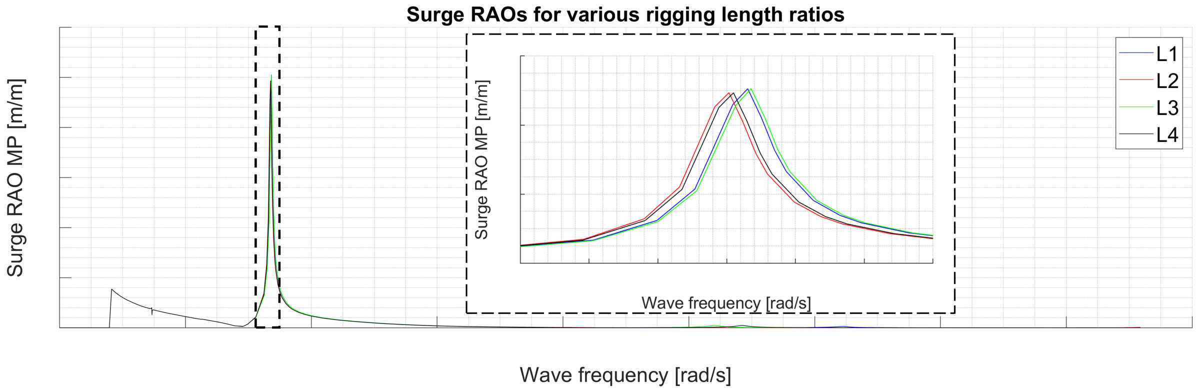

Figure 4.16: Monopile surge RAOs for various combinations of cable lengths in the monopile rigging arrangement, while keeping the monopile suspension height constant (based on a WEA of 0 deg)

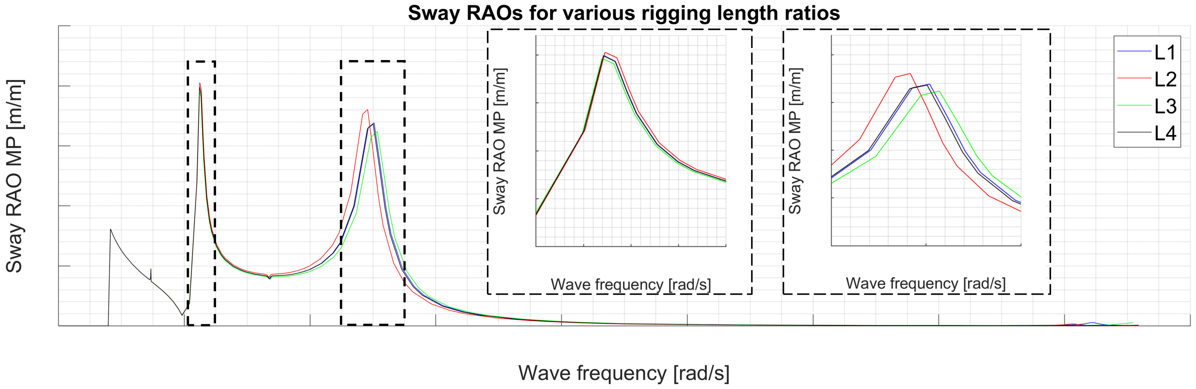

Figure 4.17: Monopile sway RAOs for various combinations of cable lengths in the monopile rigging arrangement, while keeping the monopile suspension height constant (based on a WEA of 90 deg)

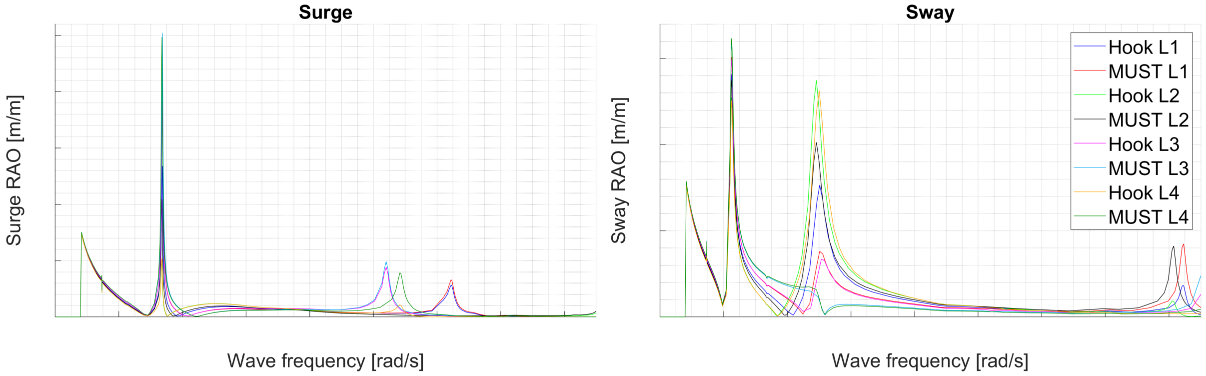

Figure 4.18: Surge (WEA taken as 0 deg) and sway (WEA taken as 90 deg) RAOs of the crane hook and the MUST-frame for various combinations of cable lengths in the rigging arrangement but with a constant monopile suspension height

4.4.3 Time domain rigging length analysis

To further analyse the effect of varying the rigging length ratios, and to confirm the slight preference for configuration L3, Time Domain (TD) simulations are performed, in which the behaviour of arrangement L3 is compared to that of configurations L1, L2 and L4. Table 4.4 provides an overview of the simulations and a reference to the corresponding figure in Appendix B. As is explained below, rigging configuration H1 refers to the exact same case as that of L3, and are used interchangeably in the remainder of this analysis.

As expected from the FD analysis, Figure B.1 to B.3 show relatively small mutual differences in the motions of the considered configurations in terms of frequency and amplitude. Figure B.1 shows that for both the rigging configurations in analysis L1_0_33, the crane hook and the MUST additionally move in phase with the monopile. This does not hold for arrangement L2 in analysis L2_0_33, in which the crane hook and the MUST move in phase but with a higher frequency than the monopile. The results of analysis L4_0_33 in Figure B.3 show that the monopile and the MUST in configuration L4 move in phase, with a similar frequency and amplitude as in configuration H1. However, the crane hook moves with a higher frequency and smaller amplitude than the other two structures. The latter may be explained due to the relatively large distance between the crane hook and the MUST-platform in this configuration.

Figure B.4 to B.6 show minimal differences between the sway motions of the three suspended structures corresponding to the four rigging configurations. Furthermore, it is observed that the sinusoidal pattern that could be recognised in the results of analyses L1_0_33 to L4_0_33 (especially regarding the monopile) is replaced by a more irregular pattern.

Analysis L1_90_50 shows that configurations H1 and L1 provide behaviour that is comparable in terms of frequency, amplitude and phase for all three suspended structures, although the amplitude of the crane hook motions in configuration L1 is slightly larger. This does not hold for analysis L2_90_50, which results in larger sway amplitudes for the crane hook and MUST than for the former configurations. The comparison between configurations H1 and L4 in Figure B.9 results in the notion the amplitude of the crane hook sway motions is larger for L4, while other describing parameters are similar. For all four configurations considered in the analyses L1_90_50 to L4_90_50 holds that the crane hook and the monopile seem to move in anti-phase. It must be mentioned that this is in the first place not induced by multiple-pendulum effects, but by the HLV roll - load sway coupled mode present for the second sway-peak, as is explained in Section 4.4.4. Furthermore, for all nine analyses summarised in Table 4.4 holds that the monopile behaviour is comparable for each rigging configuration under the same environmental conditions (as was expected based on the FD-analyses in Figure 4.16 and 4.17).

Table 4.4: Overview of the TD-simulations performed to analyses various rigging length ratios

No.	Configurations	Motion	H_s [m]	ω_p [rad/s]	WEA [deg]	Figure
L1_0_33	H1 – L1	Surge	0.40		0	Figure B.1
L2_0_33	H1 – L2	Surge	0.40		0	Figure B.2
L4_0_33	H1 – L4	Surge	0.40		0	Figure B.3
L1_90_22	H1 – L1	Sway	0.25		90	Figure B.4
L2_90_22	H1 – L2	Sway	0.25		90	Figure B.5
L4_90_22	H1 – L4	Sway	0.25		90	Figure B.6
L1_90_50	H1 – L1	Sway	0.25		90	Figure B.7
L2_90_50	H1 – L2	Sway	0.25		90	Figure B.8
L4_90_50	H1 – L4	Sway	0.25		90	Figure B.9

4.4.4 Single pendulum approximation

The fact that the monopile's behaviour does not seem to be affected by the changing rigging length ratios may be explained by its large weight w.r.t. the crane hook and the MUST, and hence single pendulum theory may be applicable to the monopile. Without any dynamic coupling, this would mean that the relationship between the total cable length and the natural frequency of the suspended system can be described by Equation 4.9. To test this proposition, both FD and TD simulations are performed for varying total lengths of the suspended system, by varying the cable length between the crane hook and the crane tip of rigging configuration L3. The latter arrangement was selected as it is considered to have slightly favourable characteristics (see Section 4.4.2). The considered cable length is given the values of 36, 30, 25, 20, 15, 10 and 5 m. The resulting systems are named H1 to H7 respectively (hence, H1 corresponds to the exact same configuration as L3).

$$\omega_n = \sqrt{\frac{g}{L}} \tag{4.9}$$

The calculated RAOs for the monopile surge and sway motions are presented in Figure 4.19 and 4.20. As expected, the natural frequency increases with the reduction of the total length of the suspended system for both directions. Furthermore, it is noted that the natural frequencies provided by Figure 4.19 can be roughly estimated using Equation 4.9 for single pendulums. For H1, the distance between the crane tip and the monopile COG is 86 m, which corresponds to an eigenfrequency of [redacted] rad/s, and for H7 this distance is 55 m, corresponding to [redacted] rad/s, while the simulation results provide the values of [redacted] and [redacted] rad/s respectively (the value for H7 constitutes the largest difference between the simulated and the estimated value of all seven simulations performed).

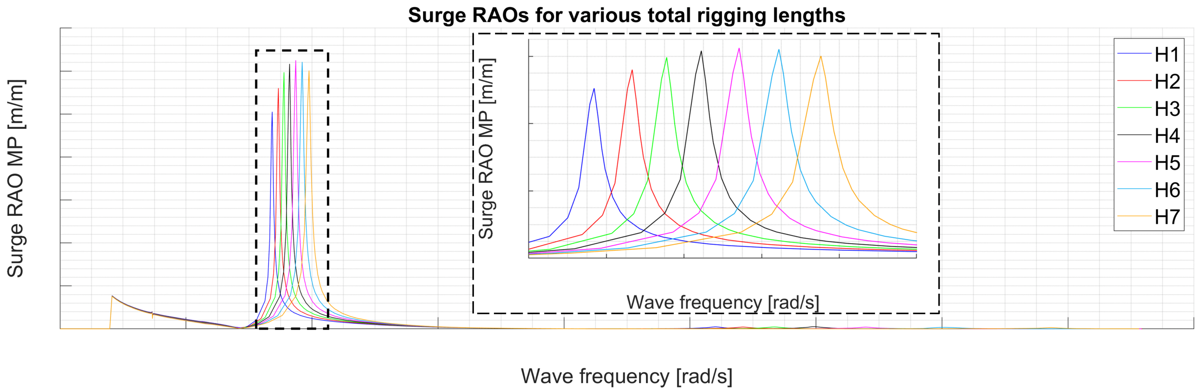

Figure 4.19: Monopile surge RAOs for various total lengths of the rigging arrangement (WEA = 0 deg)

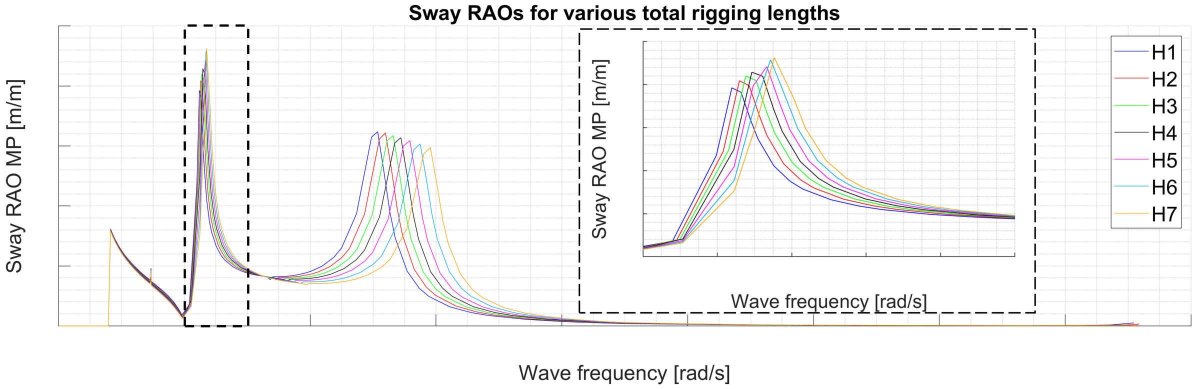

Figure 4.20: Monopile sway RAOs for various total lengths of the rigging arrangement (WEA = 90 deg)

Contrary to Figure 4.19, the results presented Figure 4.20 for the monopile sway motion cannot directly be explained by single pendulum theory, due to the fact that two peaks are present, which both deviate from the values provided by the single pendulum formula. As stipulated earlier in this section, the sway motion of the suspended system and the HLV roll motion are coupled degrees of freedom. Hence, the roll RAOs for systems H1 to H7 presented in Figure 4.21 are comparable to those presented in Figure 4.20, although the first extends the experiment of the second. Where the total rigging lengths continuously reduces from experiments H1 to H7, this length is brought back to zero in Figure 4.21 by modelling a point mass in the crane tip. Furthermore, the roll RAO for the HLV without a load in its crane is provided. It can be observed that modelling a point mass in the crane tip shifts the roll RAO towards the lower frequency region of the left peaks in Figure 4.20 and 4.21. This shift can be theoretically explained by the increase in the height of the combined COG (the VCG) w.r.t. the empty crane condition, which leads to a reduction of the GM-value. Since this value is linearly related to the vessel's roll stiffness, as described by Equation 4.10 (Journée et al., 2015), and there exists a positive relationship between the stiffness and the natural frequency (see Equation 4.11), a lower GM-value leads to a lower natural frequency. This observation, combined with the notion that the point mass curve lacks a second peak, leads to the judgment that the left peak in the sway and roll RAOs is induced by the natural roll frequency of the HLV. The fact that the point mass experiment lacks the right peak, and that the frequency corresponding to the right peak is more influenced by the total rigging length, points to the conclusion that the right peak is induced by the pendulum system. Similar results were obtained by Malenica, Orozco, and Chen (2005) and Vorhölter, Hatecke, and Feder (2015) for single pendulum systems suspended in the cranes of floating vessels. Furthermore, these studies conclude that the locations of peaks of the load's sway motion are very much dependent on the coupling with the HLV roll motion, which is an effect that is not accounted for in Equation 4.9.

$$C_{44} = \rho \cdot g \cdot \nabla \cdot GM \tag{4.10}$$

$$\omega_\phi = \sqrt{\frac{C_{44}}{I_{xx} + A_{44}}} \tag{4.11}$$

From similar reasoning can be explained that the load's surge spectrum constitutes a single peak of which the location can be predicted by the simple single pendulum formula. Namely, the coupling effects between the load's surge motion and the HLV's pitch motion are marginal due to the small HLV pitch responses, which are the result of a vessel's typically high pitch stiffness (C_{55}-value). Furthermore, such a high stiffness results in a high natural pitch frequency (a relationship similar to Equation 4.11), which may be higher than the physically possible wave frequency and hence will not be excited.

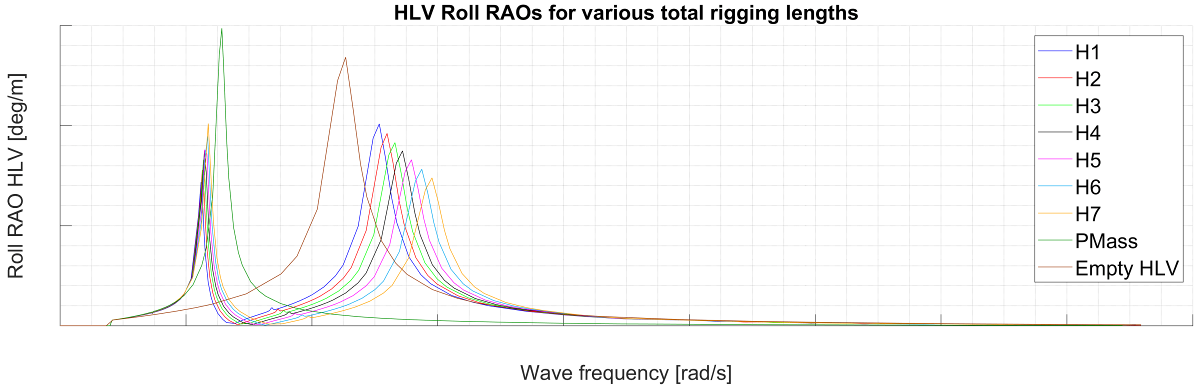

Figure 4.21: HLV roll RAOs for various total lengths of the rigging arrangement (WEA = 90 deg)

Since the type of results presented Figure 4.19 and 4.20 can to a large extent be explained by single pendulum theory, it is decided to perform additional FD and TD simulations, in which the suspended system is replaced by simply a cable suspending a point mass. The length of the cable is determined by taking the weighted average suspension height of the crane hook, the MUST frame and the monopile of rigging arrangement H1. Hence, the suspended system consists of an 80 m long cable and a point mass weighing 2920 mT (the combined suspended weight). Figure 4.22 displays the results of the FD simulation, from which can be deduced that the results of the single pendulum model approximate both the surge and the sway RAOs of the monopile in configuration H1 relatively well. The small difference can at least partly be explained by the fact in the original model the masses (i.e., the crane hook, MUST and monopile) can move relative to each other, whereas in the point mass approximation the total mass moves exactly in phase by definition.

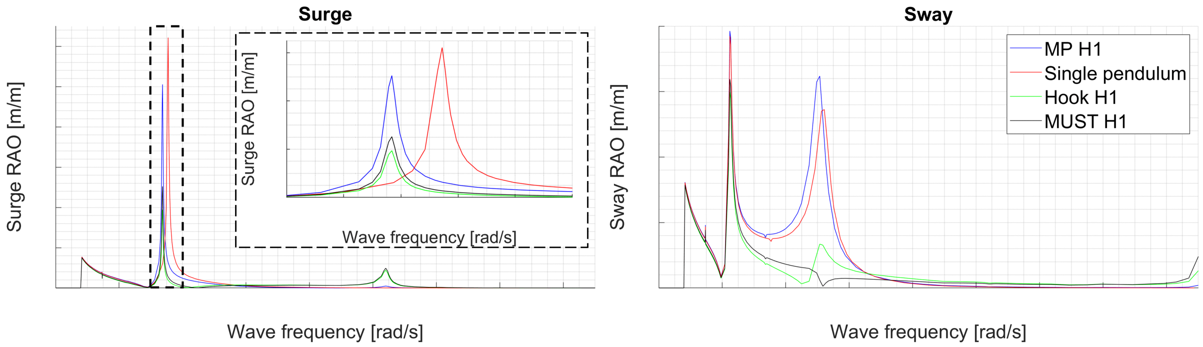

Figure 4.22: Surge (WEA = 0 deg) and sway (WEA = 90 deg) RAOs of the monopile and the single pendulum approximation compared. RAOs for the crane hook and the MUST are included as well

Figure B.10 provides a comparison between the surge motion TD simulation results of the H1 suspension configuration and the single pendulum approximation (for a peak wave frequency of [redacted] rad/s and a WEA of 0 deg). While the frequency of oscillation of the single pendulum curve appears to be only slightly larger, the amplitude is most of the time significantly larger than for the H1 configuration (which is in line with the expectations based on the RAOs in Figure 4.22). The sway motions of the point mass and the monopile plotted in Figure B.11 match very well, both in terms of frequency, amplitude and phase, despite the irregular pattern. Presumably, this good fit is due to the peak wave frequency of [redacted] rad/s this system is subjected to, which corresponds to the HLV's natural roll frequency (as derived earlier in this section). Hence, the behaviour is dominated by the vessel's roll responses, and to a less extent determined by the layout of the suspended system. In the same way, it can be explained why the results of TD experiments L1_90_22 to L4_90_22 in Section 4.4.3 differ so little. On the contrary,

Figure B.12 presents the results of the same experiment but for a peak wave frequency of [redacted] rad/s, which was appointed to be the location of the pendulum driven peak. Still, despite the significant differences in geometry, the fit at various periods in time is comparable.

Figure 4.23 and 4.24 present illustrations of the resonant modes corresponding to the two peaks in the sway spectrum. It can be observed that for the peak wave frequency of [redacted] rad/s, the sway motions of the crane tip (coupled to the vessel's roll motion) and the suspended structures are in phase, whereas for [redacted] rad/s the monopile and crane tip sway motions are in anti-phase. In the latter case, the effective point of rotation of the suspended system is situated between the crane hook and the MUST, causing those structures to move minimally. In both cases, however, the resonant modes of a single pendulum can be recognised. While the presented results are obtained by subjecting the system to irregular waves, also simulations with the system subjected to regular waves are performed, from which similar conclusions can be drawn.

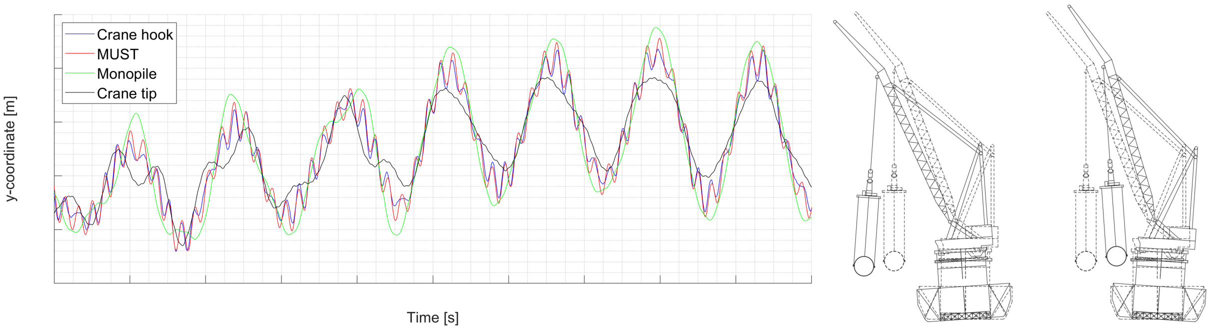

Figure 4.23: Identification of a resonant sway mode. $H_s = 0.25$ m, $\omega_p =$ [redacted] rad/s, WEA = 90 deg

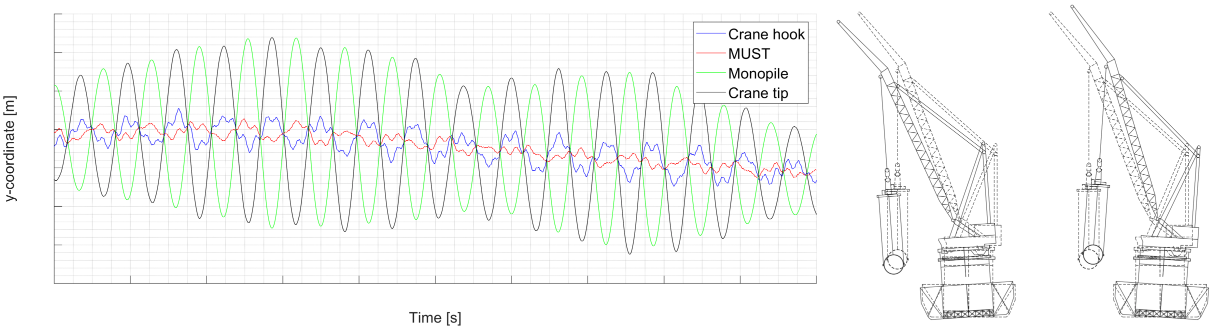

Figure 4.24: Identification of a sway resonant mode. $H_s = 0.25$ m, $\omega_p =$ [redacted] rad/s, WEA = 90 deg

Finally, in Figure B.13, a comparison is made between the H1 and the single pendulum configurations for an incident wave frequency of [redacted] rad/s and a WEA of 0 deg, which corresponds to the small surge peak for the crane hook and the MUST in Figure 4.22. The motion amplitudes of the crane hook and the MUST are significant, which influences the behaviour of the monopile. Although the effect on the monopile itself is small, such multiple pendulum (or in this case double pendulum, as the crane hook and the MUST move as one) effects can effectuate and should be accounted for.

Conclusively, it can be stated that in the series suspension on which the MUST system is based some forms of multiple pendulum behaviour can be detected. However, no chaotic behaviour (as described by Braun (2003)) or excessive motions seem to emerge as a result of these effects. In general, the monopile's behaviour can be estimated by single pendulum theory, presumably due to its large weight w.r.t. the crane hook and the MUST platform. The multiple pendulum behaviour effectuates in high-frequency motions of the crane hook and the MUST. It may be possible to dampen these motions using passive compensators, of which another application is discussed in Section 7.2.

4.5 Wind loads

In the simulations performed so far, insights were generated into the system behaviour while neglecting the effect of wind loads. Since in the previous section a monopile suspended in the vessel crane has been added to the model, it is now considered most relevant to determine the effect of wind loads on the system of analysis. According to DNVGL-RP-C205 (2019, Section 5.3.1), wind loads can be calculated using Equation 4.12, in which C is the shape coefficient, ρ_a is the density of air, S is the projected area normal to the wind direction, u is the wind speed and β is the angle between the wind direction and the axis of the exposed member. However, to calculate wind forces and moments in Aqwa, the programme needs to be supplied with drag coefficients $\mathrm{C_{d,F}}$ and $\mathrm{C_{d,M}}$ respectively (see Equation 4.13 and 4.14). By equating Equation 4.12 and 4.13, Equation 4.15 is derived, which allows for calculating coefficient $\mathrm{C_d}$, and therefore $\mathrm{C_{d,F}}$. $\mathrm{C_{d,M}}$ is subsequently calculated by multiplying $\mathrm{C_{d,F}}$ with the specific distance component between the centre of the wind catching area and the COG of the associated structure, $\mathrm{r_j}$.

$$F(\beta) = \frac{1}{2} \cdot C \cdot \rho_a \cdot S \cdot u^2 \cdot \sin\beta \tag{4.12}$$

$$F_j(\beta) = \underbrace{C_{d_j}(\beta)}_{C_{d,F}} \cdot u^2 \qquad \text{with j=1,3} \tag{4.13}$$

$$M_j(\beta) = \underbrace{C_{d_j}(\beta) \cdot r_j}_{C_{d,M}} \cdot u^2 \qquad \text{with j=3,6} \tag{4.14}$$

$$C_{d_j}(\beta) = \frac{1}{2} \cdot C \cdot \rho_a \cdot S \cdot \sin\beta_j \qquad \text{with j=1,6} \tag{4.15}$$

For this experiment, it has been decided to only consider the wind-catching effect of the HLV, the barge and the suspended monopile, and to neglect that of the crane hook and the MUST (due to their relatively small projected area). Furthermore, only the responses to environmental conditions directed perpendicular to the longitudinal axes of both floating bodies are evaluated, as this is considered to be the "worst case". Hence, the analysis is limited by the sway motion of the monopile, and the roll motion of the HLV and the barge. The resulting sway motions of the HLV and barge are not considered here, as it is assumed that the effect of the wind on these motions is compensated for by the mooring system. The shape coefficient of a cylindrical element, like a monopile, is dependent on the Reynolds number, which can be calculated using Equation 4.16. In this equation, D is the diameter of the element (since the diameter of the considered diameter varies over the length, the weighted average diameter $\mathrm{D_{W.A.}}$ is taken), u is the wind speed and ν_a is the kinematic viscosity of air. Since the calculated value of the Reynolds number is larger than 10^6 (see Figure 4.25), and the non-dimensional surface roughness is calculated to be smaller than 10^4 (assuming a corroded monopile), the shape coefficient of the monopile is taken as 0.65 (DNVGL-RP-C205, 2019, Section 6.7.1.5). The shape coefficients of the HLV and the barge are determined following the values for "three-dimensional structures on a horizontal surface", which depend on the ratios of the outer dimensions. This way, the coefficient for the HLV is determined as 1.2, and for the barge as 1.1 (DNVGL-RP-C205, 2019, Table 5-5). The projected wind catching areas and the corresponding centroids are determined using CAD-software and given in Figure 4.25. Finally, this figure presents the drag coefficients for the monopile sway and the HLV and barge roll motions, which are entered in the Aqwa model.

$$Re = \frac{D \cdot u}{\nu_a} \tag{4.16}$$

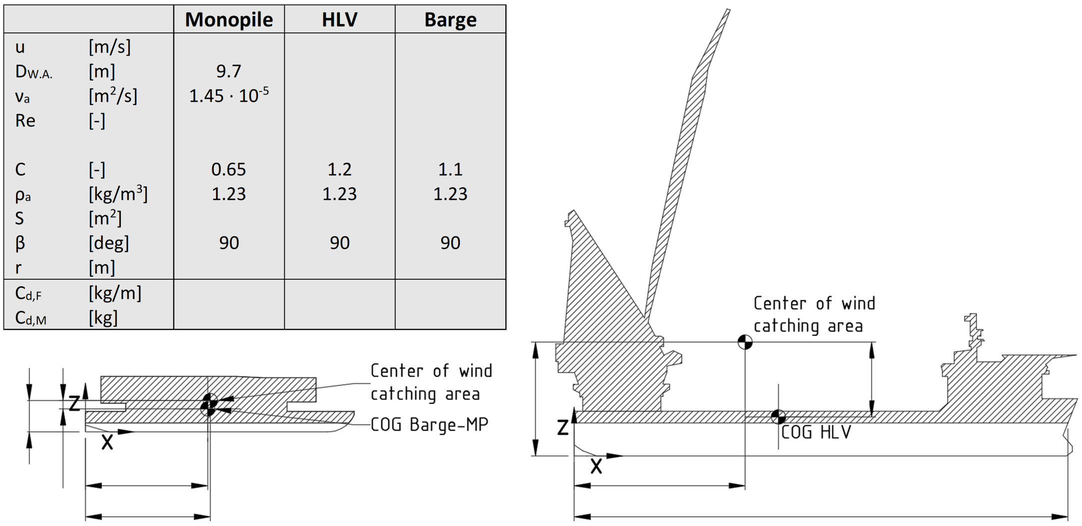

		Monopile	HLV	Barge
u	[m/s]			
$D_{W.A.}$	[m]	9.7		
ν_a	[m^2/s]	$1.45 \cdot 10^{-5}$		
Re	[-]			
C	[-]	0.65	1.2	1.1
ρ_a	[kg/m^3]	1.23	1.23	1.23
S	[m^2]			
β	[deg]	90	90	90
r	[m]			
$C_{d,F}$	[kg/m]			
$C_{d,M}$	[kg]			

Figure 4.25: Derivation of drag coefficients and the (centre of) wind catching area

In order to account for the wind speed increase over the height and variations over time, the wind spectrum by Ochi and Shin (1988) is applied (discussed more extensively in subsection A.2.3). This spectrum requires the mean wind speed at 10 meters above the mean water surface as an input value, for which a value of [redacted] m/s is taken (the same value that was used to calculate the Reynolds number of the air flow around the monopile, which corresponds to the operational limit of the HLV crane).

The calculated RAOs for the monopile sway motion are presented in Figure 4.26 for WEAs of 90 and 270 degrees, and compared to the corresponding RAOs without the inclusion of the effect of wind. It can be concluded that only a very limited difference can be observed around the [redacted] rad/s peak in both figures. The peak corresponding to the model that includes the effect of wind is in both cases slightly lower, which means that the wind has a "dampening" effect. The same is observed when analysing the roll motions of the HLV and the barge. Kanotra et al. (2012) drew similar conclusions, which confirms these findings. Therefore, in the remainder of this study, it is assumed that the results of the analyses performed are not influenced by wind loads. The same simplification was made in the six papers published by Li (2016) and in the studies by Sarkar and Gudmestad (2013) and Zhu et al. (2017).

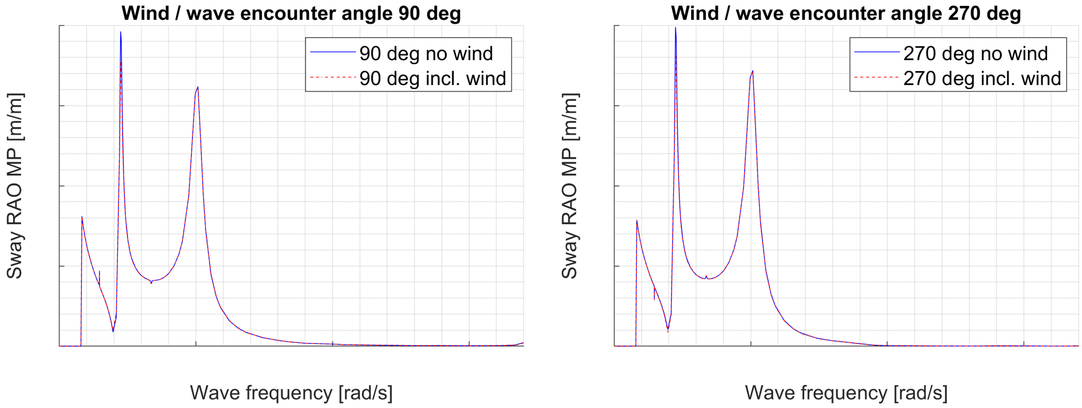

Figure 4.26: The monopile sway RAOs incorporating the effect of wind, compared to the case in which the effect of wind is excluded, for wave and wind encounter angles of 90 and 270 degrees

4.6 Tugger line design

Section 4.4 intends to provide insights into the properties of the system of analysis. However, while doing this, it deviates from reality by one important aspect: no tugger lines to control the motions of the lifted load are considered yet. Hence, in this section, the changes in the system properties due to such tugger lines are discussed. The considered tugger lines originate from winches that are positioned above the crane's slew bearing, and hence rotate with the crane. Two cables originating from different winches are connected to the monopile (one to the front, and one to the back), via sheaves on the crane's A-frame (see Figure 4.27).

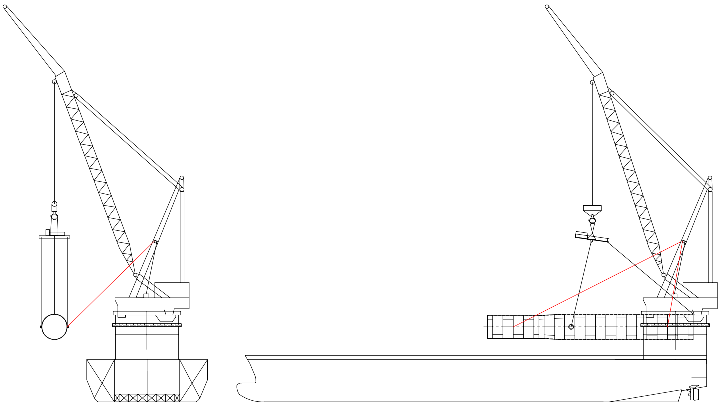

Figure 4.27: Schematic image of the implementation of tugger lines in the use of the MUST system

Figure 4.28 and 4.29 display time domain simulation results for the surge and sway responses of the monopile, for various tugger line designs. In the first simulation, no tugger lines are used, and hence this simulation corresponds to rigging configuration H1 (see Section 4.4.4). In the simulation referred to as "Line", the tugger arrangement consists of two cables of constant length, attached to the monopile, with a pre-tension of 15 mT. The curves indicated by "constant" refer to a constant pre-set tension in the tugger lines, regulated by the winches (the available cable length is varied to keep this tension constant, the winches on the considered HLV are equipped with such a system). The "Line"-curve deviates in its shape, especially in Figure 4.29. This is due to the fact that the considered cable has a constant length, and frequently becomes slack. A cable becoming slack and then taut again introduces snap loads, and hence such an arrangement is not preferable. Regarding the resulting monopile sway motions of Figure 4.29, it can be concluded that the differences are minimal between the various constant tension lines and the situation without any tugger lines. Therefore, based on the monopile surge responses presented in Figure 4.28, the notion that tugger lines are required to control the monopile's yaw motions and to provide operators with a feeling of control, it is decided to perform further analyses including 10 mT constant tension tugger lines.

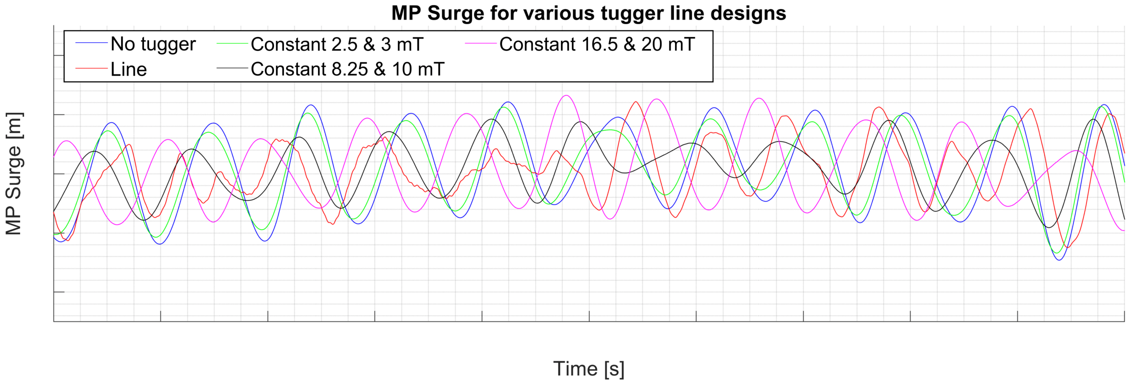

Figure 4.28: Time domain simulation results of the monopile's surge response for various tugger line arrangements. $H_s = 0.40$ m, $\omega_p =$ [redacted] rad/s, WEA = 0 deg

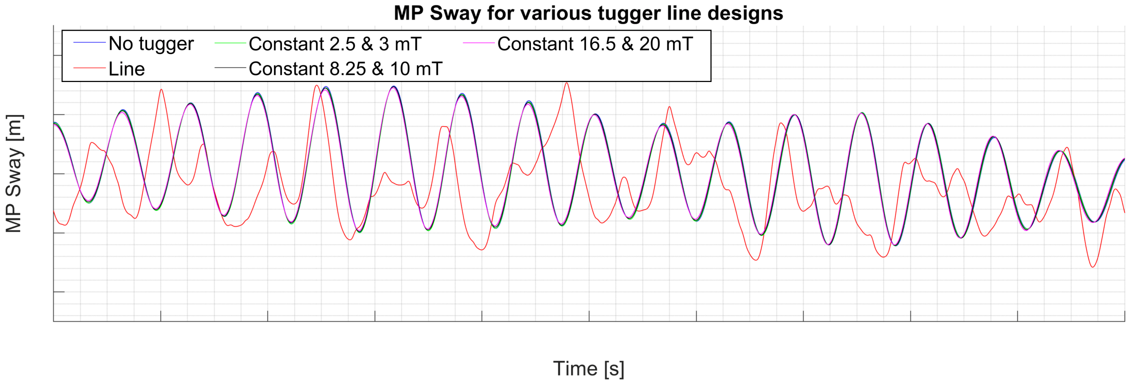

Figure 4.29: Time domain simulation results of the monopile's sway response for various tugger line arrangements. $H_s = 0.25$ m, $\omega_p =$ [redacted] rad/s, WEA = 90 deg

4.7 Conclusions regarding model development

The following conclusions can be drawn from Chapter 4. Model development.

- The considered floating system consists of five rigid bodies: the HLV, the barge, the crane hook, the MUST and the monopiles. The monopiles have a weight of 2500 mT, a length of 80 m and a maximum diameter of 10 m. Moreover, four barge loadcases are considered:
  (1.1) pre-ballasted for sailing condition (with two monopiles on deck)
  (1.2) pre-heeled condition resulting from flooding a tank (with two monopiles on deck)
  (2) condition 1.2 but with the first monopile lifted off
  (3) condition 2 but with additionally the second monopile lifted off
  The pre-heel condition of loadcase 1.2 is designed as such that it compensates for the lift-off of both monopiles, while not having to actively ballast offshore.
- From a literature review is determined that Ikeda's method is the de facto industry standard to determine viscous roll damping coefficients. This method states that the viscous roll damping is dependent on the floating body's responses. However, Aqwa only allows for supplementing a constant frequency-independent coefficient. Hence, the simplification is made to only provide the barge roll damping value for which the structure reaches its limiting roll angle (for each of its loadcases). For the HLV, a measured value is used.
- Experimental simulations show that it is of significant importance to incorporate viscous roll damping, especially for wave frequencies close to the natural roll frequency. Nonlinear roll damping effects are considered negligible for roll angles below the set limits.
- The responses of the HLV are to a limited extent affected by the presence of the barge. The responses of the barge, however, are significantly affected by hydrodynamic interaction effects. Shielding effects can reduce the responses, but for certain angles the responses can also be higher w.r.t. the case when hydrodynamic interaction effects are not included.
- Changes in the relative cable lengths between the suspended structures, while keeping the total length constant, only affect the monopile responses to a very limited extent. However, the in-line responses of the crane hook and the MUST are affected.
- The surge and sway responses of the monopile can be approximated by a single pendulum system, presumably due to its large weight w.r.t. the other suspended structures.
- The wind loads resulting from a wind speed equal to the limiting wind speed of the HLV crane slightly damp the monopile surge and sway responses and hence can be neglected.
- Tugger lines of constant length can result in snap loads. Tugger lines of constant tension are preferred. The magnitude of this tension is of limited influence on the monopile responses.

5 | Governing parameters

This chapter is focused on listing the limiting and identifying the governing parameters of the monopile lift-off operation when using the MUST. Hence, an answer to sub-question 3, posed in Section 1.4, is sought. Guachamin Acero, Li, et al. (2016) propose to do this by subjecting the system to “typical” environmental conditions. In consultation with industry experts, it is decided to interpret “typical environmental conditions”, as “the environmental conditions at a typical location of installation of monopiles”. In Section 5.1, the selected site is presented. Next, in Section 5.2, the limiting response values are provided. Finally, in Section 5.3, the governing parameters are identified based on the responses to the typical environmental conditions.

5.1 Typical installation location

Figure 5.1 displays a satellite image of the considered location, which is approximately fourteen kilometers off the coast of The Hague, The Netherlands (52°11’35”N, 4°8’15”E). This location has a water depth of 26 m, for which an eighty-meter long monopile (see Section 4.1.1) is suitable. Historically measured wave conditions for this location are used as input to identify the parameters that cross their limit first, under realistic circumstances.

Figure 5.1: Satellite image of the considered typical location of installation for monopiles (Google, n.d.)

5.2 Limiting operational values

In this study, the Seaway 7 standards are followed for the maximum values of the limiting parameters. Regarding the Heavy Lift Vessel (HLV) roll and pitch, the x, y and z-displacement of the crane tip, and the roll and pitch of the barge, fixed values are used. These values are determined based on experience and recommendations from the offshore crew and are displayed in Figure 5.2. Furthermore, the Safe Working Load (SWL) of the crane is considered, which is not allowed to be exceeded considering both static and dynamic loads.

The standard lift-off analysis condition within Seaway 7 comprises a situation in which the load is lifted three meters above its original support points. Apart from the fact that the suitability of this value is supported by years of experience, there is also a theoretical reasoning behind it. Generally, a lift-off is performed just after a maximum relative response between the vessel and the barge, such that the responses of both floating bodies contribute to quickly increasing the vertical distance between the load and the barge. The hoisting cable should subsequently be retracted sufficiently to prevent a collision of the load with the barge at the next maximum response. According to Holthuijsen (2007), “the mean distance between two consecutive groups of high waves, i.e., the length of a group of high waves plus the length of a group of low waves, is approximately seven”. This confirms an offshore crew rule of thumb, which states that two consecutive waves of maximum height are separated by six smaller waves. The same holds for the vessel responses, i.e., every seventh response is the largest (A. Mitterfellner, personal communication, 10 December 2021). Hence, the vertical clearance between the barge and the monopile at the first maximum response after lift-off is provided by the hoisting speed multiplied by seven wave periods (assuming that the subsequent maximum responses are equal in magnitude). In practice, the resulting distance is approximately three meters.

Parameter	**Limit**	
Significant wave height		[m]
HLV roll		[deg]
HLV pitch		[deg]
Crane tip x displacement		[m]
Crane tip y displacement		[m]
Crane tip z displacement		[m]
SWL crane	5000	[mT]
Barge roll		[deg]
Barge pitch		[deg]
Relative y-amplitude grillage-MP (8 points)		[m]
Relative z-amplitude grillage-MP (4 points)		[m]
MP x displacement		[m]

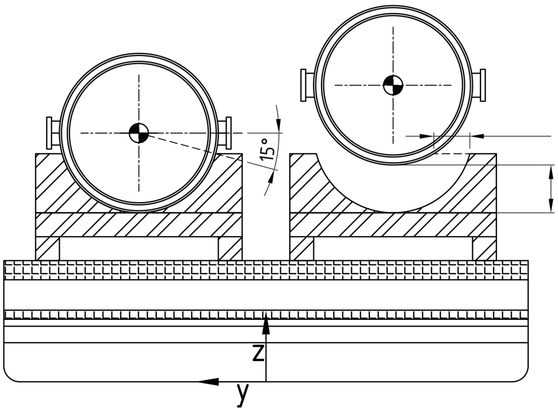

Figure 5.2: (Case-specific) limiting operational values. The presented limits are significant double amplitudes

The limiting values of Figure 5.2 are based on this condition. In order to check for the conditions in which the monopile impacts the grillage on the barge, relative motion limitations are considered. Based on a vertical distance between both structures of three meters, and on the conservative assumption that their vertical motions are in anti-phase, the Most Probable Maximum Single Amplitude (MPMSA) in z-direction is 1.5 m. Journée et al. (2015) approximate the relationship between the Significant Single Amplitude (SSA) and the MPMSA by a factor of 1.86 (based on three-hour sea states). By taking the ratio between the Significant Double Amplitude (SDA) and the SSA as two, the relationship between the MPMSA and the SDA can be written as in Equation 5.1. Hence, limiting the relative z motion between the monopile and the grillage by 1.5 m SDA can be considered conservative.

$$SSA(\omega) = \frac{SDA(\omega)}{2} \approx \frac{MPMSA(\omega)}{1.86} \xrightarrow{Rewrite} MPMSA(\omega) \approx \frac{1.86}{2} \cdot SDA(\omega) \tag{5.1}$$

Regarding the relative motion limitations in y-direction, the simplified saddle design of Figure 4.2 has been changed to a more realistic design, as visualised in Figure 5.2. The height of the saddles is lowered to a 150-degree “support angle”, which prevents overly-conservative results (as higher saddles would result in a lower limiting relative y-distance). With the monopile lifted to a three-meter height, the horizontal distance between the monopile and the saddle is approximately 2.2 m (see Figure 5.2). From the same reasoning as for the vertical distance, it can be stated that a limiting relative y-SDA of 1.1 m is conservative.

Figure 5.3 provides the numbering of the points at which the relative motions are examined in the further analyses. The middle two saddles are not considered in the post-processing, as for small monopile motions the collision limitations for these saddles are implicit in the limitations of the outer saddles. For both saddles, three relative distance measure points are implemented: two for the y-distance, and one for the z-distance. The lifted monopile has been left out of this figure for clarity purposes.

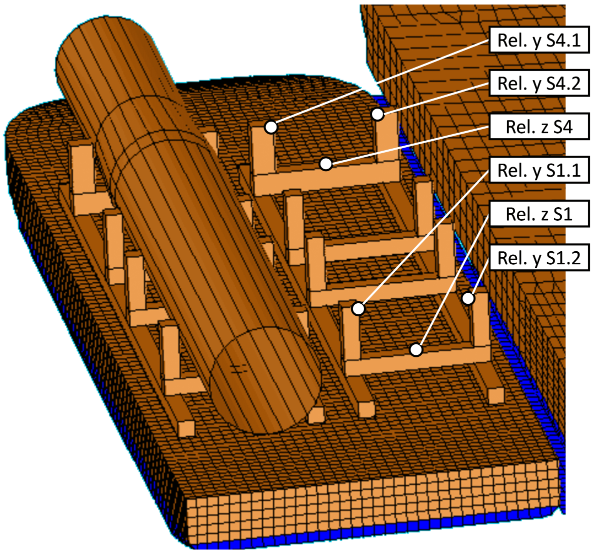

Figure 5.3: Indication of the relative distance measure points between the saddles and the monopile

5.3 Limiting parameter frequency domain responses

The historical data of the wave conditions at the considered location are supplied in the form of three-hour 2D-spectra, which provide the spectral value depending on the wave heading (θ) and frequency (ω) (similar to Figure A.4). By multiplying these wave spectra with the Response Amplitude Operator (RAO) squared, the response spectra can be determined, as discussed Section A.3.1 and mathematically expressed in Equation 5.2. RAOs are dependent on the Wave Encounter Angle (WEA), and hence, in addition to the wave frequency, the magnitude of the RAO is dependent on the vessel heading (α) relative to the wave heading (note the difference between WEA and heading: WEA is the angle of the vessel relative to the incident waves, whereas heading is the angle w.r.t. the global coordinate system).

$$S_{Response}(\omega,\alpha,\theta,t) = \left|RAO(\omega,\alpha,\theta)\right|^2 \cdot S_{Wave}(\omega,\theta,t) \tag{5.2}$$

By calculating the area under the spectral curve for a certain combination of wave and vessel heading at a certain moment in time, the corresponding zeroth moment of a particular response ($m_{0,Response}$) is determined (see Equation 5.3a). This area can be approximated by applying the trapezoidal rule (Vuik, Vermolen, Gijzen, & Vuik, 2015), which is expressed in Equation 5.3b. Subsequently, the calculated zeroth moment can be used to determine the SDA of the considered response for a certain vessel heading and the environmental conditions at a particular moment in time, by applying Equation 5.4.

$$m_{0,Response}(\alpha,\theta,t) = \int_0^\infty S_{Response}(\omega,\alpha,\theta,t)\cdot d\omega \tag{5.3a}$$

$$\approx \frac{\omega_N-\omega_0}{2N}\cdot[S_{Response}(\omega_0,\alpha,\theta,t) + 2\cdot S_{Response}(\omega_1,\alpha,\theta,t) + ... \tag{5.3b}$$

$$+ 2\cdot S_{Response}(\omega_{N-1},\alpha,\theta,t) + S_{Response}(\omega_N,\alpha,\theta,t)]$$

$$SDA_{Response}(\alpha,\theta,t) = 4\cdot\sqrt{m_{0,Response}(\alpha,\theta,t)} \tag{5.4}$$

The described procedure is followed for the parameters presented in Figure 5.2, resulting in the figures of Appendix C. To generate these figures, weather data for the year 2010 was used, as by iteration it was determined that this year provides approximately average results (w.r.t. the available weather data from 2000 to 2011). The blue mesh curve plots the SDA of the considered parameter as a function of the vessel's heading (α) and the time (the wave heading θ is included in the three-hourly varying input wave spectrum). The red plane indicates the set limit, corresponding to the values presented in Figure 5.2. Hence, time-vessel heading combinations for which the response SDA is above this plane are not workable. From Figure C.1 can be concluded that the HLV roll, the crane tip sway and the barge roll motions limit the operation for relatively many time-heading combinations. Nevertheless, for these parameters also holds that they seem to have a common optimum: for the vessel headings around 170 degrees the limit is exceeded less often than for other heading ranges. Furthermore, for no time-heading combinations the Main Hoist (MH) dynamic tension limit is exceeded (see Figure C.1f), which justifies the decision to leave this parameter out of the critical event analysis of Section 3.3. Analysing the simulation results of Figure C.2 results in similar conclusions. The response plots of the relative motion limits (Figure C.1a to C.2e) show a relatively frequent exceedance of the limit planes, but once more, crossing the limit can frequently be avoided for a vessel heading in the range of 170 degrees. Furthermore, the monopile surge motion most of the time stays well below its liming SDA except for one moment in time, halfway in December.

Despite the fact that considering all headings provides insights into the system behaviour, only the most beneficial angles are brought into practice and hence are most of interest. Following the observations in Figure C.1 and C.2, and based on the workability analysis presented in Chapter 6 (the analysis process in this study is iterative), it has been determined that averaged over the years 2000-2011 the vessel heading of 165 is the most favourable. Hence, Figure C.3 and C.4 provide the 2010 time series of the considered limiting response SDAs only for this heading. Based on a visual inspection of these figures, the conclusion can be drawn that the parameters exceeding their limit most frequently and significantly (governing parameters) are the relative z-motions at the fore and aft saddles and the barge roll motion (which are coupled). Figure C.3 and C.4 are summarised by Figure 5.4, in which the SDAs are normalised and presented as a percentage of their limiting value.

5.4 Conclusions regarding the limiting parameters

The following conclusions can be drawn from Chapter 5. Governing parameters.

- To determine the governing parameters, three-hour 2D-spectral weather data of a typical wind farm installation location on the North Sea are supplied to the developed model.
- From a frequency domain analysis is determined that the governing parameters are the relative z-motions between the monopile and the fore and aft saddles on the barge, and the roll motion of the barge.

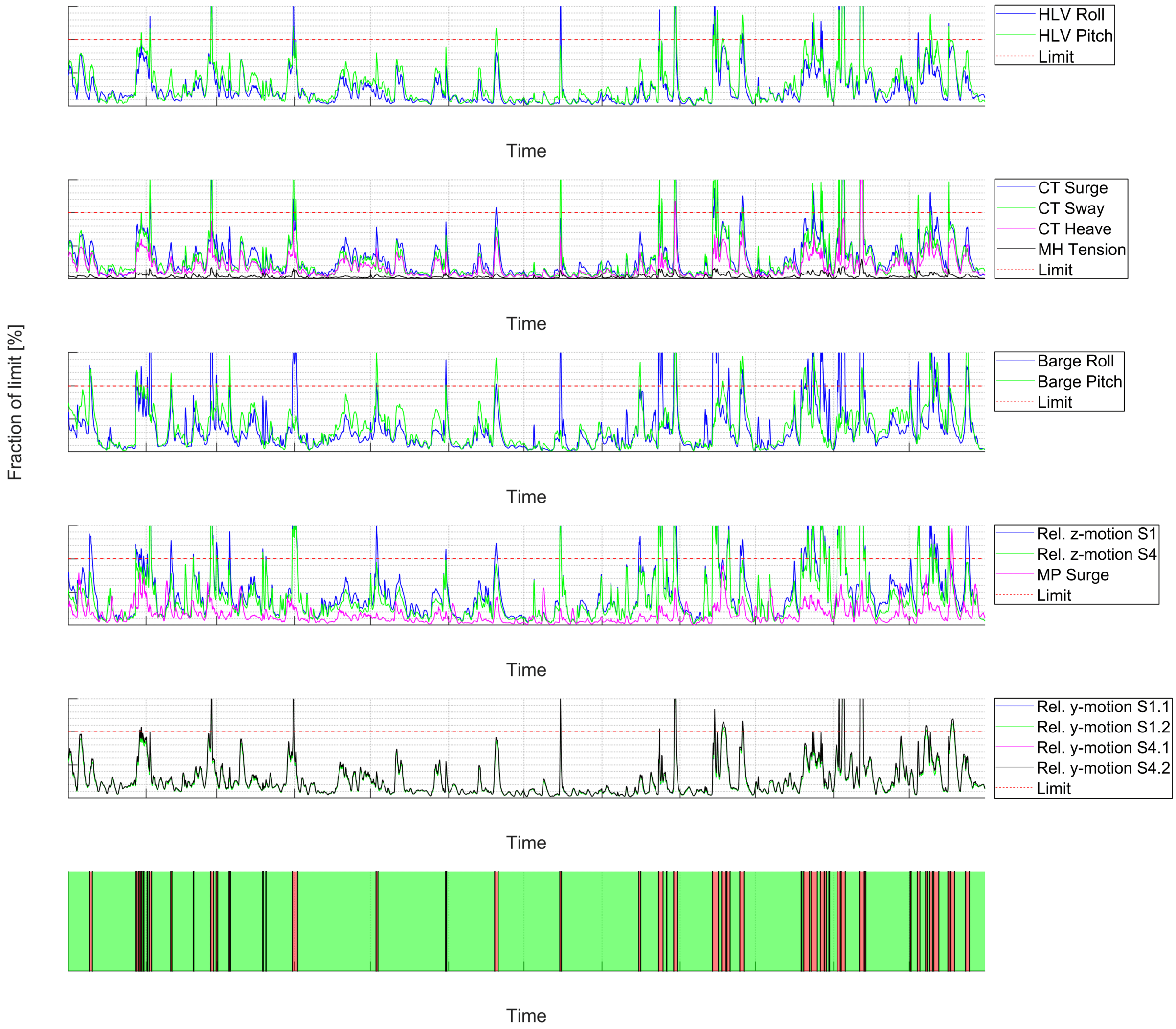

Figure 5.4: Time series of the SDA of the considered paramaters, normalised to the corresponding set limit. The bottom figure gives the time windows in which the lift-off operation can be performed

6 | Workability of the base case

In the previous chapter, the parameters on which the focus should be laid to increase the workability were identified. In this chapter, the subsequent phase in the framework of Guachamin Acero, Li, et al. (2016) is entered. Steps 7 to 9, which are summarised in sub-question 4 of Section 1.4, require to determine the workability of the "base case" of the system of analysis. While in Chapter 5 it was considered sufficient to only analyse loadcase 2 to determine the governing parameters, in this chapter a distinction is made between loadcases 2 and 3. Loadcase 2 encompasses the lift-off of the first monopile, and loadcase 3 the lift-off of the second. Making this distinction is considered important as the difference in mass of both floating barge systems is almost 30% (see Figure 4.5) and a similar conclusion can be drawn for the inertial properties (see Table 4.1). This may significantly influence the resulting behaviour. Hence, Section 6.1 discusses the workability of loadcase 2 and Section 6.2 for loadcase 3. It must be noted that for determining the workability, all of the limiting parameters are considered, not just the governing ones. Additionally, the focus is laid on the introduction of a slack winch cable, which may result into snap loads. In Section 6.3, the minimum x-distance between the trunnions and the monopile Centre Of Gravity (COG) before snap loads may occur is determined.

6.1 Loadcase 2

The bottom plot of Figure 5.4 is the result of analysing the responses of all considered parameters, and indicates for which moments in time the operation of analysis can be performed. However, this figure only does this for a single year of weather data and a single heading of the vessel. A more extensive description of the system performance would be provided if all headings would be considered and if the stochastic effect of weather conditions on the performance would be levelled out. Therefore, Figure 6.1 provides the workability percentages (the workable time as a fraction of the total time) per month and for 24 headings, averaged over 12 years of weather data. From this figure can be deduced that the optimal vessel heading is 165 degrees (in the global coordinate system), which could be expected based on the figures in Appendix C.

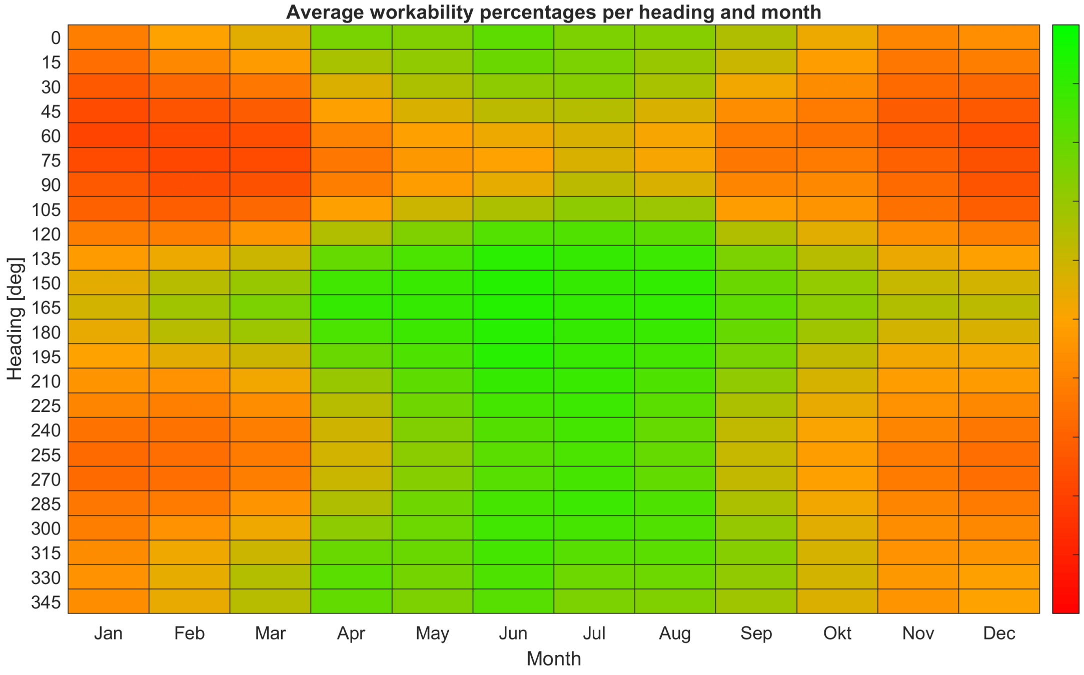

Figure 6.1: Workability percentages per heading and month, averaged over twelve years of weather data, for loadcase 2

Although Figure 6.1 provides a clear overview of the potential performance of the system of analysis, it provides limited insights into how this performance is achieved and how it is dependent on the conditions at a specific location. Hence, performance indicators providing these insights are sought. Guachamin Acero, Li, et al. (2016) propose to establish the H_s-T_p curves for each limiting parameter, which provide the combinations of H_s and T_p for which the corresponding parameter reaches its set limit. These curves are determined following the process described in Figure 6.2.

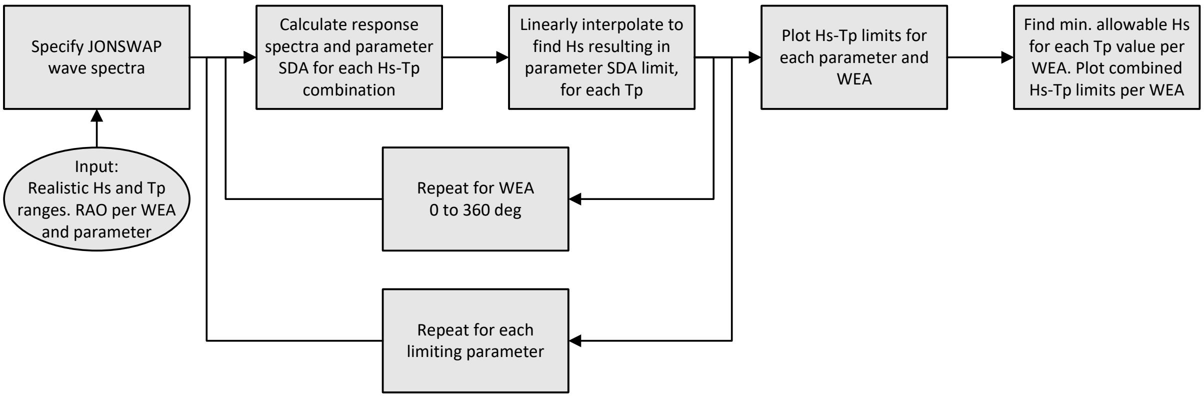

Figure 6.2: Principle of deriving H_s-T_p curves including the contribution of various limiting parameters

First of all, the realistic ranges of values for H_s and T_p are determined, and all possible combinations are made. By using these values as input for the description of JONSWAP wave spectra, for each H_s-T_p combination a spectrum is determined (following the input parameters proposed by DNVGL-RP-C205 (2019, Section 3.5.5), and with a value for the power of wave spreading of 4, as substantiated in Section 4.2). From the wave spectra and the pre-determined Response Amplitude Operators (RAOs), the response spectra and Significant Double Amplitudes (SDAs) for each parameter and for each H_s-T_p combination are calculated. Subsequently, by linear interpolation the value for H_s which results in a response equal to the corresponding limit is approximated for each T_p value. This process is repeated for all limiting parameters and 24 Wave Encounter Angles (WEAs).

Following this procedure, the curves in Appendix D are created. The H_s-T_p combinations below the curves indicate workable situations, and hence the lowest curves are limiting for the operation. The combined workable combinations are hatched in green. The overall limiting curves per WEA (which are described by the edge of the green planes adjoining the H_s-T_p curves) are presented in Figure D.5. These limiting curves are summarised in the polar plot of Figure 6.3. Clearly visible is the shielding effect of the Heavy Lift Vessel (HLV), as the allowed H_s for WEAs from a 90-degree angle are significantly larger than from a 270-degree angle (for waves with the same T_p). Similarly, the effect of the more "efficient" shape of the bow compared to the shape of the stern of both the HLV and the barge is visible. Waves coming from a 180-degree angle are allowed to arrive with a higher H_s than waves coming from a 0-degree angle. For an indication of the orientation of the WEA w.r.t. the HLV, see Figure 4.9.

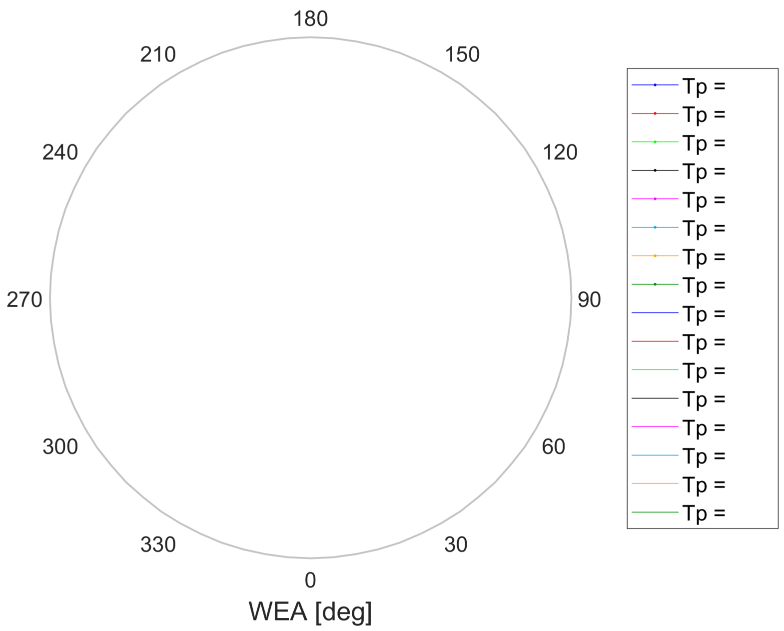

Figure 6.3: Polar plot summarising the critical H_s-T_p curves of loadcase 2, for each considered WEA

6.2 Loadcase 3

Figure 6.4 shows the workability percentages for loadcase 3, for each month and 24 vessel headings, averaged over 12 years of weather data. Where for Figure 6.1 the optimal heading was clearly close to 165 degrees, in this case the optimum lies between 165 and 180 degrees. When comparing both figures, the conclusion is drawn that, on average, the workability percentages for loadcase 2 are less than one percent point higher than for loadcase 3, and are therefore very much comparable. However, when focusing on the best performing vessel headings (e.g., 150-180 degrees), the conclusion must be drawn that the percentages for loadcase 3 are higher than for loadcase 2. Since the latter comparison is closer to reality (as in practice the vessel will generally not be positioned in a very unfavourable heading), it is concluded that loadcase 3 is slightly more workable. This difference can be explained by comparing the H_s-T_p curves in Figure D.2 and D.7. For WEAs between 120 and 165 degrees, the critical curve is lower in the first case compared to the second, predominantly due to a difference in the limits induced by the relative z-motions.

Similar to what was done for loadcase 2, the H_s-T_p curves for each limiting parameter and for each considered WEA are presented in Figure D.6 to D.9, and the critical combination curve for each WEA in Figure D.10. These results are, once more, summarised in a polar plot, which is presented in Figure 6.5. Comparing this plot to the polar plot of loadcase 2 (see Figure 6.3), results in the conclusion that loadcase 3 is slightly more sensitive to waves coming from a WEA of 270 degrees. When comparing Figure D.4 to D.9, this difference can be attributed to the barge roll motion reaching its limit. The corresponding curve for the WEA of 270 is in this latter figure slightly lower than in the first. A contributor to this difference could be the fact that the mass and inertia of the barge is significantly lower in loadcase 3 compared to loadcase 2, shifting the natural roll frequency of the barge and making it less inert.

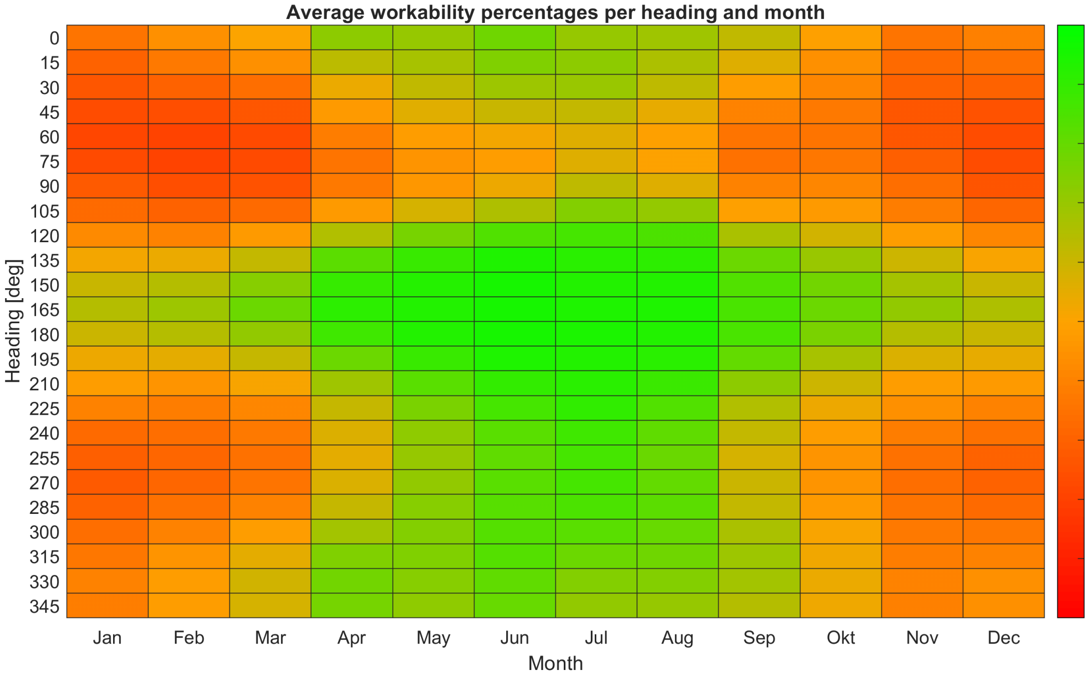

Figure 6.4: Workability percentages per heading and month, averaged over twelve years of weather data, for loadcase 3

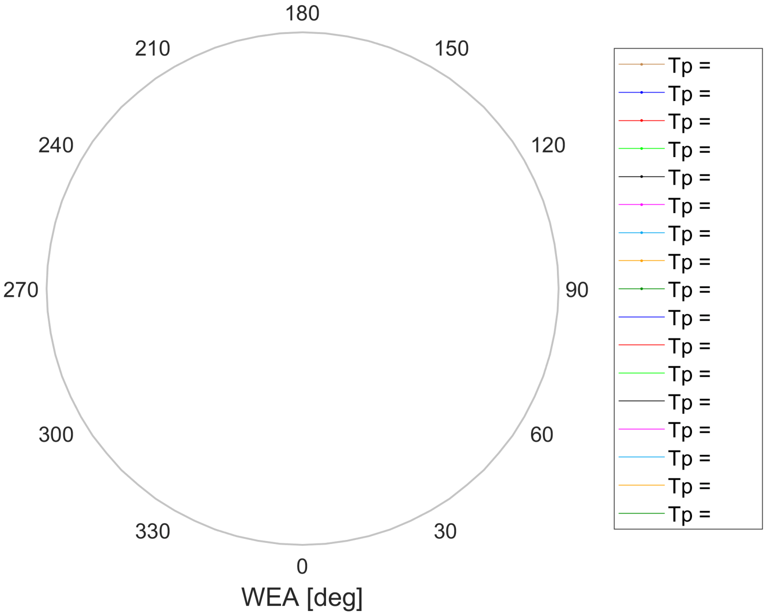

Figure 6.5: Polar plot summarising the critical H_s-T_p curves of loadcase 3, for each considered WEA

6.3 Snap loads winch cable

As discussed in the critical event analysis of Section 3.3, introducing snap loads in the winch cable of the MUST is a risk, especially if the distance between the monopile COG and the trunnions is reduced to minimise the required winch cable capacity. In order to investigate the relationship between this distance and the introduction of snap loads, Time Domain (TD)-simulations are performed. These simulations require the input of a certain sea state, and hence a selection of H_s, T_p and WEA has to be made. Therefore, it was decided to consider the situation of an optimal WEA for the HLV with a monopile suspended in its crane, but with the barge already sailed away. This takes away all the barge-related limitations (barge roll and pitch, and the relative motions), which in combination with the optimal WEA results in a maximum considered sea state. The remaining H_s-T_p curve for the optimal WEA of 180 degrees is displayed in Figure 6.6. The input sea states for the TD simulations are taken from this curve, as indicated by the red crosses. Hence, the minimum distance between the monopile COG and the trunnions for which snap loads can occur is to be iteratively sought for 17 different sea states. Doing this in Aqwa requires many time-consuming TD-simulations. Therefore, a numerical model is constructed in Matlab, solely focusing on the pendulum system (the structures suspended in the vessel crane).

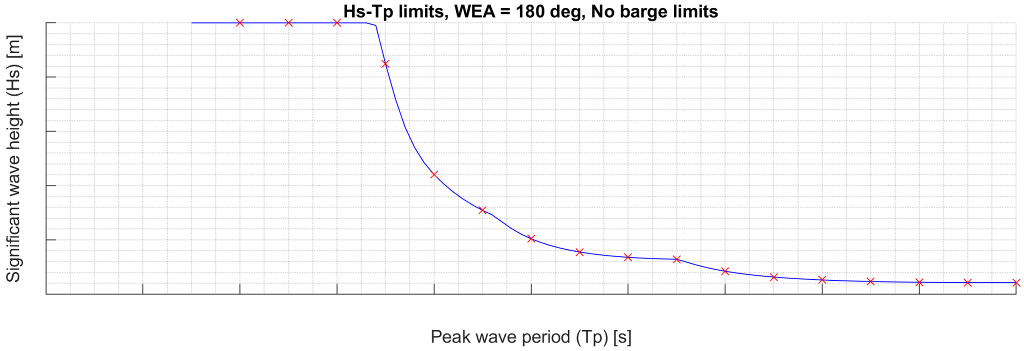

Figure 6.6: H_s-T_p curve for a WEA of 180 deg, but with the barge-related limits taken out

6.3.1 Matlab model development

Figure 6.7 shows the considered simplified pendulum system, and compares it to the system modelled in Aqwa. Three point masses are considered: the crane hook (m_1), the top of the MUST (m_2) and the bottom of the MUST (m_3). Two point masses are assumed for the latter structure, in order to be able to include its ability to rotate around its x- and y-axes. Its weight is assumed to be distributed as a quarter to the top and three quarters to the bottom. The monopile is modelled as a rigid body, of which the mass is described by m_4. In Section E.1 of Appendix E, the positions, velocities and accelerations of the four masses are described relative to the crane tip (CT) motions and as a function of the rotational motions around the x- and y-axes (θ and φ). Next, in Section E.2, the force balances in x-, y-, and z-direction for the four masses are presented. Additionally, the considered moment balance of the monopile around the y-axis is evaluated. It is assumed that the tension in the grommets from the MUST to the trunnions on the monopile is of the same magnitude. Therefore, the moment balance of the monopile around the x-axis is not evaluated, and the system is represented as depicted in the y-z plane of Figure 6.7. Next, the kinematic equations of Section E.1 are substituted into the kinetic equations of Section E.2. Aligning the resulting equations of motion allows for rewriting them to a single matrix equation in terms of $\mathbf{A}$, $\vec{B}$ and $\vec{C}$, as presented in Equation 6.1. The derived contents of the matrix and vectors are provided in Section E.3.

$$\mathbf{A}\vec{B} = \vec{C} \quad \xrightarrow{Rewrite} \quad \vec{B} = \mathbf{A}^{-1}\vec{C} \tag{6.1}$$

As can be deduced from the derived equations, the system considered in the Matlab model is limited to the location of the crane tip. This means that the motions of this node (positions, velocities and accelerations) are imported from simulations in Aqwa, resulting from the input sea states indicated in Figure 6.6. The calculation principle of the developed model is visualised in Figure 6.8. The cable lengths, (point)masses, mass moment of inertia, the x-distance between the monopile COG and the trunnions, the location of the monopile COG and the monopile diameter function as input data for the model. From these values, also the constant angles of θ_W and θ_T

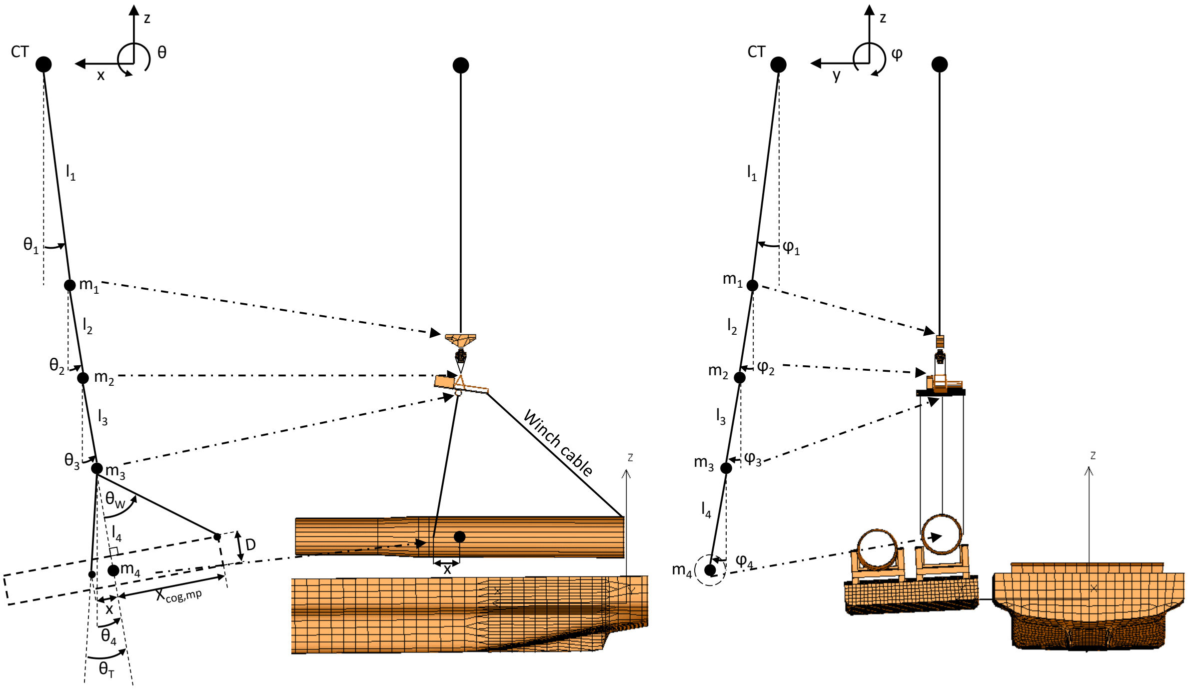

Figure 6.7: The simplified pendulum system compared to the Aqwa implementation

can be determined. Furthermore, the angular accelerations, velocities and rotations of θ_i and φ_i at t=0 have to be provided. By supplying these values to Equation 6.1, the parameters in $\vec{B}$ can be calculated. The five considered tensions at the particular time step are saved for later analysis. The eight angular accelerations (θ_i and φ_i for $i = 1,2,3,4$) are numerically integrated to determine the corresponding angles and angular velocities. To perform this integration, Matlab's ODE45-function is applied. ODE45 is a solver for ordinary differential equations, which is based on the Runge-Kutta integration method with a variable time step to increase computational efficiency (Senan, 2012). Subsequently, the determined angles and angular velocities are fed back as input into **A** and $\vec{C}$ to calculate $\vec{B}$ for the next step and the cycle is repeated. In order to express the motions of the considered masses in terms of Cartesian coordinates, the found angular values per time step are substituted in the equations of Section E.1.

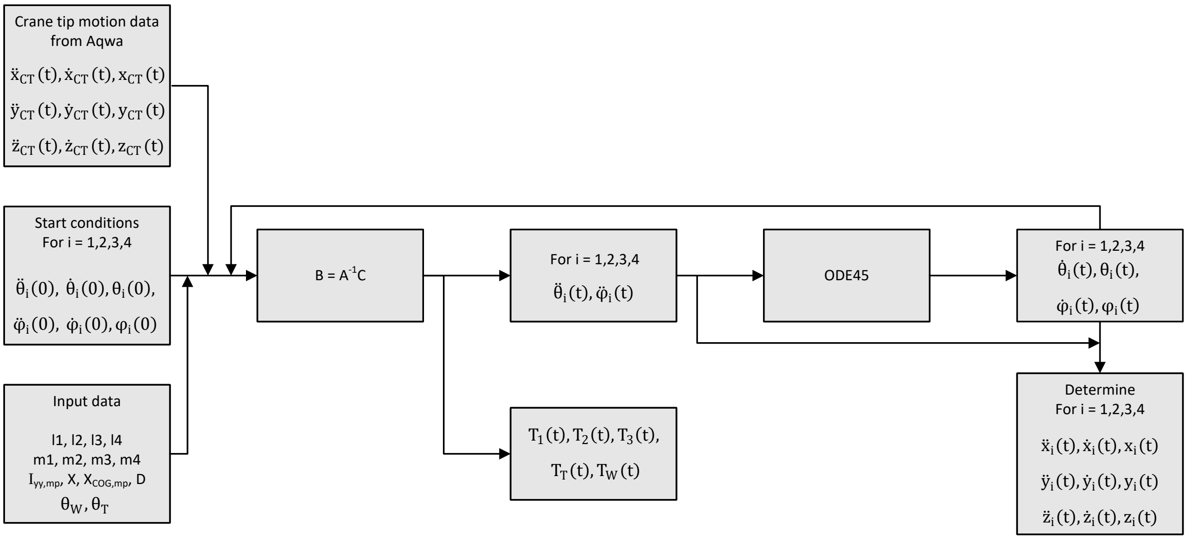

Figure 6.8: Calculation principle of the developed Matlab model

6.3.2 Matlab model verification

The simplifications made (see Figure 6.7) may affect the accuracy of the constructed model. Therefore, the implementation of the Matlab model is verified against the results obtained from the Aqwa model. Since the models are not independent, no further conclusions can be drawn about the extent to which the models represent reality (i.e., the model is verified, not validated). To make the verification cases more generalisable over different sea states, the model is verified for two of the sea states presented in Figure 6.6, which result in different types of responses. Figure 6.9 shows the comparison for the sea state with an H_s of [redacted] m and a T_p of [redacted] s. In the left column of plots, the amplitudes of the monopile COG location and of the tension in the winch cable are compared. In the right column, the corresponding frequencies are compared by means of Power Spectral Density (PSD)-spectra. These spectra are estimated based on the method by Welch (1967), which proposes the application of the Fast Fourier Transformation (FFT)-algorithm in combination with "sectioning the record, taking the modified periodograms of these sections and averaging these modified periodograms." The general conclusion from Figure 6.9 is that the output of the models provide position and tension time series with comparable amplitudes and with generally similar involved frequencies. One notable difference is that the "vibration" around the low-frequency trend of monopile COG surge and sway motions has a larger amplitude in the Matlab results than in the Aqwa results. This is considered, but not confirmed, to be the result of the simplification that the monopile is suspended to a single point in the MUST (see Figure 6.7), whereas in the Aqwa model the monopile is suspended to three different points. The latter provides additional constraints, which may result in a smaller surge and sway amplitude of the monopile. Nevertheless, the discussed minor difference does not seem to affect the output of the tension in the winch cable, which is the parameter of interest in this section. Both the amplitude and the frequency of the Matlab tension time series are in good agreement with the output from Aqwa.

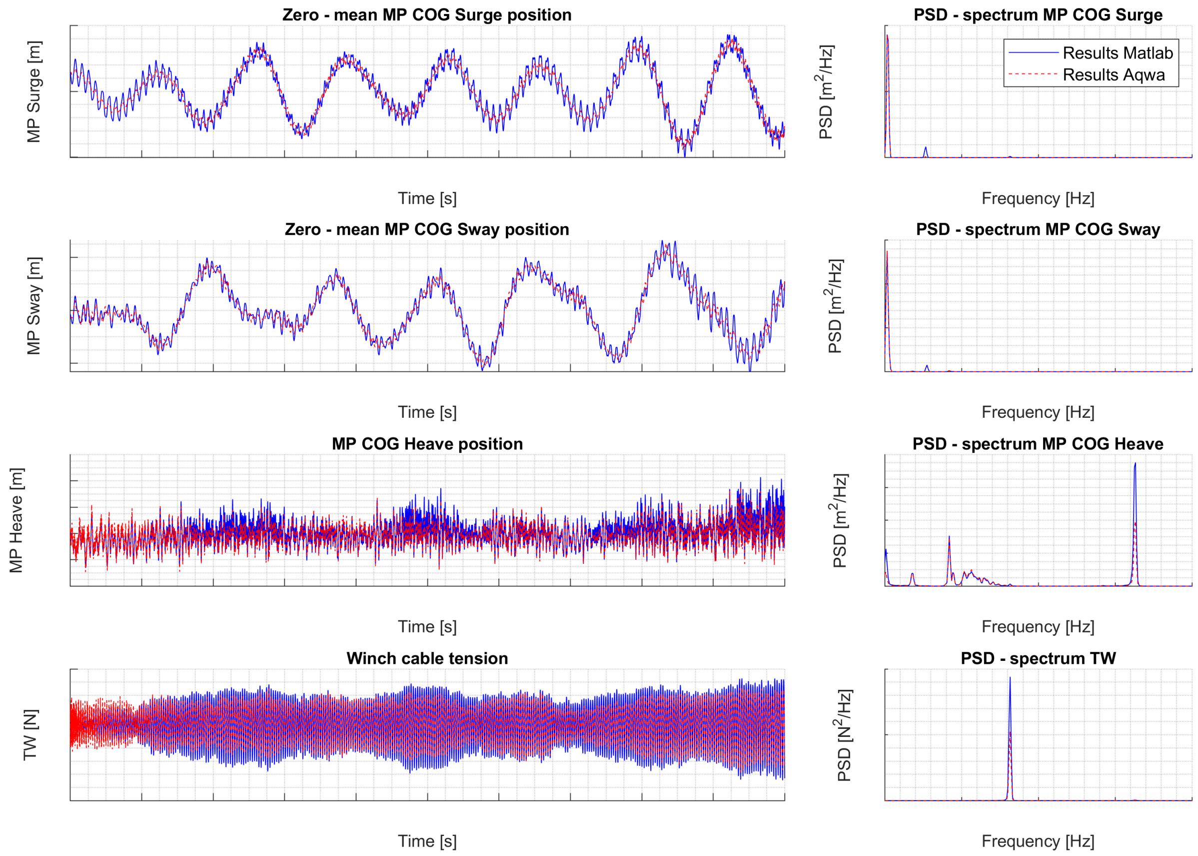

Figure 6.9: Verification Matlab model against results from Aqwa for a sea state of: WEA = 180 deg, H_s = [redacted] m, T_p = [redacted] s. TD-signal for amplitude comparison and a PSD-spectrum for frequency comparison

Figure 6.10 provides the results of both models for a sea state with an H_s of [redacted] m and a T_p of [redacted] s. The comparison of the monopile sway motion output presents the most eye-catching differences. The Matlab model output is characterised by a larger amplitude and an additional frequency peak around [redacted] Hz ($\widehat{=}$ [redacted] rad/s). This is the result of the fact that the effects of coupling between the monopile sway motion and the HLV's roll motion, which were studied in Section 4.4.4, are only included to a limited extent in the Matlab model. The additional peak corresponds to an uncoupled pendulum system, and hence is located at a similar frequency as the largest peak for the monopile surge motion (which in reality is coupled to the vessel's pitch motion but the corresponding effect is minimal due to the high stiffness of the vessel around this axis, as explained in Section 4.4.4). Regarding the monopile surge and heave motions, the models are in good agreement, both in terms of amplitude and frequency. The parameter of interest, the winch cable tension, also shows a satisfactory agreement with the Aqwa results. The amplitude is considerably smaller than for the sea state considered in Figure 6.9, but that holds for the results of both the models to approximately the same extent. Regarding the associated frequency, the Matlab model has a large emphasis on the lower frequency peak and the Aqwa model on the higher frequency peaks. Hence, the winch cable tension response described by the Matlab model seems to deviate more from that of the Aqwa model for this sea state. This is not expected to be a limitation, since the tension amplitude is found to be significantly lower for sea states with a longer peak wave period, and hence these sea states are expected not to be critical in determining the required distance between the monopile COG and the trunnions. Nevertheless, in general, the extent to which the simplifications made in the development of the Matlab model affect the accuracy seems to be limited.

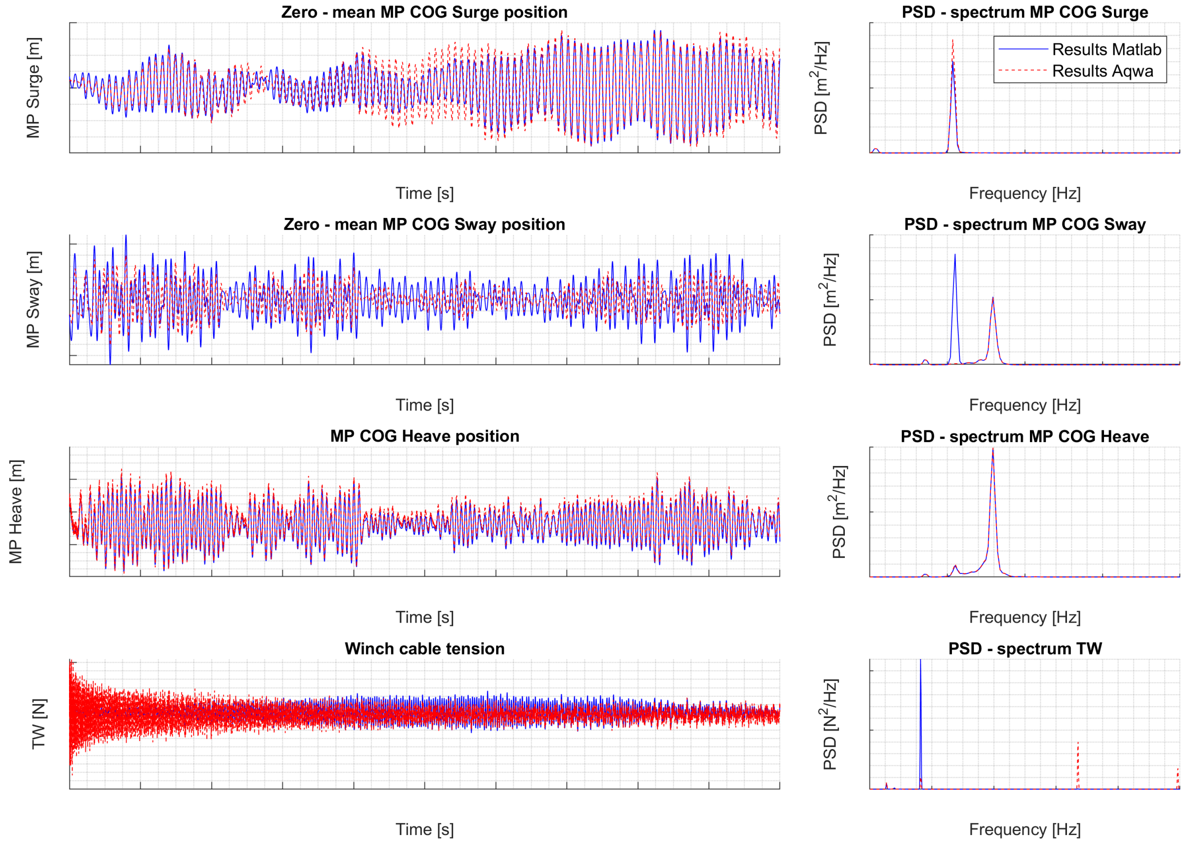

Figure 6.10: Verification Matlab model against results from Aqwa for a sea state of: WEA = 180 deg, H_s = [redacted] m, T_p = [redacted] s. TD-signal for amplitude comparison and a PSD-spectrum for frequency comparison

6.3.3 Trunnion positioning as a function of the sea state

Hsu et al. (2014) define a snap load as “a spike in tension as a sling re-engages immediately following on a slack condition, which is typically of very short duration”. This peak in the tension may result in a sling failure. Therefore, DNVGL-RP-N103 (2019, Section 4.4.3) recommends to avoid snap loads as far as possible. Moreover, they state that snap loads can occur when the dynamic component of the tension exceeds the static part. Hence, they recommend to consider a 10% margin to the start of slack slings, resulting in Equation 6.2.

$$F_{dyn} \leq 0.9 \cdot F_{static} \tag{6.2}$$

By iteration, the smallest x-distance between the trunnions and the monopile COG for which Equation 6.2 holds (x_{min}) is determined for each considered sea state (see Figure 6.6). The resulting minimum distances are presented in Figure 6.11, in combination with the H_s-T_p curve of Figure 6.6, to indicate the sea state each minimum distance corresponds to. It should be noted that the curves in the figure below are equipped with separate y-axes, which makes it a misconception to state that the x_{min}-curve follows the H_s-T_p-curve for peak wave periods larger than [redacted] seconds. Initially, each minimal x-distance was determined based on the crane tip motions derived from the Aqwa-model of which the development is described in Chapter 4. However, since for some sea states the winch cable would go slack for the initial value for x (= 8.3 m, see Figure 4.1), the imported crane-tip motions were considered not being representative. For these sea states an intermediate step was taken: first $x_{min_{inter}}$ was determined with the crane tip motions derived from the Aqwa model with x = 8.3 m, next this intermediate minimum distance was implemented in the Aqwa model and run for the particular sea state, and finally x_{min} was determined based on the crane tip motions resulting from the intermediate run. Additionally, it must be stated that in the analysis of each TD-signal to determine x_{min}, the first 500 seconds are neglected to only consider the steady state response and ignore the transient response. From Figure 6.11 can be deduced that for peak wave periods between [redacted] and [redacted] seconds, a relatively large distance between the trunnions and the monopile COG is required to prevent the winch cable from becoming slack, which can be related to the excitation of natural frequencies in the pendulum system. One main response mode with a natural period close to [redacted] seconds is visualised in Figure 6.12. It originates from the degree of freedom θ_4 (see Figure 6.7). Hence, the rotational inertia of the monopile around its y-axis, in combination with this resonant mode, appears to be the most significant inducer of a slack winch cable.

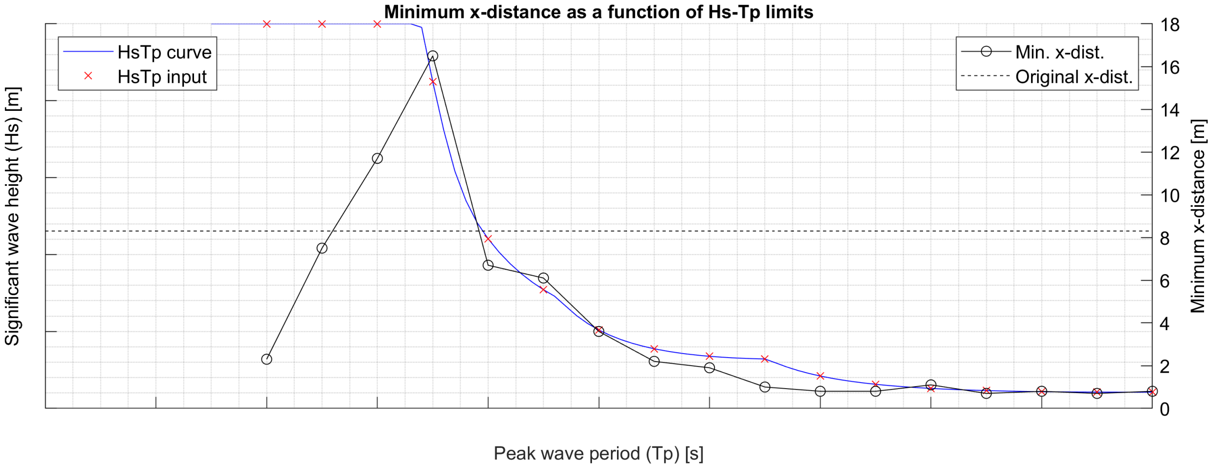

Figure 6.11: x_{min} as a function of the considered sea states. This is an extension to Figure 6.6

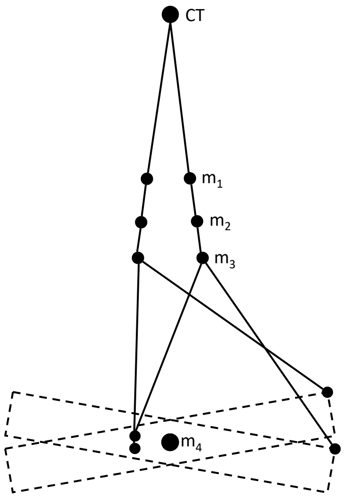

Figure 6.12: Resonant mode with a natural period close to [redacted] seconds, primarily induced by degree of freedom θ_4

So far, the Matlab model has only been verified against the Aqwa model for a single x-distance (8.3 m). Varying this distance to find the minimum value may affect the responses, and therefore the obtained results are checked with results obtained from Aqwa in a second verification round. In this verification process, the Matlab results are generated for the originally imported crane tip motions (from the Aqwa simulations in which x = 8.3 m or, in case the winch cable would go slack for that distance, $x_{\text{min}_{\text{inter}}}$), and not using the crane tip motions from the Aqwa model in which x_{min} is already implemented, to limit the dependency of the Matlab model performance on results from Aqwa. However, it was observed that the crane tip motions are only affected by the set x-distance to a limited extent, and therefore it is expected that this would have a little effect on the obtained results. For three sea states, the obtained minimum x-distances are implemented in the Aqwa model: $[H_s, T_p]$ = [[redacted] m, [redacted] s; [redacted] m, [redacted] s; [redacted] m, [redacted] s]. The latter two were already used for verification in Figure 6.9 and 6.10. The first is added as a sea state of interest, since the largest minimum x-distance corresponds to this sea state. Figure 6.13 compares the winch cable tension output of the three models in terms of a time series, to evaluate the tension amplitudes, and a PSD-spectrum, to evaluate the corresponding frequencies. For all three sea states, the amplitudes are considered to match satisfactory. For the first two sea states, the same frequencies are associated with the energy in the system. For the third sea state, a similar trend is observed as in Figure 6.10: the energy in the Matlab model is characterised by a "low" frequency component, whereas the Aqwa results also include this component but additionally encompass a "high" frequency component. Nevertheless, the conclusion is drawn that the Matlab results match satisfactory with the Aqwa results, and hence the minimum x-distances presented in Figure 6.11 are considered reliable. However, it must be noted that the presented results are based on a single random sea state seed and may deviate for different seeds. Since this is not a design study, the results in Figure 6.11 are solely presented to explain the underlying principle, and hence analysing a single seed is considered sufficient.

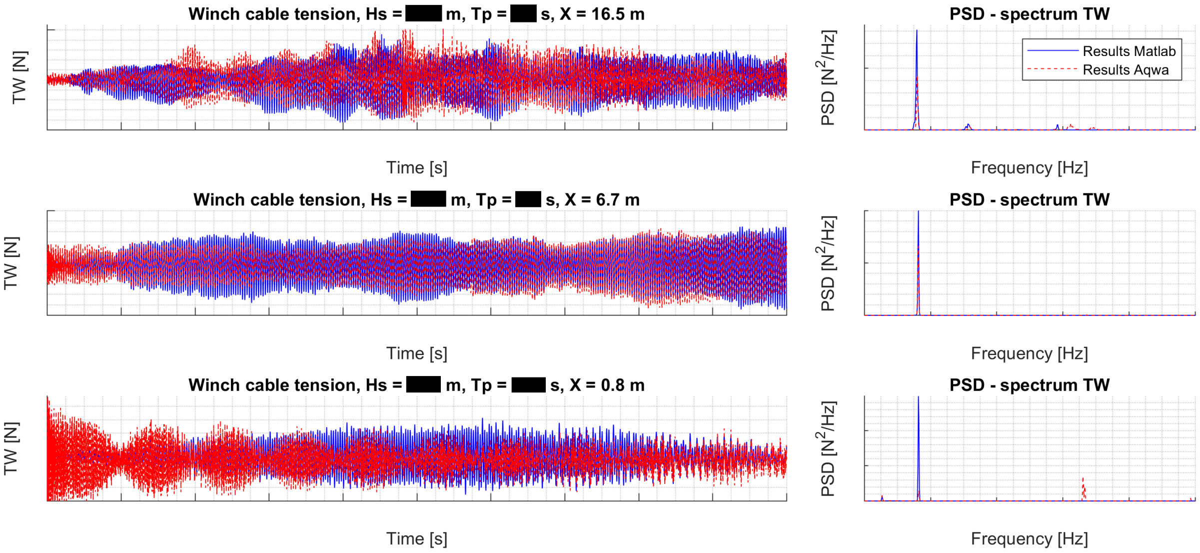

Figure 6.13: Verification of the winch cable tension results from the Matlab model against those from Aqwa, with the implementation of the minimum x-distances, for three sea states

6.4 Conclusions regarding the workability of the base case

The following conclusions can be drawn from Chapter 6. Workability of the base case.

- The optimal vessel heading for loadcase 2 (when the first monopile is lifted off), averaged over twelve years of location-specific weather data, is 165 degrees in the global coordinate system.
- The optimal vessel heading for loadcase 3 (when the second monopile is lifted off), averaged over twelve years of location-specific weather data, lies between 165 and 180 degrees in the global coordinate system.
- On average, the workability of both loadcases is very similar. When only the most favourable headings are considered, loadcase 3 is slightly more workable.
- A Matlab model was developed to iteratively determine the minimum x-distance between the monopile trunnions and COG for which the DNV-criterion to prevent snap loads is just met. The output of this model was verified against the results from Aqwa, regarding the response amplitudes and the involved frequencies.
- For low-frequency (long period) incident waves, an x-distance in the order of one meter can be sufficient to prevent snap loads in the winch cable. However, for such waves, the other limiting parameters reach their limits for relatively low significant wave heights (H_s) (see Appendix D), which means that the operability is low. Hence, the results for shorter incident waves, corresponding to a higher operability, are considered more relevant.
- For incident waves with a peak period (T_p) between [redacted] and [redacted] seconds, longer x-distances are required. The largest distance (which is governing) is expected to be required for incident waves with a T_p of [redacted] seconds. In that case, the minimum x-distance can be in the order of seventeen meters. A smaller x-distance would require a smaller winch. However, it must be realised that this will lower the H_s-T_p-curves presented in Appendix D (especially for T_ps between [redacted] and [redacted] seconds), and therefore the overall workability.
- The monopile pitch motion (rotation around the y-axis) has a natural period of approximately [redacted] seconds, which can induce a slack winch cable.

7 | Workability improvement

This section discusses principles that can be implemented to increase the workability of the considered system. Section 7.1 describes a system that reduces the influence of the relative z-motion between the barge and the monopile, and quantifies the resulting performance increase. Section 7.2 proposes a system that reduces the probability of the introduction of a slack winch cable and quantifies the advantages to the system design. Finally, in Section 7.3, the conclusions that can be drawn from Section 7.1 and 7.2 are evaluated.

7.1 Reduction of the relative z-motion limitation

The principle described in this section is based on the "hammock seafastening" system, developed by Temporary Works Design, visualised in Figure 7.1a. The hammock seafastening principle can be described by a series of aligned hammocks as depicted below, into which a monopile can be lowered. The self-weight of the monopile results in the structure gripping the monopile, securing it for safe transportation. The addition proposed here is visualised in Figure 7.1b and 7.1c. Once the transportation barge is moored alongside the Heavy Lift Vessel (HLV), the monopile is lifted from the seafastening system, using the MUST. The reduction of the self-weight resting in the hammock, results in the right clamp to be retracted by the spring. The consequence is an increase of the horizontal distance between the monopile and the seafastening structure, reducing the probability of collision. Additionally, it is proposed to release the hammock cable (see Figure 7.1c) to also increase the available vertical margin before collision happens. To be conservative, it is assumed that the limit for the relative y-motion remains the 1.1 m, as presented in Figure 5.2. However, as the height of the hammock grillage structure is to be determined during the design process, it is assumed that releasing the hammock cable results in an additional available margin of 3 m. This would increase the set limit of 1.5 (see Figure 5.2) to 3.0 m.

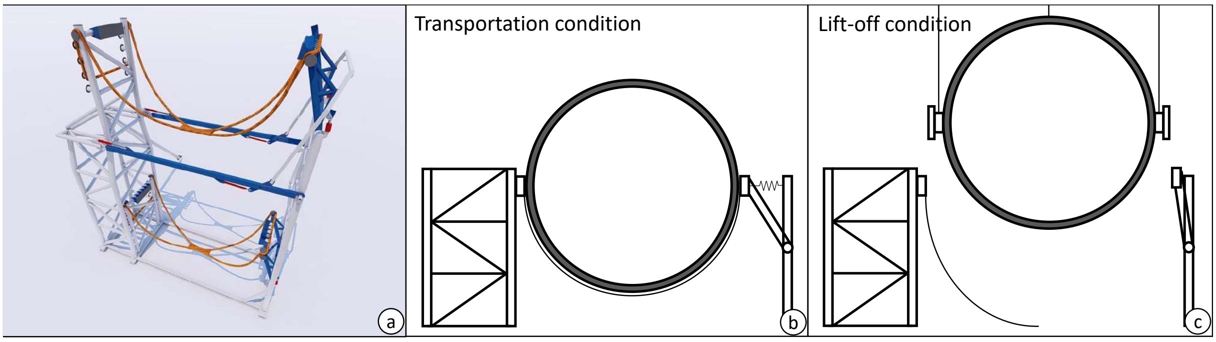

Figure 7.1: (a) TWD hammock seafastening system (TWD, n.d.), (b) Proposed system in transportation condition, (c) Proposed system in lift-off condition

Implementing this renewed limit for the vertical z-motion in the models developed in Chapter 6, and performing the same calculations, results in the workability percentages presented in Figure 7.2. Comparing the percentages for loadcase 2 (LC2) in this figure to those in Figure 6.1 and the percentages for loadcase 3 (LC3) to Figure 6.4, results in the notion that on average the workability for LC2 has increased by 2.4% and for LC3 by 0.16 %. However, since the workability increase percentages vary significantly with the selected heading and the month in which the operations are performed, a more elaborate comparison is provided in Table 7.1. Looking at the best performing headings for LC2, the workability for 165 degrees has on average increased by 5.3% and for 180 degrees by 8.3%. In general, the largest improvements are realised in the winter months (since there is more room for improvement with lower percentages). For the headings of 165, 180, 195 and 210 degrees, the maximum workability improvement is achieved in January, and amounts 10.7%, 16.1%, 15.6% and 9.8% respectively. This also means that the optimal heading for LC2 has shifted from 165 degrees to 180 degrees. Considering LC3, the workability increase percentages are significantly lower (as could be expected based on the provided average percentage). For a heading of 165 degrees, the mean improvement is 0.1%, for 180 degrees 0.3%, and for 195 degrees 1.1%. This difference can be explained by the H_s-T_p-curves presented in Appendix D, which show that LC2 is more limited by the relative z-motions compared to LC3. The latter is more limited by the barge roll and pitch motions (for which the proposed seafastening system does not compensate), induced by the difference in weight and inertia between a loaded and an empty barge.

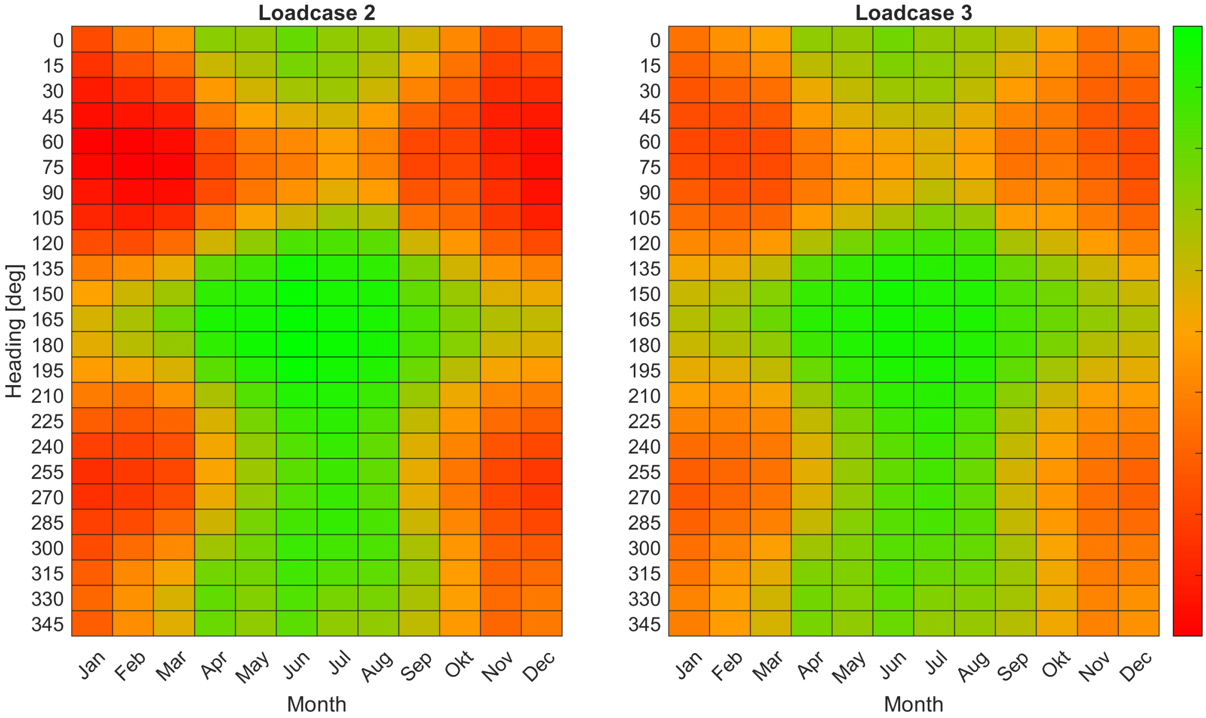

Figure 7.2: Workability percentages per heading and month, averaged over twelve years of weather data, after the implementation of the z-clearance increasing system into both loadcase 2 and 3

Table 7.1: Percentages workability increase as a result of implementing the proposed seafastening system (Figure 7.2 w.r.t. Figure 6.1 and 6.4)

Heading [deg]		0	15	30	45	60	75	90	105
LC2	Mean	0.0	0.0	0.6	2.8	3.2	1.5	0.8	0.6
	Max (Month)	0.0	0.3 (Dec)	2.6 (Jan)	9.5 (Jan)	8.0 (Jan)	3.2 (Jan)	1.8 (Feb)	1.9 (Jan)
	Min (Month)	0.0	0.0 (11x)	0.0 (3x)	0.7 (Jun)	1.2 (Jun)	0.5 (Jun)	0.1 (Jun)	0.0 (Jun)
LC3	Mean	0.0	0.0	0.0	0.0	0.0	0.0	0.0	0.0
	Max (Month)	0.0	0.0	0.0	0.0	0.0	0.0	0.0	0.0
	Min (Month)	0.0	0.0	0.0	0.0	0.0	0.0	0.0	0.0
Heading [deg]		**120**	**135**	**150**	**165**	**180**	**195**	**210**	**225**
LC2	Mean	1.6	2.6	3.6	5.3	8.3	8.3	4.9	3.2
	Max (Month)	3.0 (Jan)	4.9 (Jan)	6.7 (Jan)	10.7 (Jan)	16.1 (Jan)	15.6 (Jan)	9.8 (Jan)	6.4 (Feb)
	Min (Month)	0.7 (Jun)	1.2 (Aug)	1.9 (Aug)	2.4 (Aug)	3.9 (Jun)	3.4 (Jun)	1.9 (Jun)	1.0 (Jun)
LC3	Mean	0.0	0.1	0.1	0.1	0.3	1.1	0.5	0.7
	Max (Month)	0.0	0.3 (Jan)	0.3 (Dec)	0.6 (Dec)	0.8 (Jan)	2.3 (Jan)	1.1 (Jan)	2.0 (Feb)
	Min (Month)	0.0	0.0 (4x)	0.0 (4x)	0.0 (2x)	0.0 (Jul)	0.2 (Jun)	0.1 (May)	0.1 (Jun)
Heading [deg]		**240**	**255**	**270**	**285**	**300**	**315**	**330**	**345**
LC2	Mean	2.3	2.0	2.3	0.9	1.3	0.4	0.2	0.0
	Max (Month)	4.8 (Feb)	3.2 (Feb)	4.5 (Feb)	3.1 (Feb)	4.1 (Feb)	1.0 (Feb)	1.1 (Jan)	0.4 (Dec)
	Min (Month)	0.6 (May)	0.7 (Jun)	1.1 (Jun)	0.1 (Jun)	0.3 (Jun)	0.0 (2x)	0.0 (6x)	0.0 (11x)
LC3	Mean	0.3	0.2	0.2	0.1	0.2	0.2	0.0	0.0
	Max (Month)	1.0 (Feb)	0.4 (Apr)	0.6 (Dec)	0.8 (Feb)	0.5 (Feb)	0.6 (Jan)	0.3 (Jan)	0.0
	Min (Month)	0.0 (2x)	0.0 (3x)	0.0 (4x)	0.0 (6x)	0.0 (2x)	0.0 (5x)	0.0 (10x)	0.0

7.2 Reducing the chances of snap loads

Preventing snap loads in cables has been researched in various studies. One measure that can be taken is the implementation of a form of motion compensation. The most familiar form is heave compensation, which can be active or passive. An Active Motion Compensator (AMC) is mostly equipped with a control system that actively follows or compensates certain input motions, and hence external power supply is required. A Passive Motion Compensator (PMC) basically consists of a spring-damper system, which absorbs a part of the energy that is present in a system. Figure 7.3 provides a schematic representation of a type of PMC that is currently on the market. When the tension in the winch cable increases, the connected piston moves down a bit, which produces a pressure increase in the hydraulic oil. This results in an upward motion of the piston in the accumulator, and hence a pressure increase in the gas, until an equilibrium is found. The consequence is a (nonlinear) spring effect. The oil flow through the nozzles and the viscous effects of the oil provide the dampening effect. Cannell et al. (2016), Keprate (2015) and Driscoll et al. (2000) show that the probability of the line going slack, and thereby the introduction of snap loads, reduces with the introduction of this type of PMC. Additionally, Jianan et al. (2019) show that this type of PMC-system can result in significant motion reductions. However, all of these studies apply the principle to (vertical) heave compensation. Therefore, in this study the applicability of the system in the inclined winch cable is investigated.

Section 7.2.1 discusses the implementation of the PMC into the Matlab model developed in Section 6.3.1. Next, in Section 7.2.2, the mechanical properties of the compensator system are determined. In Section 7.2.3, the potential advantages of implementing a PMC are quantified. Subsequently, in Section 7.2.4, some required dimensions for the compensator are derived, in order to check the technical feasibility. Finally, in Section 7.2.5, some practical considerations regarding the implementation of a PMC are discussed.

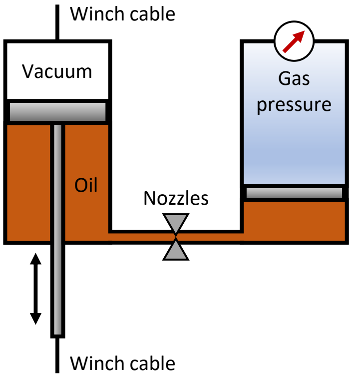

Figure 7.3: Working principle of a passive motion compensator based on a hydraulic cylinder and a gas accumulator

7.2.1 Model implementation of passive motion compensator

The spring effect provided by the device depicted in Figure 7.3 is the result of compressing a gas. Hence, a nonlinear spring coefficient could be derived based on the ideal gas law, as explained by Jianan et al. (2019) and Keprate (2015). However, since this is an exploratory study and no detailed design report, it was decided to consider a linear system to investigate the potential. Moreover, Jianan et al. (2019) show that the difference between the nonlinear and the linearised spring coefficient is very marginal, and therefore it is expected that considering the nonlinear system would not alter the results significantly. The resulting system of analysis is presented in Figure 7.4 (compare with Figure 6.7). The main difference is the implemented spring-damper system in series with the winch cable. Furthermore, a degree of freedom has been introduced due to this addition: where the motion of the monopile in the x-z plane relative to m$_3$ was first fully described by θ_4, now additionally θ_T is required. Note that in the uncompensated system, θ_4 describes a different degree of freedom.

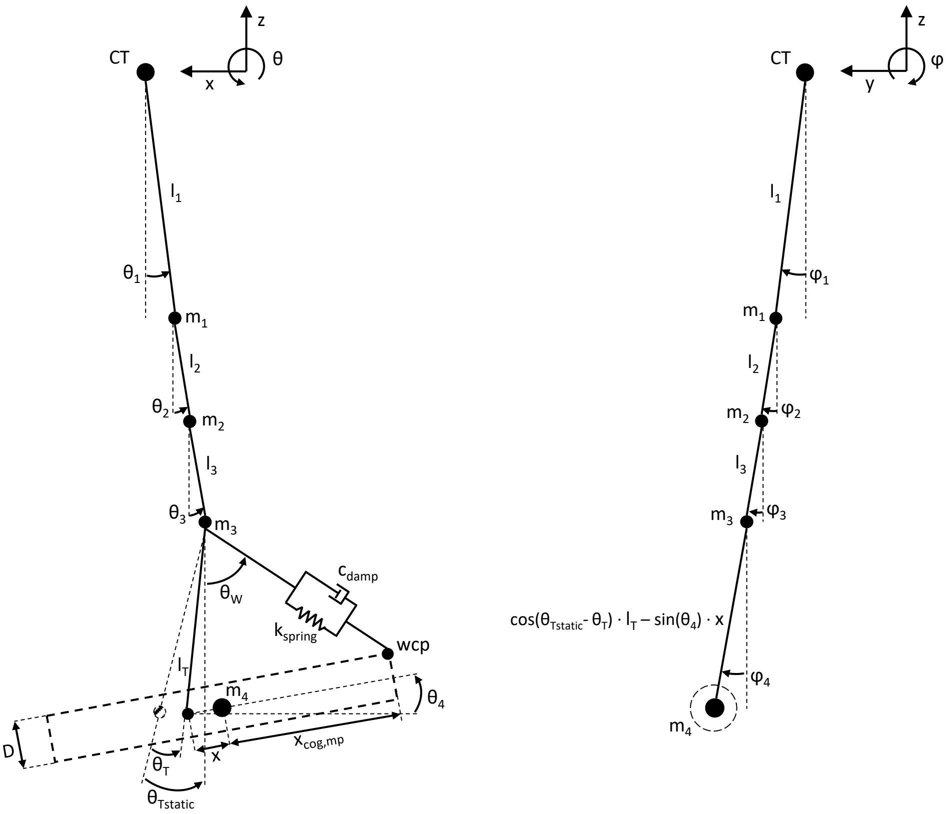

Figure 7.4: Simplified representation of the system of analysis after implementation of the PMC

Section F.1 in Appendix F presents the kinematics (positions, velocities and accelerations) of the four considered masses in the compensated model. Additionally, it provides the expressions for the position and velocity of point wcp (winch connection point) on the bottom of the monopile. The section closes with expressions for the instantaneous and initial (monopile suspended statically horizontally) value for θ_W (θ_W and $\theta_{Wstatic}$ respectively), the initial value of θ_T ($\theta_{Tstatic}$) and the unstretched length of the winch cable – spring – damper system ($\mathrm{L_{S0}}$). The latter is separately determined for each x-distance, such that for the set spring stiffness the monopile is suspended horizontally in the static condition. Next, in Section F.2, the force balances in x-, y-, and z-direction, and a moment balance around the y-axis for $\mathrm{m_4}$ are derived. Moreover, an expression for the tension in the winch cable is provided, as a function of the spring stiffness ($\mathrm{k_{spring}}$), the damping coefficient ($\mathrm{c_{damp}}$) and the relative position and velocity of $\mathrm{m_3}$ w.r.t. the wcp. When the kinematic equations are substituted into the kinetic equations and rewritten, the equations presented in matrix form in Section F.3 can be derived. It must be noted that the expressions of some cells are provided on the following pages. Using these A, B and C matrices the same calculation principle is followed as explained in Figure 6.8, but with an additional degree of freedom.

7.2.2 Determining the compensator properties

The implementation of the spring-damper system introduces new resonance frequencies in the system. In order to prevent excessive motions, the properties of the introduced system should be selected with care. The most relevant degree of freedom regarding introduced resonance is the θ_4 rotation (also because it is one of the inducers of snap loads, see Figure 6.12). To estimate the relationship between the spring stiffness and the resonance frequency corresponding to this degree of freedom, the system of analysis is further simplified to a two-dimensional system, as depicted in Figure 7.5.

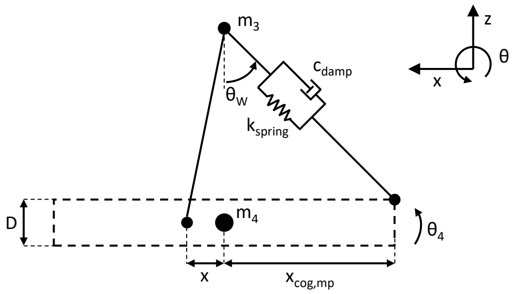

Figure 7.5: The system of analysis further simplified (compared to Figure 7.4)

The initial length of the spring-damper-winch cable system is represented by L_{s0}, and can be calculated based on its initial x- and z-length components (x_0 and z_0) using Equation 7.1. Subsequently, the length at a certain moment in time is determined by adding the components of elongation in x- and z-direction (x_s and z_s), see Equation 7.2. It must be noted that $x_s << x_0$ and $z_s << z_0$, and hence it is assumed that the components $(x_s)^2$ and $(z_s)^2$ can be neglected. Next, the latter equation is rewritten and the binomial approximation is applied, resulting in Equation 7.3. By subtracting the initial length, L_{s0}, from the resulting expression for l, the equation for the spring elongation (Δl) is determined. At the same time, it must be realised that $x_0 = sin(\theta_W) \cdot L_{s0}$, $z_0 = cos(\theta_W) \cdot L_{s0}$, $x_s = (1 - cos(\theta_4)) \cdot (x + x_{cog,mp})$ and $z_s = sin(\theta_4) \cdot (x + x_{cog,mp})$. This way, Equation 7.4 can be derived. The tension in the winch cable, T_W, is calculated by multiplying the expression for the spring elongation with the spring stiffness k_{spring}. Moreover, the equation is linearised by performing a small angle Taylor expansion on the goniometric components of the degree of freedom of analysis. Hence, $sin(\theta_4) \approx \theta_4$ and $cos(\theta_4) \approx 1$, which results in Equation 7.5.

$$L_{s0} = \sqrt{(x_0)^2 + (z_0)^2} \tag{7.1}$$

$$\begin{aligned} l &= \sqrt{(x_0 + x_s)^2 + (z_0 + z_s)^2} \quad \approx \quad \sqrt{(L_{s0})^2 + 2 \cdot x_0 \cdot x_s + 2 \cdot z_0 \cdot z_s} \\ &= L_{s0} \cdot \sqrt{1 + \frac{2 \cdot x_0 \cdot x_s + 2 \cdot z_0 \cdot z_s}{(L_{s0})^2}} \end{aligned} \tag{7.2}$$

$$\text{Application of binomial approximation:} \quad l \approx L_{s0} \left(1 + \frac{x_0 \cdot x_s + z_0 \cdot z_s}{(L_{s0})^2}\right) \tag{7.3}$$

$$\begin{aligned} \Delta l = l - L_{s0} &\approx \frac{x_0 \cdot x_s + z_0 \cdot z_s}{L_{s0}} \\ &= (x + x_{cog,mp}) \cdot \big(sin(\theta_W) \cdot (1 - cos(\theta_4)) + cos(\theta_W) \cdot sin(\theta_4)\big) \end{aligned} \tag{7.4}$$

$$T_W = k_{spring} \cdot \Delta l \approx k_{spring} \cdot cos(\theta_W) \cdot (x + x_{cog,mp}) \cdot \theta_4 \tag{7.5}$$

The equation of motion is derived by considering the moment balance around the y-axis. The starting condition of the system is assumed to be a horizontal monopile, and hence the static moment induced by gravity and the equally large compensating component induced by the spring are left out of consideration. This way, Equation 7.6 is derived, after which Equation 7.5 is substituted and the equation is rewritten.

$$\begin{aligned}\sum M_y : &- m_4 \cdot x^2 \cdot \ddot{\theta}_4 - cos(\theta_W) \cdot T_W \cdot (x + x_{cog,mp}) - sin(\theta_W) \cdot T_W \cdot \frac{D}{2} = 0 \\ \xrightarrow[rewrite]{substitute} &\quad m_4 \cdot x^2 \cdot \ddot{\theta}_4 + \left(cos(\theta_W) \cdot (x + x_{cog,mp}) + sin(\theta_W) \cdot \frac{D}{2} \right) \cdot k_{spring} \\ &\cdot cos(\theta_W) \cdot (x + x_{cog,mp}) \cdot \theta_4 = 0\end{aligned} \tag{7.6}$$

In order to determine the natural frequency, it is assumed that the response describing the motions of the considered degree of freedom is harmonic and can be described by: $\theta_4 = sin(\omega \cdot t + \phi)$. Implementing this assumption results in Equation 7.7, which is rewritten to express the natural frequency (ω_n) as a function of the spring stiffness.

$$\begin{aligned}&- \omega^2 \cdot m_4 \cdot x^2 + \left(cos(\theta_W) \cdot (x + x_{cog,mp}) + sin(\theta_W) \cdot \frac{D}{2} \right) \cdot k_{spring} \cdot cos(\theta_W) \\ &\cdot (x + x_{cog,mp}) = 0 \quad \xrightarrow{rewrite} \\ w_n = &\sqrt{\frac{k_{spring} \cdot cos(\theta_W) \cdot (x + x_{cog,mp}) \cdot \left(cos(\theta_W) \cdot (x + x_{cog,mp}) + sin(\theta_W) \cdot \frac{D}{2} \right)}{m_4 \cdot x^2}}\end{aligned} \tag{7.7}$$

The derived relationship between the spring stiffness and the natural frequency is visualised in Figure 7.6 for all of the minimal x-distances presented in Figure 6.11. As mentioned before, it may be smart to design the compensation system such that the natural frequency is situated outside the range of excitation frequencies. Regarding the total system of analysis, these frequencies originate from the incident waves. Designing the compensation system such that the introduced natural period is higher than the maximum occurring wave period may not be the most practical alternative, since very long swell waves can develop, which would result in a very soft suspension system. The latter means the compensation system would require a very large stroke only to statically suspend the monopile. Hence, it is considered to be more practical to select a stiffness resulting in a natural period lower than the naturally occurring wave periods.

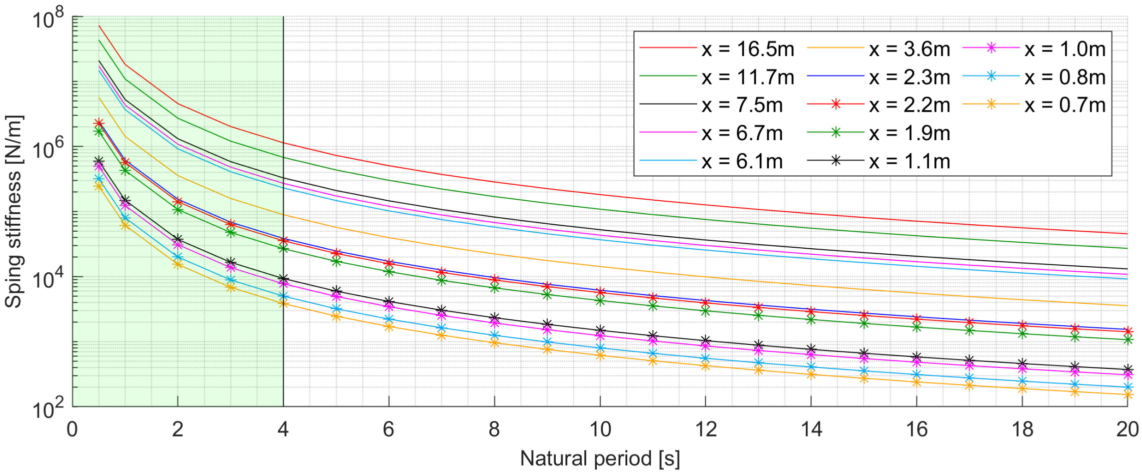

Figure 7.6: Spring stiffness plotted against corresponding natural period, for each x-distance presented in Figure 6.11

Based on a review of scatter diagrams of the North Sea provided by MetoceanView (2016) (among which the typical location of Section 5.1), the lower boundary of “frequently” occurring wave periods can be considered to be four seconds. This conclusion is substantiated by the scatter diagrams presented in (DNVGL-RP-C205, 2019, Appendix C) for North Atlantic and worldwide applications. Moreover, waves with shorter periods generally only occur with relatively low wave heights and hence carry little energy. For these reasons, it is considered safe to design the system for natural periods lower than four seconds, as indicated by the green hatched area in Figure 7.6. To implement a safety margin, it has been decided to consider a spring stiffness corresponding to a natural period of three seconds and for an x-distance of 16.5 m. The largest x-distance was selected because systems with smaller distances but with the same spring stiffness are characterised with lower natural periods (see Figure 7.6), further away from the wave excitation frequencies. Hence, a value of $2.0 \cdot 10^6$ N/m is implemented for $\mathrm{k_{spring}}$.

The damping of a passive compensation device is generally not that high: experts in hydrodynamics estimate it to be 5 - 10 % of the critical damping (B. Dai, personal communication, 29 November 2021). This estimation is affirmed by Sánchez et al. (2020), who use a value of 10%, and van der Heiden (2019), who uses values between 5% and 15%. In order to generate an idea of how the results depend on the damping of the implemented device, it has been decided to perform simulations for damping ratios of 5%, 10% and 15%. The critical damping coefficient ($\mathrm{c_{crit}}$) can be determined using Equation 7.8. Hence, the damping coefficient can be determined by multiplying $\mathrm{c_{crit}}$ with the damping ratio (ζ), as is expressed by Equation 7.9. Apart from the spring coefficient ($\mathrm{k_{spring}}$), additionally, a value for the mass is required, which is not simply the mass of the monopile, $\mathrm{m_4}$. It is the part of $\mathrm{m_4}$ which is supported by the force in-line with the spring-damper system. This component can be derived using Equation 7.10. This means that the used damping coefficient is dependent on the variable x-distance, and no single value can be given for the used damping coefficient.

$$c_{crit} = 2 \cdot \sqrt{k_{spring} \cdot m_{in-line}} \tag{7.8}$$

$$c_{damp} = 2 \cdot \zeta \cdot \sqrt{k_{spring} \cdot m_{in-line}} \tag{7.9}$$

$$m_{4,in-line} = \frac{m_4 \cdot x}{cos(\theta_{W static}) \cdot (x + x_{cog,mp}) + sin(\theta_{W static}) \cdot \frac{D}{2}} \tag{7.10}$$

7.2.3 Trunnion positioning as function of sea state and passive compensation

Similar to what was done in Section 6.3.3, in this section the minimum x-distance between the trunnions and the monopile Centre Of Gravity (COG) is determined for several cases. In these cases, passive compensation systems with the properties determined in Section 7.2.2 are installed in series with the winch cable, with the intention to reduce the probability of occurrence of a slack winch cable. Figure 7.7 is an extension to Figure 6.11, and provides the minimum x-distances for which the system complies with Equation 6.2, for the cases in which passive compensation is implemented. It shows that the minimum x-distance can be significantly reduced by the implementation of a compensation system. This is especially the case for the sea state with a peak wave period of [redacted] seconds, which was determined to excite the natural frequency mode in the system that induces a slack winch cable. For the steps from zero damping to 5% of critical damping, and from 5% to 10% of critical damping, the reduction in minimum x-distance is the largest. A smaller reduction corresponds to the step from 10% to 15% of critical damping. These are all promising results, however, it must be mentioned that the peak x-distance for the case of $\zeta = 15\%$ amounts 4.7 m, which results in a situation in which the monopile cannot be upended with the defined rigging arrangement (see Section 4.4). The top of the monopile would clash with the MUST. Hence, if an x-distance close to this value is selected, a second iteration step must be performed with slightly longer grommets between the MUST and the monopile trunnions.

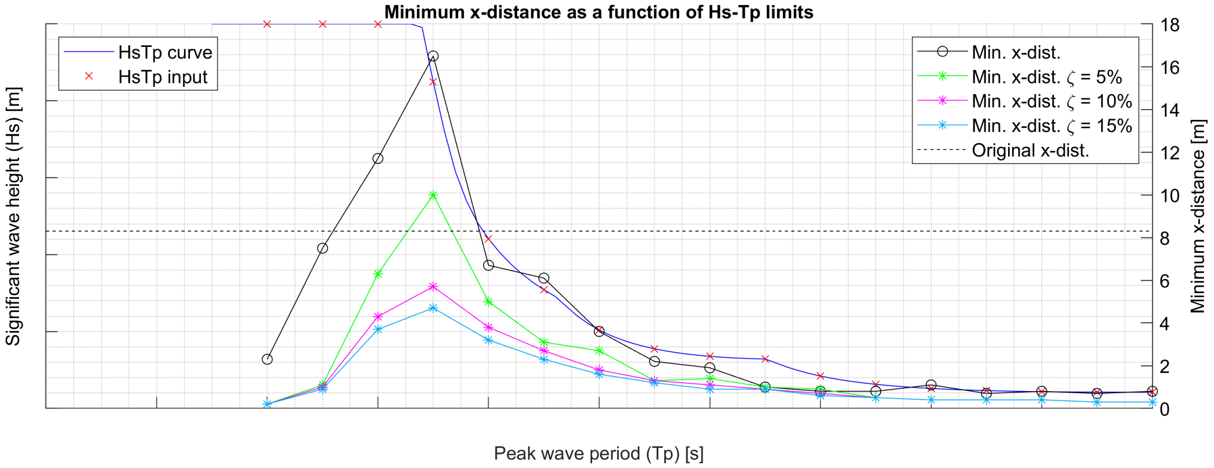

Figure 7.7: x_{min} as a function of the considered sea states, determined for four cases: without damping, and with 5%, 10% and 15% of critical damping. This is an extension to Figure 6.11

Figure 7.8 shows for the four damping cases the time domain plots of the winch cable tension responses to a sea state with an H_s of [redacted] m, a T_p of [redacted] s and a Wave Encounter Angle (WEA) of 180 deg. Moreover, it displays the response for the case that the x-distance is set to its minimum value. When the mean and the maxima in the plots are compared, an obvious conclusion that can be drawn is that they are negatively correlated with the implemented damping. The strength of this correlation is such that the implementation of 10% damping shows the potential of a reduction in the required winch capacity with a factor 2.3 (w.r.t. the undamped case). This principle also works the other way around. If (more) damping is implemented, but the x-distance is kept constant, the allowable sea state for that distance increases. Hence, the implementation of damping can help to increase the workability of the system of analysis.

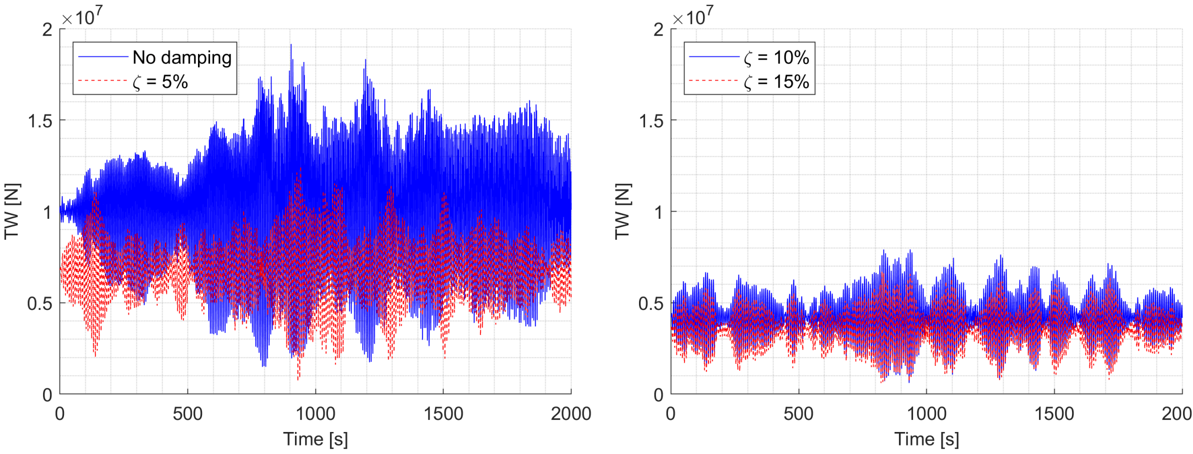

Figure 7.8: The winch cable tension responses to a sea state described by $H_s =$ [redacted] m, $T_p =$ [redacted] s and WEA = 180 deg, with the x-distance set to its minimum value, for the four cases of damping

7.2.4 Passive compensation system design

In the previous section, the potential system improvement of the implementation of a passive motion compensator was shown. In this section, the physical feasibility is investigated. This does not mean that the detailed design requirements of a compensator are provided, but it is merely checked if the assumed properties can be realised with reasonable dimensions of the tool. First, the required stroke is investigated. It was found that the largest stroke is required for the case in which $\zeta = 5\%$, $H_s =$ [redacted] m and $T_p =$ [redacted] s. In that case, the maximum stroke amplitude amounts 3.0 m and the maximum stroke 6.2 m, as can also be seen in Figure 7.9. As a standard, the company of IQIP offers passive heave compensators with a maximum capacity of 500 mT (see Figure 7.8 for an indication of the required capacity) and a maximum stroke of 4.5 m (IQIP, n.d.). However, they also state that "if a Maxine (i.e., the name of the PMC) outside this range is required, they can quickly develop a tailor-made version", and that the device can be implemented in a "single, series, parallel or series-parallel" configuration. Therefore, it is believed that the resulting required capacities will not be outside the ranges of what is technically feasible.

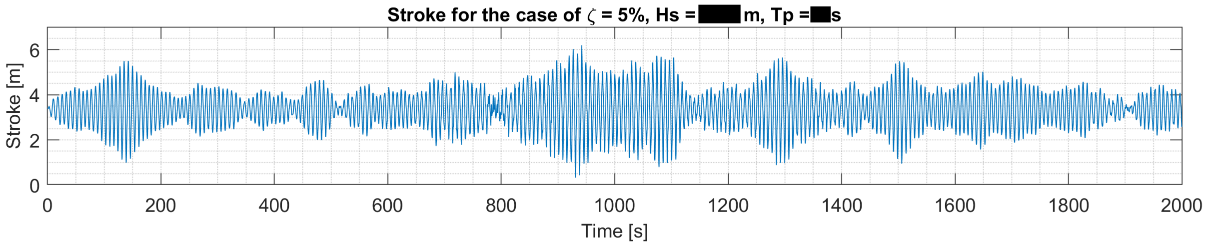

Figure 7.9: Time series of the stroke of the PMC, for a sea state with H_s = [redacted] m, T_p = [redacted] s, WEA = 180 deg and 5% of critical damping

IQIP (n.d.) and other considered suppliers do not provide information on the stiffness or damping provided by their devices. Therefore, the required dimensions to realise the defined specifications are estimated by applying physics, following the theory discussed by Jianan et al. (2019). By linearising the ideal gas law at the static equilibrium position, they derive Equation 7.11. In this equation, n is the adiabatic gas constant, P_{b0} is the initial gas pressure, A is the piston area and V_0 is the initial gas volume. Moreover, they derive Equation 7.12 based on the pressure drop resulting from viscous effects of a fluid flow through a pipe (see also (White, 2016)). In this equation, μ is the dynamic viscosity of the oil, l is the length of the pipe and d is the diameter of the pipe. Since the diameters of the cylinder and the accumulator are expected to be significantly larger than of the pipe connecting them (see Figure 7.3), only the diameter of the latter is considered here. Jianan et al. (2019) additionally derive a quadratic damping component related to the damping provided by the nozzles in the pipe. Since only linear damping is considered in the developed model, this component is neglected here. Moreover, since all of the damping must now come from viscous effects, it is expected that neglecting the effect of the nozzles provides conservative results.

$$k_{spring} = \frac{n \cdot P_{b0} \cdot A^2}{V_0} \tag{7.11}$$

$$c_{damp} = \frac{128 \cdot \mu \cdot l \cdot A^2}{\pi \cdot d^4} \tag{7.12}$$

The spring constant (k_{spring}) was determined as $2.0 \cdot 10^6$ N/m in Section 7.2.2, and the linear damping coefficient as to be dependent on the positioning of the trunnions. It was found that the largest damping coefficients in all three damped cases result from the minimum x-distances corresponding to the sea state with H_s = [redacted] m and T_p = [redacted] s. These damping values are presented in Table 7.2. According to Albers (2010), the adiabatic gas constant is approximately 1.4 for nitrogen, and the pressure in a nitrogen gas bottle is typically 270 bar. For the dynamic viscosity of the hydraulic oil, a value of 0.1 N·s/m^2 is assumed, which is substantiated by the values presented in (White, 2016). By assuming the initial gas volume to be 0.5 m^3 and the pipe diameter 2 cm, the output values for the piston area and the tube length are calculated and presented in Table 7.2. Although it must be realised that this is a very rough estimation of the required size of the device, the estimated dimensions seem reasonable. Hence, it is expected that it is feasible to construct a PMC of the considered type with the required capacities.

Table 7.2: In and output numbers regarding Equation 7.11 and 7.12, for the estimation of the required dimensions of the PMC

Input				**Output**		
n		1.4	[-]	A	0.16	[m^2]
P_{b0}		$2.7 \cdot 10^7$	[Pa]	$l_{\zeta = 5\%}$	0.17	[m]
V_0		0.5	[m^3]	$l_{\zeta = 10\%}$	0.27	[m]
μ		0.1	[$N \cdot s/m^2$]	$l_{\zeta = 15\%}$	0.38	[m]
d		0.02	[m]			
k_{spring}		$2.0 \cdot 10^6$	[N/m]			
c_{damp}	$\zeta = 5\%$	$1.2 \cdot 10^5$	[N·s/m]			
	$\zeta = 10\%$	$1.9 \cdot 10^5$	[N·s/m]			
	$\zeta = 15\%$	$2.5 \cdot 10^5$	[N·s/m]			

7.2.5 Practical implementation of passive compensation system

The spring-damper system cannot simply be installed as sketched in Figure 7.5. Installing a mass halfway a cable can result in unwanted vibrations, which may reduce the predictability of the responses of the system. It is expected that installing the compensator as close as possible to the MUST or the monopile reduces the probability of occurrence of such vibrations. A disadvantage of positioning the compensator close to the MUST, is that it increases the combined weight at the height of this structure, which increases the probability of encountering double-pendulum chaotic behaviour. Positioning it close to the monopile reduces this probability, as it increases the mass at the height of the heaviest structure. However, it may also be possible to directly attach the compensator to the MUST structure, and put it in series with the winch cable using pulleys. This way, the weight of the compensator does not add to the required winch capacity, and the mentioned vibrations in the cable are largely avoided.

7.3 Conclusions regarding workability improvement

The following conclusions can be drawn from Chapter 7. Workability improvement.

- To reduce the limiting effect of the relative z-motion between the suspended monopile and the grillage on the barge, a “hammock” seafastening system is proposed. The system allows for releasing the hammock just after lift-off, to instantaneously increase the vertical distance between the monopile and the barge.
- For the best performing headings in loadcase 2, the average workability increase resulting from the hammock system can reach up to 8.3%. The maximum workability increase percentages are mostly obtained for the winter months. For a heading of 180 degrees, the workability increase in January can reach up to 16.1%.
- Regarding loadcase 3, the hammock system only results in a very marginal workability increase. This is the case as for this loadcase, the barge roll and pitch motions are more limiting, which is not compensated for by the proposed system.
- To reduce the probability of the introduction of snap loads, or to optimise the MUST design by minimising the required winch capacity, installing a PMC in series with the winch cable is proposed.
- The implementation of the PMC is modelled in the Matlab model developed in Chapter 6. A linear spring-damper system is assumed, with a spring stiffness resulting in a natural frequency outside the wave excitation frequency range. Damping values of 5, 10 and 15% of critical damping are considered.

- The implementation of a PMC can significantly reduce the required x-distance between the trunnions and the monopile COG to prevent snap loads from occurring, especially for incident waves with peak wave periods close to the natural pitch period of the monopile. This also means that for the same x-distance, higher sea states can be allowed, and hence the workability can be increased. Based on the results presented in this chapter, a first estimate can be made for a suitable x-distance. If a PMC with 10% damping would be installed, it is advisable to design for an x-distance of at least 5.7 m (the peak in Figure 7.7 for $T_p =$ [redacted] s), to prevent losing workability. In the subsequent iteration, the tension in the winch cable can be considered as a limiting parameter in the workability calculations (to quantify the workability increase as a result of the PMC).
- W.r.t. the undamped case, the implementation of 10% damping can result in a reduction of the required winch capacity with a factor 2.3.
- Based on rough estimations, it was concluded that the required capacities and dimensions of the PMC are technically feasible.

8 | Conclusion and discussion

This chapter evaluates the conclusions that can be drawn from the process towards reaching the research objective in Section 8.1. Also, the main research question is answered in this section. In Section 8.2, the system of analysis and this study's findings are discussed in the light of related fields of science. Moreover, the limitations of this research are evaluated. Finally, in Section 8.3, recommendations for future research are made.

8.1 General conclusions

The literature review performed in this study revealed that a limited amount of scientific studies are available on determining the workability of floating installation operations of offshore wind turbine substructures. Only four studies investigating the lift-off operation of a structure (not necessarily a substructure) were identified. No study was found to propose systems to reduce the probability of a re-hit action. Moreover, while a few studies consider snap loads as a limiting condition during the lift-off phase, no study was encountered considering challenges regarding reduced stability similar to this study. Hence, the objective of this study was "to examine the limiting parameters and the workability of the monopile installation method using the MUST, and to formulate strategies that increase the corresponding weather resistance." In pursuing this objective, it was decided to follow the nine-step methodology by Guachamin Acero, Li, et al. (2016). Moreover, for the required modelling steps of this framework, it was determined that deploying the software of Ansys Aqwa results in a reliable basis of the research. Additionally, the software of Shipshape was used to determine the system's hydrostatic properties and Octopus Office was used to derive linear viscous roll damping coefficients for the barge. Matlab was used for post-processing and for developing model components to work around limitations of Aqwa.

Based on the results obtained from taking the steps proposed by Guachamin Acero, Li, et al. (2016), the following conclusions can be drawn.

- **Defining the system of analysis.** The deployment of the MUST to install monopiles involves three general phases: the barge mooring / lift-off, the upending / slewing and the lowering / driving phase. From a fault tree analysis was concluded that the most weather-sensitive operations are performed during the first stage. Based on a second fault tree analysis, merely focused on this stage, it can be expected that the most sensitive operation of the deployment of the MUST is the lift-off phase. With regard to the limited time available, it was decided to consider this as the phase of analysis.

- **Model development.** A constant viscous roll damping coefficient for the barge was determined by Ikeda's method for each considered loadcase. For the Heavy Lift Vessel (HLV), this was done using data derived from field tests. By experimental simulations, it was found that the roll response of the floating structures is significantly affected by the incorporation of viscous roll damping, especially for incident waves with a frequency close to the natural roll frequency. It is therefore recommended to incorporate the effect of viscous roll damping in hydrodynamic simulations based on potential theory.

- **Model development.** By experimental simulations, it was shown that the HLV responses are to a limited extent affected by hydrodynamic interaction effects with the barge. The responses of the latter structure, however, can increase or decrease significantly due to the presence of the HLV, depending on the Wave Encounter Angle (WEA).

- **Model development.** The surge and sway responses of the suspended monopile are to a very limited extent affected by multiple-pendulum effects induced by the in-line suspension of the crane hook and the MUST (i.e., can be approximated by a single pendulum system). The responses of the latter two structures can be affected by the rigging setup. Moreover, constant tension tugger lines are preferred over tugger lines with a constant length.

- **Governing parameters.** The parameters that are governing for the workability of the lift-off operation are the relative z-motion between the monopile and the fore and aft saddles on the barge, and the roll response of the barge.
- **Workability of the base case.** The weather sensitivity of the lift-off operation is strongly dependent on the WEA, and hence on the heading of the system. Furthermore, in the considered case study in which two monopiles are lifted from a barge at a typical wind farm location at the North Sea, no significant differences in workability are observed.
- **Workability of the base case.** For long waves, a small x-distance (e.g., one meter) between the trunnions and Centre Of Gravity (COG) of the monopile can suffice to avoid snap loads. However, for such waves, the operability is low (based on the other limiting parameters). Hence, the results for shorter incident waves are deemed more relevant.
- **Workability of the base case.** Longer x-distances are required to prevent snap loads in the winch cable from occurring for incident waves with a peak wave period (T_p) between [redacted] and [redacted] seconds. The largest distance is expected to be required for waves with a T_p of [redacted] seconds. This T_p is particularly limiting since it matches the natural period of the monopile pitch motion. The nature of this degree of freedom relates to inducing a slack winch cable. Considering the limiting sea states derived from the other non-barge related limiting parameters, the governing minimum x-distance is in the order of seventeen meters.
- **Workability improvement.** Introducing the hammock seafastening can result in an average workability increase of 8.3% for the optimal headings in loadcase (LC) 2. In January, this increase can reach up to 16.1%. Only a marginal workability increase is achieved for LC3, as in that case, the barge responses are more limiting.
- **Workability improvement.** Positioning a Passive Motion Compensator (PMC) in series with the winch cable can significantly reduce the required x-distance between the monopile trunnions and COG to avoid snap loads. This way, a PMC with 10% of critical damping can reduce the required winch capacity with a factor 2.3 (w.r.t. the uncompensated case).

Based on these findings, an answer to the main research question "*How can the weather window of the application of the MUST system on monopile installation by the Seaway Strashnov be increased?*" is formulated. Without adding any systems, the workability of the base case can be optimised based on the heading of the system of analysis relative to the incident waves. For both considered lift-off loadcases, the optimal WEA is between 155 and 170 degrees. Adding a hammock seafastening system equipped with the proposed quick-release support can increase the workability of the lift-off of the first monopile, but has a limited effect on the workability of the second. Finally, the required winch capacity can be reduced with the implementation of a PMC. Hence, it can be reasoned that for a constant x-distance and a constant winch capacity, the allowable sea state regarding the introduction of snap loads in the winch cable can be increased with the introduction of such a device. In Section 8.3, a proposition is made about determining the workability increase resulting from the implementation of a PMC in a subsequent iteration.

8.2 Discussion

This section discusses the system of analysis, the research method and the obtained results from a different perspective than has been done earlier in this study. While the MUST primarily has been analysed from a hydrodynamic point of view, in Section 8.2.1 some critical points in the design are discussed from a structural point of view. Subsequently, in Section 8.2.2, it is discussed how the advantage of an increased workability can be quantified in terms of cost reductions. Moreover, it is evaluated how the findings of this study can help to improve the quality of logistical analyses for the installation of offshore wind turbine substructures. Finally, in Section 8.2.3, the limitations of this study and the system of analysis are examined.

8.2.1 The MUST system from a structural point of view

From a structural perspective, the MUST principle may be challenging at three points of interest: the connection of the trunnions to the monopile, the connection of the shoe to the bottom of the monopile and the design of the suspended platform. Generally, monopiles are optimised in their design as such that their weight is kept to a minimum, which means that the wall thickness varies over the length and is kept small at sections where it is structurally allowed. Installing trunnions on the monopile, capable of carrying most of the weight, requires increasing the thickness in the area around the trunnions and therefore increasing the total weight. This technique has been applied before by Seaway 7, however, in that case the monopiles were only lifted vertically. The latter means that the load was introduced axially in the monopile, which is a less complex problem to solve than when the load is introduced transversely (M. Lenting, personal communication, 21 December 2021). Fatigue of the trunnion-monopile connection is not expected to result in difficulties, since large loads will only be present with a small number of cycles (during lifting), and high frequency loads only with a small magnitude (e.g., vibrations induced by the hammering process).

Regarding the shoe at the bottom of the monopile, attention should be paid to how the force of the winch cable introduces the load in the monopile. The connection point of the cable to the shoe should be chosen such that the moment introduced in the monopile is minimised. Moreover, the width of the shoe is important with regard to the load introduction. A wide shoe (which should be designed with the curvature of the monopile) contributes to reducing load concentrations. The in this study proposed PMC may be of assistance in limiting the introduced peak loads (see Figure 7.8). Finally, considering the design of the MUST, it is important to minimise the load paths through the platform. The concept design presented in Figure 3.2 results in a significant moment in the central beam, which may be avoided with more in-line rigging connection points (M. Lenting, personal communication, 21 December 2021). Nevertheless, overall the MUST concept seems feasible from a structural point of view.

8.2.2 The interaction between hydrodynamics and offshore logistics

This research has been performed in parallel with a study focused on the logistics of the installation of offshore wind turbine substructures. In this parallel study, stochastic logistical models are developed, which enable to estimate the advantages and limitations of various installation strategies in terms of installation time and costs. The models consider the weather dependency of the various offshore operations and, hence, enable to quantify the installation time and cost reductions as a result of a workability increase. The estimated cost reductions can be used as a foundation when a budget for investments in workability-increasing systems (e.g., the proposed hammock grillage system) is to be established.

It must be mentioned, however, that the weather-dependency in these logistical models is implemented in a simplified manner (using limits based on wind speed (V_w) and H_s or H_s - T_p -curves for an optimal WEA). In practice, the optimal WEA cannot always be maintained, as the HLV heading may have to be optimised for the direction of the current (which can deviate from the wave direction) or for practical installation reasons (e.g., the orientation in which a structure has to be installed). Moreover, in the logistical models, the continuity of the operations is based on relating the set limits to a time series of H_s, T_p and V_w. However, this principle does not take into account the whole spectrum of incident waves. The implementation of the weather-dependency of the logistical models can be made more sophisticated with the knowledge gained in this study. Workable weather windows can be generated based on the selected vessel heading and 2D-spectral weather data, as was done in the bottom plot of Figure 5.4. This way, also the in practice often limiting swell waves are included in the operability predictions. A disadvantage of this alternative is the required pre-processing work.

8.2.3 Limitations

With regard to the limited time available, assumptions and simplifications were made during this study, which may limit the validity of the obtained results. The limitations considered most prominent, and of which the reader should be aware, are listed below.

- One of the most important decisions in this study was made early in the process. It concerns the decision to appoint the lift-off phase as the expected limiting phase, based on a qualitative fault tree analysis and supported by the experiences of industry experts. Although this is still believed to be the best decision considering the information available, there is no quantitative back-up. It may be that one of the other phases (barge mooring, upending / slewing or lowering / driving) has stricter weather limitations, which would reduce the value of the proposed workability-increasing systems, due to the fact that these phases (except the barge mooring phase) are continuous operations. This means that these operations have to be performed in a single weather window. If this scenario plays out, the workability of the more-limiting phases has to be increased to regain the value of the proposed systems.

- Another limitation of this study is the case-specificness of some of the results. The governing parameters were determined based on input weather data at a specific location. At another location, with different typical weather conditions (e.g., a different most-probable peak wave period), different results may have been obtained. The same holds for the quantification of the workability increase induced by the hammock grillage, which is based on location-specific workability percentages. Furthermore, a limited effectiveness was reported for the deployment of the hammock grillage for the lift-off of the second monopile, since the barge responses are more limiting compared to the lift-off case of the first monopile. However, in this study a barge was assumed with dimensions that are just sufficient to transport two of the considered monopiles. In case a larger barge would have been selected, the hammock grillage may have been more effective for the lift-off of the second monopile, as the barge responses can be expected to be smaller.

- In this study, installing a PMC in series with the winch cable is proposed to allow for minimising the required winch capacity, by minimising the x-distance between the monopile trunnions and COG. This may have negative consequences for the subsequent phases. Once the monopile is brought to a vertical position, but before it is set down on the seabed, the reduced stability corresponding to a small x-distance in combination with wave and current-induced forces may result in significant angular rotations of the monopile around the axis through the trunnions. For larger x-distances, this is less imminent due to the larger correcting moment. Since only the in-air case is considered in this study, limited knowledge about the extent of this problem is available.

- Verification of the developed Matlab model was performed by comparing its output with the output from the Aqwa model. These models are not independent, since the Matlab model imports the crane tip motions from the Aqwa model, which means that conclusions can only be drawn to a certain extent. Similar results substantiate the correct implementation of the model components and suggest that the simplifications made in the Matlab model affect the output to a limited extent. However, no conclusions can be drawn about the models representing reality. For that, validation against model or field test results is preferred.

8.3 Recommendations for future research

Before the MUST can be considered a theoretically validated concept, more research is required. In this section, follow-up studies are proposed which are considered the most relevant.

- To confirm the validity of the MUST concept, and the results obtained in this study, it is recommended to analyse the subsequent phases of upending / slewing and lowering / driving. As stated before, the proposed workability-increasing measures provide most value if the workability of the subsequent phases is relatively high. It is expected that the upending phase will provide the largest challenges. Lowering the monopile through the splash zone, in combination with a small x-distance between the trunnions and the COG may result in snap loads. Additionally, as stated in Section 8.2.3, current and wave loads may result in large rotational angles for monopiles with reduced stability during the lowering phase. This effect may be enhanced by vortex-induced vibrations as a result of the water flow around the partly-submerged monopile, which can, in theory, result in sloshing and standing waves inside the monopile. The extent of these problems is recommended to be investigated. Furthermore, it must be mentioned that Aqwa only allows for flooding a monopile by modelling it as a Morrison element. A disadvantage of this, is that the shielding effects of the HLV on the monopile cannot be accounted for using the theory implemented in Aqwa for hydrodynamic interaction, since it only applies to panel models. An alternative could be to determine the drag coefficient of the monopile with the presence of the HLV by a CFD analysis, and provide Aqwa with this coefficient.
- A disadvantage of the adopted research approach is that validation has been performed to a limited extent. As discussed in Section 1.6, earlier studies have shown that the software packages of Ansys Aqwa and Octopus Office can provide results that are in good agreement with those from model test. Moreover, an internal study performed by Seaway 7 has shown that hull shape of the Seaway Strashnov modelled in Aqwa provides vessel responses that are in line with field tests. However, the behaviour of the monopile suspended by the MUST has not been validated. The fact that the responses provided by the Aqwa model and the Matlab model are similar is no evidence for the fact that these responses represent reality, since these models are not independent. Therefore, it is recommended to validate the simulation results against model tests. This also holds for the analysis of the subsequent phases. Especially the operation of lowering a structure through the splash zone, while simultaneously upending it, is an activity that is rarely performed and expected to be complex to model. Hence, model tests are believed to be of added value.
- In this study, a relatively small barge for its intended purpose was selected (considering the generalisability of the results), which may have contributed to the fact that the governing parameters (the relative z-motion and the barge roll response, see Section 5.3) are related to the barge motions. Hence, it is recommended to investigate the advantage of deploying a larger transportation barge in terms of workability (also considering the effectivity of the hammock grillage, see Section 8.2.3). The economic advantage can subsequently be estimated using the logistical models developed in the parallel study (see Section 8.2.2).
- Although some processes in the followed methodology are iterative, some decisions were made in a sequential order. The rigging arrangement has been optimised based on the surge and sway responses of the crane hook, the MUST and the monopile. In a later phase, the winch cable snap load analysis was performed. Hence, the influence of the rigging arrangement on the introduction of snap loads has not been investigated, which is a disadvantage of the methodology. It recommended to investigate this effect, since this may result in relatively simple and cheap system optimisations (e.g., regarding the winch capacity and workability).

- It is recommended to further investigate the implementation of a PMC in the design of the MUST system, based on the potential it has shown in this study. Before it can be practically implemented, a more detailed analysis into the effect of the PMC on the system behaviour is required. For this, two model improvements are proposed. The first is to incorporate the nonlinear effects of the spring-damper system of the PMC. This way, the decision to consider a linear system can be justified. The second is to additionally model the vessel responses (rather than importing the crane tip motions), by importing the hydrodynamic databases generated by Aqwa-Line. This way, the coupling effects between the vessel and the suspended structures can be accounted for (especially the monopile sway - vessel roll coupling is considered relevant).
- For subsequent iteration steps in follow-up studies, it is advised to consider the tension in the winch cable (regarding snap loads) as a limiting parameter while determining the workability of the system. The results of this study provide a basis to estimate values for the x-distance, which do not result in snap loads being governing for the workability, for the cases with and without the implementation of a PMC. Converting the developed Matlab model to a Frequency Domain (FD) simulation tool allows for quantifying the workability increase resulting from the implementation of a PMC. It is specifically mentioned to convert the Matlab model for this purpose, since the software of Ansys Aqwa does not allow for modelling sping-damper systems.
- In the parallel study (see Section 8.2.2), logistical models are developed, which can quantify the advantage (or disadvantage) of a workability increase (or decrease) in terms of cost reduction (or increase). It is recommended to involve these models in finding a balance between the x-distance, the required winch capacity and the resulting workability.
- It is recommended to investigate the potential of deploying the MUST in a floating monopile transportation strategy. With monopiles continuously increasing in size, it may become more economic to transport them floating rather than on a barge. The “lift-off” may in that case be less critical since no re-hit action is possible and the limiting parameters related to the barge responses are absent. Instead, other challenges will arise, e.g., providing the monopile with sufficient roll stability, removing the bottom plug and remotely connecting the grommets to the trunnions and the winch cable to the bottom plug of the monopile. Moreover, the flooding and upending of the monopile are still part of the process.
- For detailed Time Domain (TD) design analyses, it is recommended to run the analysis for multiple seeds of random sea states. Practical experience shows that the maximum system responses may vary per seed. Seaway 7 uses the rule of thumb that considering five different seeds of sea states is sufficient to identify the (close to) maximum responses.
- For hydrodynamic analyses with a lot of iterations, it is recommended to first construct a simplified model, which enables to estimate the value that is iteratively sought. The experience from this study is that this can reduce the total time of analysis significantly, as it reduces the number of time-consuming time domain analyses performed in Aqwa.

References

Albers, P. (2010). Heave compensation. In *Motion control in offshore and dredging* (chap. 9). Springer. doi: 10.1007/978-90-481-8803-1

ANSYS. (n.d.). *Ansys Aqwa - Hydrodynamics Simulation & Diffranction Analysis.* Retrieved from `https://www.ansys.com/products/structures/ansys-aqwa`

ANSYS. (2015). *Aqwa Theory Manual* (16.0 ed.). Canonsburg.

ANSYS. (2016a). *Ansys Aqwa Suite (Aqwa-Line) - Introduction to hydrodynamic analysis with Ansys Aqwa - Aqwa core programs (Presentation).*

ANSYS. (2016b). *Introduction to hydrodynamic analysis with Ansys Aqwa - Ship and pier hydrodynamic interaction (Presentation).*

Baar, J., Pijfers, J., & Van Santen, J. (1992). Hydromechanically coupled motions of a crane vessel and a transport barge. *24th Offshore Technology Conference, Houston*, 1–14.

Bakker Sliedrecht. (n.d.). *Seaway 7 - Seaway Strashnov - Heavy lifting vessel.* Retrieved from `https://www.bakkersliedrecht.com/en/references/seaway-7-seaway-strashnov-heavy-lifting-vessel/`

Barlow, E., Öztürk, D. T., Revie, M., Boulougouris, E., Day, A. H., & Akartunali, K. (2015). Exploring the impact of innovative developments to the installation process for an offshore wind farm. *Ocean Engineering*, *109*, 623–634. doi: 10.1016/j.oceaneng.2015.09.047

Bhattacharya, S., Nikitas, G., Arany, L., & Nikitas, N. (2017). Soil-Structure Interactions (SSI) for Offshore Wind Turbines. *The Institution of Engineering and Technology*, 1–23. doi: 10.1049/etr.2016.0019

Bosch, A. L., & Zwart, J. M. (2021). *Upending elongate structures offshore.* World Intellectual Property Organization. Retrieved from `https://worldwide.espacenet.com/patent/search/family/070278631/publication/WO2021175871A2?q=pn%3DWO2021175871`

Boukhanovsky, A. V., Lopatoukhin, L. J., & Soares, C. G. (2007). Spectral wave climate of the North Sea. *Applied Ocean Research*, *29*(3), 146–154. doi: 10.1016/j.apor.2007.08.004

Braun, M. (2003). On some properties of the multiple pendulum. *Archive of Applied Mechanics*, *72*, 899–910. doi: 10.1007/s00419-002-0263-4

Cannell, D., Miller, C., Riddell, S., Gonsholt, S. V., & Sannes, S. (2016). Adaptive passive heave compensation systems - The next generation. *Offshore Technology Conference Asia 2016, OTCA 2016*, 94–107. doi: 10.4043/26544-ms

Chartron, S. (2018). Evaluating and Improving Logistics Costs During Offshore Wind Turbine Construction. *Science Publishing Group*, *4*(4), 65–74. doi: 10.11648/j.ijtet.20180404.11

Chen, C. W., Chen, Y., & Cai, Q. W. (2019). Hydrodynamic-interaction analysis of an autonomous underwater hovering vehicle and ship withwave effects. *Symmetry*, *11*(10). doi: 10.3390/sym11101213

Chen, X. (2011). Offshore hydrodynamics and applications. *IES Journal Part A: Civil and Structural Engineering*, *4*(3), 124–142. doi: 10.1080/19373260.2011.595903

Cummins, W. (1962). *The impulse response function and ship motions* (Tech. Rep.). Hamburg (David Taylor Model Basin): Institut für Schiffbau der Universität Hamburg.

Dai, B., & Weustink, R. (2020). *Memorandum Vineyard WOW estimate (Seaway 7, 28-05-2020).* Zoetermeer.

DNV-OS-H101. (2011). *Marine Operations, General* (Tech. Rep.). Det Norske Veritas.

DNVGL-RP-C205. (2019). *Environmental conditions and environmental loads* (Tech. Rep.). Det Norske Veritas.

DNVGL-RP-N103. (2019). *Modelling and analysis of marine operations* (Tech. Rep.). Det Norske Veritas.

DNVGL-ST-N001. (2020). *Marine operations and marine warranty* (Tech. Rep.). Det Norske Veritas.

Drago, M., Del Guzzo, A., Vitali, L., & Bruschi, R. (2017). Weather stand-by assessment in offshore operations using motion limit criteria. *Proceedings of the 27th International Ocean and Polar Engineering Conference*, 494–501.

Driscoll, F. R., Buckham, B., & Nahon, M. (2000). Numerical optimization of a cage-mounted passive heave compensation system. *OCEANS 2000 MTS/IEEE Conference and Exhibition*, *2*, 1121–1127. doi: 10.1109/OCEANS.2000.881753

Eijssen, M. (2011). Offshore wind farm construction; Easier, safer and more cost effective. *Proceedings of the ASME 2011 30th International Conference on Ocean, Offshore and Arctic Engineering (OMAE2011)*, 701–709. doi: 10.1115/OMAE2011-49847

Falzarano, J., Somayajula, A., & Seah, R. (2015). An overview of the prediction methods for roll damping of ships. *Ocean Systems Engineering*, *5*(2), 55–76. doi: 10.12989/ose.2015.5.2.055

Fernández-Guillamón, A., Das, K., Cutululis, N. A., & Molina-García, A. (2019). Offshore wind power integration into future power systems: Overview and trends. *Journal of Marine Science and Engineering*, *7*(11). doi: 10.3390/jmse7110399

Gintautas, T., & Sørensen, J. D. (2016). Evaluating a novel approach to reliability decision support for offshore wind turbine installation. *Progress in Renewable Energies Offshore: proceedings of RENEW2016, 2nd international conference on renewable energies offshore*, 733–740. doi: 10.1201/9781315229256-86

Gintautas, T., & Sørensen, J. D. (2017a). Improved methodology of weather window prediction for offshore operations based on probabilities of operation failure. *Journal of Marine Science and Engineering*, *5*(2), 1–23. doi: 10.3390/jmse5020020

Gintautas, T., & Sørensen, J. D. (2017b). Influence of met-ocean condition forecasting uncertainties on weather window predictions for offshore operations. *Proceedings of the 27th International Ocean and Polar Engineering Conference*, 186–193.

Gintautas, T., Sørensen, J. D., & Vatne, S. R. (2016). Towards a risk-based decision support for offshore wind turbine installation and operation & maintenance. *Energy Procedia*, *94*, 207–217. doi: 10.1016/j.egypro.2016.09.225

Google. (n.d.). *Google Earth view North Sea.* Retrieved from `https://earth.google.com/web/@52.57672095,3.21373846,28.19694184a,252473.98588479d,35y,-0.00000001h,2.92460187t,0r`

Gordon, R. B., Grytøyr, G., & Dhaigude, M. (2013). Modeling suction pile lowering through the splash zone. *Proceedings of the ASME 2013 32nd International Conference on Ocean, Offshore and Arctic Engineering (OMAE2013)*, *1*, 1–9.

Gourlay, T., von Graefe, A., Shigunov, V., & Lataire, E. (2015). Comparison of Aqwa, GL Rankine, MOSES, OCTOPUS, PDStrip and WAMIT with model test results for cargo ship wave-induced motions in shallow water. *Proceedings of the ASME 2015 34th International Conference on Ocean, Offshore and Arctic Engineering (OMAE2015).* doi: 10.1115/omae2015-41691

Guachamin Acero, W., Gao, Z., & Moan, T. (2016). Assessment of the dynamic responses and allowable sea states for a novel offshore wind turbine installation concept based on the inverted pendulum principle. *Energy Procedia*, *94*, 61–71. doi: 10.1016/j.egypro.2016.09.198

Guachamin Acero, W., Li, L., Gao, Z., & Moan, T. (2016). Methodology for assessment of the operational limits and operability of marine operations. *Ocean Engineering*, *125*, 308–327. doi: 10.1016/j.oceaneng.2016.08.015

Hatecke, H., Krüger, S., Christiansen, J., & Vorhölter, H. (2014). A fast sea-keeping simulation method for heavy-lift operations based on multi-body system dynamics. *Proceedings of the ASME 2014 33rd International Conference on Ocean, Offshore and Arctic Engineering (OMAE2014)*, 1–10. doi: 10.1115/OMAE2014-23456

Himeno, Y. (1981). *Prediction of ship roll damping - state of the art* (Tech. Rep. No. 239). University of Michigan, Department of Naval Architecture and Marine Engineering.

Holthuijsen, L. H. (2007). *Waves in oceanic and coastal waters* (1st ed.). New York: Cambridge

University Press.

Hsu, W. T., Thiagarajan, K. P., Hall, M., MaCnicoll, M., & Akers, R. (2014). Snap loads on mooring lines of a floating offshore wind turbine structure. *Proceedings of the ASME 2014 33th International Conference on Ocean, Offshore and Arctic Engineering (OMAE2014)*. doi: 10.1115/OMAE2014-23587

Ikeda, Y., Himeno, Y., & Tanaka, N. (1978). Components of roll damping of ship at forward speed. *Journal of the Society of Naval Architects of Japan*, *143*, 1–14.

IQIP. (n.d.). *Increase your weather window offshore with our Maxine.* Retrieved from `https://www.ihciqip.com/en/products/lifting-equipment/maxine`

IRENA. (2019). *Future of wind - Deployment, investment, technology, grid integration and socio-economic aspects.* International Renewable Energy Agency.

IX Wind. (2021). *Sif Offshore Foundations.* Retrieved from `https://www.ixwind.com/services/sifoffshorefoundations/`

Jeong, D.-H., Roh, M. I., & Ham, S. H. (2016). Lifting simulation of an offshore supply vessel considering various operating conditions. *Advances in Mechanical Engineering*, *8*(6), 1–13. doi: 10.1177/1687814016654633

Jianan, X., Shanglong, Z., Yong, Z., & Jing, L. (2019). Research on passive heave compensation system for synchronous lifting and salvage of shipwreck. *Proceedings of 2019 IEEE International Conference on Mechatronics and Automation, ICMA 2019*, 2150–2156. doi: 10.1109/ICMA.2019.8816216

Journée, J., & Adegeest, L. (2012). *Theoretical Manual Octopus* (Tech. Rep.). ABB.

Journée, J., Massie, W., & Huijsmans, R. (2015). *Offshore Hydromechanics* (3rd ed.) (No. January). Delft.

Kanotra, R., Aboumalwa, M., Joe-Joe, C., Nair, S., & Koottungal, V. (2012). Dynamics of heavy deck lift-off from transportation barge. *Proceedings of the ASME 2012 31st International Conference on Ocean, Offshore and Arctic Engineering (OMAE2012)*, 1–9. doi: 10.1115/OMAE2012-83458

Kato, H. (1957). On the frictional resistance to the rolling of ships. *Journal of Zosen Kiokai*(102), 115–122. doi: 10.2534/jjasnaoe1952.1957.102{_}115

Keprate, A. (2015). Impact of passive heave compensator on offshore lifting. *Journal of Shipping and Ocean Engineering*, *5*, 166–180. doi: 10.17265/2159-5879/2015.04.003

Korpus, R. A., & Falzarano, J. M. (1997). Prediction of viscous ship roll damping by unsteady Navier-Stokes techniques. *Journal of Offshore Mechanics and Arctic Engineering*, *119*(2), 108–113. doi: 10.1115/1.2829050

Lacal-Arántegui, R., & Jäger-Waldau, A. (2018). Photovoltaics and wind status in the European Union after the Paris Agreement. *Renewable and Sustainable Energy Reviews*, *81*, 2460–2471. doi: 10.1016/j.rser.2017.06.052

Lacal-Arántegui, R., Yusta, J. M., & Domínguez-Navarro, J. A. (2018). Offshore wind installation: Analysing the evidence behind improvements in installation time. *Renewable and Sustainable Energy Reviews*, *92*, 133–145. doi: 10.1016/j.rser.2018.04.044

Lee, J., Feng, Z., Dutton, A., Backwell, B., Qiao, L., Lim, S., … Liang, W. (2020). *Global Offshore Wind Report 2020* (Tech. Rep.). Brussels: Global Wind Energy Council (GWEC).

Li, L. (2016). *Dynamic Analysis of the Installation of Monopiles for Offshore Wind Turbines* (Unpublished doctoral dissertation). Norwegian University of Science and Technology, Trondheim.

Li, L., Gao, Z., & Moan, T. (2013). Numerical simulations for installation of offshore wind turbine monopiles using floating vessels. *Proceedings of the ASME 32th International Conference on Ocean, Offshore and Arctic Engineering (OMAE2013)*, 1–11. doi: 10.1115/OMAE2013-11200

Li, L., Gao, Z., & Moan, T. (2015a). Comparative study of lifting operations of offshore wind turbine monopile and jacket substructures considering vessel shielding effects. *Proceedings* *of the 25th International Ocean and Polar Engineering Conference*, 1290–1298.

Li, L., Gao, Z., & Moan, T. (2015b). Response analysis of a nonstationary lowering operation for an offshore wind turbine monopile substructure. *Journal of Offshore Mechanics and Arctic Engineering*, *137*(5), 1–15. doi: 10.1115/1.4030871

Li, L., Gao, Z., & Moan, T. (2016). Operability analysis of monopile lowering operation using different numerical approaches. *International Journal of Offshore and Polar Engineering*, *26*(2), 88–99. doi: 10.17736/ijope.2016.jdsr04

Li, L., Gao, Z., Moan, T., & Ormberg, H. (2014). Analysis of lifting operation of a monopile for an offshore wind turbine considering vessel shielding effects. *Marine Structures*, *39*, 287–314. doi: 10.1016/j.marstruc.2014.07.009

Li, L., Karatas, I. G., Zhu, X., & Ong, M. C. (2020). Dynamic analysis of lift-off operation of a subsea spool from a barge using different fender models. *Proceedings of the International Offshore and Polar Engineering Conference*, 944–953.

Malenica, S., Orozco, J. M., & Chen, X. B. (2005). Some aspects of seakeeping of the floating body with attached pendulum.

MetoceanView. (2016). *Hindcast North Sea wave.* Retrieved from `https://app.metoceanview.com/hindcast-squared/#/`

Naaijen, P. (2018). *Course notes - Motions and loading of structures in waves* (1st ed.). Delft: Delft University of Technology.

Ochi, M. K., & Shin, Y. S. (1988). Wind turbulent spectra for design consideration of offshore structures. *Proceedings of the Annual Offshore Technology Conference*, 461–467. doi: 10.4043/5736-ms

Offshore WIND. (n.d.). *Seaway Yudin - Seaway Heavy Lifting.* Retrieved from `https://www.offshorewind.biz/vessels/seaway-yudin/`

Oh, S., Utsunomiya, T., & Saiki, K. (2018). On-site measurement and numerical modelling of a lifting operation for caissons using floating crane. *Proceedings of the ASME 2018 37th International Conference on Ocean, Offshore and Arctic Engineering (OMAE2018)*, *6*, 1–6. doi: 10.1115/OMAE2018-77132

Peña, B., & Mcdougall, A. (2016). An investigation into the limitations of the panel method and the gap effect for a fixed and a floating structure subject to waves. *Proceedings of the ASME 2011 35th International Conference on Ocean, Offshore and Arctic Engineering (OMAE2016)*, *7*, 1–13.

Pierson, W. J., Neumann, G., & James, R. W. (1955). *Practical methods for observing and forecasting ocean waves by means of wave spectra and statistics* (1st ed.). Washington.

Pinkster, J. (1995). Hydrodynamic interaction effects in waves. *Proceedings of the Fifth (1995) International Offshore and Polar Engineering Conference*, *3*, 1–6.

Sánchez, W. H. C., Neto, A. B., & Fortaleza, E. L. F. (2020). Effects of nonlinear friction of passive heave compensator on drilling operation Part I: Modeling and analysis. *Ocean Engineering*, *213*, 1–13. Retrieved from `https://doi.org/10.1016/j.oceaneng.2020.107743` doi: 10.1016/j.oceaneng.2020.107743

Sarkar, A., & Gudmestad, O. T. (2013). Study on a new method for installing a monopile and a fully integrated offshore wind turbine structure. *Marine Structures*, *33*, 160–187. doi: 10.1016/j.marstruc.2013.06.001

Seaway 7. (n.d.-a). *About us.* Retrieved from `https://www.seaway7.com/about-us/`

Seaway 7. (n.d.-b). *Our Fleet.* Retrieved from `https://www.seaway7.com/our-fleet/`

Seaway 7. (n.d.-c). *Our services.* Retrieved from `https://www.seaway7.com/`

Seaway 7. (2016). *Memorandum Seaway Strashnov motion study for monopile installation on anchoring* (Tech. Rep.). Zoetermeer.

Seaway 7. (2020a). *Seaway Strashnov - Vessel Info* (Tech. Rep.). Retrieved from `https://www.subsea7.com/content/dam/subsea7-corporate2018/Datasheets/Vessel/Renewables/Seaway_Strashnov.pdf.downloadasset.pdf`

Seaway 7. (2020b). *Seaway Yudin - Vessel Info* (Tech. Rep.). Retrieved from `https://www.subsea7.com/content/dam/subsea7-corporate2018/Datasheets/Vessel/Renewables/Seaway_Yudin.pdf.downloadasset.pdf`

Senan, N. A. F. (2012). A brief introduction to using ode45 in Matlab. *University of California at Berkeley*, 1–6.

Silver, A., Hughes, M., Conrad, R., Lee, S., Klamo, J., & Park, J. (2008). Evaluation of multi-vessel ship motion prediction codes. *Naval surface warfare center*.

Solaas, F., Sandvik, P. C., Pâkozdi, C., Kendon, T., Larsen, K., & Myhre, E. (2017). Dynamic forces and limiting sea states for installation of GRP protection covers. *Proceedings of the ASME 2017 36th International Conference on Ocean, Offshore and Arctic Engineering (OMAE2017)*, 1–10.

Subsea 7. (2017, 3). *Subsea 7 announces acquisition of Seaway Heavy Lifting.* Luxembourg. Retrieved from `https://www.subsea7.com/en/media/company-news.html?tab1=archive&page=3`

Subsea 7. (2018, 4). *Subsea 7 announces completion of Siem Offshore Contractors acquisition.* Luxembourg. Retrieved from `https://www.subsea7.com/en/media/company-news.html?tab1=2018&page=4`

Thurston, K. W., Swanson, R. C., & Kopp, F. (2011). Statistical characterization of slacking and snap loading during offshore lifting and lowering in a wave environment. *Proceedings of the ASME 2011 30th International Conference on Ocean, Offshore and Arctic Engineering (OMAE2011)*, 1–9.

TWD. (n.d.). *Innovation - Hammock Seafastening.* Retrieved from `https://twd.nl/innovation/innovation-hammock-seafastening/`

van der Heiden, A. J. (2019). Vessel and cargo motions - A frequency domain method to study combined vessel and cargo responses. *Delft University of Technology (Master Thesis)*, 1–160.

Van Dorp, R., Moscoso, N., Bielefeld, M., & Verbeek, G. (2019). Prediction and monitoring of installation of offshore foundation monopiles for windfarms. *Proceedings of the Annual Offshore Technology Conference*. doi: 10.4043/29400-ms

Vorhölter, H., Hatecke, H., & Feder, D.-f. (2015). Design study of floating crane vessels for lifting operations in the offshore wind industry. *International Marine Design Conference*, *2*, 273–285.

Vuik, C., Vermolen, F., Gijzen, M. v., & Vuik, M. (2015). Trapezoidal rule. In *Numerical methods for ordinary differential equations* (2nd ed., chap. 5.3.3). Delft Academic Press.

Welch, P. D. (1967). The use of Fast Fourier Transform for the estimation of power spectra. *IEEE Transactions on audio and electroacoustics*, *15*(2), 70–73.

White, F. M. (2016). *Fluid mechanics* (8th ed.). McGraw-Hill Education.

Zhao, W., Efthymiou, M., McPhail, F., & Wille, S. (2016). Nonlinear roll damping of a barge with and without liquid cargo in spherical tanks. *Journal of Ocean Engineering and Science*, *1*(1), 84–91. doi: 10.1016/j.joes.2015.12.002

Zhu, H., Li, L., & Ong, M. C. (2017). Study of lifting operation of a tripod foundation for offshore wind turbine. *IOP Conference Series: Materials Science and Engineering*, *276*(1), 1–19. doi: 10.1088/1757-899X/276/1/012012

Appendices

A | Theory floating body dynamics

As stated in Section 1.4, to research the workability of the newly developed monopile installation method, the software of Ansys Aqwa is used. To use such hydrodynamics simulation software constructively, the theory behind the software should be known and understood. This chapter discusses the main theoretical concepts behind the hydrodynamic simulations performed in Aqwa.

A.1 Rigid body kinematics

In order to describe the motions of rigid bodies, resulting from external forces and moments, pre-defined coordinate systems are required. This section discusses the conventional coordinate systems used to express ship motions. In the analysis of this thesis, five rigid bodies are considered: the installation vessel, the crane hook, the MUST, the monopile to be installed and the transportation barge. An individual body able to move freely in a three-dimensional space has six degrees of freedom, three of which are translations in the directions of three orthogonal axes and the other three represent rotations around those axes, as listed in Figure A.1. For floating body motions, each of these six degrees of freedom has been given a specific name and symbol, which are also listed. Additionally, Figure A.1 displays the corresponding local coordinate system of a floating body. However, floating body motions are normally expressed with respect to a stationary global axis system (which is not displayed in the considered figure).

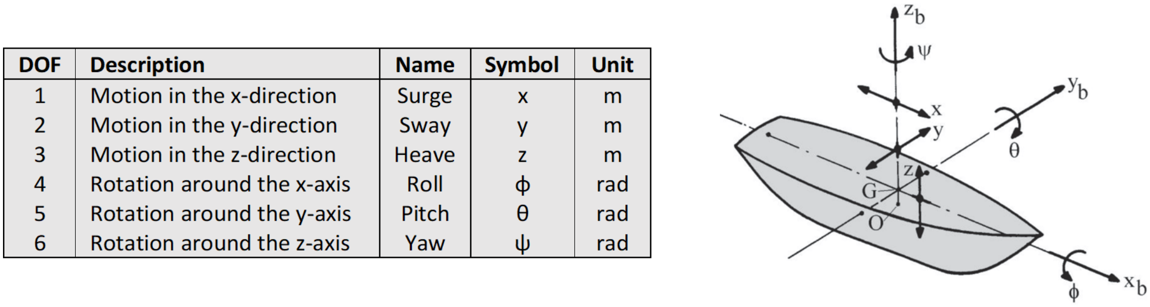

DOF	Description	Name	Symbol	Unit
1	Motion in the x-direction	Surge	x	m
2	Motion in the y-direction	Sway	y	m
3	Motion in the z-direction	Heave	z	m
4	Rotation around the x-axis	Roll	ϕ	rad
5	Rotation around the y-axis	Pitch	θ	rad
6	Rotation around the z-axis	Yaw	ψ	rad

Figure A.1: Definition of the local coordinate system of rigid bodies and the corresponding six degrees of freedom (image from (Journée et al., 2015))

To describe the location of a point in the global coordinate system, Equation A.1 can be applied. This equation describes the coordinates of a point of the rigid body, in the global coordinate system ($[X_P; Y_P; Z_P]$), in terms of the location of the Centre Of Gravity (COG) of the body in the global coordinate system ($[X_G; Y_G; Z_G]$), an Euler rotation matrix ($\mathbf{E}$) and the location of the point in the local coordinate system ($[x; y; z]$).

$$\begin{bmatrix} X_P \\ Y_P \\ Z_P \end{bmatrix} = \begin{bmatrix} X_G \\ Y_G \\ Z_G \end{bmatrix} + \mathbf{E} \cdot \begin{bmatrix} x \\ y \\ z \end{bmatrix} \tag{A.1}$$

In addition to the global and the local coordinate systems, an intermediate coordinate system is defined. The latter system moves with the translations of the body, as its origin stays at the COG, but its axes remain parallel to the corresponding axes of the global coordinate system. ANSYS (2015) defines the Euler rotation matrix as a sequence of three rotations, which can be calculated by multiplying the rotation matrices for the rotations around the intermediate X-, Y and Z-axes (see Equations A.2a to A.2c), in that specific order ($\mathbf{E} = \mathbf{E}_z\mathbf{E}_y\mathbf{E}_x$). When small rotational motions are assumed, the sine- and cosine-components in the $\mathbf{E}$-matrix can be linearised by applying Taylor expansions: $\sin(\alpha) \approx \alpha$ and $\cos(\alpha) \approx 1$. The resulting Euler rotation matrix is given in Equation A.3.

$$\mathbf{E}_x = \begin{bmatrix} 1 & 0 & 0 \\ 0 & cos(\phi) & -sin(\phi) \\ 0 & sin(\phi) & cos(\phi) \end{bmatrix} \tag{A.2a}$$

$$\mathbf{E}_z = \begin{bmatrix} cos(\psi) & -sin(\psi) & 0 \\ sin(\psi) & cos(\psi) & 0 \\ 0 & 0 & 1 \end{bmatrix} \tag{A.2c}$$

$$\mathbf{E}_y = \begin{bmatrix} cos(\theta) & 0 & sin(\theta) \\ 0 & 1 & 0 \\ -sin(\theta) & 0 & cos(\theta) \end{bmatrix} \tag{A.2b}$$

$$\mathbf{E} = \begin{bmatrix} 1 & -\psi & \theta \\ \psi & 1 & -\phi \\ -\theta & \phi & 1 \end{bmatrix} \tag{A.3}$$

A.2 Environmental loading

This section describes the theory behind determining the environmental loads interacting with the system of analysis. First, in Section A.2.1, the theory implemented in Ansys Aqwa to describe the kinematics of ocean waves is introduced. Subsequently, in Section A.2.2, the calculation principles used to determine wave loads, based on the kinematic wave description, are introduced. Next, in Section A.2.3, the principles behind calculating wind and current loads are discussed. Moreover, it is explained why wind and current loads are not considered in this thesis.

A.2.1 Ocean wave description

Offshore wave conditions are a complex system of interacting waves, coming from different directions and with different frequencies. To be able to model these waves with reduced complexity, a variety of simplifying theories have been presented in the literature. Aqwa applies numerous of these theories in its models (ANSYS, 2015).

The most straightforward description of an ocean wave is the linear regular wave, which is mathematically expressed in equation Equation A.4. This equation gives the surface elevation for a (unidirectional) wave with a certain frequency, moving in x-direction. However, most of the time the ocean surface cannot be represented by a sinusoidal wave with a single frequency. The “irregular waves” that are usually observed, can be seen as a superposition of regular waves with different frequencies and phases. This is mathematically expressed (for unidirectional waves) by Equation A.5 (Journée et al., 2015).

$$\zeta(x,t) = \zeta_a \cdot cos(kx - \omega t) \tag{A.4}$$

$$\zeta(x,t) = \sum_{n=1}^{N} \zeta_{a_n} \cdot cos(k_n x - \omega_n t + \alpha_n) \tag{A.5}$$

A visual representation of the principle of Equation A.5 is provided by Figure A.2a, in which two different unidirectional regular waves are added to form a more irregular-looking wave pattern. This superposition is repeated for many more regular wave components, with varying directions, to describe an irregular sea state (see Figure A.2b). This process is mathematically described by Equation A.6 (Holthuijsen, 2007).

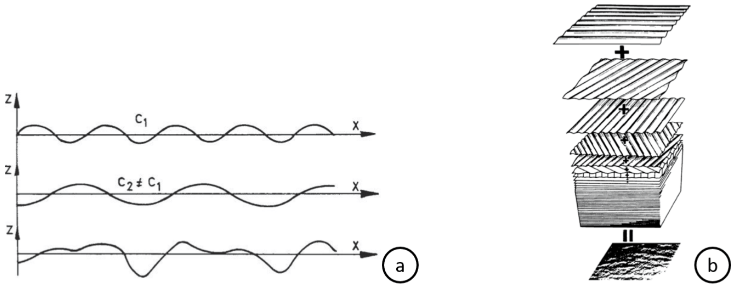

Figure A.2: (a) Superposition of two unidirectional regular waves (Journée et al., 2015); (b) Superposition of many regular waves with varying directions (Pierson et al., 1955)

$$\zeta(x,y,t)=\sum_{n=1}^{N}\sum_{m=1}^{M}\zeta_{a_{n,m}}\cdot cos(k_{n,m}\cdot x\cdot cos(\theta_m)+k_{n,m}\cdot y\cdot sin(\theta_m)-\omega_{n,m}\cdot t+\alpha_{n,m}) \qquad \text{(A.6)}$$

In this equation, $\zeta(x,y,t)$ is the wave elevation as a function of the x and y-coordinate and time, ζ_a is the wave amplitude, k is the wave number ($k=\frac{2\pi}{L}$, with L as the wavelength), x is the position in x-direction, y is the position in y-direction, θ is the direction of wave propagation relative to the positive x-axis, ω is the wave frequency, t is the time, α is the random phase angle, N is the number of wave components and M is the number of wave directions.

Irregular sea states can be represented by a so-called (unidirectional) “wave energy spectrum” ($S_\zeta(\omega_n)$), which can be defined as the expressions of Equation A.7. (Journée et al., 2015). In this equation, $\Delta\omega$ describes a constant difference between two successive frequencies, as is visualised in Figure A.3. If the value for $\Delta\omega$ approaches zero, the definition can be written in the form of the right part of Equation A.7. Wave energy spectra can be derived from time-domain measurements of irregular waves. By performing a Fourier series analysis, the irregular wave record can be expressed in terms of a summation of regular wave components. These components each have a single amplitude, frequency and phase. For each frequency, the value for $S_\zeta(\omega)$ can be calculated and plotted, to construct the wave energy spectrum (see Figure A.3b).

$$S_\zeta(\omega_n)\cdot\Delta\omega=\sum_{\omega_n}^{\omega_n+\Delta\omega}\frac{1}{2}\zeta_{a_n}^2(\omega) \qquad \xrightarrow{\Delta\omega\rightarrow 0} \qquad S_\zeta(\omega_n)\cdot d\omega=\frac{1}{2}\zeta_{a_n}^2(\omega) \qquad \text{(A.7)}$$

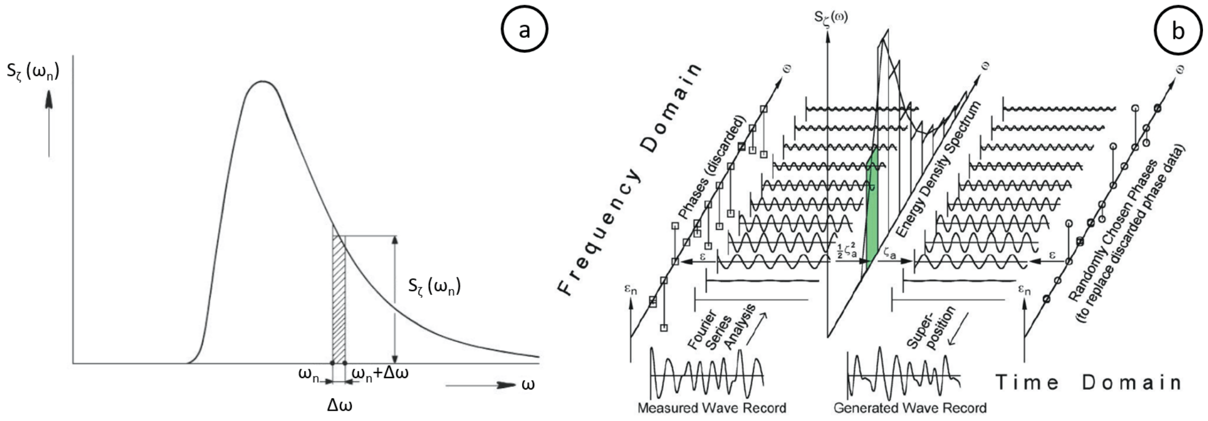

Figure A.3: (a) Definition of spectral density; (b) Relationship between measured wave record in time domain and an energy density spectrum in frequency domain (Journée et al., 2015)

Once the wave energy spectrum is constructed, the values in the curve can be described in terms of a fitted equation. For certain regions, standard wave spectra have been developed by performing extensive measurements. An example is the Joint North Sea Wave Project (JONSWAP) spectrum, which was developed for the North Sea. A commonly used parameter corresponding to wave spectra is the “significant wave height” (H_s), which is defined as “the average wave height of the highest one-third of the waves in the record” (Journée et al., 2015). Apart from considering the wave heights of individual waves in a record, the value for the significant wave height can also be calculated based on wave spectra, as expressed by Equation A.8. Furthermore, during offshore operations it is often preferable to have an indication of the largest wave height that could be encountered during a storm. Considering a maximum wave height probability of exceedance of once per thousand waves, and assuming a Rayleigh distribution, the maximum wave height can be calculated using Equation A.9.

$$H_s = 4 \cdot \sqrt{m_{0\zeta}} \qquad \text{in which} \qquad m_{n\zeta} = \int_0^\infty \omega^n \cdot S_\zeta(\omega) \cdot d\omega \tag{A.8}$$

$$H_{max} = 1.86 \cdot H_s \tag{A.9}$$

To generate a time record of the surface elevation, based on an energy density spectrum, the superposition principle of Equation A.5 can be applied (see Figure A.3b). This will probably not result in the same wave record as was originally used to develop the spectrum, but it will provide a record with the same statistical properties. Normally, consecutive values with equal intervals are chosen for ω_n. The wave amplitudes can next be calculated by rewriting Equation A.7 to Equation A.10. The value for the wave number (k_n) should be found by applying a suitable dispersion relationship (Journée et al., 2015).

$$\zeta_{a_n} = \sqrt{2 \cdot S_\zeta(\omega_n) \cdot \Delta\omega} \tag{A.10}$$

In addition to the discussed unidirectional wave spectra, wave conditions can also be represented by two-dimensional wave spectra. In such spectra, the wave energy density is not only related to the wave frequency, but also to the direction of wave propagation. Figure A.4 displays such a two-dimensional spectrum, in which two combinations of wave frequency and direction are indicated corresponding to the highest energy density.

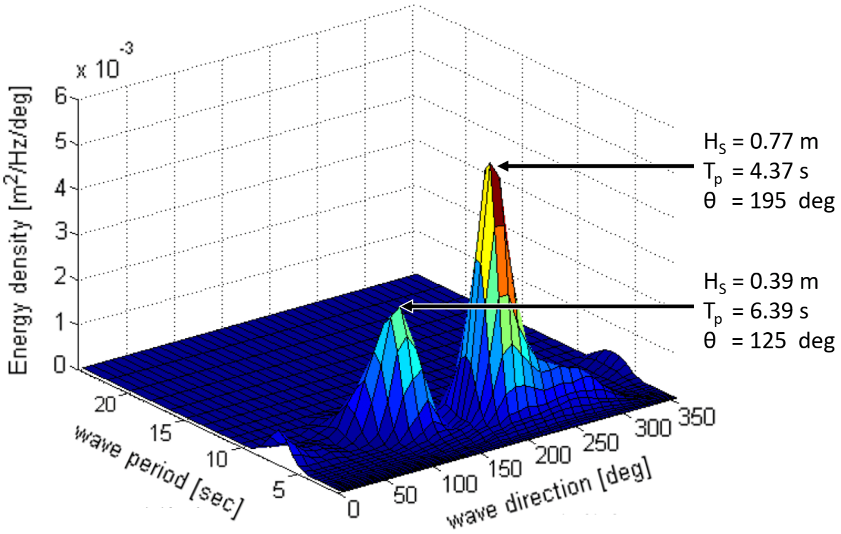

Figure A.4: Two-dimensional wave spectrum with two peaks

The required input values for Aqwa to generate a sea state which can be described by a two-dimensional spectrum are: the input parameters to describe a one-dimensional spectrum (e.g., a JONSWAP-spectrum, $S(\omega)$), a mean direction (which holds for any frequency, $\overline{\theta}(\omega)$) and a function to describe the spreading of the wave directions around the mean $G(\omega, \theta)$. The description of the two-dimensional spectrum is mathematically expressed in Equation A.11a, and the spreading function in Equation A.11b. In the latter equation, n represents the power of the wave spreading and C is a parameter that ensures that the total energy in the spectrum remains constant, as expressed in Equation A.12.

$$S(\omega,\theta) = G(\omega,\theta)\cdot S(\omega) \tag{A.11a}$$

$$G(\omega,\theta) = C\cdot cos^n\left(\frac{\pi}{\Delta\theta}\cdot(\theta-\overline{\theta})\right) \quad \text{for} \quad -\frac{\Delta\theta}{2}\leq\theta-\overline{\theta}\leq\frac{\Delta\theta}{2} \tag{A.11b}$$

$$\int_{-\frac{\Delta\theta}{2}}^{\frac{\Delta\theta}{2}} G(\omega,\theta) = 1 \tag{A.12}$$

A.2.2 Hydrodynamic loading

For the hydrodynamic analysis of offshore operations, normally three types of loads are of concern: wave excitation, radiation and drag loads (ANSYS, 2015). First order wave excitation loads comprise two components: the Froude-Krylov force (also known as the first order incident wave force) and the diffraction force. The Froude-Krylov force is calculated by integrating the fluid pressure of the undisturbed incident wave over the wetted body surface, while the diffraction force is a correction on the Froude-Krylov force for the disturbance of the incident wave by the floating body (Journée et al., 2015). Radiation forces are generated due to the motions of the body of analysis (with the assumption of the surrounding water to be still), and drag loads are present due to the viscosity of the water around the body.

To determine the wave excitation and radiation forces, fluid potential theories are normally used. A potential flow function can be defined as a "function whose derivative in any direction equals the flow velocity in that direction" (Naaijen, 2018). The use of linear potential theory encompasses the following assumptions (ANSYS, 2015):

- The forward velocity of the body of analysis is (almost) zero
- The fluid is inviscid and incompressible
- The fluid flow is irrotational
- The incident waves have a small amplitude-to-length ratio
- The resulting body motions are of first order and therefore described by a small amplitude

Apart from determining velocities, potential functions can also be used to determine pressures. This is done by linearising the Bernoulli equation, resulting in Equation A.13a (Journée et al., 2015). Since the linear fluid velocity potential includes the incident undisturbed wave potential, the diffraction potential and the radiation potential, the linearised Bernoulli equation can be rewritten as Equation A.13b. In both equations, the hydrostatic part of the pressure is included by the component of $\rho g z$. If a sinusoidal wave pattern is assumed, and the requirements of the Laplace equation, the seabed boundary condition and the free surface boundary condition are considered, the incident undisturbed wave potential can be written as Equation A.14 (Journée et al., 2015). The expressions for the diffraction potential and the radiation potential are not considered here.

$$p = -\rho\cdot\frac{\partial\Phi}{\partial t} - \rho g z \tag{A.13a}$$

$$= -\rho\left(\frac{\partial\Phi_w}{\partial t}+\frac{\partial\Phi_d}{\partial t}+\frac{\partial\Phi_r}{\partial t}\right) - \rho g z \tag{A.13b}$$

$$\Phi_w = \frac{\zeta_a g}{\omega}\cdot\frac{cosh(k(h+z))}{cosh(kh)}\cdot sin(kx-\omega t) \tag{A.14}$$

In these equations, p is the pressure in the fluid, ρ is the fluid density, Φ is the fluid velocity potential, Φ_w is the incident undisturbed wave potential, Φ_d is the diffraction potential, Φ_r is the radiation potential, g is the acceleration of gravity, z is the distance in vertical direction (positive upward) and h is the water depth.

Hydrodynamic interaction

Hydrodynamic interaction refers to the interaction between the (potential) flow fields of multiple floating bodies (ANSYS, 2015). A part of this interaction is described by the superposition of the radiation potentials of the considered bodies. Additionally, shielding effects are included in the concept. Two important factors that influence the degree of interaction are the distance between the bodies and their relative sizes. Due to hydrodynamic interaction, the body responses to waves (expressed in terms of, e.g., Response Amplitude Operators (RAOs)) differ from a case in which a single body would be considered. The RAOs depend on the radiation and diffraction potentials, which change as a result of the presence of other floating bodies. Equation A.15 mathematically expresses the flow potential for a certain body, as a function of the motions of the other present structures (ANSYS, 2015; C. W. Chen, Chen, & Cai, 2019). In this equation, $\varphi_{r_{j,m}}$ describes the radiation potential induced by the j$^{\text{th}}$ degree of freedom of the m$^{\text{th}}$ structure (assuming that the other structures remain stationary). For each structure, the amplitudes of the degrees of freedom are described by $x_{j,m}$. Hence, a superposition of the radiation potentials induced by all degrees of freedom of all present structures can be recognised in this equation.

$$\Phi_{Multi\_body} = \Phi_w + \Phi_d + \sum_{m=1}^{M} \sum_{j=1}^{6} \varphi_{r_{j,m}} \cdot x_{j,m} \tag{A.15}$$

Pressure integration

By integrating the pressures, that can be calculated using Equation A.13b, over the wetted surface of the body under analysis, Aqwa determines the forces (F) acting on the body (see Equation A.16a). Equation A.16b is the result of substituting Equation A.13b into Equation A.16a. Since usually no analytical function is given for the shape of the hull, it is numerically described by relatively small body surface elements. The vector "n" represents the outward normal vector on such an element, with surface area dS. A similar principle can be applied to calculating the moments (M) working on the body of analysis, as has been done for Equation A.17a and A.17b. The added component here is the vector "r", describing the location of the surface element dS on the hull. To subsequently calculate the total present forces and moments, a summation is performed of all the forces and moments acting on the individual body surface elements.

$$\vec{F} = -\int\int_S p \cdot \vec{n} \cdot dS \tag{A.16a}$$

$$= \rho \int\int_S \left(\frac{\partial \Phi_w}{\partial t} + \frac{\partial \Phi_d}{\partial t} + \frac{\partial \Phi_r}{\partial t} \right) \vec{n} \cdot dS \tag{A.16b}$$

$$\vec{M} = -\int\int_S p \cdot (\vec{r} \times \vec{n}) \cdot dS \tag{A.17a}$$

$$= \rho \int\int_S \left(\frac{\partial \Phi_w}{\partial t} + \frac{\partial \Phi_d}{\partial t} + \frac{\partial \Phi_r}{\partial t} \right) (\vec{r} \times \vec{n}) \cdot dS \tag{A.17b}$$

A.2.3 Current and wind loads

Apart from inducing loads by waves, the water surrounding a floating object can also exert forces on that object due to current. To calculate the forces resulting from current, normally a horizontal flow is assumed, of which the velocity varies over the water depth (e.g., for the change in tidal current speed over the water depth generally a “1/7 power decay” is applied (ANSYS, 2015)). The current velocity over time is normally assumed to be constant.

Wind influences offshore operations both directly and indirectly. Air flow above the waterline generates wind-induces waves, influencing the system of analysis indirectly, but it also induces wind loads on the part of the structure above the waterline, influencing the system directly. To describe the air flow, it is assumed that its direction is always in the horizontal plane although the magnitude of the velocity can alter over the height. An example wind profile description, which can be implemented in Aqwa, is provided by the research of Ochi and Shin (1988). They describe the mean wind velocity as a function of the height above the mean water line, depending of the ten-meter mean wind velocity (ANSYS, 2015; Ochi & Shin, 1988). Additionally, Ochi and Shin develop a (unidirectional) wind speed spectral density description, enabling to describe the wind velocity as a function of time.

Accurately determining current and wind loads on floating objects is a complex effort. However, if the Reynolds number is relatively high, these loads can be approximated by Equation A.18. In this equation, u represents the relative current or wind velocity, β the relative heading angle between the structure and the current or wind and $C_d(\beta)$ the current or wind drag coefficient as a function of the relative heading angle. Moreover, subscripts j=1 to j=3 indicate the drag force components in the vessel's local x,y and z-direction, whereas subscripts j=4 to j=6 represent the moment components due to drag forces around the vessel's local x,y and z-axes.

$$F_j(\beta) = C_{d_j}(\beta)|u|\,u \quad \text{with j=1,6} \tag{A.18}$$

Due to the fact that the current velocity can be considered constant, a constant force acting on a considered floating structure can be expected. The same assumption can be made for wind loads, as wind velocity generally fluctuates around a certain mean wind velocity. Therefore, regarding the floating structure motions during offshore operations, an equilibrium can be assumed between current and wind loads, and the mooring system. Additionally, based on the experience of experts within Seaway 7, it can be stated that for a situation with a load suspended in a Heavy Lift Vessel (HLV)-crane (above the waterline), wind and current loads only play a marginal role in the resulting system motions and internal loads. Additionally, wind often has a damping effect during lifting operations, which is shown by experimental simulations in Section 4.5. Similar conclusions were drawn by Kanotra et al. (2012). Therefore, in this thesis, an HLV with zero netto surge and sway motions is assumed, performing a lift-off operation that is not influenced by wind loads. Similar assumptions were made in the six papers presented by Li (2016) and in the studies by Sarkar and Gudmestad (2013) and Zhu et al. (2017).

A.3 System responses

The behaviour of a system can be studied in the frequency or in the time domain. For the Frequency Domain (FD) approach, it is a requirement that “the behaviour is linearly related to the displacement, velocity and acceleration” of the system under analysis (Journée et al., 2015). However, often this assumption of linearity does not hold. In those cases, Time Domain (TD) analyses are required. TD analyses, however, are more time-consuming than FD analyses.

A.3.1 Frequency domain approach

To perform FD analyses, it has to be made sure that the system of analysis is linear. Components that are nonlinear (such as drag forces) first have to be linearised. For a linear system, the equation of motion in FD can be expressed as Equation A.19a. The vector $\vec{F}_{ext}$ can be replaced by $\vec{H}_{F,\zeta_a} \cdot \zeta_a$. In this equation, $\vec{H}_{F,\zeta_a}$ is a complex wave force transfer function, describing the ratio between the amplitude of the incident wave and the resulting external forces and moments acting on the structure of analysis. Moreover, it is a function of the hull shape of the considered vessel(s) and the wave frequency (ω). Subsequently, Equation A.19a can be rewritten to Equation A.19b, leaving the ratio between the motion response vector (which is complex) and the incident wave amplitude on the right-hand side of the equation. The magnitude of this ratio, $\left|\frac{\vec{X}}{\zeta_a}\right|$, is often called the RAO.

$$\left[-\omega^2\left(\mathbf{M}+\mathbf{A}(\omega)\right)+i\omega\mathbf{B}(\omega)+\mathbf{K}\right]\vec{X} = \vec{F}_{ext} \tag{A.19a}$$

$$= \vec{H}_{F,\zeta_a} \cdot \zeta_a$$

$$\left[-\omega^2\left(\mathbf{M}+\mathbf{A}(\omega)\right)+i\omega\mathbf{B}(\omega)+\mathbf{K}\right]^{-1}\vec{H}_{F,\zeta_a} = \frac{\vec{X}}{\zeta_a} \tag{A.19b}$$

In these equations, $\mathbf{M}$ is the mass matrix of the system, $\mathbf{A}(\omega)$ is the added mass matrix, $\mathbf{B}(\omega)$ is the damping matrix, $\mathbf{K}$ is the stiffness matrix, $\vec{X}$ is the motion response vector, $\vec{F}_{ext}$ is the external forces and moments vector, $\vec{H}_{F,\zeta_a}$ is the wave force transfer function and ζ_a is the incident wave amplitude.

RAOs can be used to calculate response spectra, by multiplying the wave spectrum with the RAO squared. This process is visualised in Figure A.5. The figure also indicates that if the peak of the transfer function (the RAO) and the peak of the wave spectrum are present at (almost) the same wave frequency, large responses can be expected. However, it is also possible to have a large RAO for a frequency with little wave energy. In those cases, the responses will also remain small.

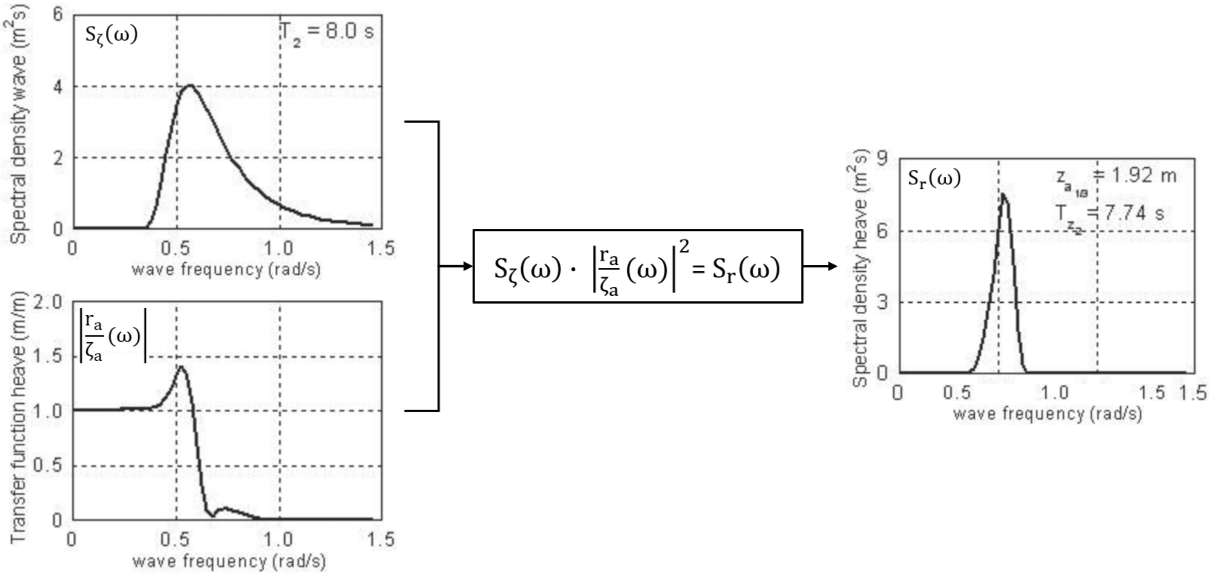

Figure A.5: The principle of calculating the response spectrum, based on the wave spectrum and the corresponding RAO (Graphs from (Journée et al., 2015))

A.3.2 Time domain approach

The FD method provides a relatively simple and fast approach to analyse the motions of floating structures induced by environmental conditions, assuming a linear system. However, there are numerous situations where this assumption does not hold, e.g., when forces and moments induced by wind or current or second order wave loads have to be accounted for (Journée et al., 2015). These conditions provide nonlinear systems, for which the superposition principle, on which the FD method is based, does not hold. In those cases, the TD approach can be applied. In this approach, the differential equations of motion, derived from Newton's second law, are integrated to determine the structure's positions and velocities at the subsequent time step. The values describing the state of the system at the end of the previous time step, function as starting conditions for the current time step (ANSYS, 2015). The the TD approach requires the input variables to be provided to the model as a function of time, such that a time record of the output variables can be produced. However, often, the only available information about the environmental conditions at a particular location is provided by a spectrum (e.g., a wave spectrum). In those cases, a weather time series has to be generated based on the provided spectrum. To generate a wave time series, the wave superposition principle can be applied, as described in Section A.2.1.

Cummins (1962) proposes an equation in the time domain, based on potential theory, to calculate radiation forces. According to his formulation, the radiation forces can be computed by including the added mass at infinite frequency and a convolution term, as mathematically expressed in Equation A.20. The convolution term serves a "memory" function, which includes the influence of the motions in previous time intervals on the motions in the current interval (Cummins, 1962; Journée et al., 2015).

$$\vec{F}_{rad}(t) = \mathbf{A}_\infty \ddot{\vec{X}}(t) + \int_{-\infty}^{t} \mathbf{B}(t-\tau)\dot{\vec{X}}(\tau)d\tau \tag{A.20}$$

By adding a hydrostatic stiffness term $(\mathbf{K})$ and external loads $(\vec{F}_{ext}(t))$ to Equation A.20, and by a replacing "τ" with "$t-\tau$" and adapting the integration limits, Equation A.21a is constructed (Cummins, 1962; Journée et al., 2015). The latter equation is known as the "Cummins equation". ANSYS (2015) mentions the following external force components to be included in this equation: first and second order wave excitation forces, drag forces due to current and wind, bilge roll damping forces, mooring forces and additional external forces. By substituting these force components for $\vec{F}_{ext}(t)$, Equation A.21a can be rewritten to Equation A.21b.

$$\vec{F}_{ext}(t) = (\mathbf{M} + \mathbf{A}_\infty)\ddot{\vec{X}}(t) + \int_{0}^{\infty} \mathbf{B}(\tau)\dot{\vec{X}}(t-\tau)d\tau + \mathbf{K}\vec{X}(t) \tag{A.21a}$$

$$\begin{aligned}(\mathbf{M} + \mathbf{A}_\infty)\ddot{\vec{X}}(t) = &-\int_{0}^{\infty} \mathbf{B}(\tau)\dot{\vec{X}}(t-\tau)d\tau - \mathbf{K}\vec{X}(t) + \vec{F}^{(1)}(t) + \vec{F}^{(2)}(t) \\ &+ \vec{F}_c(t) + \vec{F}_w(t) + \vec{F}_b(t) + \vec{F}_t(t) + \vec{F}_e(t)\end{aligned} \tag{A.21b}$$

In this equation, $\mathbf{A}_\infty$ is the added mass matrix at infinite frequency, $\vec{F}^{(1)}(t)$ is the first order wave excitation load vector, $\vec{F}^{(2)}(t)$ is the second order wave excitation load vector, $\vec{F}_c(t)$ is the current drag load vector, $\vec{F}_w(t)$ is the wind drag load vector, $\vec{F}_b(t)$ is the bilge roll damping load vector, $\vec{F}_t(t)$ is the mooring load vector and $\vec{F}_e(t)$ is the additional external load vector.

B | Rigging analysis

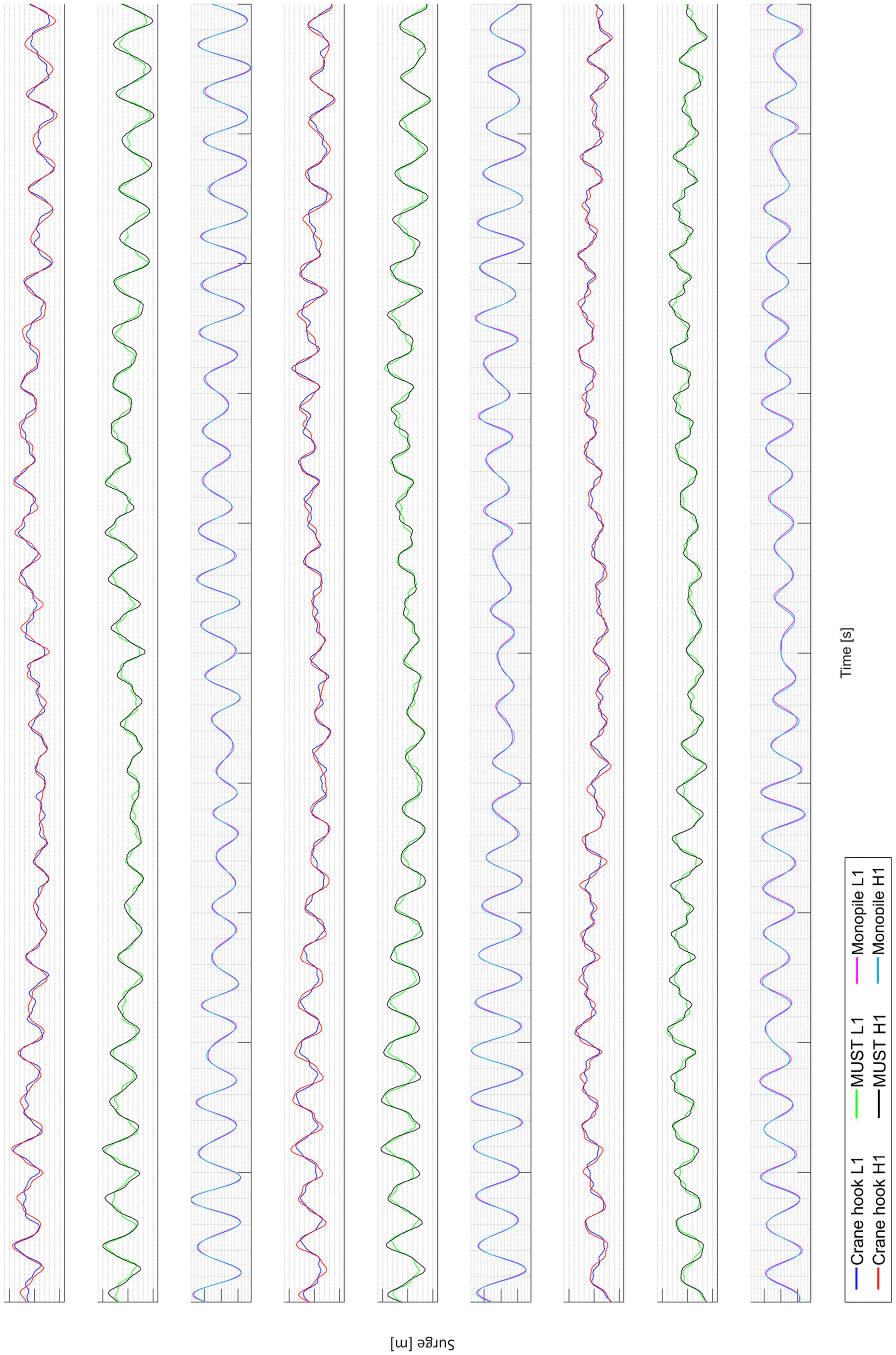

Figure B.1: TD simulation comparison H1-L1. $H_s = 0.40$ m, ω_p = [redacted] rad/s, WEA = 0 deg

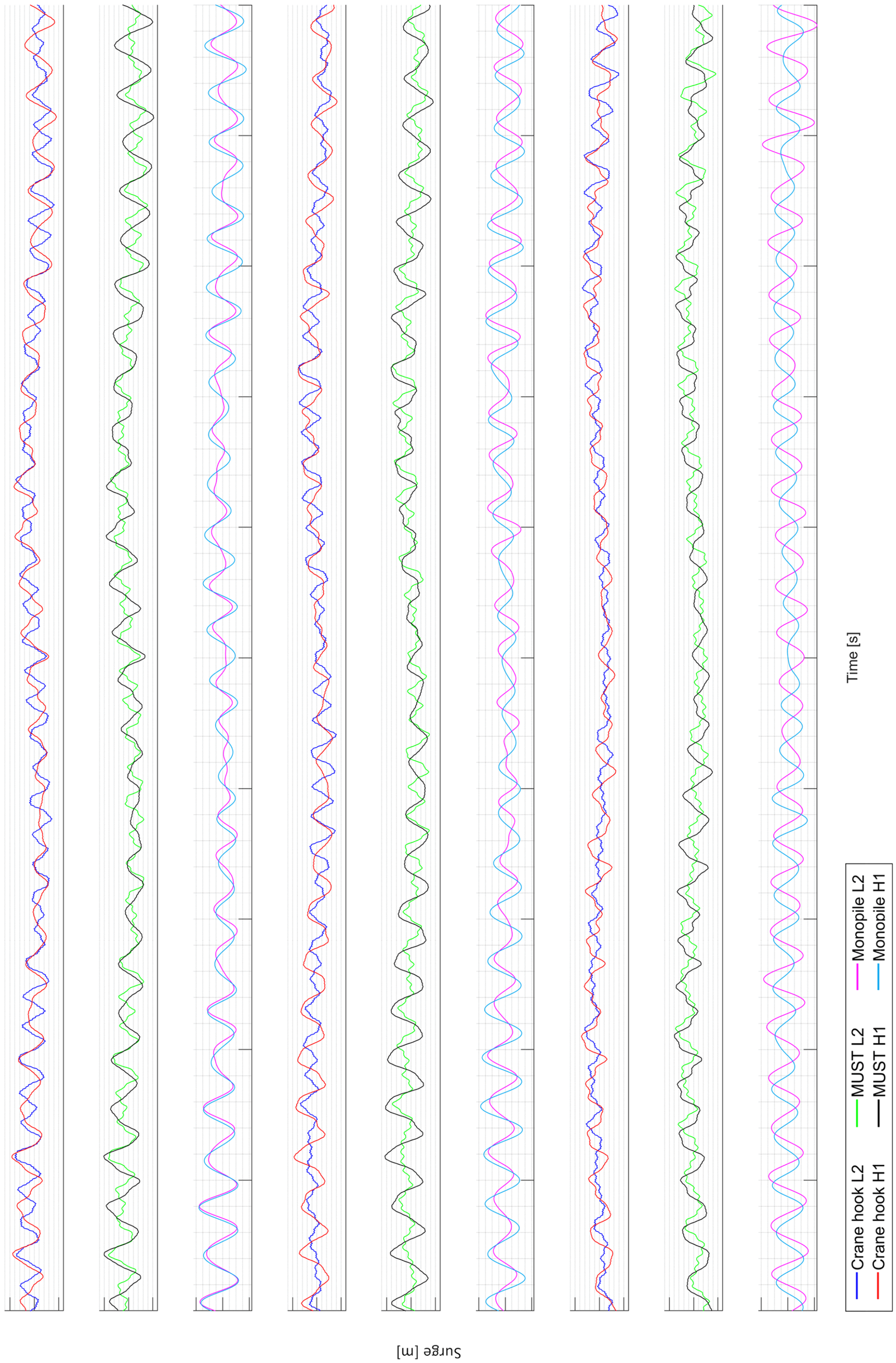

Figure B.2: TD simulation comparison H1-L2. $H_s = 0.40$ m, $\omega_p =$ [redacted] rad/s, WEA = 0 deg

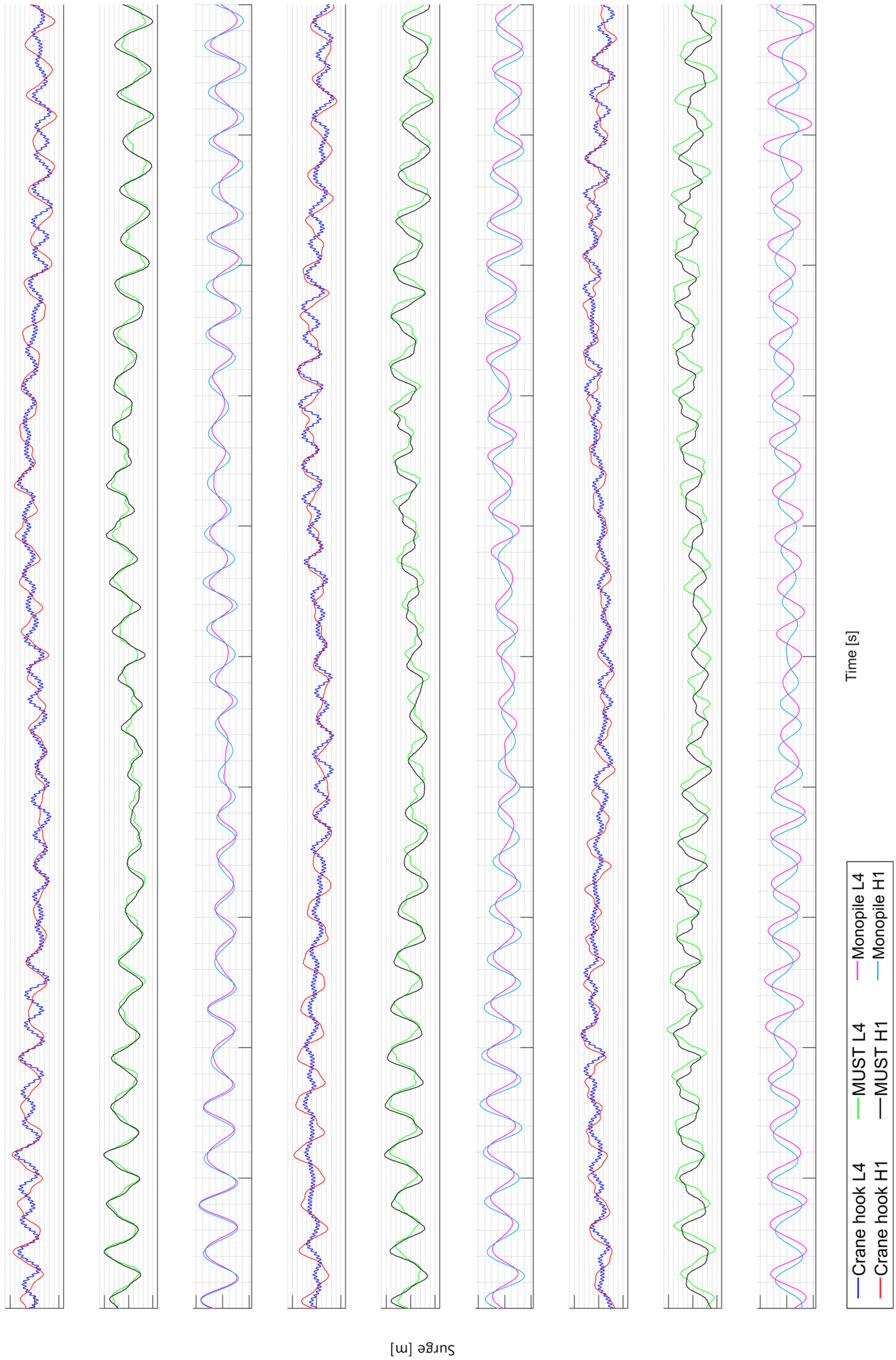

Figure B.3: TD simulation comparison H1-L4. $H_s = 0.40$ m, $\omega_p =$ [redacted] rad/s, WEA = 0 deg

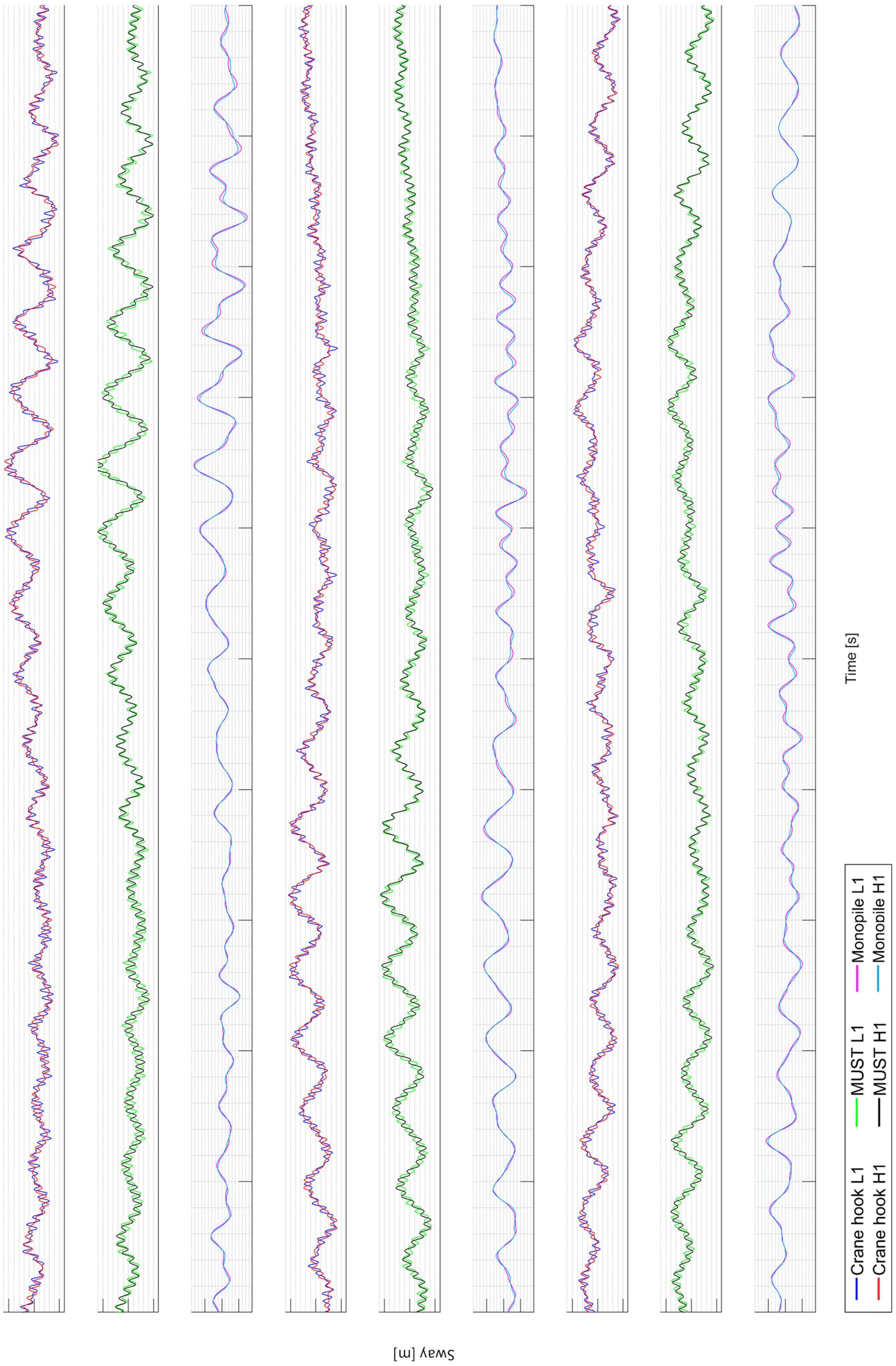

Figure B.4: TD simulation comparison H1-L1. $H_s = 0.25$ m, $\omega_p =$ [redacted] rad/s, WEA = 90 deg

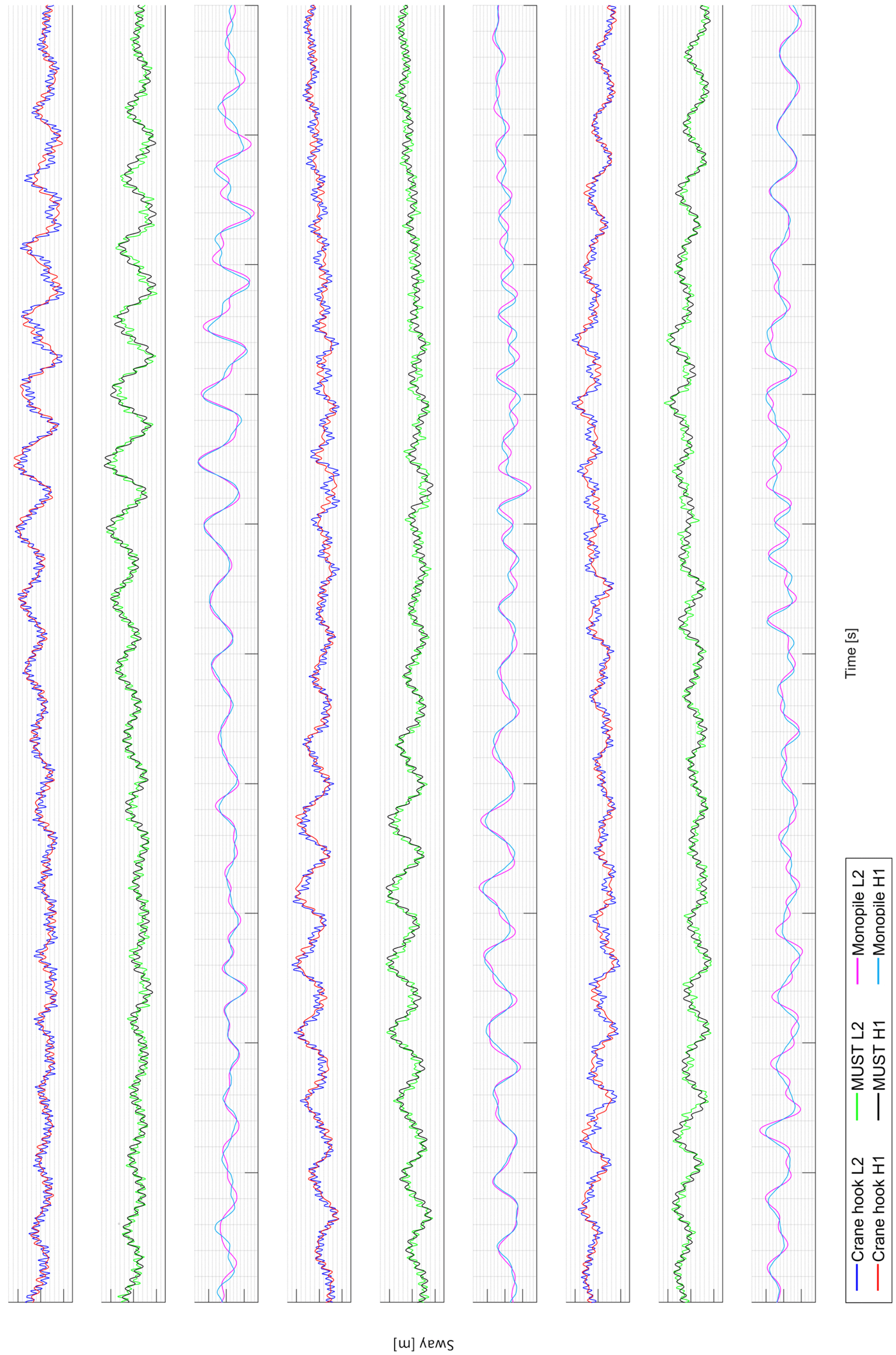

Figure B.5: TD simulation comparison H1-L2. $H_s = 0.25$ m, $\omega_p =$ [redacted] rad/s, WEA = 90 deg

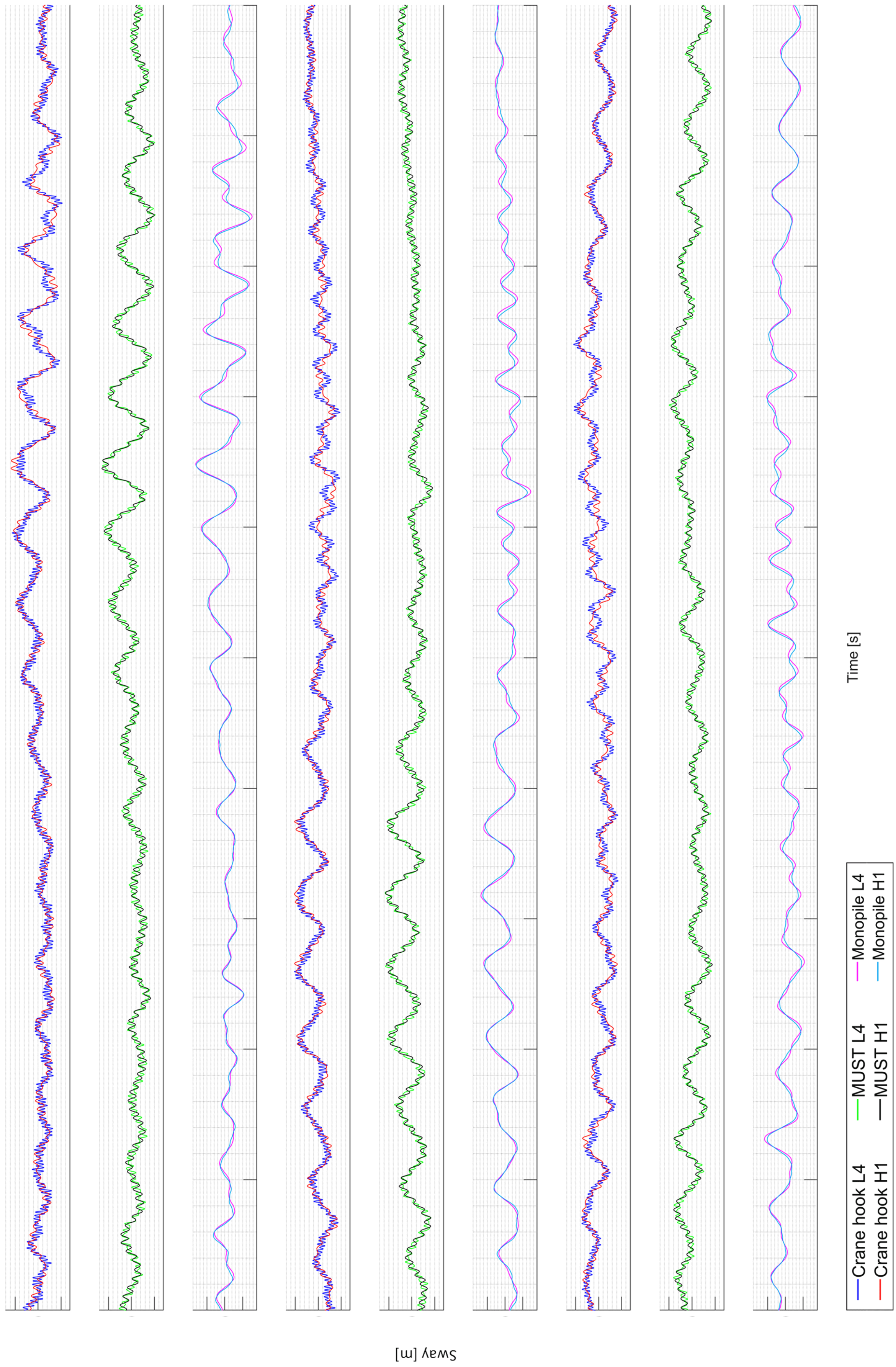

Figure B.6: TD simulation comparison H1-L4. $H_s = 0.25$ m, $\omega_p =$ [redacted] rad/s, WEA = 90 deg

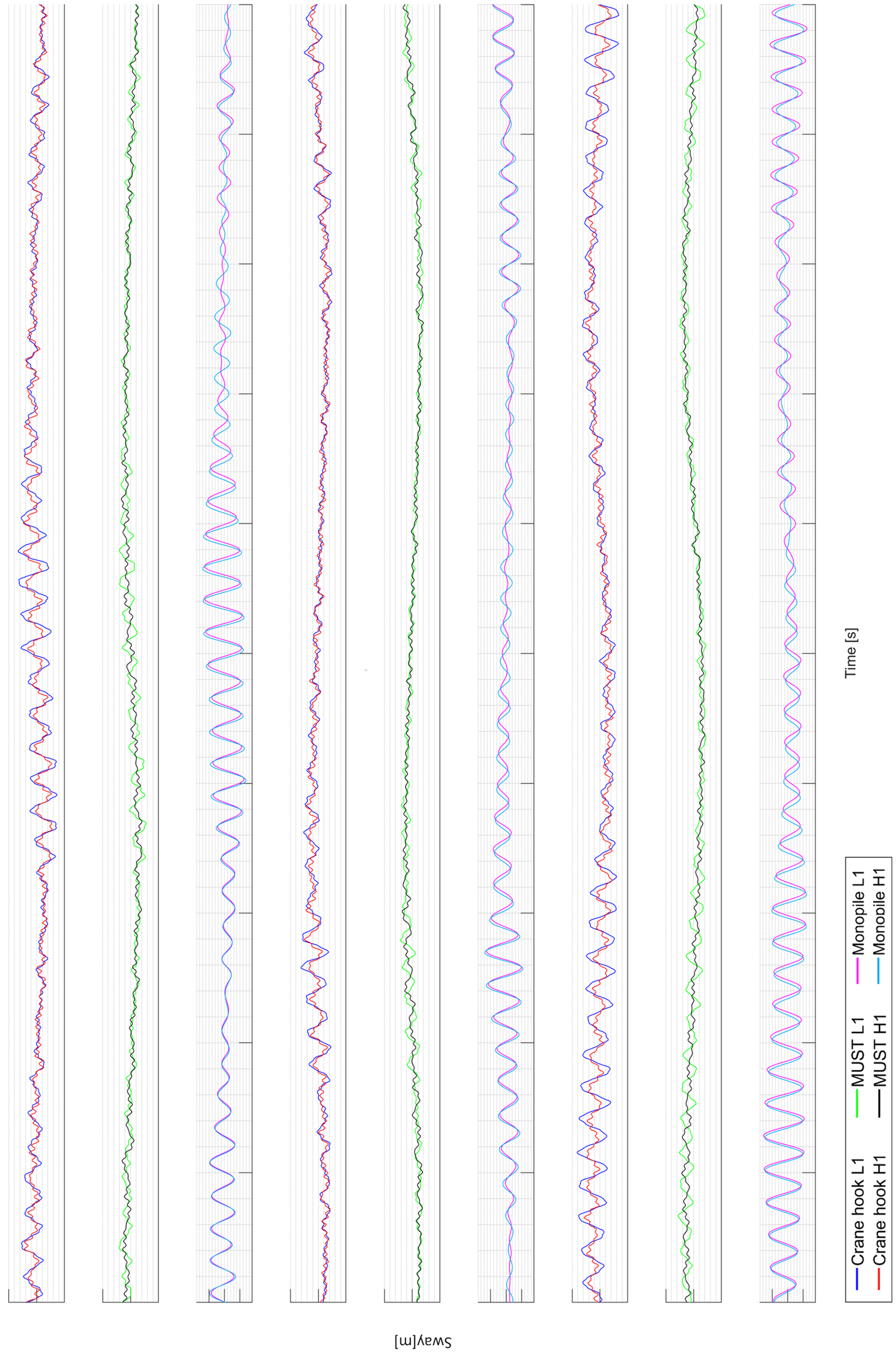

Figure B.7: TD simulation comparison H1-L1. $H_s = 0.25$ m, $\omega_p =$ [redacted] rad/s, WEA = 90 deg

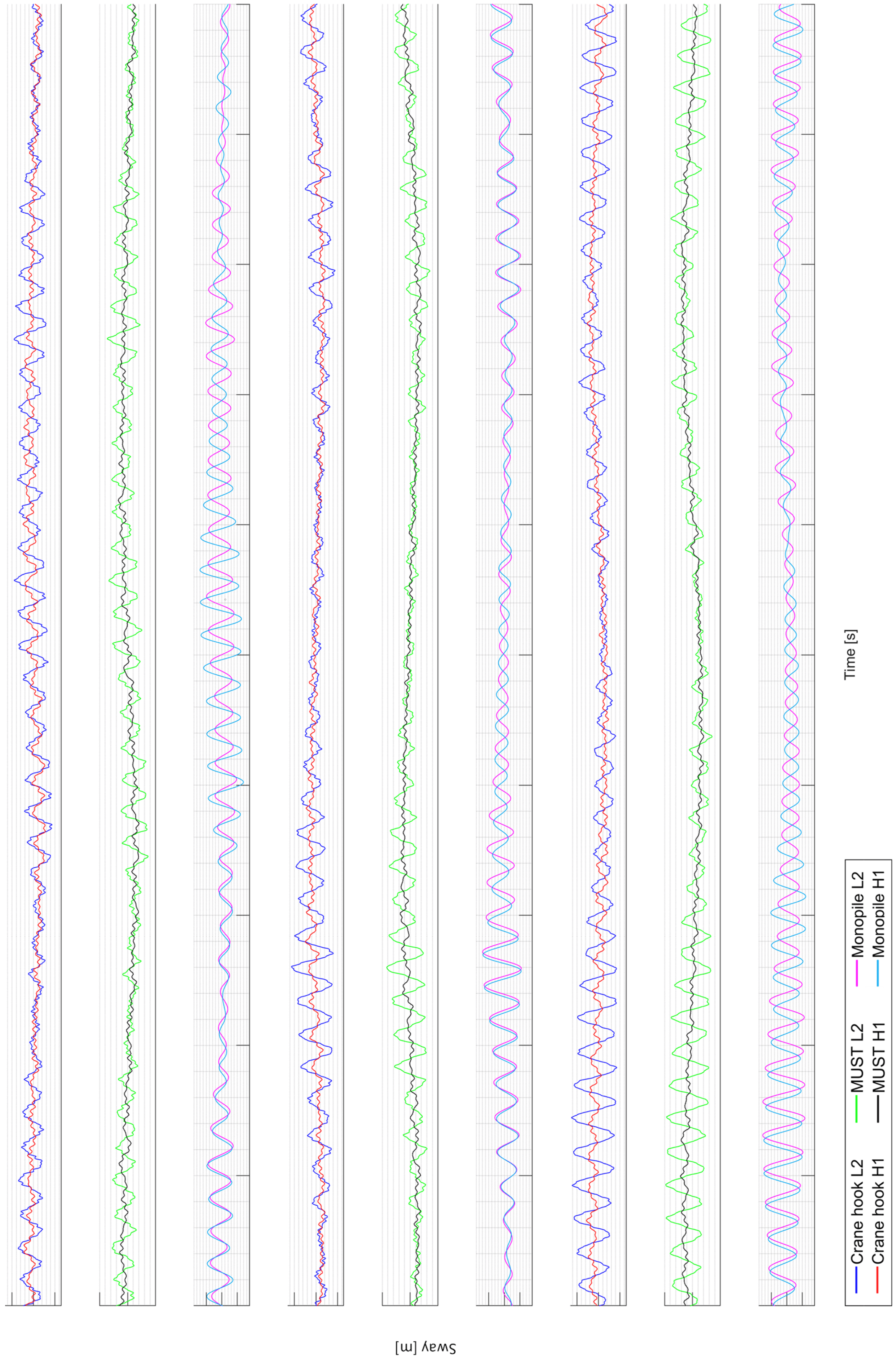

Figure B.8: TD simulation comparison H1-L2. $H_s = 0.25$ m, $\omega_p =$ [redacted] rad/s, WEA = 90 deg

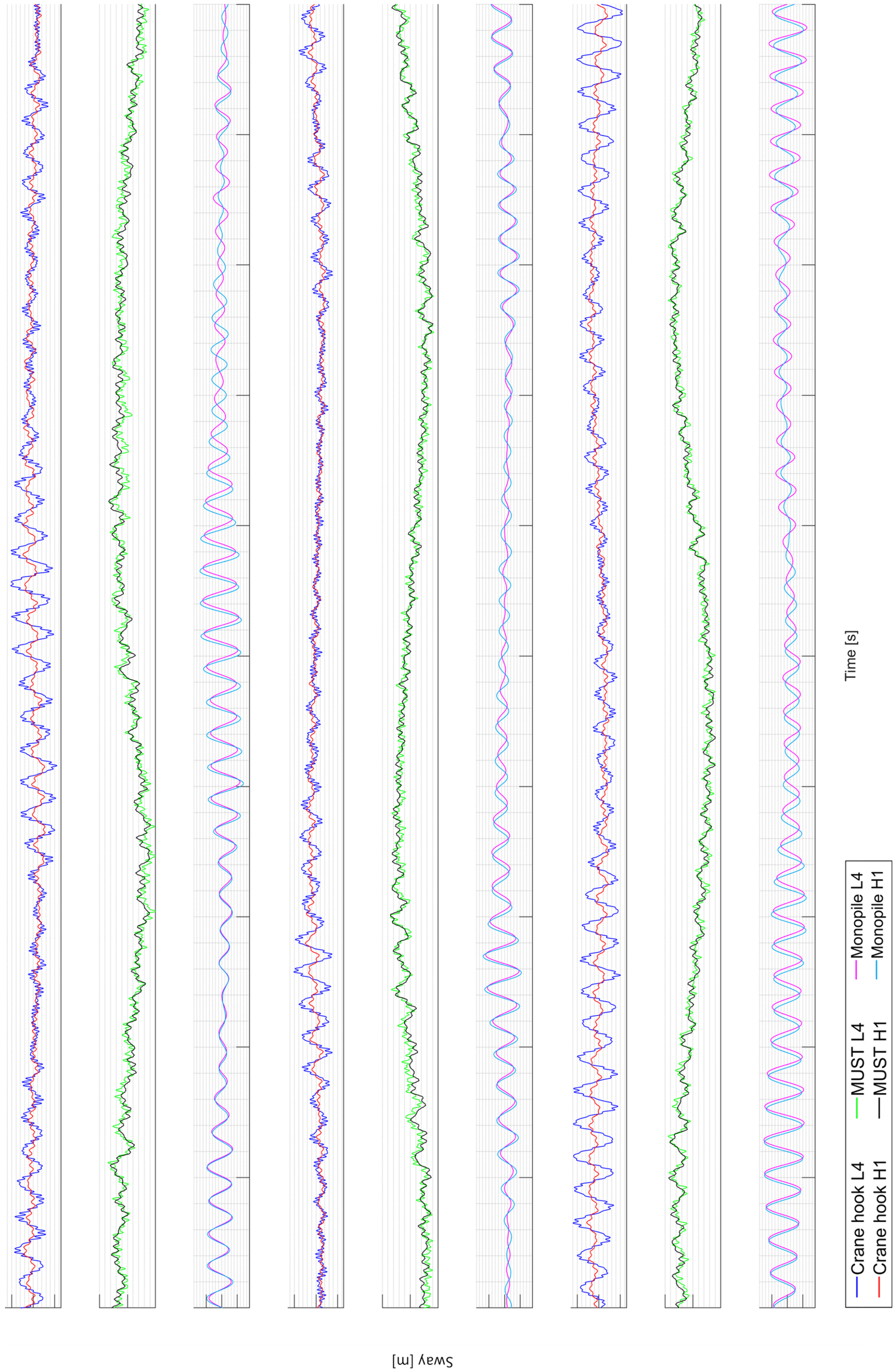

Figure B.9: TD simulation comparison H1-L4. $H_s = 0.25$ m, $\omega_p =$ [redacted] rad/s, WEA = 90 deg

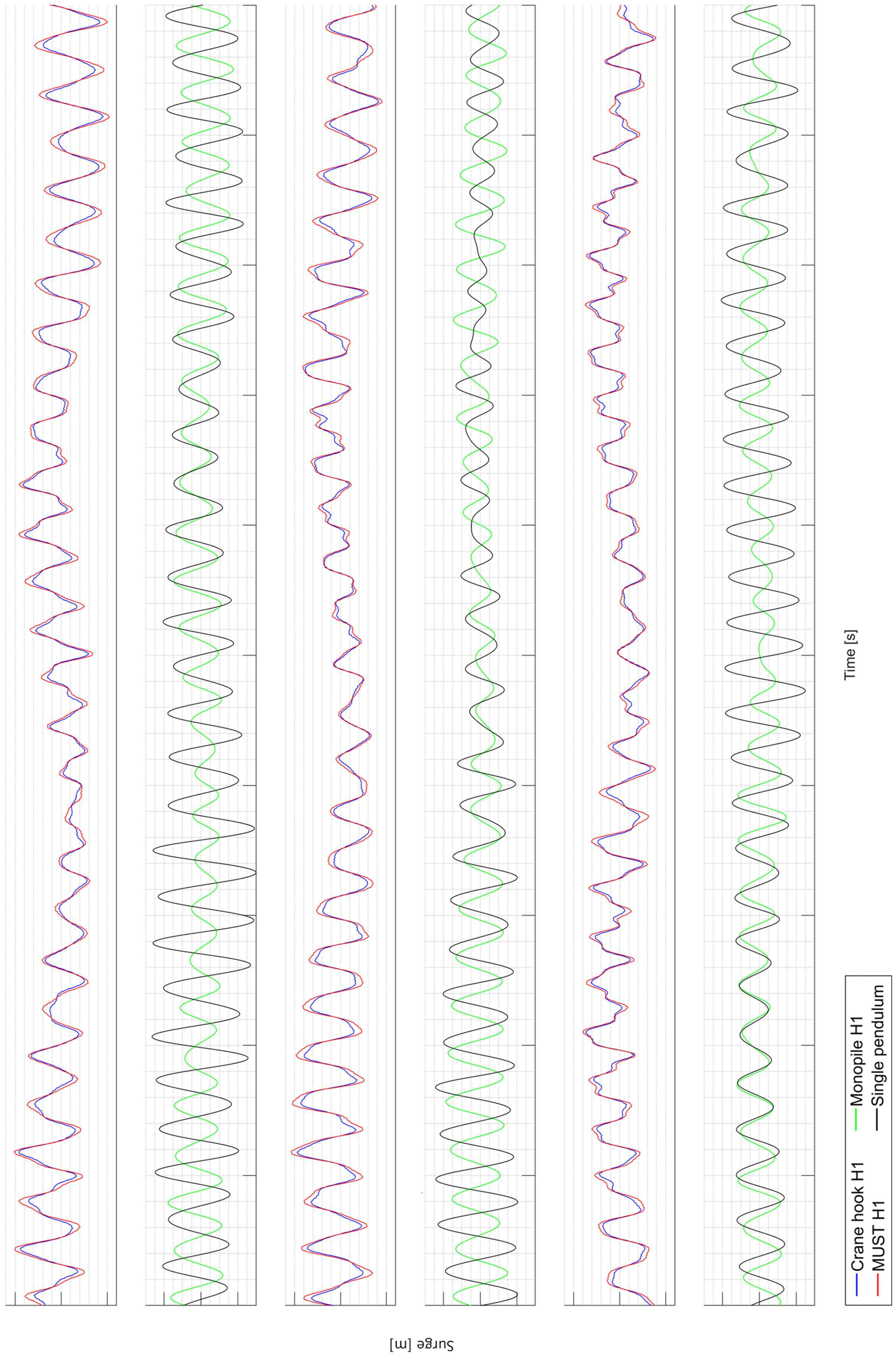

Figure B.10: TD simulation comparison H1-Single pendulum. $H_s = 0.40$ m, $\omega_p =$ [redacted] rad/s, WEA = 0 deg

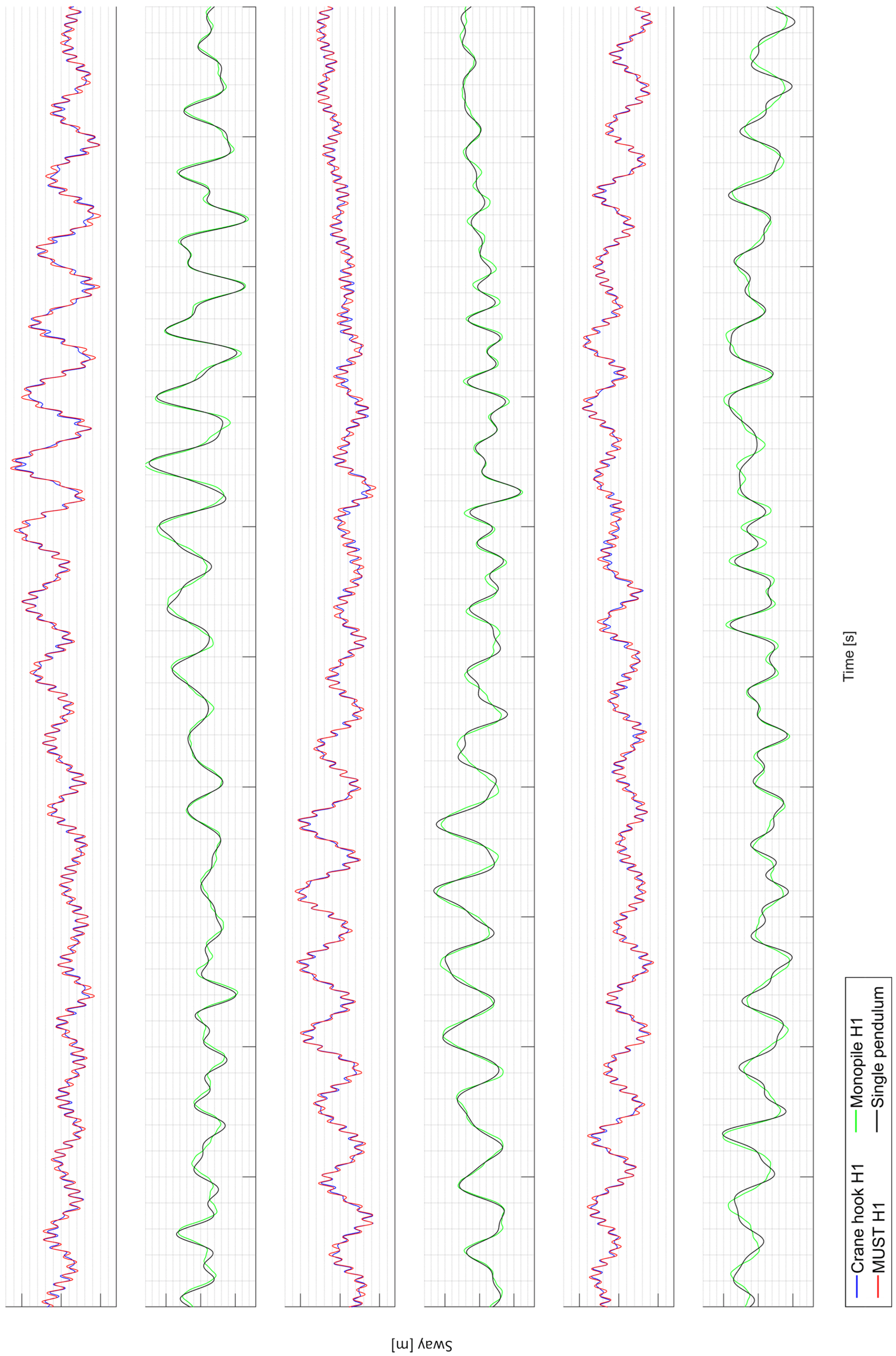

Figure B.11: TD simulation comparison H1-Single pendulum. $H_s = 0.25$ m, $\omega_p =$ [redacted] rad/s, WEA = 90 deg

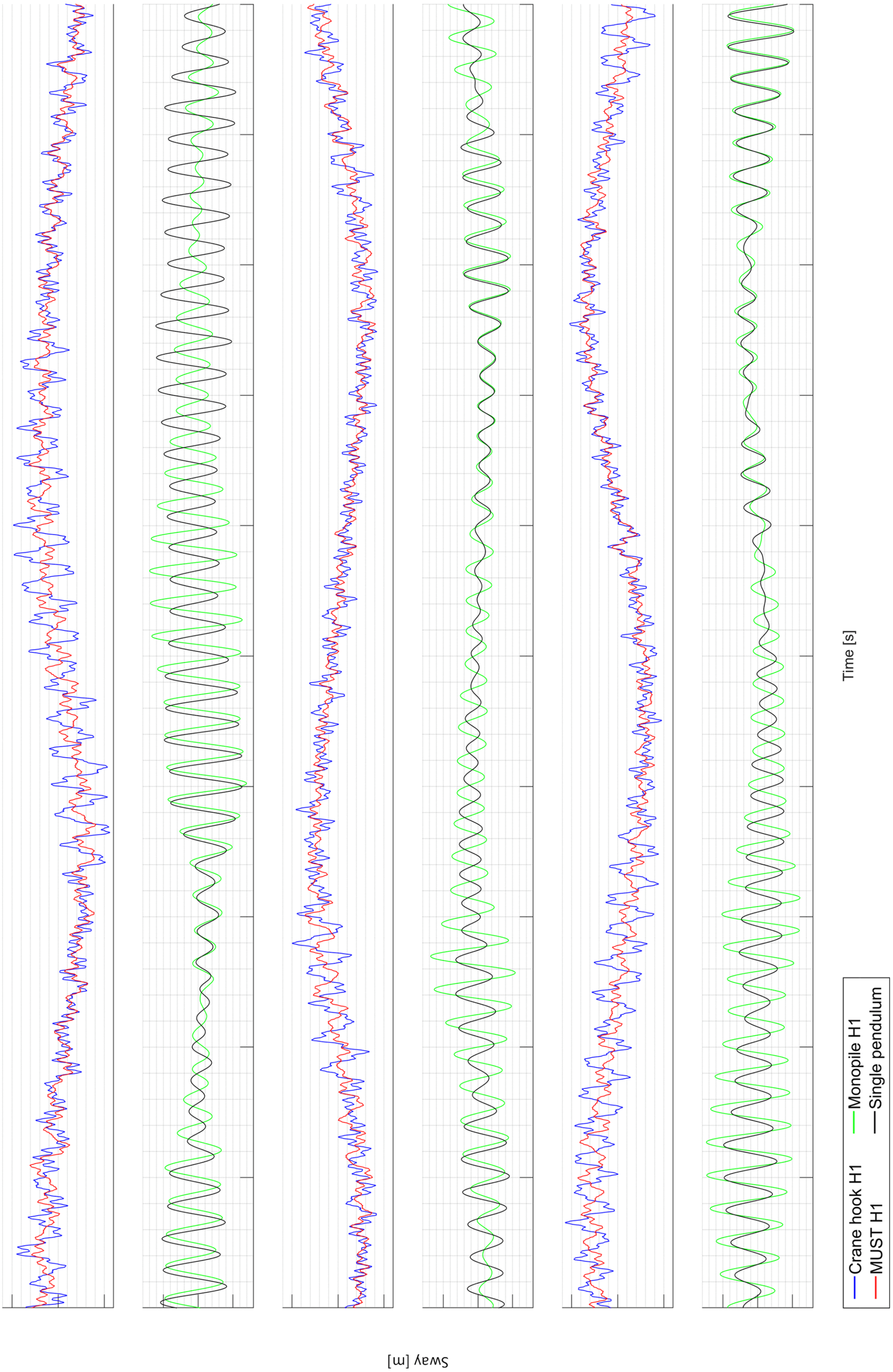

Figure B.12: TD simulation comparison H1-Single pendulum. $H_s = 0.25$ m, $\omega_p =$ [redacted] rad/s, WEA = 90 deg

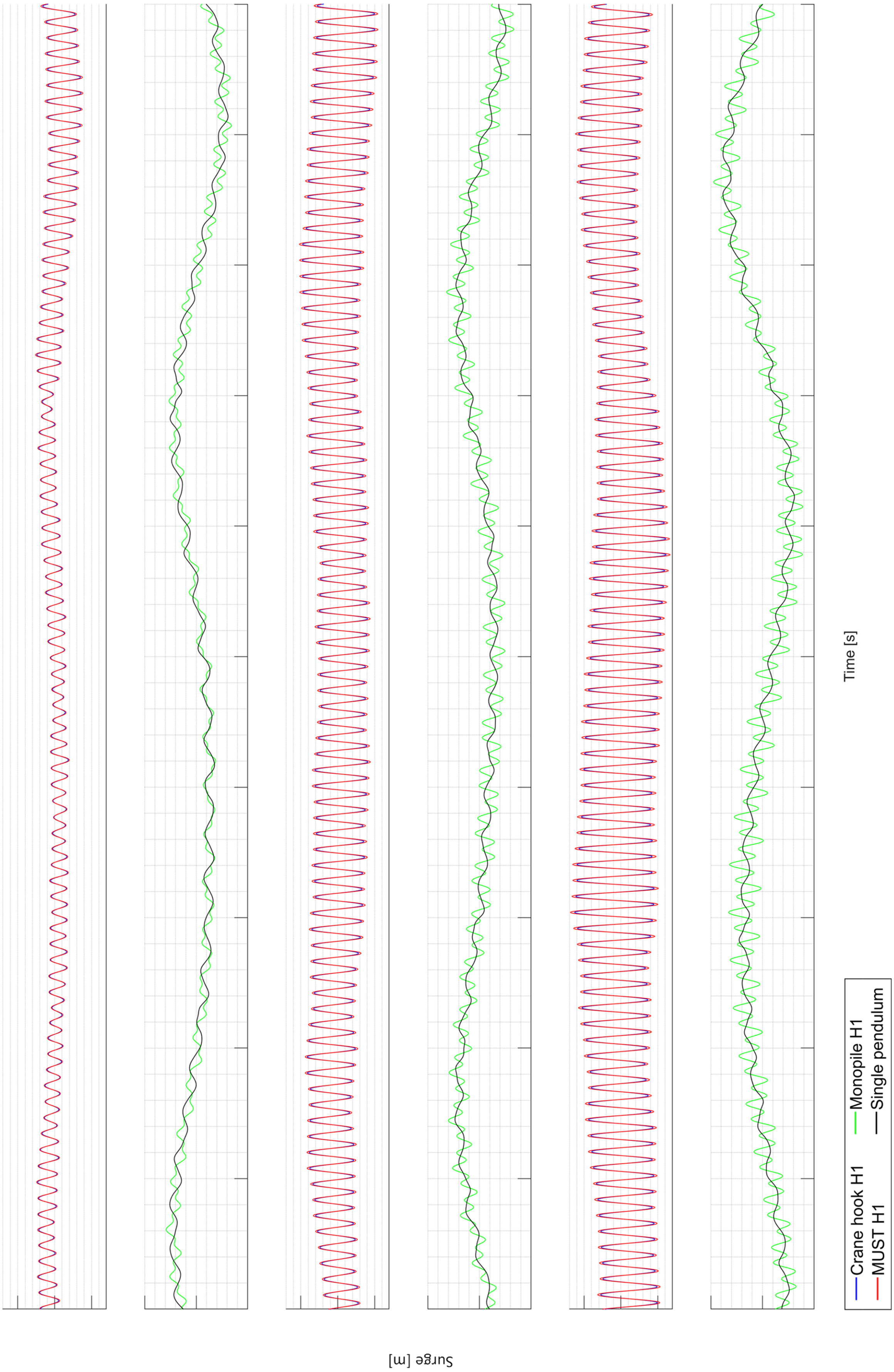

Figure B.13: TD simulation comparison H1-Single pendulum. $H_s = 0.40$ m, $\omega_p =$ [redacted] rad/s, WEA = 0 deg

C Finding governing parameters

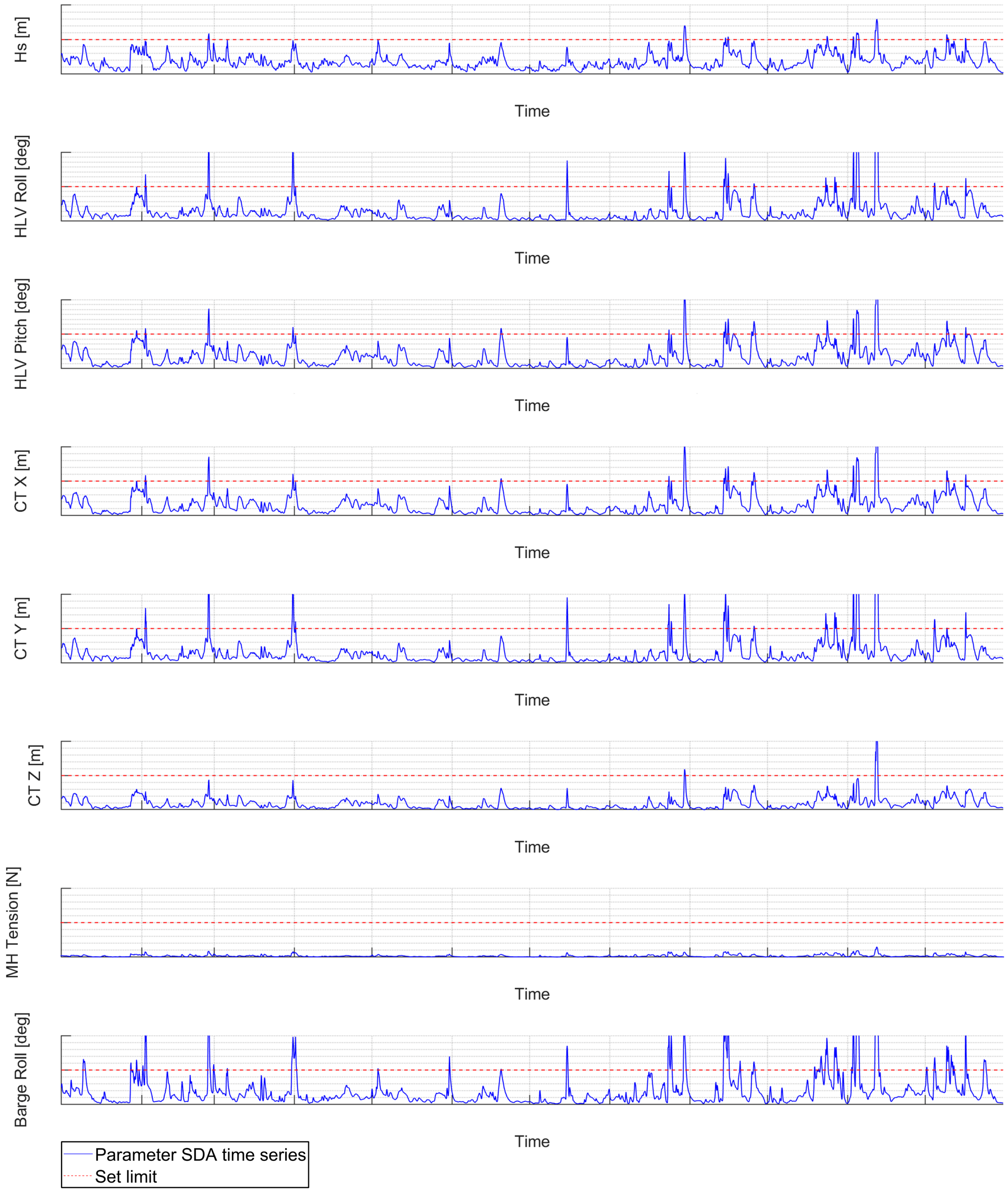

Figure C.3: Significant double amplitude responses as a function of the time, for an optimal vessel heading of 165 deg (limiting parameters 1-7 and H_s as a function of time)

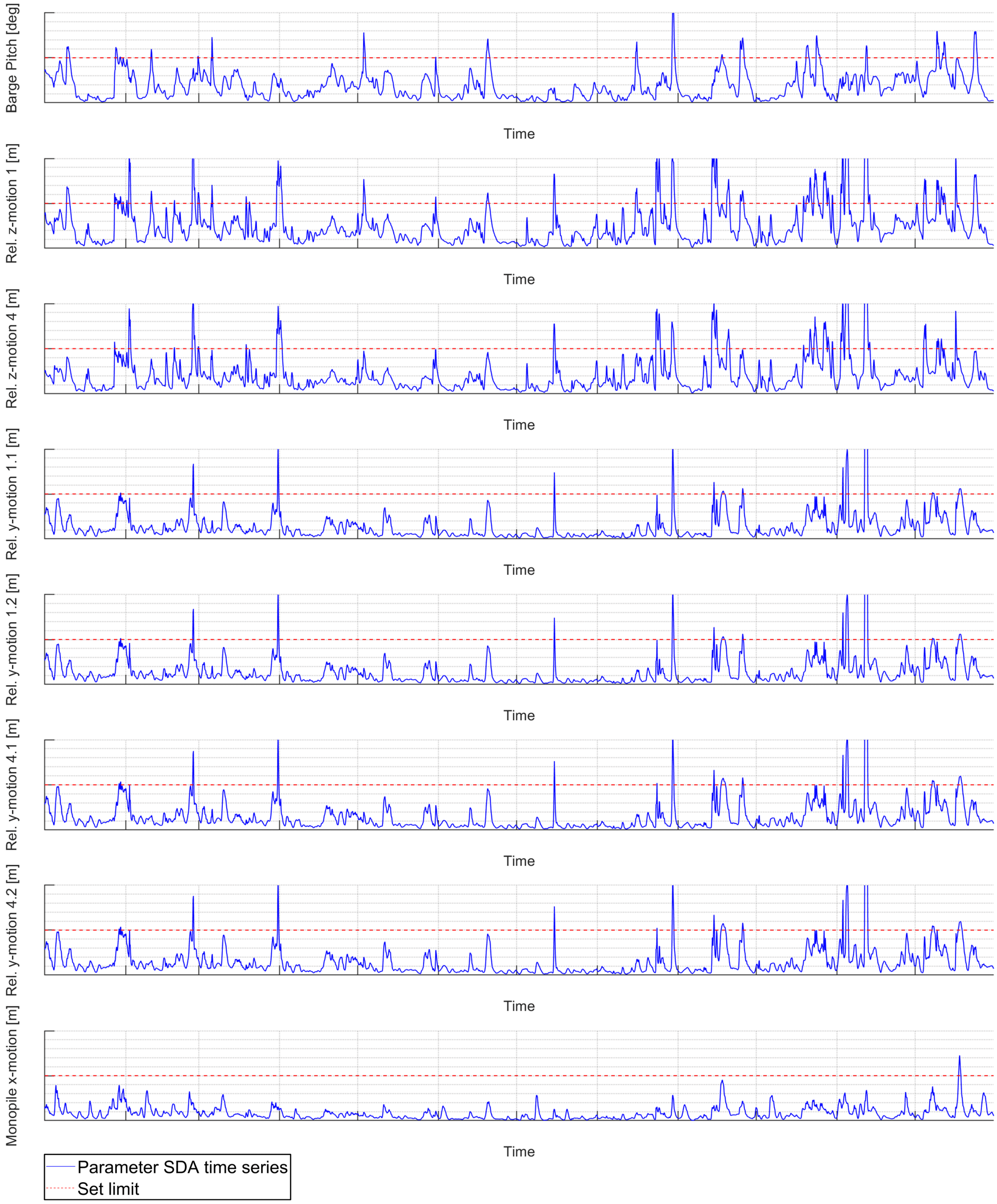

Figure C.4: Significant double amplitude responses as a function of the time, for an optimal vessel heading of 165 deg (limiting parameters 8-15)

E | EoM base case

E.1 Kinematics

$$\begin{aligned}
x_1 &= -l_1 \cdot sin(\theta_1) + x_{CT} \\
x_2 &= -l_1 \cdot sin(\theta_1) - l_2 \cdot sin(\theta_2) + x_{CT} \\
x_3 &= -l_1 \cdot sin(\theta_1) - l_2 \cdot sin(\theta_2) - l_3 \cdot sin(\theta_3) + x_{CT} \\
x_4 &= -l_1 \cdot sin(\theta_1) - l_2 \cdot sin(\theta_2) - l_3 \cdot sin(\theta_3) - l_4 \cdot sin(\theta_4) + x_{CT}
\end{aligned}$$

$$\begin{aligned}
y_1 &= l_1 \cdot sin(\varphi_1) + y_{CT} \\
y_2 &= l_1 \cdot sin(\varphi_1) + l_2 \cdot sin(\varphi_2) + y_{CT} \\
x_3 &= l_1 \cdot sin(\varphi_1) + l_2 \cdot sin(\varphi_2) + l_3 \cdot sin(\varphi_3) + y_{CT} \\
y_4 &= l_1 \cdot sin(\varphi_1) + l_2 \cdot sin(\varphi_2) + l_3 \cdot sin(\varphi_3) + l_4 \cdot sin(\varphi_4) + y_{CT}
\end{aligned}$$

$$\begin{aligned}
z_1 &= -l_1 \cdot cos(\theta_1) \cdot cos(\varphi_1) + z_{CT} \\
z_2 &= -l_1 \cdot cos(\theta_1) \cdot cos(\varphi_1) - l_2 \cdot cos(\theta_2) \cdot cos(\varphi_2) + z_{CT} \\
z_3 &= -l_1 \cdot cos(\theta_1) \cdot cos(\varphi_1) - l_2 \cdot cos(\theta_2) \cdot cos(\varphi_2) - l_3 \cdot cos(\theta_3) \cdot cos(\varphi_3) + z_{CT} \\
z_4 &= -l_1 \cdot cos(\theta_1) \cdot cos(\varphi_1) - l_2 \cdot cos(\theta_2) \cdot cos(\varphi_2) - l_3 \cdot cos(\theta_3) \cdot cos(\varphi_3) \\
&\quad - l_4 \cdot cos(\theta_4) \cdot cos(\varphi_4) + z_{CT}
\end{aligned}$$

$$\begin{aligned}
\dot{x}_1 &= -l_1 \cdot \dot{\theta}_1 \cdot cos(\theta_1) + \dot{x}_{CT} \\
\dot{x}_2 &= -l_1 \cdot \dot{\theta}_1 \cdot cos(\theta_1) - l_2 \cdot \dot{\theta}_2 \cdot cos(\theta_2) + \dot{x}_{CT} \\
\dot{x}_3 &= -l_1 \cdot \dot{\theta}_1 \cdot cos(\theta_1) - l_2 \cdot \dot{\theta}_2 \cdot cos(\theta_2) - l_3 \cdot \dot{\theta}_3 \cdot cos(\theta_3) + \dot{x}_{CT} \\
\dot{x}_4 &= -l_1 \cdot \dot{\theta}_1 \cdot cos(\theta_1) - l_2 \cdot \dot{\theta}_2 \cdot cos(\theta_2) - l_3 \cdot \dot{\theta}_3 \cdot cos(\theta_3) - l_4 \cdot \dot{\theta}_4 \cdot cos(\theta_4) + \dot{x}_{CT}
\end{aligned}$$

$$\begin{aligned}
\dot{y}_1 &= l_1 \cdot \dot{\varphi}_1 \cdot cos(\varphi_1) + \dot{y}_{CT} \\
\dot{y}_2 &= l_1 \cdot \dot{\varphi}_1 \cdot cos(\varphi_1) + l_2 \cdot \dot{\varphi}_2 \cdot cos(\varphi_2) + \dot{y}_{CT} \\
\dot{y}_3 &= l_1 \cdot \dot{\varphi}_1 \cdot cos(\varphi_1) + l_2 \cdot \dot{\varphi}_2 \cdot cos(\varphi_2) + l_3 \cdot \dot{\varphi}_3 \cdot cos(\varphi_3) + \dot{y}_{CT} \\
\dot{y}_4 &= l_1 \cdot \dot{\varphi}_1 \cdot cos(\varphi_1) + l_2 \cdot \dot{\varphi}_2 \cdot cos(\varphi_2) + l_3 \cdot \dot{\varphi}_3 \cdot cos(\varphi_3) + l_4 \cdot \dot{\varphi}_4 \cdot cos(\varphi_4) + \dot{y}_{CT}
\end{aligned}$$

$$\begin{aligned}
\dot{z}_1 &= l_1 \cdot \dot{\theta}_1 \cdot sin(\theta_1) \cdot cos(\varphi_1) + l_1 \cdot \dot{\varphi}_1 \cdot cos(\theta_1) \cdot sin(\varphi_1) + \dot{z}_{CT} \\
\dot{z}_2 &= l_1 \cdot \dot{\theta}_1 \cdot sin(\theta_1) \cdot cos(\varphi_1) + l_1 \cdot \dot{\varphi}_1 \cdot cos(\theta_1) \cdot sin(\varphi_1) \\
&\quad + l_2 \cdot \dot{\theta}_2 \cdot sin(\theta_2) \cdot cos(\varphi_2) + l_2 \cdot \dot{\varphi}_2 \cdot cos(\theta_2) \cdot sin(\varphi_2) + \dot{z}_{CT} \\
\dot{z}_3 &= l_1 \cdot \dot{\theta}_1 \cdot sin(\theta_1) \cdot cos(\varphi_1) + l_1 \cdot \dot{\varphi}_1 \cdot cos(\theta_1) \cdot sin(\varphi_1) \\
&\quad + l_2 \cdot \dot{\theta}_2 \cdot sin(\theta_2) \cdot cos(\varphi_2) + l_2 \cdot \dot{\varphi}_2 \cdot cos(\theta_2) \cdot sin(\varphi_2) \\
&\quad + l_3 \cdot \dot{\theta}_3 \cdot sin(\theta_3) \cdot cos(\varphi_3) + l_3 \cdot \dot{\varphi}_3 \cdot cos(\theta_3) \cdot sin(\varphi_3) + \dot{z}_{CT} \\
\dot{z}_4 &= l_1 \cdot \dot{\theta}_1 \cdot sin(\theta_1) \cdot cos(\varphi_1) + l_1 \cdot \dot{\varphi}_1 \cdot cos(\theta_1) \cdot sin(\varphi_1) \\
&\quad + l_2 \cdot \dot{\theta}_2 \cdot sin(\theta_2) \cdot cos(\varphi_2) + l_2 \cdot \dot{\varphi}_2 \cdot cos(\theta_2) \cdot sin(\varphi_2) \\
&\quad + l_3 \cdot \dot{\theta}_3 \cdot sin(\theta_3) \cdot cos(\varphi_3) + l_3 \cdot \dot{\varphi}_3 \cdot cos(\theta_3) \cdot sin(\varphi_3) \\
&\quad + l_4 \cdot \dot{\theta}_4 \cdot sin(\theta_4) \cdot cos(\varphi_4) + l_4 \cdot \dot{\varphi}_4 \cdot cos(\theta_4) \cdot sin(\varphi_4) + \dot{z}_{CT}
\end{aligned}$$

$$
\begin{aligned}
\ddot{x}_1 &= -l_1 \cdot \ddot{\theta}_1 \cdot cos(\theta_1) + l_1 \cdot (\dot{\theta}_1)^2 \cdot sin(\theta_1) + \ddot{x}_{CT} \\
\ddot{x}_2 &= -l_1 \cdot \ddot{\theta}_1 \cdot cos(\theta_1) + l_1 \cdot (\dot{\theta}_1)^2 \cdot sin(\theta_1) - l_2 \cdot \ddot{\theta}_2 \cdot cos(\theta_2) + l_2 \cdot (\dot{\theta}_2)^2 \cdot sin(\theta_2) + \ddot{x}_{CT} \\
\ddot{x}_3 &= -l_1 \cdot \ddot{\theta}_1 \cdot cos(\theta_1) + l_1 \cdot (\dot{\theta}_1)^2 \cdot sin(\theta_1) - l_2 \cdot \ddot{\theta}_2 \cdot cos(\theta_2) + l_2 \cdot (\dot{\theta}_2)^2 \cdot sin(\theta_2) \\
&\quad - l_3 \cdot \ddot{\theta}_3 \cdot cos(\theta_3) + l_3 \cdot (\dot{\theta}_3)^2 \cdot sin(\theta_3) + \ddot{x}_{CT} \\
\ddot{x}_4 &= -l_1 \cdot \ddot{\theta}_1 \cdot cos(\theta_1) + l_1 \cdot (\dot{\theta}_1)^2 \cdot sin(\theta_1) - l_2 \cdot \ddot{\theta}_2 \cdot cos(\theta_2) + l_2 \cdot (\dot{\theta}_2)^2 \cdot sin(\theta_2) \\
&\quad - l_3 \cdot \ddot{\theta}_3 \cdot cos(\theta_3) + l_3 \cdot (\dot{\theta}_3)^2 \cdot sin(\theta_3) - l_4 \cdot \ddot{\theta}_4 \cdot cos(\theta_4) + l_4 \cdot (\dot{\theta}_4)^2 \cdot sin(\theta_4) + \ddot{x}_{CT}
\end{aligned}
$$

$$
\begin{aligned}
\ddot{y}_1 &= l_1 \cdot \ddot{\varphi}_1 \cdot cos(\varphi_1) - l_1 \cdot (\dot{\varphi}_1)^2 \cdot sin(\varphi_1) + \ddot{y}_{CT} \\
\ddot{y}_2 &= l_1 \cdot \ddot{\varphi}_1 \cdot cos(\varphi_1) - l_1 \cdot (\dot{\varphi}_1)^2 \cdot sin(\varphi_1) + l_2 \cdot \ddot{\varphi}_2 \cdot cos(\varphi_2) - l_2 \cdot (\dot{\varphi}_2)^2 \cdot sin(\varphi_2) + \ddot{y}_{CT} \\
\ddot{y}_3 &= l_1 \cdot \ddot{\varphi}_1 \cdot cos(\varphi_1) - l_1 \cdot (\dot{\varphi}_1)^2 \cdot sin(\varphi_1) + l_2 \cdot \ddot{\varphi}_2 \cdot cos(\varphi_2) - l_2 \cdot (\dot{\varphi}_2)^2 \cdot sin(\varphi_2) \\
&\quad + l_3 \cdot \ddot{\varphi}_3 \cdot cos(\varphi_3) - l_3 \cdot (\dot{\varphi}_3)^2 \cdot sin(\varphi_3) + \ddot{y}_{CT} \\
\ddot{y}_4 &= l_1 \cdot \ddot{\varphi}_1 \cdot cos(\varphi_1) - l_1 \cdot (\dot{\varphi}_1)^2 \cdot sin(\varphi_1) + l_2 \cdot \ddot{\varphi}_2 \cdot cos(\varphi_2) - l_2 \cdot (\dot{\varphi}_2)^2 \cdot sin(\varphi_2) \\
&\quad + l_3 \cdot \ddot{\varphi}_3 \cdot cos(\varphi_3) - l_3 \cdot (\dot{\varphi}_3)^2 \cdot sin(\varphi_3) + l_4 \cdot \ddot{\varphi}_4 \cdot cos(\varphi_4) - l_4 \cdot (\dot{\varphi}_4)^2 \cdot sin(\varphi_4) + \ddot{y}_{CT}
\end{aligned}
$$

$$
\begin{aligned}
\ddot{z}_1 &= l_1 \cdot \Big(\ddot{\theta}_1 \cdot sin(\theta_1) + (\dot{\theta}_1)^2 \cdot cos(\theta_1)\Big) \cdot cos(\varphi_1) - l_1 \cdot \dot{\theta}_1 \cdot sin(\theta_1) \cdot \dot{\varphi}_1 \cdot sin(\varphi_1) \\
&\quad + l_1 \cdot \Big(\ddot{\varphi}_1 \cdot sin(\varphi_1) + (\dot{\varphi}_1)^2 \cdot cos(\varphi_1)\Big) \cdot cos(\theta_1) - l_1 \cdot \dot{\varphi}_1 \cdot sin(\varphi_1) \cdot \dot{\theta}_1 \cdot sin(\theta_1) + \ddot{z}_{CT} \\
\ddot{z}_2 &= l_1 \cdot \Big(\ddot{\theta}_1 \cdot sin(\theta_1) + (\dot{\theta}_1)^2 \cdot cos(\theta_1)\Big) \cdot cos(\varphi_1) - l_1 \cdot \dot{\theta}_1 \cdot sin(\theta_1) \cdot \dot{\varphi}_1 \cdot sin(\varphi_1) \\
&\quad + l_1 \cdot \Big(\ddot{\varphi}_1 \cdot sin(\varphi_1) + (\dot{\varphi}_1)^2 \cdot cos(\varphi_1)\Big) \cdot cos(\theta_1) - l_1 \cdot \dot{\varphi}_1 \cdot sin(\varphi_1) \cdot \dot{\theta}_1 \cdot sin(\theta_1) \\
&\quad + l_2 \cdot \Big(\ddot{\theta}_2 \cdot sin(\theta_2) + (\dot{\theta}_2)^2 \cdot cos(\theta_2)\Big) \cdot cos(\varphi_2) - l_2 \cdot \dot{\theta}_2 \cdot sin(\theta_2) \cdot \dot{\varphi}_2 \cdot sin(\varphi_2) \\
&\quad + l_2 \cdot \Big(\ddot{\varphi}_2 \cdot sin(\varphi_2) + (\dot{\varphi}_2)^2 \cdot cos(\varphi_2)\Big) \cdot cos(\theta_2) - l_2 \cdot \dot{\varphi}_2 \cdot sin(\varphi_2) \cdot \dot{\theta}_2 \cdot sin(\theta_2) + \ddot{z}_{CT} \\
\ddot{z}_3 &= l_1 \cdot \Big(\ddot{\theta}_1 \cdot sin(\theta_1) + (\dot{\theta}_1)^2 \cdot cos(\theta_1)\Big) \cdot cos(\varphi_1) - l_1 \cdot \dot{\theta}_1 \cdot sin(\theta_1) \cdot \dot{\varphi}_1 \cdot sin(\varphi_1) \\
&\quad + l_1 \cdot \Big(\ddot{\varphi}_1 \cdot sin(\varphi_1) + (\dot{\varphi}_1)^2 \cdot cos(\varphi_1)\Big) \cdot cos(\theta_1) - l_1 \cdot \dot{\varphi}_1 \cdot sin(\varphi_1) \cdot \dot{\theta}_1 \cdot sin(\theta_1) \\
&\quad + l_2 \cdot \Big(\ddot{\theta}_2 \cdot sin(\theta_2) + (\dot{\theta}_2)^2 \cdot cos(\theta_2)\Big) \cdot cos(\varphi_2) - l_2 \cdot \dot{\theta}_2 \cdot sin(\theta_2) \cdot \dot{\varphi}_2 \cdot sin(\varphi_2) \\
&\quad + l_2 \cdot \Big(\ddot{\varphi}_2 \cdot sin(\varphi_2) + (\dot{\varphi}_2)^2 \cdot cos(\varphi_2)\Big) \cdot cos(\theta_2) - l_2 \cdot \dot{\varphi}_2 \cdot sin(\varphi_2) \cdot \dot{\theta}_2 \cdot sin(\theta_2) \\
&\quad + l_3 \cdot \Big(\ddot{\theta}_3 \cdot sin(\theta_3) + (\dot{\theta}_3)^2 \cdot cos(\theta_3)\Big) \cdot cos(\varphi_3) - l_3 \cdot \dot{\theta}_3 \cdot sin(\theta_3) \cdot \dot{\varphi}_3 \cdot sin(\varphi_3) \\
&\quad + l_3 \cdot \Big(\ddot{\varphi}_3 \cdot sin(\varphi_3) + (\dot{\varphi}_3)^2 \cdot cos(\varphi_3)\Big) \cdot cos(\theta_3) - l_3 \cdot \dot{\varphi}_3 \cdot sin(\varphi_3) \cdot \dot{\theta}_3 \cdot sin(\theta_3) + \ddot{z}_{CT}
\end{aligned}
$$

$$
\begin{aligned}
\ddot{z}_4 = l_1 \cdot \Big(\ddot{\theta}_1 \cdot sin(\theta_1) + (\dot{\theta}_1)^2 \cdot cos(\theta_1)\Big) \cdot cos(\varphi_1) - l_1 \cdot \dot{\theta}_1 \cdot sin(\theta_1) \cdot \dot{\varphi}_1 \cdot sin(\varphi_1) \\
+ l_1 \cdot \Big(\ddot{\varphi}_1 \cdot sin(\varphi_1) + (\dot{\varphi}_1)^2 \cdot cos(\varphi_1)\Big) \cdot cos(\theta_1) - l_1 \cdot \dot{\varphi}_1 \cdot sin(\varphi_1) \cdot \dot{\theta}_1 \cdot sin(\theta_1) \\
+ l_2 \cdot \Big(\ddot{\theta}_2 \cdot sin(\theta_2) + (\dot{\theta}_2)^2 \cdot cos(\theta_2)\Big) \cdot cos(\varphi_2) - l_2 \cdot \dot{\theta}_2 \cdot sin(\theta_2) \cdot \dot{\varphi}_2 \cdot sin(\varphi_2) \\
+ l_2 \cdot \Big(\ddot{\varphi}_2 \cdot sin(\varphi_2) + (\dot{\varphi}_2)^2 \cdot cos(\varphi_2)\Big) \cdot cos(\theta_2) - l_2 \cdot \dot{\varphi}_2 \cdot sin(\varphi_2) \cdot \dot{\theta}_2 \cdot sin(\theta_2) \\
+ l_3 \cdot \Big(\ddot{\theta}_3 \cdot sin(\theta_3) + (\dot{\theta}_3)^2 \cdot cos(\theta_3)\Big) \cdot cos(\varphi_3) - l_3 \cdot \dot{\theta}_3 \cdot sin(\theta_3) \cdot \dot{\varphi}_3 \cdot sin(\varphi_3) \\
+ l_3 \cdot \Big(\ddot{\varphi}_3 \cdot sin(\varphi_3) + (\dot{\varphi}_3)^2 \cdot cos(\varphi_3)\Big) \cdot cos(\theta_3) - l_3 \cdot \dot{\varphi}_3 \cdot sin(\varphi_3) \cdot \dot{\theta}_3 \cdot sin(\theta_3) \\
+ l_4 \cdot \Big(\ddot{\theta}_4 \cdot sin(\theta_4) + (\dot{\theta}_4)^2 \cdot cos(\theta_4)\Big) \cdot cos(\varphi_4) - l_4 \cdot \dot{\theta}_4 \cdot sin(\theta_4) \cdot \dot{\varphi}_4 \cdot sin(\varphi_4) \\
+ l_4 \cdot \Big(\ddot{\varphi}_4 \cdot sin(\varphi_4) + (\dot{\varphi}_4)^2 \cdot cos(\varphi_4)\Big) \cdot cos(\theta_4) - l_4 \cdot \dot{\varphi}_4 \cdot sin(\varphi_4) \cdot \dot{\theta}_4 \cdot sin(\theta_4) + \ddot{z}_{CT}
\end{aligned}
$$

E.2 Kinetics

$$
\begin{aligned}
\sum F_{x_1} :&\quad sin(\theta_1) \cdot T_1 - sin(\theta_2) \cdot T_2 - m_1 \cdot \ddot{x}_1 = 0 \\
\sum F_{y_1} :&\quad - sin(\varphi_1) \cdot T_1 + sin(\varphi_2) \cdot T_2 - m_1 \cdot \ddot{y}_1 = 0 \\
\sum F_{z_1} :&\quad T_1 \cdot cos(\theta_1) \cdot cos(\varphi_1) - T_2 \cdot cos(\theta_2) \cdot cos(\varphi_2) - m_1 \cdot g - m_1 \cdot \ddot{z}_1 = 0
\end{aligned}
$$

$$
\begin{aligned}
\sum F_{x_2} :&\quad sin(\theta_2) \cdot T_2 - sin(\theta_3) \cdot T_3 - m_2 \cdot \ddot{x}_2 = 0 \\
\sum F_{y_2} :&\quad - sin(\varphi_2) \cdot T_2 + sin(\varphi_3) \cdot T_3 - m_2 \cdot \ddot{y}_2 = 0 \\
\sum F_{z_2} :&\quad T_2 \cdot cos(\theta_2) \cdot cos(\varphi_2) - T_3 \cdot cos(\theta_3) \cdot cos(\theta_3) \cdot cos(\varphi_3) - m_2 \cdot g - m_2 \cdot \ddot{z}_2 = 0
\end{aligned}
$$

$$
\begin{aligned}
\sum F_{x_3} :&\quad sin(\theta_3) \cdot T_3 + 2 \cdot T_T \cdot sin(\theta_T - \theta_4) - T_W \cdot sin(\theta_W + \theta_4) - m_3 \cdot \ddot{x}_3 = 0 \\
\sum F_{y_3} :&\quad - sin(\varphi_3) \cdot T_3 + sin(\varphi_4) \cdot \big(cos(\theta_W \cdot T_W + cos(\theta_T) \cdot 2 \cdot T_T\big) - m_3 \cdot \ddot{y}_3 = 0 \\
\sum F_{z_3} :&\quad T_3 \cdot cos(\theta_3) \cdot cos(\varphi_3) - \big(cos(\theta_W) \cdot T_W + cos(\theta_T) \cdot 2 \cdot T_T\big) \cdot cos(\theta_4) \cdot cos(\varphi_4) \\
&\qquad - m_3 \cdot \ddot{z}_3 - m_3 \cdot g = 0
\end{aligned}
$$

$$
\begin{aligned}
\sum F_{x_4} :&\quad - 2 \cdot T_T \cdot sin(\theta_T - \theta_4) + sin(\theta_4 + \theta_W) \cdot T_W - m_4 \cdot \ddot{x}_4 = 0 \\
\sum F_{y_4} :&\quad - sin(\varphi_4) \cdot \big(cos(\theta_W) \cdot T_W + cos(\theta_T) \cdot 2 \cdot T_T\big) - m_4 \cdot \ddot{y}_4 = 0 \\
\sum F_{z_4} :&\quad \big(cos(\theta_W) \cdot T_W + cos(\theta_T) \cdot 2 \cdot T_T\big) \cdot cos(\theta_4) \cdot cos(\varphi_4) - m_4 \cdot g - m_4 \cdot \ddot{z}_4 = 0 \\
\sum M_{y_4} :&\quad \left(\frac{sin(\theta_W) \cdot D}{2} + cos(\theta_W) \cdot x_{cog,mp}\right) \cdot T_W - 2 \cdot cos(\theta_T) \cdot T_T \cdot x - I_{yy_{mp}} \cdot \ddot{\theta}_4 = 0
\end{aligned}
$$

E.3 Equations of motion in matrix form

$$\mathbf{A} = \begin{bmatrix} m_1\cdot l_1\cdot cos(\theta_1) & 0 & 0 & 0 & 0 & 0 & 0 & 0 & sin(\theta_1) & -sin(\theta_2) & 0 & 0 & 0 \\ 0 & -m_1\cdot l_1\cdot cos(\varphi_1) & 0 & 0 & 0 & 0 & 0 & 0 & -sin(\varphi_1) & sin(\varphi_2) & 0 & 0 & 0 \\ -m_1\cdot l_1\cdot sin(\theta_1)\cdot cos(\varphi_1) & -m_1\cdot l_1\cdot sin(\varphi_1)\cdot cos(\theta_1) & 0 & 0 & 0 & 0 & 0 & 0 & cos(\theta_1)\cdot cos(\varphi_1) & -cos(\theta_2)\cdot cos(\varphi_2) & 0 & 0 & 0 \\ m_2\cdot l_1\cdot cos(\theta_1) & 0 & m_2\cdot l_2\cdot cos(\theta_2) & 0 & 0 & 0 & 0 & 0 & 0 & sin(\theta_2) & -sin(\theta_3) & 0 & 0 \\ 0 & -m_2\cdot l_1\cdot cos(\varphi_1) & 0 & -m_2\cdot l_2\cdot cos(\varphi_2) & 0 & 0 & 0 & 0 & 0 & -sin(\varphi_2) & sin(\varphi_3) & 0 & 0 \\ -m_2\cdot l_1\cdot sin(\theta_1)\cdot cos(\varphi_1) & -m_2\cdot l_1\cdot sin(\varphi_1)\cdot cos(\theta_1) & -m_2\cdot l_2\cdot sin(\theta_2)\cdot cos(\varphi_2) & -m_2\cdot l_2\cdot sin(\varphi_2)\cdot cos(\theta_2) & 0 & 0 & 0 & 0 & 0 & cos(\theta_2)\cdot cos(\varphi_2) & -cos(\theta_3)\cdot cos(\varphi_3) & 0 & 0 \\ m_3\cdot l_1\cdot cos(\theta_1) & 0 & m_3\cdot l_2\cdot cos(\theta_2) & 0 & m_3\cdot l_3\cdot cos(\theta_3) & 0 & 0 & 0 & 0 & 0 & sin(\theta_3) & -sin(\theta_W+\theta_4) & -2\cdot sin(-\theta_T+\theta_4) \\ 0 & -m_3\cdot l_1\cdot cos(\varphi_1) & 0 & -m_3\cdot l_2\cdot cos(\varphi_2) & 0 & -m_3\cdot l_3\cdot cos(\varphi_3) & 0 & 0 & 0 & 0 & -sin(\varphi_3) & sin(\varphi_4)\cdot cos(\theta_W) & 2\cdot sin(\varphi_4)\cdot cos(\theta_T) \\ -m_3\cdot l_1\cdot sin(\theta_1)\cdot cos(\varphi_1) & -m_3\cdot l_1\cdot sin(\varphi_1)\cdot cos(\theta_1) & -m_3\cdot l_2\cdot sin(\theta_2)\cdot cos(\varphi_2) & -m_3\cdot l_2\cdot sin(\varphi_2)\cdot cos(\theta_2) & -m_3\cdot l_3\cdot sin(\theta_3)\cdot cos(\varphi_3) & -m_3\cdot l_3\cdot sin(\varphi_3)\cdot cos(\theta_3) & 0 & 0 & 0 & 0 & cos(\theta_3)\cdot cos(\varphi_3) & -cos(\theta_W)\cdot cos(\theta_4)\cdot cos(\varphi_4) & -2\cdot cos(\theta_T)\cdot cos(\theta_4)\cdot cos(\varphi_4) \\ m_4\cdot l_1\cdot cos(\theta_1) & 0 & m_4\cdot l_2\cdot cos(\theta_2) & 0 & m_4\cdot l_3\cdot cos(\theta_3) & 0 & m_4\cdot l_4\cdot cos(\theta_4) & 0 & 0 & 0 & 0 & sin(\theta_W+\theta_4) & 2\cdot sin(-\theta_T+\theta_4) \\ 0 & -m_4\cdot l_1\cdot cos(\varphi_1) & 0 & -m_4\cdot l_2\cdot cos(\varphi_2) & 0 & -m_4\cdot l_3\cdot cos(\varphi_3) & 0 & -m_4\cdot l_4\cdot cos(\varphi_4) & 0 & 0 & 0 & -sin(\varphi_4)\cdot cos(\theta_W) & -2\cdot sin(\varphi_4)\cdot cos(\theta_T) \\ -m_4\cdot l_1\cdot sin(\theta_1)\cdot cos(\varphi_1) & -m_4\cdot l_1\cdot sin(\varphi_1)\cdot cos(\theta_1) & -m_4\cdot l_2\cdot sin(\theta_2)\cdot cos(\varphi_2) & -m_4\cdot l_2\cdot sin(\varphi_2)\cdot cos(\theta_2) & -m_4\cdot l_3\cdot sin(\theta_3)\cdot cos(\varphi_3) & -m_4\cdot l_3\cdot sin(\varphi_3)\cdot cos(\theta_3) & -m_4\cdot l_4\cdot sin(\theta_4)\cdot cos(\varphi_4) & -m_4\cdot l_4\cdot sin(\varphi_4)\cdot cos(\theta_4) & 0 & 0 & 0 & cos(\theta_W)\cdot cos(\theta_4)\cdot cos(\varphi_4) & 2\cdot cos(\theta_T)\cdot cos(\theta_4)\cdot cos(\varphi_4) \\ 0 & 0 & 0 & 0 & 0 & 0 & -I_{yy_{mp}} & 0 & 0 & 0 & 0 & sin(\theta_W)\cdot\frac{1}{2}\cdot D+cos(\theta_W)\cdot X_{cog_{mp}} & -2\cdot cos(\theta_T)\cdot X \end{bmatrix}$$

$$\vec{B} = \begin{bmatrix} \ddot{\theta}_1 \\ \ddot{\varphi}_1 \\ \ddot{\theta}_2 \\ \ddot{\varphi}_2 \\ \ddot{\theta}_3 \\ \ddot{\varphi}_3 \\ \ddot{\theta}_4 \\ \ddot{\varphi}_4 \\ T_1 \\ T_2 \\ T_3 \\ T_W \\ T_T \end{bmatrix}$$

$$\vec{C} = \begin{bmatrix} m_1\cdot\left(l_1\cdot\dot{\theta}_1^2\cdot sin(\theta_1)+\ddot{X}_{ct}\right) \\ m_1\cdot\left(-l_1\cdot\dot{\varphi}_1^2\cdot sin(\varphi_1)+\ddot{Y}_{ct}\right) \\ m_1\cdot\left(l_1\cdot\dot{\theta}_1^2\cdot cos(\theta_1)\cdot cos(\varphi_1)+l_1\cdot{\dot{\varphi}_1}^2\cdot cos(\varphi_1)\cdot cos(\theta_1)-2\cdot l_1\cdot\dot{\theta}_1\cdot sin(\theta_1)\cdot\dot{\varphi}_1\cdot sin(\varphi_1)+\ddot{Z}_{ct}+g\right) \\ m_2\cdot\left(l_1\cdot\dot{\theta}_1^2\cdot sin(\theta_1)+l_2\cdot\dot{\theta}_2^2\cdot sin(\theta_2)+\ddot{X}_{ct}\right) \\ m_2\cdot\left(-l_1\cdot\dot{\varphi}_1^2\cdot sin(\varphi_1)-l_2\cdot\dot{\varphi}_2^2\cdot sin(\varphi_2)+\ddot{Y}_{ct}\right) \\ m_2\cdot\left(l_1\cdot\dot{\theta}_1^2\cdot cos(\theta_1)\cdot cos(\varphi_1)+l_1\cdot\dot{\varphi}_1^2\cdot cos(\varphi_1)\cdot cos(\theta_1)+l_2\cdot\dot{\theta}_2^2\cdot cos(\theta_2)\cdot cos(\varphi_2)+l_2\cdot\dot{\varphi}_2^2\cdot cos(\varphi_2)\cdot cos(\theta_2)-2\cdot l_1\cdot\dot{\theta}_1\cdot sin(\theta_1)\cdot\dot{\varphi}_1\cdot sin(\varphi_1)-2\cdot l_2\cdot\dot{\theta}_2\cdot sin(\theta_2)\cdot\dot{\varphi}_2\cdot sin(\varphi_2)+\ddot{Z}_{ct}+g\right) \\ m_3\cdot\left(l_1\cdot\dot{\theta}_1^2\cdot sin(\theta_1)+l_2\cdot\dot{\theta}_2^2\cdot sin(\theta_2)+l_3\cdot\dot{\theta}_3^2\cdot sin(\theta_3)+\ddot{X}_{ct}\right) \\ m_3\cdot\left(-l_1\cdot\dot{\varphi}_1^2\cdot sin(\varphi_1)-l_2\cdot\dot{\varphi}_2^2\cdot sin(\varphi_2)-l_3\cdot\dot{\varphi}_3^2\cdot sin(\varphi_3)+\ddot{Y}_{ct}\right) \\ m_3\cdot\left(l_1\cdot\dot{\theta}_1^2\cdot cos(\theta_1)\cdot cos(\varphi_1)+l_1\cdot\dot{\varphi}_1^2\cdot cos(\varphi_1)\cdot cos(\theta_1)+l_2\cdot\dot{\theta}_2^2\cdot cos(\theta_2)\cdot cos(\varphi_2)+l_2\cdot\dot{\varphi}_2^2\cdot cos(\varphi_2)\cdot cos(\theta_2)+l_3\cdot\dot{\theta}_3^2\cdot cos(\theta_3)\cdot cos(\varphi_3)+l_3\cdot\dot{\varphi}_3^2\cdot cos(\varphi_3)\cdot cos(\theta_3)-2\cdot l_1\cdot\dot{\theta}_1\cdot sin(\theta_1)\cdot\dot{\varphi}_1\cdot sin(\varphi_1)-2\cdot l_2\cdot\dot{\theta}_2\cdot sin(\theta_2)\cdot\dot{\varphi}_2\cdot sin(\varphi_2)-2\cdot l_3\cdot\dot{\theta}_3\cdot sin(\theta_3)\cdot\dot{\varphi}_3\cdot sin(\varphi_3)+\ddot{Z}_{ct}+g\right) \\ m_4\cdot\left(l_1\cdot\dot{\theta}_1^2\cdot sin(\theta_1)+l_2\cdot\dot{\theta}_2^2\cdot sin(\theta_2)+l_3\cdot\dot{\theta}_3^2\cdot sin(\theta_3)+l_4\cdot\dot{\theta}_4^2\cdot sin(\theta_4)+\ddot{X}_{ct}\right) \\ m_4\cdot\left(-l_1\cdot\dot{\varphi}_1^2\cdot sin(\varphi_1)-l_2\cdot\dot{\varphi}_2^2\cdot sin(\varphi_2)-l_3\cdot\dot{\varphi}_3^2\cdot sin(\varphi_3)-l_4\cdot\dot{\varphi}_4^2\cdot sin(\varphi_4)+\ddot{Y}_{ct}\right) \\ m_4\cdot\left(l_1\cdot\dot{\theta}_1^2\cdot cos(\theta_1)\cdot cos(\varphi_1)+l_1\cdot\dot{\varphi}_1^2\cdot cos(\varphi_1)\cdot cos(\theta_1)+l_2\cdot\dot{\theta}_2^2\cdot cos(\theta_2)\cdot cos(\varphi_2)+l_2\cdot\dot{\varphi}_2^2\cdot cos(\varphi_2)\cdot cos(\theta_2)+l_3\cdot\dot{\theta}_3^2\cdot cos(\theta_3)\cdot cos(\varphi_3)+l_3\cdot\dot{\varphi}_3^2\cdot cos(\varphi_3)\cdot cos(\theta_3)+l_4\cdot\dot{\theta}_4^2\cdot cos(\theta_4)\cdot cos(\varphi_4)+l_4\cdot\dot{\varphi}_4^2\cdot cos(\varphi_4)\cdot cos(\theta_4)-2\cdot l_1\cdot\dot{\theta}_1\cdot sin(\theta_1)\cdot\dot{\varphi}_1\cdot sin(\varphi_1)-2\cdot l_2\cdot\dot{\theta}_2\cdot sin(\theta_2)\cdot\dot{\varphi}_2\cdot sin(\varphi_2)-2\cdot l_3\cdot\dot{\theta}_3\cdot sin(\theta_3)\cdot\dot{\varphi}_3\cdot sin(\varphi_3)-2\cdot l_4\cdot\dot{\theta}_4\cdot sin(\theta_4)\cdot\dot{\varphi}_4\cdot sin(\varphi_4)+\ddot{Z}_{ct}+g\right) \\ 0 \end{bmatrix}$$

F | EoM compensated case

F.1 Kinematics

$$
\begin{aligned}
x_1 &= -l_1 \cdot sin(\theta_1) + x_{CT} \\
x_2 &= -l_1 \cdot sin(\theta_1) - l_2 \cdot sin(\theta_2) + x_{CT} \\
x_3 &= -l_1 \cdot sin(\theta_1) - l_2 \cdot sin(\theta_2) - l_3 \cdot sin(\theta_3) + x_{CT} \\
x_4 &= -l_1 \cdot sin(\theta_1) - l_2 \cdot sin(\theta_2) - l_3 \cdot sin(\theta_3) + l_T \cdot sin(\theta_{Tstatic} - \theta_T) - cos(\theta_4) \cdot x + x_{CT}
\end{aligned}
$$

$$
\begin{aligned}
y_1 &= l_1 \cdot sin(\varphi_1) + y_{CT} \\
y_2 &= l_1 \cdot sin(\varphi_1) + l_2 \cdot sin(\varphi_2) + y_{CT} \\
y_3 &= l_1 \cdot sin(\varphi_1) + l_2 \cdot sin(\varphi_2) + l_3 \cdot sin(\varphi_3) + y_{CT} \\
y_4 &= l_1 \cdot sin(\varphi_1) + l_2 \cdot sin(\varphi_2) + l_3 \cdot sin(\varphi_3) + \big(cos(\theta_{Tstatic} - \theta_T) \cdot l_T - sin(\theta_4) \cdot x\big) \cdot sin(\varphi_4) \\
&\qquad + y_{CT}
\end{aligned}
$$

$$
\begin{aligned}
z_1 &= -l_1 \cdot cos(\theta_1) \cdot cos(\varphi_1) + z_{CT} \\
z_2 &= -l_1 \cdot cos(\theta_1) \cdot cos(\varphi_1) - l_2 \cdot cos(\theta_2) \cdot cos(\varphi_2) + z_{CT} \\
z_3 &= -l_1 \cdot cos(\theta_1) \cdot cos(\varphi_1) - l_2 \cdot cos(\theta_2) \cdot cos(\varphi_2) - l_3 \cdot cos(\theta_3) \cdot cos(\varphi_3) + z_{CT} \\
z_4 &= -l_1 \cdot cos(\theta_1) \cdot cos(\varphi_1) - l_2 \cdot cos(\theta_2) \cdot cos(\varphi_2) - l_3 \cdot cos(\theta_3) \cdot cos(\varphi_3) \\
&\qquad - \big(cos(\theta_{Tstatic} - \theta_T) \cdot l_T - sin(\theta_4) \cdot x\big) \cdot cos(\varphi_4) + z_{CT}
\end{aligned}
$$

$$
\begin{aligned}
\dot{x}_1 &= -l_1 \cdot \dot{\theta}_1 \cdot cos(\theta_1) + \dot{x}_{CT} \\
\dot{x}_2 &= -l_1 \cdot \dot{\theta}_1 \cdot cos(\theta_1) - l_2 \cdot \dot{\theta}_2 \cdot cos(\theta_2) + \dot{x}_{CT} \\
\dot{x}_3 &= -l_1 \cdot \dot{\theta}_1 \cdot cos(\theta_1) - l_2 \cdot \dot{\theta}_2 \cdot cos(\theta_2) - l_3 \cdot \dot{\theta}_3 \cdot cos(\theta_3) + \dot{x}_{CT} \\
\dot{x}_4 &= -l_1 \cdot \dot{\theta}_1 \cdot cos(\theta_1) - l_2 \cdot \dot{\theta}_2 \cdot cos(\theta_2) - l_3 \cdot \dot{\theta}_3 \cdot cos(\theta_3) - l_T \cdot \dot{\theta}_T \cdot cos(\theta_{Tstatic} - \theta_T) \\
&\qquad + sin(\theta_4) \cdot \dot{\theta}_4 \cdot x + \dot{x}_{CT}
\end{aligned}
$$

$$
\begin{aligned}
\dot{y}_1 &= l_1 \cdot \dot{\varphi}_1 \cdot cos(\varphi_1) + \dot{y}_{CT} \\
\dot{y}_2 &= l_1 \cdot \dot{\varphi}_1 \cdot cos(\varphi_1) + l_2 \cdot \dot{\varphi}_2 \cdot cos(\varphi_2) + \dot{y}_{CT} \\
\dot{y}_3 &= l_1 \cdot \dot{\varphi}_1 \cdot cos(\varphi_1) + l_2 \cdot \dot{\varphi}_2 \cdot cos(\varphi_2) + l_3 \cdot \dot{\varphi}_3 \cdot cos(\varphi_3) + \dot{y}_{CT} \\
\dot{y}_4 &= l_1 \cdot \dot{\varphi}_1 \cdot cos(\varphi_1) + l_2 \cdot \dot{\varphi}_2 \cdot cos(\varphi_2) + l_3 \cdot \dot{\varphi}_3 \cdot cos(\varphi_3) + l_T \cdot \dot{\theta}_T \cdot sin(\theta_{Tstatic} - \theta_T) \cdot sin(\varphi_4) \\
&\qquad + l_T \cdot \dot{\varphi}_4 \cdot cos(\varphi_4) \cdot cos(\theta_{Tstatic} - \theta_T) - x \cdot \dot{\theta}_4 \cdot cos(\theta_4) \cdot sin(\varphi_4) \\
&\qquad - x \cdot \dot{\varphi}_4 \cdot cos(\varphi_4) \cdot sin(\theta_4) + \dot{y}_{CT}
\end{aligned}
$$

$$
\begin{aligned}
\dot{z}_1 &= l_1 \cdot \dot{\theta}_1 \cdot sin(\theta_1) \cdot cos(\varphi_1) + l_1 \cdot \dot{\varphi}_1 \cdot cos(\theta_1) \cdot sin(\varphi_1) + \dot{z}_{CT} \\
\dot{z}_2 &= l_1 \cdot \dot{\theta}_1 \cdot sin(\theta_1) \cdot cos(\varphi_1) + l_1 \cdot \dot{\varphi}_1 \cdot cos(\theta_1) \cdot sin(\varphi_1) \\
&\qquad + l_2 \cdot \dot{\theta}_2 \cdot sin(\theta_2) \cdot cos(\varphi_2) + l_2 \cdot \dot{\varphi}_2 \cdot cos(\theta_2) \cdot sin(\varphi_2) + \dot{z}_{CT} \\
\dot{z}_3 &= l_1 \cdot \dot{\theta}_1 \cdot sin(\theta_1) \cdot cos(\varphi_1) + l_1 \cdot \dot{\varphi}_1 \cdot cos(\theta_1) \cdot sin(\varphi_1) \\
&\qquad + l_2 \cdot \dot{\theta}_2 \cdot sin(\theta_2) \cdot cos(\varphi_2) + l_2 \cdot \dot{\varphi}_2 \cdot cos(\theta_2) \cdot sin(\varphi_2) \\
&\qquad + l_3 \cdot \dot{\theta}_3 \cdot sin(\theta_3) \cdot cos(\varphi_3) + l_3 \cdot \dot{\varphi}_3 \cdot cos(\theta_3) \cdot sin(\varphi_3) + \dot{z}_{CT}
\end{aligned}
$$

$$
\begin{aligned}
\dot{z}_4 = {} & l_1 \cdot \dot{\theta}_1 \cdot sin(\theta_1) \cdot cos(\varphi_1) + l_1 \cdot \dot{\varphi}_1 \cdot cos(\theta_1) \cdot sin(\varphi_1) \\
& + l_2 \cdot \dot{\theta}_2 \cdot sin(\theta_2) \cdot cos(\varphi_2) + l_2 \cdot \dot{\varphi}_2 \cdot cos(\theta_2) \cdot sin(\varphi_2) \\
& + l_3 \cdot \dot{\theta}_3 \cdot sin(\theta_3) \cdot cos(\varphi_3) + l_3 \cdot \dot{\varphi}_3 \cdot cos(\theta_3) \cdot sin(\varphi_3) \\
& - l_T \cdot \dot{\theta}_T \cdot sin(\theta_{Tstatic} - \theta_T) \cdot cos(\varphi_4) + l_T \cdot \dot{\varphi}_4 \cdot cos(\theta_{Tstatic} - \theta_T) \cdot sin(\varphi_4) \\
& + x \cdot \dot{\theta}_4 \cdot cos(\theta_4) \cdot cos(\varphi_4) - x \cdot \dot{\varphi}_4 \cdot sin(\varphi_4) \cdot sin(\theta_4) + \dot{z}_{CT}
\end{aligned}
$$

$$
\begin{aligned}
\ddot{x}_1 = {} & -l_1 \cdot \ddot{\theta}_1 \cdot cos(\theta_1) + l_1 \cdot (\dot{\theta_1})^2 \cdot sin(\theta_1) + \ddot{x}_{CT} \\
\ddot{x}_2 = {} & -l_1 \cdot \ddot{\theta}_1 \cdot cos(\theta_1) + l_1 \cdot (\dot{\theta_1})^2 \cdot sin(\theta_1) - l_2 \cdot \ddot{\theta}_2 \cdot cos(\theta_2) + l_2 \cdot (\dot{\theta_2})^2 \cdot sin(\theta_2) + \ddot{x}_{CT} \\
\ddot{x}_3 = {} & -l_1 \cdot \ddot{\theta}_1 \cdot cos(\theta_1) + l_1 \cdot (\dot{\theta_1})^2 \cdot sin(\theta_1) - l_2 \cdot \ddot{\theta}_2 \cdot cos(\theta_2) + l_2 \cdot (\dot{\theta_2})^2 \cdot sin(\theta_2) \\
& - l_3 \cdot \ddot{\theta}_3 \cdot cos(\theta_3) + l_3 \cdot (\dot{\theta_3})^2 \cdot sin(\theta_3) + \ddot{x}_{CT} \\
\ddot{x}_4 = {} & -l_1 \cdot \ddot{\theta}_1 \cdot cos(\theta_1) + l_1 \cdot (\dot{\theta_1})^2 \cdot sin(\theta_1) - l_2 \cdot \ddot{\theta}_2 \cdot cos(\theta_2) + l_2 \cdot (\dot{\theta_2})^2 \cdot sin(\theta_2) \\
& - l_3 \cdot \ddot{\theta}_3 \cdot cos(\theta_3) + l_3 \cdot (\dot{\theta_3})^2 \cdot sin(\theta_3) - l_T \cdot \ddot{\theta}_T \cdot cos(\theta_{Tstatic} - \theta_T) \\
& - l_T \cdot (\dot{\theta_T})^2 \cdot sin(\theta_{Tstatic} - \theta_T) + x \cdot \ddot{\theta}_4 \cdot sin(\theta_4) + x \cdot (\dot{\theta_4})^2 \cdot cos(\theta_4) + \ddot{x}_{CT}
\end{aligned}
$$

$$
\begin{aligned}
\ddot{y}_1 = {} & l_1 \cdot \ddot{\varphi}_1 \cdot cos(\varphi_1) - l_1 \cdot (\dot{\varphi}_1)^2 \cdot sin(\varphi_1) + \ddot{y}_{CT} \\
\ddot{y}_2 = {} & l_1 \cdot \ddot{\varphi}_1 \cdot cos(\varphi_1) - l_1 \cdot (\dot{\varphi}_1)^2 \cdot sin(\varphi_1) + l_2 \cdot \ddot{\varphi}_2 \cdot cos(\varphi_2) - l_2 \cdot (\dot{\varphi}_2)^2 \cdot sin(\varphi_2) + \ddot{y}_{CT} \\
\ddot{y}_3 = {} & l_1 \cdot \ddot{\varphi}_1 \cdot cos(\varphi_1) - l_1 \cdot (\dot{\varphi}_1)^2 \cdot sin(\varphi_1) + l_2 \cdot \ddot{\varphi}_2 \cdot cos(\varphi_2) - l_2 \cdot (\dot{\varphi}_2)^2 \cdot sin(\varphi_2) \\
& + l_3 \cdot \ddot{\varphi}_3 \cdot cos(\varphi_3) - l_3 \cdot (\dot{\varphi}_3)^2 \cdot sin(\varphi_3) + \ddot{y}_{CT} \\
\ddot{y}_4 = {} & l_1 \cdot \ddot{\varphi}_1 \cdot cos(\varphi_1) - l_1 \cdot (\dot{\varphi}_1)^2 \cdot sin(\varphi_1) + l_2 \cdot \ddot{\varphi}_2 \cdot cos(\varphi_2) - l_2 \cdot (\dot{\varphi}_2)^2 \cdot sin(\varphi_2) \\
& + l_3 \cdot \ddot{\varphi}_3 \cdot cos(\varphi_3) - l_3 \cdot (\dot{\varphi}_3)^2 \cdot sin(\varphi_3) + l_T \cdot \ddot{\theta}_T \cdot sin(\theta_{Tstatic} - \theta_T) \cdot sin(\varphi_4) \\
& - l_T \cdot (\dot{\theta_T})^2 \cdot cos(\theta_{Tstatic} - \theta_T) \cdot sin(\varphi_4) + l_T \cdot \dot{\theta}_T \dot{\varphi}_4 \cdot sin(\theta_{Tstatic} - \theta_T) \cdot cos(\varphi_4) \\
& + l_T \cdot \ddot{\varphi}_4 \cdot cos(\varphi_4) \cdot cos(\theta_{Tstatic} - \theta_T) - l_T \cdot (\dot{\varphi}_4)^2 \cdot sin(\varphi_4) \cdot cos(\theta_{Tstatic} - \theta_T) \\
& + l_T \cdot \dot{\varphi}_4 \cdot \dot{\theta}_T \cdot cos(\varphi_4) \cdot sin(\theta_{Tstatic} - \theta_T) - x \cdot \ddot{\theta}_4 \cdot cos(\theta_4) \cdot sin(\varphi_4) \\
& + x \cdot (\dot{\theta}_4)^2 \cdot sin(\theta_4) \cdot sin(\varphi_4) - x \cdot \dot{\theta}_4 \cdot \dot{\varphi}_4 \cdot cos(\theta_4) \cdot cos(\varphi_4) - x \cdot \ddot{\varphi}_4 \cdot cos(\varphi_4) \cdot sin(\theta_4) \\
& + x \cdot (\dot{\varphi}_4)^2 \cdot sin(\varphi_4) \cdot sin(\theta_4) - x \cdot \dot{\varphi}_4 \cdot \dot{\theta}_4 \cdot cos(\varphi_4) \cdot cos(\theta_4) + \ddot{y}_{CT}
\end{aligned}
$$

$$
\begin{aligned}
\ddot{z}_1 = {} & l_1 \cdot \Big(\ddot{\theta}_1 \cdot sin(\theta_1) + (\dot{\theta}_1)^2 \cdot cos(\theta_1)\Big) \cdot cos(\varphi_1) - l_1 \cdot \dot{\theta}_1 \cdot sin(\theta_1) \cdot \dot{\varphi}_1 \cdot sin(\varphi_1) \\
& + l_1 \cdot \Big(\ddot{\varphi}_1 \cdot sin(\varphi_1) + (\dot{\varphi}_1)^2 \cdot cos(\varphi_1)\Big) \cdot cos(\theta_1) - l_1 \cdot \dot{\varphi}_1 \cdot sin(\varphi_1) \cdot \dot{\theta}_1 \cdot sin(\theta_1) + \ddot{z}_{CT} \\
\ddot{z}_2 = {} & l_1 \cdot \Big(\ddot{\theta}_1 \cdot sin(\theta_1) + (\dot{\theta}_1)^2 \cdot cos(\theta_1)\Big) \cdot cos(\varphi_1) - l_1 \cdot \dot{\theta}_1 \cdot sin(\theta_1) \cdot \dot{\varphi}_1 \cdot sin(\varphi_1) \\
& + l_1 \cdot \Big(\ddot{\varphi}_1 \cdot sin(\varphi_1) + (\dot{\varphi}_1)^2 \cdot cos(\varphi_1)\Big) \cdot cos(\theta_1) - l_1 \cdot \dot{\varphi}_1 \cdot sin(\varphi_1) \cdot \dot{\theta}_1 \cdot sin(\theta_1) \\
& + l_2 \cdot \Big(\ddot{\theta}_2 \cdot sin(\theta_2) + (\dot{\theta}_2)^2 \cdot cos(\theta_2)\Big) \cdot cos(\varphi_2) - l_2 \cdot \dot{\theta}_2 \cdot sin(\theta_2) \cdot \dot{\varphi}_2 \cdot sin(\varphi_2) \\
& + l_2 \cdot \Big(\ddot{\varphi}_2 \cdot sin(\varphi_2) + (\dot{\varphi}_2)^2 \cdot cos(\varphi_2)\Big) \cdot cos(\theta_2) - l_2 \cdot \dot{\varphi}_2 \cdot sin(\varphi_2) \cdot \dot{\theta}_2 \cdot sin(\theta_2) + \ddot{z}_{CT}
\end{aligned}
$$

$$
\begin{aligned}
\ddot{z}_3 = {} & l_1 \cdot \Big(\ddot{\theta}_1 \cdot sin(\theta_1) + (\dot{\theta}_1)^2 \cdot cos(\theta_1)\Big) \cdot cos(\varphi_1) - l_1 \cdot \dot{\theta}_1 \cdot sin(\theta_1) \cdot \dot{\varphi}_1 \cdot sin(\varphi_1) \\
& + l_1 \cdot \Big(\ddot{\varphi}_1 \cdot sin(\varphi_1) + (\dot{\varphi}_1)^2 \cdot cos(\varphi_1)\Big) \cdot cos(\theta_1) - l_1 \cdot \dot{\varphi}_1 \cdot sin(\varphi_1) \cdot \dot{\theta}_1 \cdot sin(\theta_1) \\
& + l_2 \cdot \Big(\ddot{\theta}_2 \cdot sin(\theta_2) + (\dot{\theta}_2)^2 \cdot cos(\theta_2)\Big) \cdot cos(\varphi_2) - l_2 \cdot \dot{\theta}_2 \cdot sin(\theta_2) \cdot \dot{\varphi}_2 \cdot sin(\varphi_2) \\
& + l_2 \cdot \Big(\ddot{\varphi}_2 \cdot sin(\varphi_2) + (\dot{\varphi}_2)^2 \cdot cos(\varphi_2)\Big) \cdot cos(\theta_2) - l_2 \cdot \dot{\varphi}_2 \cdot sin(\varphi_2) \cdot \dot{\theta}_2 \cdot sin(\theta_2) \\
& + l_3 \cdot \Big(\ddot{\theta}_3 \cdot sin(\theta_3) + (\dot{\theta}_3)^2 \cdot cos(\theta_3)\Big) \cdot cos(\varphi_3) - l_3 \cdot \dot{\theta}_3 \cdot sin(\theta_3) \cdot \dot{\varphi}_3 \cdot sin(\varphi_3) \\
& + l_3 \cdot \Big(\ddot{\varphi}_3 \cdot sin(\varphi_3) + (\dot{\varphi}_3)^2 \cdot cos(\varphi_3)\Big) \cdot cos(\theta_3) - l_3 \cdot \dot{\varphi}_3 \cdot sin(\varphi_3) \cdot \dot{\theta}_3 \cdot sin(\theta_3) + \ddot{z}_{CT} \\
\ddot{z}_4 = {} & l_1 \cdot \Big(\ddot{\theta}_1 \cdot sin(\theta_1) + (\dot{\theta}_1)^2 \cdot cos(\theta_1)\Big) \cdot cos(\varphi_1) - l_1 \cdot \dot{\theta}_1 \cdot sin(\theta_1) \cdot \dot{\varphi}_1 \cdot sin(\varphi_1) \\
& + l_1 \cdot \Big(\ddot{\varphi}_1 \cdot sin(\varphi_1) + (\dot{\varphi}_1)^2 \cdot cos(\varphi_1)\Big) \cdot cos(\theta_1) - l_1 \cdot \dot{\varphi}_1 \cdot sin(\varphi_1) \cdot \dot{\theta}_1 \cdot sin(\theta_1) \\
& + l_2 \cdot \Big(\ddot{\theta}_2 \cdot sin(\theta_2) + (\dot{\theta}_2)^2 \cdot cos(\theta_2)\Big) \cdot cos(\varphi_2) - l_2 \cdot \dot{\theta}_2 \cdot sin(\theta_2) \cdot \dot{\varphi}_2 \cdot sin(\varphi_2) \\
& + l_2 \cdot \Big(\ddot{\varphi}_2 \cdot sin(\varphi_2) + (\dot{\varphi}_2)^2 \cdot cos(\varphi_2)\Big) \cdot cos(\theta_2) - l_2 \cdot \dot{\varphi}_2 \cdot sin(\varphi_2) \cdot \dot{\theta}_2 \cdot sin(\theta_2) \\
& + l_3 \cdot \Big(\ddot{\theta}_3 \cdot sin(\theta_3) + (\dot{\theta}_3)^2 \cdot cos(\theta_3)\Big) \cdot cos(\varphi_3) - l_3 \cdot \dot{\theta}_3 \cdot sin(\theta_3) \cdot \dot{\varphi}_3 \cdot sin(\varphi_3) \\
& + l_3 \cdot \Big(\ddot{\varphi}_3 \cdot sin(\varphi_3) + (\dot{\varphi}_3)^2 \cdot cos(\varphi_3)\Big) \cdot cos(\theta_3) - l_3 \cdot \dot{\varphi}_3 \cdot sin(\varphi_3) \cdot \dot{\theta}_3 \cdot sin(\theta_3) \\
& - l_T \cdot \ddot{\theta}_T \cdot sin(\theta_{Tstatic} - \theta_T) \cdot cos(\varphi_4) + l_T \cdot (\dot{\theta}_T)^2 \cdot cos(\theta_{Tstatic} - \theta_T) \cdot cos(\varphi_4) \\
& + l_T \cdot \dot{\theta}_T \cdot \dot{\varphi}_4 \cdot sin(\theta_{Tstatic} - \theta_T) \cdot sin(\varphi_4) + l_T \cdot \ddot{\varphi}_4 \cdot sin(\varphi_4) \cdot cos(\theta_{Tstatic} - \theta_T) \\
& + l_T \cdot (\dot{\varphi}_4)^2 \cdot cos(\varphi_4) \cdot cos(\theta_{Tstatic} - \theta_T) + l_T \cdot \dot{\varphi}_4 \cdot \dot{\theta}_T \cdot sin(\varphi_4) \cdot sin(\theta_{Tstatic} - \theta_T) \\
& + x \cdot \ddot{\theta}_4 \cdot cos(\theta_4) \cdot cos(\varphi_4) - x \cdot (\dot{\theta}_4)^2 \cdot sin(\theta_4) \cdot cos(\varphi_4) - x \cdot \dot{\theta}_4 \cdot \dot{\varphi}_4 \cdot cos(\theta_4) \cdot sin(\varphi_4) \\
& - x \cdot \ddot{\varphi}_4 \cdot sin(\varphi_4) \cdot sin(\theta_4) - x \cdot (\dot{\varphi}_4)^2 \cdot cos(\varphi_4) \cdot sin(\theta_4) - x \cdot \dot{\varphi}_4 \cdot \dot{\theta}_4 \cdot sin(\varphi_4) \cdot cos(\theta_4) \\
& + \ddot{z}_{CT}
\end{aligned}
$$

$$
\begin{aligned}
x_{wcp} = {} & -l_1 \cdot sin(\theta_1) - l_2 \cdot sin(\theta_2) - l_3 \cdot sin(\theta_3) + l_T \cdot sin(\theta_{Tstatic} - \theta_T) - cos(\theta_4) \cdot x \\
& - cos(\theta_4) \cdot x_{cog,mp} + sin(\theta_4) \cdot \frac{1}{2} \cdot D + x_{CT} \\
y_{wcp} = {} & l_1 \cdot sin(\varphi_1) + l_2 \cdot sin(\varphi_2) + l_3 \cdot sin(\varphi_3) + \big(cos(\theta_{Tstatic} - \theta_T) \cdot l_T - sin(\theta_4) \cdot x\big) \cdot sin(\varphi_4) \\
& - sin(\varphi_4) \cdot \frac{1}{2} \cdot D + y_{CT} \\
z_{wcp} = {} & -l_1 \cdot cos(\theta_1) \cdot cos(\varphi_1) - l_2 \cdot cos(\theta_2) \cdot cos(\varphi_2) - l_3 \cdot cos(\theta_3) \cdot cos(\varphi_3) \\
& - \big(cos(\theta_{Tstatic} - \theta_T) \cdot l_T - sin(\theta_4) \cdot x\big) \cdot cos(\varphi_4) \\
& + \left(sin(\theta_4) \cdot x_{cog,mp} + cos(\theta_4) \cdot \frac{1}{2} \cdot D\right) \cdot cos(\varphi_4) + z_{CT}
\end{aligned}
$$

$$
\begin{aligned}
\dot{x}_{wcp} = {} & -l_1 \cdot \dot{\theta}_1 \cdot cos(\theta_1) - l_2 \cdot \dot{\theta}_2 \cdot cos(\theta_2) - l_3 \cdot \dot{\theta}_3 \cdot cos(\theta_3) - l_T \cdot \dot{\theta}_T \cdot cos(\theta_{Tstatic} - \theta_T) \\
& + sin(\theta_4) \cdot \dot{\theta}_4 \cdot x + x_{cog,mp} \cdot \dot{\theta}_4 \cdot sin(\theta_4) + \dot{\theta}_4 \cdot cos(\theta_4) \cdot \frac{1}{2} \cdot D + \dot{x}_{CT} \\
\dot{y}_{wcp} = {} & l_1 \cdot \dot{\varphi}_1 \cdot cos(\varphi_1) + l_2 \cdot \dot{\varphi}_2 \cdot cos(\varphi_2) + l_3 \cdot \dot{\varphi}_3 \cdot cos(\varphi_3) + l_T \cdot \dot{\theta}_T \cdot sin(\theta_{Tstatic} - \theta_T) \cdot sin(\varphi_4) \\
& + l_T \cdot \dot{\varphi}_4 \cdot cos(\varphi_4) \cdot cos(\theta_{Tstatic} - \theta_T) - x \cdot \dot{\theta}_4 \cdot cos(\theta_4) \cdot sin(\varphi_4) \\
& - x \cdot \dot{\varphi}_4 \cdot cos(\varphi_4) \cdot sin(\theta_4) - \frac{1}{2} \cdot D \cdot \dot{\varphi}_4 + \dot{y}_{CT}
\end{aligned}
$$

$$\begin{aligned}\dot{z}_{wcp} = {} & l_1 \cdot \dot{\theta}_1 \cdot sin(\theta_1) \cdot cos(\varphi_1) + l_1 \cdot \dot{\varphi}_1 \cdot cos(\theta_1) \cdot sin(\varphi_1) \\ & + l_2 \cdot \dot{\theta}_2 \cdot sin(\theta_2) \cdot cos(\varphi_2) + l_2 \cdot \dot{\varphi}_2 \cdot cos(\theta_2) \cdot sin(\varphi_2) \\ & + l_3 \cdot \dot{\theta}_3 \cdot sin(\theta_3) \cdot cos(\varphi_3) + l_3 \cdot \dot{\varphi}_3 \cdot cos(\theta_3) \cdot sin(\varphi_3) \\ & - l_T \cdot \dot{\theta}_T \cdot sin(\theta_{Tstatic} - \theta_T) \cdot cos(\varphi_4) + l_T \cdot \dot{\varphi}_4 \cdot cos(\theta_{Tstatic} - \theta_T) \cdot sin(\varphi_4) \\ & + x \cdot \dot{\theta}_4 \cdot cos(\theta_4) \cdot cos(\varphi_4) - x \cdot \dot{\varphi}_4 \cdot sin(\varphi_4) \cdot sin(\theta_4) + x_{cog,mp} \cdot \dot{\theta}_4 \cdot cos(\theta_4) \cdot cos(\varphi_4) \\ & - x_{cog,mp} \cdot \dot{\varphi}_4 \cdot sin(\varphi_4) \cdot sin(\theta_4) - \frac{1}{2} \cdot D \cdot \dot{\theta}_4 \cdot sin(\theta_4) \cdot cos(\varphi_4) \\ & - \frac{1}{2} \cdot D \cdot \dot{\varphi}_4 \cdot sin(\varphi_4) \cdot cos(\theta_4) + \dot{z}_{CT}\end{aligned}$$

$$\begin{aligned}\theta_W &= tan^{-1}\left(\frac{x_3 - x_{wcp}}{z_3 - z_{wcp}}\right) \\ \theta_{Tstatic} &= sin^{-1}\left(\frac{x}{l_T}\right) \\ \theta_{Wstatic} &= tan^{-1}\left(\frac{x_{cog,mp}}{cos(\theta_{Tstatic}) \cdot l_T - 1/2 \cdot D}\right) \\ L_{S0} &= \sqrt{(cos(\theta_{Tstatic}) \cdot l_T - 1/2 \cdot D)^2 + (x_{cog,mp})^2)} \\ & \quad - \frac{m_4 \cdot g \cdot x}{k \cdot (cos(\theta_{Wstatic}) \cdot (x + x_{cog,mp}) + sin(\theta_{Wstatic}) \cdot 1/2 \cdot D)}\end{aligned}$$

F.2 Kinetics

$$\begin{aligned}T_W = {} & k_{spring} \cdot \left(\sqrt{(x_3 - x_{wcp})^2 + (y_3 - y_{wcp})^2 + (z_3 - z_{wcp})^2} - L_{s0}\right) \\ & + c_{damp} \cdot \frac{1}{\sqrt{(x_3 - x_{wcp})^2 + (y_3 - y_{wcp})^2 + (z_3 - z_{wcp})^2}} \cdot \Big(x_3 \cdot \dot{x}_3 - \dot{x}_3 \cdot x_{wcp} \\ & - x_3 \cdot \dot{x}_{wcp} + x_{wcp} \cdot \dot{x}_{wcp} + y_3 \cdot \dot{y}_3 - \dot{y}_3 \cdot y_{wcp} - y_3 \cdot \dot{y}_{wcp} + y_{wcp} \cdot \dot{y}_{wcp} + z_3 \cdot \dot{z}_3 \\ & - \dot{z}_3 \cdot z_{wcp} - z_3 \cdot \dot{z}_{wcp} + z_{wcp} \cdot \dot{z}_{wcp}\Big)\end{aligned}$$

$$\begin{aligned}&\sum F_{x_1}: \quad sin(\theta_1) \cdot T_1 - sin(\theta_2) \cdot T_2 - m_1 \cdot \ddot{x}_1 = 0 \\ &\sum F_{y_1}: \quad - sin(\varphi_1) \cdot T_1 + sin(\varphi_2) \cdot T_2 - m_1 \cdot \ddot{y}_1 = 0 \\ &\sum F_{z_1}: \quad T_1 \cdot cos(\theta_1) \cdot cos(\varphi_1) - T_2 \cdot cos(\theta_2) \cdot cos(\varphi_2) - m_1 \cdot g - m_1 \cdot \ddot{z}_1 = 0\end{aligned}$$

$$\begin{aligned}&\sum F_{x_2}: \quad sin(\theta_2) \cdot T_2 - sin(\theta_3) \cdot T_3 - m_2 \cdot \ddot{x}_2 = 0 \\ &\sum F_{y_2}: \quad - sin(\varphi_2) \cdot T_2 + sin(\varphi_3) \cdot T_3 - m_2 \cdot \ddot{y}_2 = 0 \\ &\sum F_{z_2}: \quad T_2 \cdot cos(\theta_2) \cdot cos(\varphi_2) - T_3 \cdot cos(\theta_3) \cdot cos(\theta_3) \cdot cos(\varphi_3) - m_2 \cdot g - m_2 \cdot \ddot{z}_2 = 0\end{aligned}$$

$$
\begin{aligned}
\sum F_{x_3}:&\quad sin(\theta_3)\cdot T_3 + 2\cdot T_T\cdot sin(\theta_{Tstatic}-\theta_T) - T_W\cdot sin(\theta_W) - m_3\cdot \ddot{x}_3 = 0\\
\sum F_{y_3}:&\quad -sin(\varphi_3)\cdot T_3 + sin(\varphi_4)\cdot \big(cos(\theta_W)\cdot T_W + cos(\theta_{Tstatic}-\theta_T)\cdot 2\cdot T_T\big) - m_3\cdot \ddot{y}_3 = 0\\
\sum F_{z_3}:&\quad T_3\cdot cos(\theta_3)\cdot cos(\varphi_3) - 2\cdot T_T\cdot cos(\theta_{Tstatic}-\theta_T)\cdot cos(\varphi_4) - T_W\cdot cos(\theta_W)\cdot cos(\varphi_4)\\
&\qquad - m_3\cdot g - m_3\cdot \ddot{z}_3 = 0
\end{aligned}
$$

$$
\begin{aligned}
\sum F_{x_4}:&\quad -2\cdot T_T\cdot sin(\theta_{Tstatic}-\theta_T) + sin(\theta_W)\cdot T_W - m_4\cdot \ddot{x}_4 = 0\\
\sum F_{y_4}:&\quad -cos(\theta_W)\cdot sin(\varphi_4)\cdot T_W - cos(\theta_{Tstatic}-\theta_T)\cdot sin(\varphi_4)\cdot 2\cdot T_T - m_4\cdot \ddot{y}_4 = 0\\
\sum F_{z_4}:&\quad cos(\theta_W)\cdot cos(\varphi_4)\cdot T_W + cos(\theta_{Tstatic}-\theta_T)\cdot cos(\varphi_4)\cdot 2\cdot T_T - m_4\cdot g - m_4\cdot \ddot{z}_4 = 0\\
\sum M_{y_4}:&\quad -cos(\theta_{Tstatic}-\theta_T)\cdot 2\cdot T_T\cdot cos(\theta_4)\cdot x + sin(\theta_{Tstatic}-\theta_T)\cdot 2\cdot T_T\cdot sin(\theta_4)\cdot x +\\
&\qquad cos(\theta_W)\cdot T_W\cdot \left(cos(\theta_4)\cdot x_{cog,mp} - sin(\theta_4)\cdot \frac{1}{2}\cdot D\right)\\
&\qquad + sin(\theta_W)\cdot T_W\cdot \left(sin(\theta_4)\cdot x_{cog,mp} + cos(\theta_4)\cdot \frac{1}{2}\cdot D\right) - I_{yy_{mp}}\cdot \ddot{\theta}_4 = 0
\end{aligned}
$$

F.3 Equations of motion of the compensated case in matrix form

$$\mathbf{A}=\begin{bmatrix}
m_1\cdot l_1\cdot cos(\theta_1) & 0 & 0 & 0 & 0 & 0 & 0 & 0 & 0 & sin(\theta_1) & -sin(\theta_2) & 0 & 0 & 0\\
0 & -m_1\cdot l_1\cdot cos(\varphi_1) & 0 & 0 & 0 & 0 & 0 & 0 & 0 & -sin(\varphi_1) & sin(\varphi_2) & 0 & 0 & 0\\
-m_1\cdot l_1\cdot sin(\theta_1)\cdot cos(\varphi_1) & -m_1\cdot l_1\cdot sin(\varphi_1)\cdot cos(\theta_1) & 0 & 0 & 0 & 0 & 0 & 0 & 0 & cos(\theta_1)\cdot cos(\varphi_1) & -cos(\theta_2)\cdot cos(\varphi_2) & 0 & 0 & 0\\
m_2\cdot l_1\cdot cos(\theta_1) & 0 & m_2\cdot l_2\cdot cos(\theta_2) & 0 & 0 & 0 & 0 & 0 & 0 & 0 & sin(\theta_2) & -sin(\theta_3) & 0 & 0\\
0 & -m_2\cdot l_1\cdot cos(\varphi_1) & 0 & -m_2\cdot l_2\cdot cos(\varphi_2) & 0 & 0 & 0 & 0 & 0 & 0 & -sin(\varphi_2) & sin(\varphi_3) & 0 & 0\\
-m_2\cdot l_1\cdot sin(\theta_1)\cdot cos(\varphi_1) & -m_2\cdot l_1\cdot sin(\varphi_1)\cdot cos(\theta_1) & -m_2\cdot l_2\cdot sin(\theta_2)\cdot cos(\varphi_2) & -m_2\cdot l_2\cdot sin(\varphi_2)\cdot cos(\theta_2) & 0 & 0 & 0 & 0 & 0 & 0 & cos(\theta_2)\cdot cos(\varphi_2) & -cos(\theta_3)\cdot cos(\varphi_3) & 0 & 0\\
m_3\cdot l_1\cdot cos(\theta_1) & 0 & m_3\cdot l_2\cdot cos(\theta_2) & 0 & m_3\cdot l_3\cdot cos(\theta_3) & 0 & 0 & 0 & 0 & 0 & 0 & sin(\theta_3) & A(7{,}13) & -2\cdot sin(-\theta_{Tstatic}+\theta_T)\\
0 & -m_3\cdot l_1\cdot cos(\varphi_1) & 0 & -m_3\cdot l_2\cdot cos(\varphi_2) & 0 & -m_3\cdot l_3\cdot cos(\varphi_3) & 0 & 0 & 0 & 0 & 0 & -sin(\varphi_3) & A(8{,}13) & 2\cdot sin(\varphi_4)\cdot cos(-\theta_{Tstatic}+\theta_T)\\
-m_3\cdot l_1\cdot sin(\theta_1)\cdot cos(\varphi_1) & -m_3\cdot l_1\cdot sin(\varphi_1)\cdot cos(\theta_1) & -m_3\cdot l_2\cdot sin(\theta_2)\cdot cos(\varphi_2) & -m_3\cdot l_2\cdot sin(\varphi_2)\cdot cos(\theta_2) & -m_3\cdot l_3\cdot sin(\theta_3)\cdot cos(\varphi_3) & -m_3\cdot l_3\cdot sin(\varphi_3)\cdot cos(\theta_3) & 0 & 0 & 0 & 0 & 0 & cos(\theta_3)\cdot cos(\varphi_3) & A(9{,}13) & -2\cdot cos(-\theta_{Tstatic}+\theta_T)\cdot cos(\varphi_4)\\
m_4\cdot l_1\cdot cos(\theta_1) & 0 & m_4\cdot l_2\cdot cos(\theta_2) & 0 & m_4\cdot l_3\cdot cos(\theta_3) & 0 & m_4\cdot cos(-\theta_{Tstatic}+\theta_T)\cdot l_T & 0 & -m_4\cdot sin(\theta_4)\cdot x & 0 & 0 & 0 & A(10{,}13) & 2\cdot sin(-\theta_{Tstatic}+\theta_T)\\
0 & -m_4\cdot l_1\cdot cos(\varphi_1) & 0 & -m_4\cdot l_2\cdot cos(\varphi_2) & 0 & -m_4\cdot l_3\cdot cos(\varphi_3) & m_4\cdot sin(\varphi_4)\cdot sin(-\theta_{Tstatic}+\theta_T)\cdot l_T & A(11{,}8) & m_4\cdot cos(\theta_4)\cdot sin(\varphi_4)\cdot x & 0 & 0 & 0 & A(11{,}13) & -2\cdot sin(\varphi_4)\cdot cos(-\theta_{Tstatic}+\theta_T)\\
-m_4\cdot l_1\cdot sin(\theta_1)\cdot cos(\varphi_1) & -m_4\cdot l_1\cdot sin(\varphi_1)\cdot cos(\theta_1) & -m_4\cdot l_2\cdot sin(\theta_2)\cdot cos(\varphi_2) & -m_4\cdot l_2\cdot sin(\varphi_2)\cdot cos(\theta_2) & -m_4\cdot l_3\cdot sin(\theta_3)\cdot cos(\varphi_3) & -m_4\cdot l_3\cdot sin(\varphi_3)\cdot cos(\theta_3) & -m_4\cdot l_T\cdot sin(-\theta_{Tstatic}+\theta_T)\cdot cos(\varphi_4) & A(12{,}8) & -m_4\cdot x\cdot cos(\theta_4)\cdot cos(\varphi_4) & 0 & 0 & 0 & A(12{,}13) & 2\cdot cos(-\theta_{Tstatic}+\theta_T)\cdot cos(\varphi_4)\\
0 & 0 & 0 & 0 & 0 & 0 & 0 & 0 & -I_{yy_{mp}} & 0 & 0 & 0 & A(13{,}13) & A(13{,}14)\\
0 & 0 & 0 & 0 & 0 & 0 & 0 & 0 & 0 & 0 & 0 & 0 & 1 & 0
\end{bmatrix}$$

$$\vec{B}=\begin{bmatrix}\ddot{\theta}_1\\ \ddot{\varphi}_1\\ \ddot{\theta}_2\\ \ddot{\varphi}_2\\ \ddot{\theta}_3\\ \ddot{\varphi}_3\\ \ddot{\theta}_T\\ \ddot{\varphi}_4\\ \ddot{\theta}_4\\ T_1\\ T_2\\ T_3\\ T_W\\ T_T\end{bmatrix}$$

$$\vec{C}=\begin{bmatrix}
m_1\cdot\Big(l_1\cdot(\dot{\theta}_1)^2\cdot sin(\theta_1)+\ddot{X}_{ct}\Big)\\
m_1\cdot\Big(-l_1\cdot(\dot{\varphi}_1)^2\cdot sin(\varphi_1)+\ddot{Y}_{ct}\Big)\\
m_1\cdot\Big(l_1\cdot(\dot{\theta}_1)^2\cdot cos(\theta_1)\cdot cos(\varphi_1)+l_1\cdot(\dot{\varphi}_1)^2\cdot cos(\varphi_1)\cdot cos(\theta_1)-2\cdot l_1\cdot\dot{\theta}_1\cdot sin(\theta_1)\cdot\dot{\varphi}_1\cdot sin(\varphi_1)+\ddot{Z}_{ct}+g\Big)\\
m_2\cdot\Big(l_1\cdot(\dot{\theta}_1)^2\cdot sin(\theta_1)+l_2\cdot(\dot{\theta}_2)^2\cdot sin(\theta_2)+\ddot{X}_{ct}\Big)\\
m_2\cdot\Big(-l_1\cdot(\dot{\varphi}_1)^2\cdot sin(\varphi_1)-l_2\cdot(\dot{\varphi}_2)^2\cdot sin(\varphi_2)+\ddot{Y}_{ct}\Big)\\
m_2\cdot\Big(l_1\cdot(\dot{\theta}_1)^2\cdot cos(\theta_1)\cdot cos(\varphi_1)+l_1\cdot(\dot{\varphi}_1)^2\cdot cos(\varphi_1)\cdot cos(\theta_1)+l_2\cdot(\dot{\theta}_2)^2\cdot cos(\theta_2)\cdot cos(\varphi_2)+l_2\cdot(\dot{\varphi}_2)^2\cdot cos(\varphi_2)\cdot cos(\theta_2)-2\cdot l_1\cdot\dot{\theta}_1\cdot sin(\theta_1)\cdot\dot{\varphi}_1\cdot sin(\varphi_1)-2\cdot l_2\cdot\dot{\theta}_2\cdot sin(\theta_2)\cdot\dot{\varphi}_2\cdot sin(\varphi_2)+\ddot{Z}_{ct}+g\Big)\\
m_3\cdot\Big(l_1\cdot(\dot{\theta}_1)^2\cdot sin(\theta_1)+l_2\cdot(\dot{\theta}_2)^2\cdot sin(\theta_2)+l_3\cdot(\dot{\theta}_3)^2\cdot sin(\theta_3)+\ddot{X}_{ct}\Big)\\
m_3\cdot\Big(-l_1\cdot(\dot{\varphi}_1)^2\cdot sin(\varphi_1)-l_2\cdot(\dot{\varphi}_2)^2\cdot sin(\varphi_2)-l_3\cdot(\dot{\varphi}_3)^2\cdot sin(\varphi_3)+\ddot{Y}_{ct}\Big)\\
m_3\cdot\Big(l_1\cdot(\dot{\theta}_1)^2\cdot cos(\theta_1)\cdot cos(\varphi_1)+l_1\cdot(\dot{\varphi}_1)^2\cdot cos(\varphi_1)\cdot cos(\theta_1)+l_2\cdot(\dot{\theta}_2)^2\cdot cos(\theta_2)\cdot cos(\varphi_2)+l_2\cdot(\dot{\varphi}_2)^2\cdot cos(\varphi_2)\cdot cos(\theta_2)+l_3\cdot(\dot{\theta}_3)^2\cdot cos(\theta_3)\cdot cos(\varphi_3)+l_3\cdot(\dot{\varphi}_3)^2\cdot cos(\varphi_3)\cdot cos(\theta_3)-2\cdot l_1\cdot\dot{\theta}_1\cdot sin(\theta_1)\cdot\dot{\varphi}_1\cdot sin(\varphi_1)-2\cdot l_2\cdot\dot{\theta}_2\cdot sin(\theta_2)\cdot\dot{\varphi}_2\cdot sin(\varphi_2)-2\cdot l_3\cdot\dot{\theta}_3\cdot sin(\theta_3)\cdot\dot{\varphi}_3\cdot sin(\varphi_3)+\ddot{Z}_{ct}+g\Big)\\
m_4\cdot\Big(l_1\cdot(\dot{\theta}_1)^2\cdot sin(\theta_1)+l_2\cdot(\dot{\theta}_2)^2\cdot sin(\theta_2)+l_3\cdot(\dot{\theta}_3)^2\cdot sin(\theta_3)+l_T\cdot(\dot{\theta}_T)^2\cdot sin(-\theta_{Tstatic}+\theta_T)+x\cdot(\dot{\theta}_4)^2\cdot cos(\theta_4)+\ddot{X}_{ct}\Big)\\
m_4\cdot\Big(-l_1\cdot(\dot{\varphi}_1)^2\cdot sin(\varphi_1)-l_2\cdot(\dot{\varphi}_2)^2\cdot sin(\varphi_2)-l_3\cdot(\dot{\varphi}_3)^2\cdot sin(\varphi_3)-l_T\cdot(\dot{\theta}_T)^2\cdot cos(-\theta_{Tstatic}+\theta_T)\cdot sin(\varphi_4)-2\cdot l_T\cdot\dot{\theta}_T\cdot\dot{\varphi}_4\cdot sin(-\theta_{Tstatic}+\theta_T)\cdot cos(\varphi_4)+x\cdot(\dot{\theta}_4)^2\cdot sin(\theta_4)\cdot sin(\varphi_4)-2\cdot x\cdot\dot{\theta}_4\cdot\cdot\dot{\varphi}_4\cdot cos(\theta_4)\cdot cos(\varphi_4)-l_T\cdot(\dot{\varphi}_4)^2\cdot sin(\varphi_4)\cdot cos(-\theta_{Tstatic}+\theta_T)+x\cdot(\dot{\varphi}_4)^2\cdot sin(\varphi_4)\cdot sin(\theta_4)+\ddot{Y}_{ct}\Big)\\
C(12)\\
0\\
C(14)
\end{bmatrix}$$

$$A(11,8) = -m4 \cdot (cos(-\theta_{Tstatic} + \theta_T) \cdot cos(\varphi_4) \cdot l_T - sin(\theta_4) \cdot cos(\varphi_4) \cdot x)$$

$$A(12,8) = -m_4 \cdot (l_T \cdot sin(\varphi_4) \cdot cos(-\theta_{Tstatic} + \theta_T) - x \cdot sin(\varphi_4) \cdot sin(\theta_4))$$

$$A(7,13) = \frac{-(l_T \cdot sin(-\theta_{Tstatic} + \theta_T) + cos(\theta_4) \cdot x + cos(\theta_4) \cdot x_{cog,mp} - 1/2 \cdot sin(\theta_4) \cdot D)}{(((cos(-\theta_{Tstatic} + \theta_T) \cdot l_T - sin(\theta_4) \cdot x) \cdot cos(\varphi_4) - (sin(\theta_4) \cdot x_{cog,mp} + 1/2 \cdot (cos(\theta_4) \cdot D)) \cdot cos(\varphi_4)) \cdot \sqrt{1 + \frac{(l_T\cdot sin(-\theta_{Tstatic}+\theta_T)+cos(\theta_4)\cdot x+cos(\theta_4)\cdot x_{cog,mp}-1/2\cdot sin(\theta_4)\cdot D)^2}{((cos(-\theta_{Tstatic}+\theta_T)\cdot l_T-sin(\theta_4)\cdot x)\cdot cos(\varphi_4)-(sin(\theta_4)\cdot x_{cog,mp}+1/2\cdot cos(\theta_4)\cdot D)\cdot cos(\varphi_4))^2}}}$$

$$A(8,13) = \frac{sin(\varphi_4)}{\sqrt{1 + \frac{(l_T\cdot sin(-\theta_{Tstatic}+\theta_T)+cos(\theta_4)\cdot x+cos(\theta_4)\cdot x_{cog,mp}-1/2\cdot sin(\theta_4)\cdot D)^2}{((cos(-\theta_{Tstatic}+\theta_T)\cdot l_T-sin(\theta_4)\cdot x)\cdot cos(\varphi_4)-(sin(\theta_4)\cdot x_{cog,mp}+1/2\cdot cos(\theta_4)\cdot D)\cdot cos(\varphi_4))^2}}}$$

$$A(9,13) = \frac{-cos(\varphi_4)}{\sqrt{1 + \frac{(l_T\cdot sin(-\theta_{Tstatic}+\theta_T)+cos(\theta_4)\cdot x+cos(\theta_4)\cdot x_{cog,mp}-1/2\cdot sin(\theta_4)\cdot D)^2}{((cos(-\theta_{Tstatic}+\theta_T)\cdot l_T-sin(\theta_4)\cdot x)\cdot cos(\varphi_4)-(sin(\theta_4)\cdot x_{cog,mp}+1/2\cdot cos(\theta_4)\cdot D)\cdot cos(\varphi_4))^2}}}$$

$$A(10,13) = \frac{l_T \cdot sin(-\theta_{Tstatic} + \theta_T) + cos(\theta_4) \cdot x + cos(\theta_4) \cdot x_{cog,mp} - 1/2 \cdot sin(\theta_4) \cdot D}{((cos(-\theta_{Tstatic} + \theta_T) \cdot l_T - sin(\theta_4) \cdot x) \cdot cos(\varphi_4) - (sin(\theta_4) \cdot x_{cog,mp} + 1/2 \cdot cos(\theta_4) \cdot D) \cdot cos(\varphi_4)) \cdot \sqrt{1 + \frac{(l_T\cdot sin(-\theta_{Tstatic}+\theta_T)+cos(\theta_4)\cdot x+cos(\theta_4)\cdot x_{cog,mp}-1/2\cdot sin(\theta_4)\cdot D)^2}{((cos(-\theta_{Tstatic}+\theta_T)\cdot l_T-sin(\theta_4)\cdot x)\cdot cos(\varphi_4)-(sin(\theta_4)\cdot x_{cog,mp}+1/2\cdot cos(\theta_4)\cdot D)\cdot cos(\varphi_4))^2}}}$$

$$A(11,13) = \frac{-sin(\varphi_4)}{\sqrt{1 + \frac{(l_T\cdot sin(-\theta_{Tstatic}+\theta_T)+cos(\theta_4)\cdot x+cos(\theta_4)\cdot x_{cog,mp}-1/2\cdot sin(\theta_4)\cdot D)^2}{((cos(-\theta_{Tstatic}+\theta_T)\cdot l_T-sin(\theta_4)\cdot x)\cdot cos(\varphi_4)-(sin(\theta_4)\cdot x_{cog,mp}+1/2\cdot cos(\theta_4)\cdot D)\cdot cos(\varphi_4))^2}}}$$

$$A(12,13) = \frac{cos(\varphi_4)}{\sqrt{1 + \frac{(l_T\cdot sin(-\theta_{Tstatic}+\theta_T)+cos(\theta_4)\cdot x+cos(\theta_4)\cdot x_{cog,mp}-1/2\cdot sin(\theta_4)\cdot D)^2}{((cos(-\theta_{Tstatic}+\theta_T)\cdot l_T-sin(\theta_4)\cdot x)\cdot cos(\varphi_4)-(sin(\varphi_4)\cdot x_{cog,mp}+1/2\cdot cos(\theta_4)\cdot D)\cdot cos(\varphi_4))^2}}}$$

$$\begin{aligned} A(13,13) = {} & \frac{cos(\theta_4) \cdot x_{cog,mp} - 1/2 \cdot sin(\theta_4) \cdot D}{\sqrt{1 + \frac{(l_T\cdot sin(-\theta_{Tstatic}+\theta_T)+cos(\theta_4)\cdot x+cos(\theta_4)\cdot x_{cog,mp}-1/2\cdot sin(\theta_4)\cdot D)^2}{((cos(-\theta_{Tstatic}+\theta_T)\cdot l_T-sin(\theta_4)\cdot x)\cdot cos(\varphi_4)-(sin(\theta_4)\cdot x_{cog,mp}+1/2\cdot cos(\theta_4)\cdot D)\cdot cos(\varphi_4))^2}}} \\ & + \frac{(l_T \cdot sin(-\theta_{Tstatic} + \theta_T) + cos(\theta_4) \cdot x + cos(\theta_4) \cdot x_{cog,mp} - 1/2 \cdot sin(\theta_4) \cdot D) \cdot (sin(\theta_4) \cdot x_{cog,mp} + 1/2 \cdot cos(\theta_4) \cdot D)}{((cos(-\theta_{Tstatic} + \theta_T) \cdot l_T - sin(\theta_4) \cdot X) \cdot cos(\varphi_4) - (sin(\theta_4) \cdot x_{cog,mp} + 1/2 \cdot cos(\theta_4) \cdot D) \cdot cos(\varphi_4)) \cdot \sqrt{1 + \frac{(l_T\cdot sin(-\theta_{Tstatic}+\theta_T)+cos(\theta_4)\cdot x+cos(\theta_4)\cdot x_{cog,mp}-1/2\cdot sin(\theta_4)\cdot D)^2}{((cos(-\theta_{Tstatic}+\theta_T)\cdot l_T-sin(\theta_4)\cdot x)\cdot cos(\varphi_4)-(sin(\theta_4)\cdot x_{cog,mp}+1/2\cdot cos(\theta_4)\cdot D)\cdot cos(\varphi_4))^2}}} \end{aligned}$$

$$A(13,14) = -2 \cdot cos(-\theta_{Tstatic} + \theta_T) \cdot cos(\theta_4) \cdot x - 2 \cdot sin(-\theta_{Tstatic} + \theta_T) \cdot sin(\theta_4) \cdot x$$

$$
\begin{aligned}
C(12) = m_4 \cdot \Big(& l_1 \cdot (\dot{\theta}_1)^2 \cdot cos(\theta_1) \cdot cos(\varphi_1) + l_1 \cdot (\dot{\varphi}_1)^2 \cdot cos(\varphi_1) \cdot cos(\theta_1) + l_2 \cdot (\dot{\theta}_2)^2 \cdot cos(\theta_2) \cdot cos(\varphi_2) + l_2 \cdot (\dot{\varphi}_2)^2 \cdot cos(\varphi_2) \cdot cos(\theta - 2) + l_3 \cdot (\dot{\theta}_3)^2 \cdot cos(\theta_3) \cdot cos(\varphi_3) + l_3 \cdot (\dot{\varphi}_3)^2 \cdot cos(\varphi_3) \cdot cos(\theta_3) + l_T \cdot (\dot{\theta}_T)^2 \cdot cos(-\theta_{Tstatic} + \theta_T) \cdot cos(\varphi_4) + l_T \cdot (\dot{\varphi}_4)^2 \cdot cos(\varphi_4) \cdot cos(-\theta_{Tstatic} + \theta_T) - x \cdot (\dot{\theta}_4)^2 \cdot sin(\theta_4) \cdot cos(\varphi_4) - x \cdot (\dot{\varphi}_4)^2 \cdot cos(\varphi_4) \cdot sin(\theta_4) \\
& - 2 \cdot l_1 \cdot \dot{\theta}_1 \cdot sin(\theta_1) \cdot \dot{\varphi}_1 \cdot sin(\varphi_1) - 2 \cdot l_2 \cdot \dot{\theta}_2 \cdot sin(\theta_2) \cdot \dot{\varphi}_2 \cdot sin(\varphi_2) - 2 \cdot l_3 \cdot \dot{\theta}_3 \cdot sin(\theta_3) \cdot \dot{\varphi}_3 \cdot sin(\varphi_3) - 2 \cdot l_T \cdot \dot{\theta}_T \cdot \dot{\varphi}_4 \cdot sin(-\theta_{Tstatic} + \theta_T) \cdot sin(\varphi_4) - 2 \cdot x \cdot \dot{\varphi}_4 \cdot \dot{\theta}_4 \cdot sin(\varphi_4) \cdot cos(\theta_4) + \ddot{Z}_{ct} + g \Big)
\end{aligned}
$$

$$
\begin{aligned}
C(14) = k_{spring} \cdot \Big(& \sqrt{(l_T \cdot sin(-\theta_{Tstatic} + \theta_T) + cos(\theta_4) \cdot x + cos(\theta_4) \cdot x_{cog,mp} - 1/2 \cdot sin(\theta_4) \cdot D)^2 + (-(cos(-\theta_{Tstatic} + \theta_T) \cdot l_T - sin(\theta_4) \cdot x) \cdot sin(\varphi_4) + 1/2 \cdot sin(\varphi_4) \cdot D)^2 + ((cos(-\theta_{Tstatic} + \theta_T) \cdot l_T - sin(\theta_4) \cdot x) \cdot cos(\varphi_4) - (sin(\theta_4) \cdot x_{cog,mp} + 1/2 \cdot cos(\theta_4) \cdot D) \cdot cos(\varphi_4))^2} - L_{s0} \Big) \\
+ c_{damp} \cdot & \frac{1}{2 \cdot \sqrt{(l_T \cdot sin(-\theta_{Tstatic} + \theta_T) + cos(\theta_4) \cdot x + cos(\theta_4) \cdot x_{cog,mp} - 1/2 \cdot sin(\theta_4) \cdot D)^2 + (-(cos(-\theta_{Tstatic} + \theta_T) \cdot l_T - sin(\theta_4) \cdot x) \cdot sin(\varphi_4) + 1/2 \cdot sin(\varphi_4) \cdot D)^2 + ((cos(-\theta_{Tstatic} + \theta_T) \cdot l_T - sin(\theta_4) \cdot x) \cdot cos(\varphi_4) - (sin(\theta_4) \cdot x_{cog,mp} + 1/2 \cdot cos(\theta_4) \cdot D) \cdot cos(\varphi_4))^2}} \\
& \cdot \Bigg(2 \cdot \Big(- l_1 \cdot sin(\theta_1) - l_2 \cdot sin(\theta_2) - l_3 \cdot sin(\theta_3) + X_{ct} \Big) \cdot \Big(- l_1 \cdot \dot{\theta}_1 \cdot cos(\theta_1) - l_2 \cdot \dot{\theta}_2 \cdot cos(\theta_2) - l_3 \cdot \dot{\theta}_3 \cdot cos(\theta_3) + \dot{X}_{ct} \Big) - 2 \cdot \Big(- l_1 \cdot \dot{\theta}_1 \cdot cos(\theta_1) - l_2 \cdot \dot{\theta}_2 \cdot cos(\theta_2) - l_3 \cdot \dot{\theta}_3 \cdot cos(\theta_3) + \dot{X}_{ct} \Big) \cdot \Big(- l_1 \cdot sin(\theta_1) - l_2 \cdot sin(\theta_2) - l_3 \cdot sin(\theta_3) - l_T \cdot sin(-\theta_{Tstatic} + \theta_T) \\
& - cos(\theta_4) \cdot x - cos(\theta_4) \cdot x_{cog,mp} + 1/2 \cdot sin(\theta_4) \cdot D + X_{ct} \Big) - 2 \cdot \Big(- l_1 \cdot sin(\theta_1) - l_2 \cdot sin(\theta_2) - l_3 \cdot sin(\theta_3) + X_{ct} \Big) \cdot \Big(- l_1 \cdot \dot{\theta}_1 \cdot cos(\theta_1) - l_2 \cdot \dot{\theta}_2 \cdot cos(\theta_2) - l_3 \cdot \dot{\theta}_3 \cdot cos(\theta_3) - l_T \cdot \dot{\theta}_T \cdot cos(-\theta_{Tstatic} + \theta_T) + sin(\theta_4) \cdot \dot{\theta}_4 \cdot x + x_{cog,mp} \cdot \dot{\theta}_4 \cdot sin(\theta_4) + 1/2 \cdot \dot{\theta}_4 \cdot cos(\theta_4) \cdot D + \dot{X}_{ct} \Big) \\
& + 2 \cdot \Big(- l_1 \cdot sin(\theta_1) - l_2 \cdot sin(\theta_2) - l_3 \cdot sin(\theta_3) - l_T \cdot sin(-\theta_{Tstatic} + \theta_T) - cos(\theta_4) \cdot x - cos(\theta_4) \cdot x_{cog,mp} + 1/2 \cdot sin(\theta_4) \cdot D + X_{ct} \Big) \cdot \Big(- l_1 \cdot \dot{\theta}_1 \cdot cos(\theta_1) - l_2 \cdot \dot{\theta}_2 \cdot cos(\theta_2) - l_3 \cdot \dot{\theta}_3 \cdot cos(\theta_3) - l_T \cdot \dot{\theta}_T \cdot cos(-\theta_{Tstatic} + \theta_T) + sin(\theta_4) \cdot \dot{\theta}_4 \cdot x + x_{cog,mp} \cdot \dot{\theta}_4 \cdot sin(\theta_4) + 1/2 \cdot \dot{\theta}_4 \cdot cos(\theta_4) \cdot D + \dot{X}_{ct} \Big) \\
& + 2 \cdot \Big(l_1 \cdot sin(\varphi_1) + l_2 \cdot sin(\varphi_2) + l_3 \cdot sin(\varphi_3) + Y_{ct} \Big) \cdot \Big(l_1 \cdot \dot{\varphi}_1 \cdot cos(\varphi_1) + l_2 \cdot \dot{\varphi}_2 \cdot cos(\varphi_2) + l_3 \cdot \dot{\varphi}_3 \cdot cos(\varphi_3) + \dot{Y}_{ct} \Big) - 2 \cdot \Big(l_1 \cdot \dot{\varphi}_1 \cdot cos(\varphi_1) + l_2 \cdot \dot{\varphi}_2 \cdot cos(\varphi_2) + l_3 \cdot \dot{\varphi}_3 \cdot cos(\varphi_3) + \dot{Y}_{ct} \Big) \cdot \Big(l_1 \cdot sin(\varphi_1) + l_2 \cdot sin(\varphi_2) + l_3 \cdot sin(\varphi_3) + (cos(-\theta_{Tstatic} + \theta_T) \cdot l_T - sin(\theta_4) \cdot x) \cdot sin(\varphi_4) - 1/2 \cdot sin(\varphi_4) \cdot D + Y_{ct} \Big) \\
& - 2 \cdot \Big(l_1 \cdot sin(\varphi_1) + l_2 \cdot sin(\varphi_2) + l_3 \cdot sin(\varphi_3) + Y_{ct} \Big) \cdot \Big(l_1 \cdot \dot{\varphi}_1 \cdot cos(\varphi_1) + l_2 \cdot \dot{\varphi}_2 \cdot cos(\varphi_2) + l_3 \cdot \dot{\varphi}_3 \cdot cos(\varphi_3) - l_T \cdot \dot{\theta}_T \cdot sin(-\theta_{Tstatic} + \theta_T) \cdot sin(\varphi_4) + l_T \cdot \dot{\varphi}_4 \cdot cos(\varphi_4) \cdot cos(-\theta_{Tstatic} + \theta_T) - x \cdot \dot{\theta}_4 \cdot cos(\theta_4) \cdot sin(\varphi_4) - x \cdot \dot{\varphi}_4 \cdot cos(\varphi_4) \cdot sin(\theta_4) - 1/2 \cdot D \cdot \dot{\varphi}_4 \cdot cos(\varphi_4) + \dot{Y}_{ct} \Big) \\
& + 2 \cdot \Big(l_1 \cdot sin(\varphi_1) + l_2 \cdot sin(\varphi_2) + l_3 \cdot sin(\varphi_3) + (cos(-\theta_{Tstatic} + \theta_T) \cdot l_T - sin(\theta_4) \cdot x) \cdot sin(\varphi_4) - 1/2 \cdot sin(\varphi_4) \cdot D + Y_{ct} \Big) \cdot \Big(l_1 \cdot \dot{\varphi}_1 \cdot cos(\varphi_1) + l_2 \cdot \dot{\varphi}_2 \cdot cos(\varphi_2) + l_3 \cdot \dot{\varphi}_3 \cdot cos(\varphi_3) - l_T \cdot \dot{\theta}_T \cdot sin(-\theta_{Tstatic} + \theta_T) \cdot sin(\varphi_4) + l_T \cdot \dot{\varphi}_4 \cdot cos(\varphi_4) \cdot cos(-\theta_{Tstatic} + \theta_T) - x \cdot \dot{\theta}_4 \cdot cos(\theta_4) \cdot sin(\varphi_4) \\
& - x \cdot \dot{\varphi}_4 \cdot cos(\varphi_4) \cdot sin(\theta_4) - 1/2 \cdot D \cdot \dot{\varphi}_4 \cdot cos(\varphi_4) + \dot{Y}_{ct} \Big) + 2 \cdot \Big(- l_1 \cdot cos(\theta_1) \cdot cos(\varphi_1) - l_2 \cdot cos(\theta_2) \cdot cos(\varphi_2) - l_3 \cdot cos(\theta_3) \cdot cos(\varphi_3) + Z_{ct} \Big) \cdot \Big(l_1 \cdot \dot{\theta}_1 \cdot sin(\theta_1) \cdot cos(\varphi_1) + l_1 \cdot \dot{\varphi}_1 \cdot cos(\theta_1) \cdot sin(\varphi_1) + l_2 \cdot \dot{\theta}_2 \cdot sin(\theta_2) \cdot cos(\varphi_2) + l_2 \cdot \dot{\varphi}_2 \cdot cos(\theta_2) \cdot sin(\varphi_2) + l_3 \cdot \dot{\theta}_3 \cdot sin(\theta_3) \cdot cos(\varphi_3) + l_3 \cdot \dot{\varphi}_3 \cdot cos(\theta_3) \cdot sin(\varphi_3) \cdot \dot{Z}_{ct} \Big) \\
& - 2 \cdot \Big(l_1 \cdot \dot{\theta}_1 \cdot sin(\theta_1) \cdot cos(\varphi_1) + l_1 \cdot \dot{\varphi}_1 \cdot cos(\theta_1) \cdot sin(\varphi_1) + l_2 \cdot \dot{\theta}_2 \cdot sin(\theta_2) \cdot cos(\varphi_2) + l_2 \cdot \dot{\varphi}_2 \cdot cos(\theta_2) \cdot sin(\varphi_2) + l_3 \cdot \dot{\theta}_3 \cdot sin(\theta_3) \cdot cos(\varphi_3) + l_3 \cdot \dot{\varphi}_3 \cdot cos(\theta_3) \cdot sin(\varphi_3) \cdot \dot{Z}_{ct} \Big) \cdot \Big(- l_1 \cdot cos(\theta_1) \cdot cos(\varphi_1) - l_2 \cdot cos(\theta_2) \cdot cos(\varphi_2) - l_3 \cdot cos(\theta_3) \cdot cos(\varphi_3) - (cos(-\theta_{Tstatic} + \theta_T) \cdot l_T - sin(\theta_4) \cdot x) \cdot cos(\varphi_4) \\
& + (sin(\theta_4) \cdot x_{cog,mp} + 1/2 \cdot cos(\theta_4) \cdot D) \cdot cos(\varphi_4) + Z_{ct} \Big) - 2 \cdot \Big(- l_1 \cdot cos(\theta_1) \cdot cos(\varphi_1) - l_2 \cdot cos(\theta_2) \cdot cos(\varphi_2) - l_3 \cdot cos(\theta_3) \cdot cos(\varphi_3) + Z_{ct} \Big) \cdot \Big(l_1 \cdot \dot{\theta}_1 \cdot sin(\theta_1) \cdot cos(\varphi_1) + l_1 \cdot \dot{\varphi}_1 \cdot cos(\theta_1) \cdot sin(\varphi_1) + l_2 \cdot \dot{\theta}_2 \cdot sin(\theta_2) \cdot cos(\varphi_2) + l_2 \cdot \dot{\varphi}_2 \cdot cos(\theta_2) \cdot sin(\varphi_2) + l_3 \cdot \dot{\theta}_3 \cdot sin(\theta_3) \cdot cos(\varphi_3) + l_3 \cdot \dot{\varphi}_3 \cdot cos(\theta_3) \cdot sin(\varphi_3) \\
& + l_T \cdot \dot{\theta}_T \cdot sin(-\theta_{Tstatic} + \theta_T) \cdot cos(\varphi_4) + l_T \cdot \dot{\varphi}_4 \cdot sin(\varphi_4) \cdot cos(-\theta_{Tstatic} + \theta_T) + x \cdot \dot{\theta}_4 \cdot cos(\theta_4) \cdot cos(\varphi_4) - x \cdot \dot{\varphi}_4 \cdot sin(\varphi_4) \cdot sin(\theta_4) + x_{cog,mp} \cdot \dot{\theta}_4 \cdot cos(\theta_4) \cdot cos(\varphi_4) - x_{cog,mp} \cdot \dot{\varphi}_4 \cdot sin(\varphi_4) \cdot sin(\theta_4) - 1/2 \cdot D \cdot \dot{\theta}_4 \cdot sin(\theta_4) \cdot cos(\varphi_4) - 1/2 \cdot D \cdot \dot{\varphi}_4 \cdot sin(\varphi_4) \cdot cos(\theta_4) + \dot{Z}_{ct} \Big) \\
& + 2 \cdot \Big(- l_1 \cdot cos(\theta_1) \cdot cos(\varphi_1) - l_2 \cdot cos(\theta_2) \cdot cos(\varphi_2) - l_3 \cdot cos(\theta_3) \cdot cos(\varphi_3) - (cos(-\theta_{Tstatic} + \theta_T) \cdot l_T - sin(\theta_4) \cdot x) \cdot cos(\varphi_4) + (sin(\theta_4) \cdot x_{cog,mp} + 1/2 \cdot cos(\theta_4) \cdot D) \cdot cos(\varphi_4) + Z_{ct} \Big) \cdot \Big(l_1 \cdot \dot{\theta}_1 \cdot sin(\theta_1) \cdot cos(\varphi_1) + l_1 \cdot \dot{\varphi}_1 \cdot cos(\theta_1) \cdot sin(\varphi_1) + l_2 \cdot \dot{\theta}_2 \cdot sin(\theta_2) \cdot cos(\varphi_2) + l_2 \cdot \dot{\varphi}_2 \cdot cos(\theta_2) \cdot sin(\varphi_2) \\
& + l_3 \cdot \dot{\theta}_3 \cdot sin(\theta_3) \cdot cos(\varphi_3) + l_3 \cdot \dot{\varphi}_3 \cdot cos(\theta_3) \cdot sin(\varphi_3) + l_T \cdot \dot{\theta}_T \cdot sin(-\theta_{Tstatic} + \theta_T) \cdot cos(\varphi_4) + l_T \cdot \dot{\varphi}_4 \cdot sin(\varphi_4) \cdot cos(-\theta_{Tstatic} + \theta_T) + x \cdot \dot{\theta}_4 \cdot cos(\theta_4) \cdot cos(\varphi_4) - x \cdot \dot{\varphi}_4 \cdot sin(\varphi_4) \cdot sin(\theta_4) + x_{cog,mp} \cdot \dot{\theta}_4 \cdot cos(\theta_4) \cdot cos(\varphi_4) - x_{cog,mp} \cdot \dot{\varphi}_4 \cdot sin(\varphi_4) \cdot sin(\theta_4) - 1/2 \cdot D \cdot \dot{\theta}_4 \cdot sin(\theta_4) \cdot cos(\varphi_4) \\
& - 1/2 \cdot D \cdot \dot{\varphi}_4 \cdot sin(\varphi_4) \cdot cos(\theta_4) + \dot{Z}_{ct} \Big) \Bigg)
\end{aligned}
$$